Proposals for probing BSM in unexplored corners of Top physics and Next-to-Minimal Supersymmetric Standard Model (NMSSM)

A thesis submitted for the degree of

Doctor of Philosophy

in the Faculty of Science

by

Amandip De

under the guidance of

Prof. Rohini M. Godbole & Prof. Sudhir Vempati

भारतीय विज्ञान संस्थान

Centre for High Energy Physics

Indian Institute of Science

Bangalore - 560012, India

August, 2024

To

My Parents

DECLARATION

I hereby declare that the work presented in this thesis entitled "**Proposals for probing BSM in unexplored corners of Top physics and Next-to-Minimal Supersymmetric Standard Model (NMSSM)**" is the outcome of studies and analyses performed by me under the supervision of Prof. Rohini M. Godbole at the Centre for High Energy Physics, Indian Institute of Science, Bengaluru, India. Prof. Sudhir Vempati served as co-supervisor throughout my entire PhD program, providing guidance to ensure the smooth progress of my doctoral studies. The work presented in this thesis has not been submitted elsewhere for obtaining any degree or diploma in any university or institute. Due citations and acknowledgements have been made wherever the work of other investigations have been described.

Date: January 24, 2025

Amandip De

Certified by:

Prof. Sudhir Vempati
Centre for High Energy Physics
Indian Institute of Science
Bengaluru-560012
India

ACKOWLEDGEMENTS

LIST OF PUBLICATION

This thesis is based on the following articles:

1. A. Chakraborty, **A. De**, R. M. Godbole, M. Guchait, "`Tagging a boosted top quark with a` τ `final state`", Phys. Rev. D, 108(3):035011, 2023, [arXiv:2304.12846]

2. A. Adhikary, R. K. Barman, B. Bhattacherjee, A. De, R. M. Godbole, S. Kulkarni, "`Long-lived NLSP in the NMSSM`", Phys.Rev.D 108 (3):035020, 2023, [arXiv:2207.00600]

3. A. Adhikary, R. K. Barman, B. Bhattacherjee, A. De, R. M. Godbole, "`Exploring the Singlino-dominated Thermal Neutralino Dark Matter in the` Z_3 `invariant NMSSM`", [arXiv:2408.03656]

SYNOPSIS

Attempts to arrive at a clear understanding of the laws of nature governing the phenomenon in the universe have guided us to form the Standard Model (SM) of particle physics. The framework of SM, based on the gauge group $SU(3) \times SU(2)_L \times U(1)_Y$ describes nature's fundamental particles and the forces that govern their interactions. Over the last century the SM has been validated by numerous experiments and has helped to understand the nature of matter and energy at the smallest scales. However, despite its triumphs with weak, electromagnetic, and strong interactions, the SM falls short in addressing many experimental observations and theoretical puzzles. Explanation of these necessitates postulation of new physics beyond those in the SM (BSM). Our studies include different approaches to unveil the nature of BSM physics, i.e. particles and/or interactions, ranging from searching for deviations in interactions of known particles like the top quark, which could hint at new forces or couplings in various measurements of the particle properties at high-energy colliders, to direct searches at the collider for the hypothetical particles occurring in some of the possible extensions of the SM, postulated to address its shortcomings.

In the first work, we focus on devising a tagging method in a model-independent framework to identify top quarks in large momentum limit, decaying leptonically to a τ-lepton in the final state. In many SM extensions top quark holds a particular interest since its mass ($m_t \sim 173$ GeV) is near the electroweak symmetry-breaking scale. As a result it becomes a valuable probe to test the Higgs sector of the SM as well as BSM physics. Moreover, compared to the well-understood first two generations, experimental measurements of the properties of third-generation fermions (including the top quark) provide some leeway for potential deviations from the SM, hinting new interactions. Our tagging method makes use of the jet substructure techniques to obtain subjets by reclustering the constituents of the top fatjet with radius of $R = 1.5$. The boosted semileptonically decaying top originates from the decay of a heavy gauge boson viz, W' with $m_{W'} = 1$ TeV following $pp \to W' \to tb \to b\tau\nu_\tau$. The b- and τ- like subjets are identified by applying their standard identification algorithms, where τ-jet identification relies on low multiplicity of highly collimated charged tracks in a cone while b-jets are specified from the nearest B-hadrons. The backgrounds can be rejected

effectively using several kinematic variables constructed from these subjets that fall in a fat-jet mass window of [60,160] GeV, in view of the inability to reconstruct the full top mass due to large missing energy. These variables are (a)the fraction of energy of the fatjet, carried by the identified b- and τ- subjets, (b)the difference of the masses of the $b - \tau$ system and top fatjet, (c)the transverse mass of $b - \tau$ system, (d)subjettiness of a toplike fatjet etc. Utilizing these discriminators in a multivariate technique, a signal efficiency of around 77% can be achieved while keeping the mistagging rate of the QCD jets to 3% level and hadronic top jets to 5%. A strategy similar to this can be applied to other BSM scenarios, including decays of light-charged Higgs, 3rd generation Leptoquark etc. Another unique aspect of the top quark is that the kinematic distributions of its decay products, especially leptons, are sensitive to top polarization, which can reveal information about the chiral structure (including BSM interactions), responsible for its production. In the same work, using observables based on the energy profile of b- and τ- tagged subjets along with their angular correlations measured in the rest frame of $b - \tau$ system, we observe that it is possible to differentiate between the left and right-handed top quarks quite efficiently.

For our next explorations, we turn to one of the most favoured and well-established extensions of the SM within the framework of supersymmetry viz, the next-to-minimal supersymmetric model (NMSSM), which introduces an additional singlet superfield along with two Higgs doublets. The NMSSM extends the Higgs sector with seven Higgs bosons: three CP even, two CP-odd neutrals, and two charged ones, while the electroweak sector constitutes five electrically neutral physical states called as neutralinos arising from mixing of fermionic counterparts of singlet, gauge and Higgs fields viz, singlino, bino, wino and two Higgsinos, respectively. Along with these, there are two charged fermion states (charginos) resulting from the admixture of charged wino and charged Higgsinos. We investigate two corners of the NMSSM parameter space with singlino-like neutralino as the lightest supersymmetric particle (LSP), which is also a dark matter (DM) candidate. First, we explore one of the exotic signatures of BSM physics involving Long-Lived Particles (LLPs) produced in BSM, characterized by a small decay width, $\Gamma \leq 10^{-13}$ GeV. In the later work, by first finding simultaneous compliance with recent results from the analyses performed with LHC data and those from various DM experiments, we proceed to identify interesting signals involving electroweakino decays via BSM Higgs to be explored in colliders.

Experimental searches have largely constrained the parameter space with prompt BSM particles leading to conventional signatures, while LLPs offer intriguing collider signatures

like displaced vertices (DVs), usually uncommon to the SM. We start by searching for long-lived electroweakinos (neutralinos and charginos) in the region of parameter space allowed by current experimental and theoretical constraints for NMSSM. Our investigation shows in the limit of $m_{\mathrm{NLSP}} - m_{\mathrm{LSP}} < m_Z$, it is possible to obtain long-lived binos which undergo three-body decays to singlino-like LSP. We identify viable cascade decay chains featuring the long-lived NLSP decays from chargino-neutralino pair production. This results in a multiboson plus missing energy type signatures in the final state, which is unique to NMSSM. However, due to the high pile-up (140-200 interactions per bunch crossing), it is difficult to extrapolate the reach of current LLP analyses to the HL-LHC level since they primarily use dedicated triggers. In this work, we present a strategy to explore the long-lived decays employing standard triggers like isolated, promptly decaying leptons (e, μ), originating from the decay of gauge and scalar bosons. The DVs concerning LLP decays are identified from the tracks with large transverse impact parameters, $d_0 \geq 2$ mm in close proximity, within the tracker region of the detector. While properties of DV tracks like impact factor, track multiplicity, scalar p_T sum of tracks, etc., allow us to efficiently neglect the very small level of backgrounds exhibited by the SM particle, there are additional background contributions arising from instrumental effects. These are rather challenging to simulate in a pure phenomenological analysis. To overcome this difficulty, we evaluate the instrumental background in a *realistic* signal region adopted by previous CMS and ATLAS analyses and additionally, triple their background estimate while scaling to the HL-LHC luminosity. Our analysis yields a signal significance well above 5σ for the representative benchmark points, suggesting a novel way to probe otherwise challenging regions of the electroweakino parameter space.

In our final exploration, we performed a more general scan to identify the region of NMSSM parameter space where singlino-dominated LSP satisfies the experimentally measured upper limit of the abundance of dark matter in the universe, dubbed as relic density. Our scan covers a large range of LSP mass from 4 GeV to 1 TeV. The resonant s-channel annihilation via the exchange of singlet-like Higgs bosons As/Hs, the Z boson, and the SM-like Higgs boson H_{SM} dominates for relatively light LSP ($\lesssim 100$ GeV) and in the region with LSP mass $\gtrsim 100$ GeV, t-channel annihilation via the exchange of a chargino or neutralino, and co-annihilation with the NLSP predicts approximate relic. We focus on the region $m_{LSP} \lesssim 50$ GeV where DM annihilation takes place primarily via the s-channel exchange of light A_s/H_s with $m_{A_s/H_s} \sim 2m_{LSP}$. The light singlet scalars A_s/H_s proceed to have collimated decays

to $b\bar{b}/\tau^+\tau^-$. These specific BSM Higgs can be incorporated in a cascade chain from similar higgsino-like chargino-neutralino production as our previous work. This can lead to a final state with tri-bosons, a quite distinct possibility of the NMSSM compared to other supersymmetric models. The BSM Higgs ($m_{A_s/H_s} << m_{H_{SM}}$) is reconstructed using similar jet-substructure technique that was adopted in our first project. The other bosons can lead to leptons and missing energy at the collider. The unique peak corresponding to this Higgs in the invariant mass distribution of $b\bar{b}/\tau^+\tau^-$ jets is crucial in reducing all the SM backgrounds. Additional handle comes from the discriminators constructed out of kinematic correlations between the leptons and the reconstructed light Higgs. Our HL-LHC projections show that a high level of signal significance can be attained for this type of experimental signature. Thus, this presents a possibility of exploring the nature of DM in a corner of NMSSM, where direct detection experiments may not have a significant reach in years to come.

CONTENTS

LIST OF TABLES

LIST OF TABLES

LIST OF FIGURES

LIST OF FIGURES

LIST OF FIGURES

CHAPTER 1

INTRODUCTION

The Standard Model (SM) is our current best understanding of fundamental particles and forces in the universe which withstood rigorous experimental tests for decades, making it a cornerstone of modern physics. Despite its remarkable success, SM does not incorporate gravity and fails to account for observed phenomena like dark matter and dark energy. These limitations, along with the experimental discrepancies in measurements of muon magnetic moment, B-meson decays, etc., have invigorated explorations of many extensions of the SM. We begin this chapter with a brief overview of the SM particle spectrum and its underlying gauge structure, the spontaneous electroweak symmetry breaking (EWSB), electroweak currents and how all these explain various experimental results in Sec. 1.1. A concise phenomenology of the SM Higgs boson, including its production and decay modes, with regards to searches performed at the Large Hadron Collider (LHC), is summarized in Sec. 1.2. In many extensions of SM proposed so far, the heaviest fermion, the top quark, plays a crucial role primarily because of its large coupling to the Higgs boson. Next, in Sec. 1.3, we review the production and decay of the top quark, focusing on its special property of polarization where non-SM couplings of the top quark with particles that are expected in Beyond the Standard Model(BSM) physics can occur. The identification of the top (with semileptonic decay to tau) and measurement of its polarization in large momentum limit constitute the basis of Chapter 2. The motivations for exploring the BSM avenues are discussed in Sec. 1.4.

A major part of the thesis explores diverse phenomenological aspects of a well-motivated BSM model, the Next-to-MSSM (NMSSM), a singlet extension of the Minimal Supersymmetric Standard Model (MSSM). We, therefore, review some basics of SUSY, introduce the Minimal Supersymmetric Standard Model (MSSM) and describe the NMSSM in Sec. 1.5-1.8. Along with prompt decays, time-delayed signatures from long-lived particles (LLP) open a new direction for studies to search for BSM physics. We discuss the motivation behind LLP studies, their signatures like displaced vertices (explored in Chapter 3), and challenges associated with them in Sec. 1.9. One of the major drawbacks of SM is that it lacks a suitable dark matter (DM) candidate, and the NMSSM solves this by providing a singlino, fermionic superpartner of singlet, as a DM candidate. With reference to Chapter 4, where the current status of singlino being the DM candidate in light of recent constraints from experiments is studied, we discuss primary DM detection methods and current as well as future limits on DM detection from various experiments in Sec. 1.10. We conclude the present chapter with the structure of this thesis.

1.1 The Standard Model

The SM offers a comprehensive framework for understanding three fundamental forces, i.e. electromagnetic, weak, and strong, while categorizing all identified elementary particles. It encompasses quarks and leptons as the building blocks of matter, along with force-carrying bosons that mediate these interactions. The crowning achievement of the SM was the discovery of the Higgs boson in 2012 [1, 2], which concluded the particle roster and explained the origin of mass for fundamental particles. Various properties of all the SM particles, like mass, charge, spin, and lifetime, along with their discovery timeline, are shown in Fig. 1.1.

1.1.1 Framework of SM

The mathematical framework of SM stands on relativistically invariant quantum field theories (QFT), along with gauge symmetries. To explain the three fundamental forces of nature, it employs a Yang-Mills type QFT, which is grounded in the principle of local gauge invariance of a 'grand unified group' G_{SM} [3–6] as

$$G_{SM} \supset \underbrace{SU(3)_C}_{\text{strong}} \otimes \underbrace{SU(2)_L \otimes U(1)_Y}_{\text{electroweak}} \xrightarrow{\text{EW breaking}} SU(3)_C \otimes \underbrace{U(1)_{em}}_{\text{electromagnetic}} , \qquad (1.1)$$
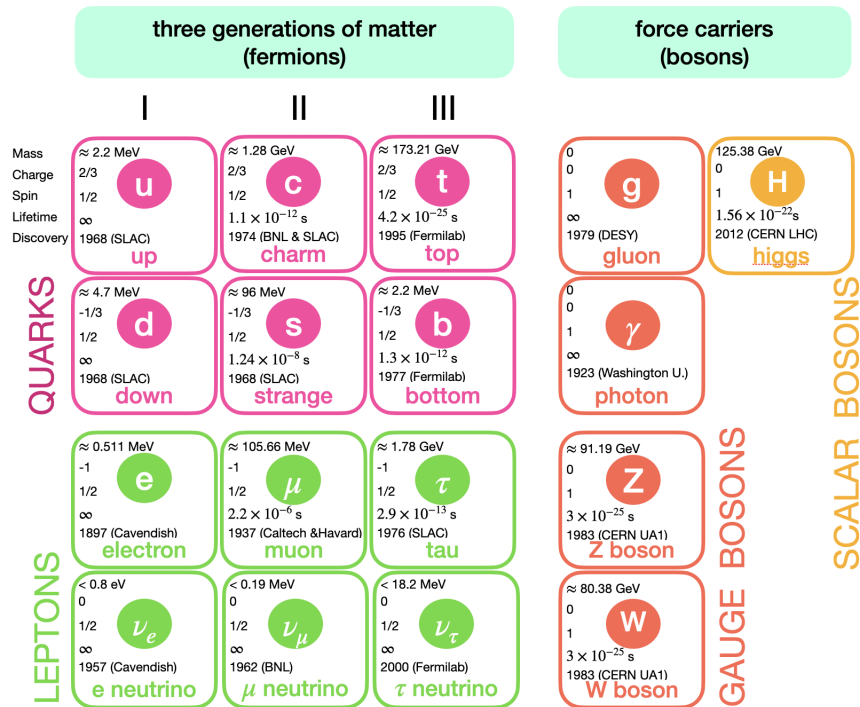
Figure 1.1: Particle spectrum of known elementary particles, predicted in the framework of SM, where *magenta* and *green* depicts the three generations of quarks and leptons respectively, *red* shows the gauge bosons, and *yellow* shows the only fundamental scalar in the SM, the Higgs boson. Each box contains the particle's information, including the discovery timeline and measured properties like mass, charge, spin, and lifetime.

albeit the $SU(2)_L \otimes U(1)_Y$ symmetry is broken spontaneously by *Higgs* mechanism to $U(1)_{em}$. The strong interaction, referred to as quantum chromodynamics (QCD), respects symmetry group $SU(3)_C$ where subscript 'C' refers to color. The $SU(2)_L \otimes U(1)_Y$ describes the unified interactions of weak and electromagnetic as electroweak. The 'L' in $SU(2)_L$ implies solely the left-chiral fermions (and right-chiral anti-fermions) transform non-trivially in the weak theory, which induces parity violation. The subscript 'Y' represents the hypercharge of the fields that define their couplings to the gauge bosons, corresponding to $U(1)$ symmetry. SM incorporates fields with spins $0, \frac{1}{2}$, and 1. The spin $1/2$ fermion fields (quarks and leptons) can be arranged in a threefold family where the quarks come in a triplet of color $alpha$,

$\alpha = 1, 2, 3$. The left-chiral (right-chiral) fields serve as eigenfunctions of chiral projection operators $P_L(P_R)$, denoted as $\psi_L(\psi_R)$ following:

$$\psi_{L,R} = P_{L,R}\psi, \; P_{L,R} = \frac{1 \mp \gamma^5}{2}, \text{ with } \gamma^5 = i\gamma^0\gamma^1\gamma^2\gamma^3. \tag{1.2}$$

All the fermions have both left and right-chiral counterparts, while neutrinos are only left-chiral. The transformation properties of SM fields under these gauge groups before electroweak symmetry breaking (EWSB) are formulated in Table 1.1

Fields	labels	spin	$SU(3)_C \otimes SU(2)_L \otimes U(1)_Y$
Quarks	$Q_{Li}^\alpha = \begin{pmatrix} u_{Li}^\alpha \\ d_{Li}^\alpha \end{pmatrix} \equiv \begin{pmatrix} u_L^\alpha \\ d_L^\alpha \end{pmatrix}, \begin{pmatrix} c_L^\alpha \\ s_L^\alpha \end{pmatrix}, \begin{pmatrix} t_L^\alpha \\ b_L^\alpha \end{pmatrix}$	$\frac{1}{2}$	$(3, \, 2, \, \frac{1}{6})$
	$U_{Ri}^\alpha = u_{Ri}^\alpha \equiv u_R^\alpha, c_R^\alpha, t_R^\alpha$	$\frac{1}{2}$	$(\overline{3}, \, 1, \, \frac{2}{3})$
	$D_{Ri}^\alpha = d_{Ri}^\alpha \equiv d_R^\alpha, s_R^\alpha, b_R^\alpha$	$\frac{1}{2}$	$(\overline{3}, \, 1, \, -\frac{1}{3})$
Leptons	$L_{Li} = \begin{pmatrix} \nu_{Li} \\ e_{Li} \end{pmatrix} \equiv \begin{pmatrix} \nu_e \\ e_L \end{pmatrix}, \begin{pmatrix} \nu_\mu \\ \mu_L \end{pmatrix}, \begin{pmatrix} \nu_\tau \\ \tau_L \end{pmatrix}$	$\frac{1}{2}$	$(1, \, 2, \, -\frac{1}{2})$
	$E_{Ri} = e_{Ri} \equiv e_R, \mu_R, \tau_R$	$\frac{1}{2}$	$(1, \, 1, \, -1)$
Gluons	G_μ^a	1	$(8, \, 1, \, 0)$
W bosons	W_μ^I	1	$(1, \, 3, \, 0)$
B boson	B_μ	1	$(1, \, 1, \, 0)$
Higgs doublet	$\Phi \equiv \begin{pmatrix} \phi^+ \\ \phi^0 \end{pmatrix} \equiv \begin{pmatrix} \phi_1 + i\phi_2 \\ \phi_3 + i\phi_4 \end{pmatrix}$	0	$(1, \, 2, \, \frac{1}{2})$

Table 1.1: The field representations, spins, and gauge transformation properties of the fermions, gauge bosons and Higgs doublet (as a fundamental complex scalar) under the SM gauge group G_{SM} before electroweak symmetry breaking; $i = 1, 2, 3$, $\alpha = 1, 2, 3$, $a = 1, ..., 8$, $I = 1, 2, 3$. The concept of this table is taken from [7].

The left-chiral fermions form isospin doublets ($T = 1/2$) under $SU(2)_L$, while right-chiral fermions correspond to $T = 0$[1]. Q_{Li}^α represents three generations ($i = 1, 2, 3$) with left-handed[2] quark doublets consists of up-type ($T_3 = 1/2$) and down-type ($T_3 = -1/2$) quarks from each generation. They are fundamental representations of triplet and doublet

---

[1]Each representation of $SU(2)$ group has two quantum numbers: T and T_3, where $T : 0, 1/2, 1, 3/2..$ etc. $T_3 \in [-T, T]$ for a specified T.

[2]In the context of massless fermions the word handedness and chirality become synonymous.

under $SU(3)_C$ and $SU(2)_L$ gauge symmetry, respectively. Similarly, with the leptons, the left-chiral charged leptons ($T_3 = -1/2$) and neutrinos ($T_3 = 1/2$) form three generations of left-handed doublets L_{Li} under $SU(2)_L$ while all the leptons are singlet under $SU(3)_C$. All the right-handed fermions are $SU(2)_L$ singlet: $U_{Ri}^\alpha, D_{Ri}^\alpha, E_{Ri}$; while the right-handed quarks denoted by U_{Ri}^α and D_{Ri}^α transform as triplet under $SU(3)_C$. The numbers in the parenthesis in the last column of Table 1.1 represent the transformation properties of the fields under G_{SM}. For example, quark doublet $(u_L^\alpha, d_L^\alpha)^T$ transforms as a triple (3) under $SU(3)_C$, doublet (2) under electroweak group $SU(2)_L \otimes U(1)_Y$ carrying a hypercharge (denoted as $Y/2$) of $1/6$. The assignment of quantum numbers of the electroweak sector is determined from weak isospin T and weak hypercharge Y. A charged fermion's electromagnetic charge (Q) remains constant regardless of its chirality. Additionally, since gauge interaction conserves chirality, the same $U(1)_Y$ charge has to be retained by two left-chiral fermions of distant electromagnetic charges. This ensures that $U(1)_{em}$ can not be the same as the hypercharge, and it arises as a linear combination of $U(1)_Y$ and a $U(1)$ subgroup of $SU(2)_L$ as,

$$Q = T_3 + Y/2. \tag{1.3}$$

Along with the fermion fields, there exist spin 1 gauge bosons associated with the fundamental interactions which interact with the fermions. G_μ^a with $a = 1, ..., 8$ represents gluon fields which mediate the strong interaction between quarks transforms as an octet under adjoint of $SU(3)_C$ corresponding to $3^2 - 1 = 8$ generators of $SU(3)_C$. The generators are 3×3 complex Gell-Mann matrices ($\lambda_a = 1, ..., 8$), which form an 8-dimensional vector space. The gluons and quarks carry an additional colour degree of freedom, ensuring gluons themselves participate in the interaction. W_μ^I, $I = 1, 2, 3$ are the three gauges bosons associated with $T = 1$ representation, an adjoint representation of $SU(2)_L$' where the generators are 2×2 Pauli matrices, σ^I, $I = 1, 2, 3$. Similar to QED, the $U(1)_Y$ gauge group is characterized by a solitary generator B_μ.

In the Lagrangian density, the kinetic terms for fermions and the gauge bosons, along with the self-interactions of the gauge fields, are given by,

$$\mathcal{L}_{Gauge,Fermion} = -\frac{1}{4} B_{\mu\nu} B^{\mu\nu} - \frac{1}{4} W_{\mu\nu}^I W^{\mu\nu I} - \frac{1}{4} G_{\mu\nu}^a G^{\mu\nu\alpha} + \underbrace{i\bar{\psi}_f D_\mu \gamma^\mu \psi_f}_{\mathcal{L}_{fermkin}} \tag{1.4}$$

where $B_{\mu\nu}$, $W_{\mu\nu}^I$ and $G_{\mu\nu}^a$ are the B, W bosons and gluon field strength tensors correspond-

ing to $U(1)_Y$, $SU(2)_L$ and $SU(3)_C$ respectively, defined as

$$B_{\mu\nu} = \partial_\mu B_\nu - \partial_\nu B_\mu$$
$$W^I_{\mu\nu} = \partial_\mu W^I_\nu - \partial_\nu W^I_\mu + g\epsilon^{I\beta\gamma}W^\beta_\mu W^\gamma_\nu, \quad I = 1,2,3 \tag{1.5}$$
$$G^a_{\mu\nu} = \partial_\mu G^a_\nu - \partial_\nu G^a_\mu + g_s f^{abc}W^b_\mu W^c_\nu, \quad a = 1,...,8$$

where f^{abc} and $\epsilon^{I\beta\gamma}$ represents structure constants while g_s and (g) denotes coupling of $SU(3)_C$ and $(SU(2)_L)$ group respectively. The first three terms in Eq.(1.4) describe the kinetic interaction of the gauge fields and their self-interactions, while the last term, $\mathcal{L}_{fermkin}$ represents the kinetic term for fermions and their interactions with gauge bosons. $\mathcal{L}_{fermkin}$ accumulates all five types of fermion fields expressed by the subscript 'f': $\psi_f = (Q^\alpha_{Li}, U^\alpha_{Ri}, D^\alpha_{Ri}, L_{Li}, E_{Ri})$ as

$$\mathcal{L}_{fermikin} = \sum_{i=1}^{3} \left[iL_{Li}\slashed{D}L_{Li} + iE_{Ri}\slashed{D}E_{Ri} + iQ^\alpha_{Li}\slashed{D}Q^\alpha_{Li} + iU^\alpha_{Ri}\slashed{D}U^\alpha_{Ri} + iD^\alpha_{Ri}\slashed{D}D^\alpha_{Ri} \right] \tag{1.6}$$

where D_μ is the covariant derivative whose takes a distinct form when applied on quark and lepton fields with different helicity. For different SM fermions D_μ is expressed as

$$D_\mu Q^\alpha_{Li} = \left(\partial_\mu - i\frac{g'}{2}YB_\mu - i\frac{g}{2}\sigma_I W^I_\mu - i\frac{g_s}{2}G^a_\mu \lambda_a \right) Q^\alpha_{Li}$$
$$D_\mu U^\alpha_{Ri}(D^\alpha_{Ri}) = \left(\partial_\mu - i\frac{g'}{2}YB_\mu - i\frac{g_s}{2}G^a_\mu \lambda_a \right) U^\alpha_{Ri}(D^\alpha_{Ri})$$
$$D_\mu L_{Li} = \left(\partial_\mu - i\frac{g'}{2}YB_\mu - i\frac{g}{2}\sigma_I W^I_\mu \right) L_{Li} \tag{1.7}$$
$$D_\mu E_{Ri} = \left(\partial_\mu - i\frac{g'}{2}YB_\mu \right) E_{Ri}$$

where g' is the $U(1)_Y$ coupling constant.

There is no mass term included in the SM Lagrangian we discussed till now. The reason is that mass terms will violate gauge invariance in the Yang-Mills theory. Explicit breaking of gauge invariance by adding mass terms can violet unitarity and can mean loss of renormalizability. Also, a mass term for fermions will connect a left-handed (transform as a doublet of $SU(2)_L$) to a right-handed spinor field (singlet of $SU(2)_L$), which directly conflicts with the transformation of the $SU(2)$ group. However, various experiments mentioned in Fig. 1.1 observed massive fermions and gauge bosons. In fact, the sole reason of weak interaction being weak at low energy is the suppression from massive mediators by powers

of $1/m_{W,Z}$. A remarkable idea due to Robert Brought, Francois Englert, Peter Higgs and others was put forward such that all the fermions along with W, Z bosons acquire nonzero mass, upholding the mediator of electromagnetic interactions, the photon, massless, while maintaining gauge invariance of $SU(2)_L \otimes U(1)_Y$ [8–11]. We now explain this idea of EWSB via the *Higgs mechanism* and its implications.

1.1.2 Electroweak symmetry breaking and masses

The Eq. (1.4) describes SM Lagrangian for massless gauge bosons where the mass terms are protected by gauge symmetry while the masses of fermions ψ_f are deterred by the chiral symmetry. The Higgs mechanism generates mass terms for SM fields through *'spontaneous'* breaking of the local $SU(2) \otimes U(1)_Y$ symmetry. In context of QFT, spontaneous symmetry breaking (SSB) entails no explicit breaking of the symmetry and is characterized by causing the vacuum, i.e. the ground state of the theory, non-invariant under that symmetry while the Lagrangian still being invariant, keeping the associated currents conserved. SSB commences with the assumption of a complex scalar field Φ, a colour singlet and an $SU(2)_L$ doublet having hypercharge $Y_\Phi = 1$, denoted as

$$\Phi = \begin{pmatrix} \phi_1 + i\phi_2 \\ \phi_3 + i\phi_4 \end{pmatrix} \equiv \begin{pmatrix} \phi^+ \\ \phi^0 \end{pmatrix}. \tag{1.8}$$

Here, Φ is a complex doublet comprised of four real scalar fields (4 degrees of freedom) since we need to generate mass for three vector fields, hence the absorption of 3 independent massless scalars (Goldstone bosons), and $(3 + 1) = 4$ scalar fields[3]. Eq. (1.3) forces the charges of the components of Φ not to be electrically neutral at the same time. One of the components should be neutral such that it can acquire a vacuum expectation value (VEV) without any disastrous physical consequences, and the other component should differ by one unit of charge. However, this implies two choices of hypercharges $Y_\Phi = 1$ (neutral upper component) or $Y_\Phi = -1$ (neutral lower component). It turns out both doubles are needed, which can be achieved by choosing a $Y_\Phi = 1$ doublet of the form of Eq. (1.8),

---

[3]Goldstone theorem: If a global, continuous symmetry G of the complete Lagrangian is spontaneously broken to H which denotes vacuum invariance after SSB, then the number of massless Goldstone bosons is dim(G/H) = dim G - dim H. In gauge theories, the Goldstone bosons are absorbed into the longitudinal degrees of freedom of the massive gauge bosons through SSB. In SM, the associated number of Goldstone bosons = $d_{EW} - d_{em} = 4 - 1 = 3$. Furthermore, after SSB, the number of Higgs particle is $d_D - (d_{EW} - d_{em}) = 4 - (4 - 1) = 1$

where the other doublet is obtained by complex conjugation on Φ as: $\widetilde{\Phi} = i\sigma^2\Phi^* \Rightarrow \widetilde{\Phi}^\dagger = (\phi_3 + i\phi_4, -\phi_1 + i\phi_2)$. Only one Higgs doublet is sufficient to generate masses for both up-type and down-type fermions. The Lagrangian corresponding to Φ reads as

$$\mathcal{L}_{Higgs} = (D_\mu\Phi)^\dagger(D_\mu)\Phi - V(\Phi) \tag{1.9}$$

where D_μ includes the gauge-field couplings:

$$D_\mu\Phi = \left(\partial_\mu - i\frac{g'}{2}YB_\mu - i\frac{g}{2}\sigma_I W^I_\mu\right)\Phi \tag{1.10}$$

and the scalar potential for the Higgs field takes the form of

$$V(\Phi) = -\mu^2\Phi^\dagger\Phi + \lambda(\Phi^\dagger\Phi)^2. \tag{1.11}$$

with $\mu^2 > 0$. The variation of $V(\Phi)$ for different signs of μ^2 and λ is shown in Fig. 1.2. If
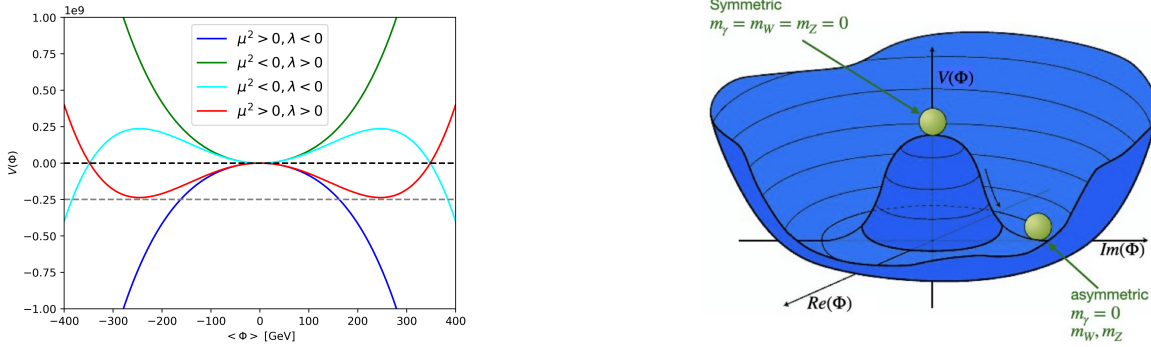
Figure 1.2: *Left:* Plots of Higgs scalar potential $V(\Phi)$ for following Eq. (1.11) for different sign conventions of μ^2 and λ with their absolute values considered at electroweak scale. *Right:* EWSB of the Mexican hat potential of Higgs for $\mu^2, \lambda > 0$.

$\mu^2 > 0$ and $\lambda < 0$, then the potential is not bounded from below, implying the absence of a stable minimum. In case of $\mu^2 < 0, \lambda > 0$, the function $V(\Phi)$ has a stable minimum at $\langle\Phi^\dagger\Phi\rangle_0 = 0$. The choice of $\mu^2, \lambda > 0$ produces a Mexican hat-like potential (referred to as Higgs potential) with a minimum $\langle\Phi^\dagger\Phi\rangle_0 = \mu^2/2\lambda$. An interesting case with $\mu^2 < 0$ and negative λ shows that $V(\Phi)$ is still decreasing for large values of $\langle\Phi\rangle$ and a deeper 'well' or in other words a 'true vacuum' might exist for $\langle\Phi^\dagger\Phi\rangle_0 >> \mu^2/2\lambda$.

In fact, the choice $\mu^2, \lambda > 0$ indicates the classical point $(Re)\phi = (Im)\phi = 0$ is a local maximum, and there exists a nonzero continuum of minima along the rim of the hat, as

displayed in the right panel of Fig. 1.2, all are related by $U(1)$ symmetry transformation of the corresponding Lagrangian. The μ term has an opposite sign compared to the mass terms of the free complex scalar field and is essential for SSB. SSB occurs when one of the four real scalar fields attains a VEV corresponding to one of the minima and breaks the symmetry; here, we choose $\phi_3 = v/\sqrt{(2)}$. The system is characterized by the quantum fluctuations around this minima. When the vacuum fields choose a particular direction in $\phi_1 - \phi_2$ space the $SU(2)$ symmetry is also broken. The vacuum is invariant under the $U(1)$ transformation, which is electromagnetism, and the gauge boson that remains massless is the photon. If ϕ^+ gets a non-zero VEV, then the electric charge would not be conserved. Consequently, only real, electrically neutral scalar fields are permitted to have non-zero VEV ($Q\phi_0 = (T_3 + Y/2)\phi_0 = 0$). This pattern of SSB implies the form of $\langle\Phi_0\rangle$ for $Y_\Phi = 1$ is

$$\langle\Phi\rangle_0 = \begin{pmatrix} 0 \\ v/\sqrt{2} \end{pmatrix}, \text{ with } v = \frac{\mu^2}{2\lambda}. \tag{1.12}$$

Introducing a small fluctuation by a real scalar field $h(x)$ around the VEV, the filed Φ with a new parametrization $\theta_a, a = 1, ...3$ can be expressed as

$$\Phi(x) = \frac{1}{\sqrt{2}} \begin{pmatrix} \theta_2 + i\theta_1 \\ v + h(x) - i\theta_3 \end{pmatrix} \xrightarrow{\theta_a, h(x) \to 0} \exp\left(\frac{i\vec{\theta}(x) \cdot \vec{\sigma}}{v}\right) \begin{pmatrix} 0 \\ v + h(x) \end{pmatrix}. \tag{1.13}$$

This choice is similar to a $SU(2)_L$ gauge transformation of $\Phi \to \Phi' = \exp\left(\frac{i\vec{\theta}(x) \cdot \vec{\sigma}}{v}\right)\Phi$. Eq. (1.12) ensures the VEV of $h(x)$ is also zero. In the *Unitary* gauge, the three scalar degrees of freedom $\vec{\theta}$ correspond to three Goldstone bosons can be rotated away as

$$\Phi'(x) = \frac{1}{\sqrt{2}} \begin{pmatrix} 0 \\ v + h(x) \end{pmatrix}. \tag{1.14}$$

We will see that these three fields will be absorbed by the $W^\pm$ and Z bosons to endow them with longitudinal polarization and, therefore, mass.

Mass generation of bosons

Expanding the kinetic terms of Eq. (1.9) and collecting the quadratic terms in gauge boson fields, we get

$$\frac{1}{8}(v + h)^2[g(W^1_\mu + iW^2_\mu)^2 + (gW^3_\mu - g'B_\mu)^2]. \tag{1.15}$$

Redefining the gauge and photon fields as:

$$W_\mu^\pm = (W^1 \mp iW_m^2 u)$$
$$Z_\mu = \cos\theta_W W_\mu^3 - \sin\theta_W B_\mu \tag{1.16}$$
$$A_\mu = \sin\theta_W W_\mu^3 + \cos\theta_W B_\mu,$$

where the physical neutral fields Z_μ and A_μ results from orthogonal rotation in the W_μ^3, B_μ plane by the electroweak mixing angle θ_W, referred to as the Wienberg angle and is given by

$$\cos\theta_W = \frac{g}{\sqrt{g^2 + g'^2}} \tag{1.17}$$

which is experimentally measured as $\sin^2\theta_W \approx 0.22337 \pm 0.00010$ [12, 13]. With the field transformations mentioned in Eq. (1.16) the mass terms corresponding to $W^\pm, Z, A$ from Eq. (1.15) can be read as

$$\frac{1}{8}v^2[2g^2 W_\mu^+ W^{\mu-} + (g^2 + g'^2)Z_\mu Z^\mu] \tag{1.18}$$

which implies the following masses:

$$M_{W^\pm} = \frac{vg}{2}, \quad M_Z = \frac{1}{2}v\sqrt{g^2 + g'^2} = \frac{M_{W^\pm}}{\cos\theta_W}, \quad M_A = 0. \tag{1.19}$$

Hence, SSB has achieved generating masses for gauge bosons using the gauge invariant kinetic terms of the scalar field, while the photon remains massless but keeps the desired coupling of the photon field A_μ with fermions intact. Further, $M_W^\pm$ and M_Z are related, and Z is generically heavier than the $W^\pm$, which is a direct consequence of electroweak mixing. A theoretical prediction of the SM is a ratio ρ predicted to be unity is defined as

$$\rho = \frac{M_W^2}{M_Z^2 \cos^2\theta_W} = 1. \tag{1.20}$$

The full form of $\mathcal{L}_{Higgs}$ from Eq. (1.9) in terms of field Φ' (see Eq. (1.14)) in Unitary gauge can be expressed as:

$$\mathcal{L}_{Higgs(\Phi')} = \left[M_W^2 W_\mu^+ W^{\mu-} + \frac{1}{2}M_Z^2 Z_\mu Z^\mu\right]\left(1 + \frac{h}{v}\right)^2 + \frac{1}{2}(\partial_\mu h)^2 - \mu^2 h^2 - \lambda v h^3 - \frac{\lambda}{4}h^4$$
$$\equiv \mathcal{L}_{VVh} + \mathcal{L}_h. \tag{1.21}$$

This infers that the VVh coupling strength is directly proportional to the mass of the gauge boson. The mass of the Higgs ($h(x)$) can be derived from Eq. (1.21) as

$$M_h = \sqrt{2}\mu = v\sqrt{2\lambda} \tag{1.22}$$

which is given in terms of self-coupling λ and the VEV v. VEV, v, is determined from the measured Fermi constant (G_μ) to be $v = \sqrt{1/\sqrt{2}G_\mu} \simeq 246$ GeV [12] which is the typical energy scale associated with the electroweak physics. In SM, the masses and the couplings of all the electroweak bosons $M_{W^\pm}, Z$ and h at tree level are determined by g, g', v and λ. Though electroweak precision measurements provided 'indirect' constraints on the Higgs mass, M_h is a free parameter of the SM, and λ is also arbitrary and not fixed by any condition. The experimental discovery of the Higgs boson from CMS and ATLAS collaborations shows its precise mass $M_h = 125.38 \pm 0.14$ GeV [1,2]. This determines self-coupling λ following Eq. (1.22) to be $\lambda = 0.5 M_h^2/v^2 \simeq 0.13$. However, the triple and quartic Higgs couplings (see Eq. (1.21)) still need to be verified 'directly' from experimental measurements.

Flavour mixing

Before moving on to further discussions, we must be alert to the flavour mixing of different generations of fermions. One can naively think that for the hadronic case, due to the doublet configuration of three generations, the weak charge current only allows transition between $u \leftrightarrow d$ and $c \leftrightarrow s$, i.e.

$$J_\mu^{h\,naive} = \bar{u}\gamma_\mu(1-\gamma_5)d + \bar{c}\gamma_\mu(1-\gamma_5)s. \tag{1.23}$$

This type of structure would lead to generation-wise conservation laws, which do not hold true in nature. Experiments do not indicate any separate conservation laws for up/down quarks and strange/charmed quarks. In fact, $K^+(u\bar{s})$ is unstable and the decay $K^+ \to \mu^+\nu_\mu$ occurs with lifetime 1.2×10^{-8}s. Observations like this can be accommodated in a rotated quark doublet, keeping the lepton universality (the coupling constant for the weak charge current, g is universal):

$$\begin{pmatrix} u \\ d' \end{pmatrix}, \begin{pmatrix} c \\ s' \end{pmatrix}, \begin{pmatrix} t \\ b' \end{pmatrix} \tag{1.24}$$

with

$$d' = d\cos\theta_C + s\sin\theta_C$$
$$s' = -d\sin\theta_C + s\cos\theta_C \tag{1.25}$$

where θ_C measures the extent of flavour-mixing, called *Cabibbo angle*[4]. In 1963, Cabibbo first introduced this, whose experimental measured value is $\theta_C \approx 13.04°$. This d' and s' are not quantum states for mass. Hence, we call them "flavor eigenstates"while the original d and s quarks as "mass eigenstates". The b quark from the third doublet also mixes with d and s so that they can couple to u, c, and t, which we address in Sec. 1.1.3. An equivalent current of Eq. (1.23) for leptons means electron-type and muon-type lepton numbers are conserved individually. If the neutrinos are massless, then there would be no mixing, but neutrino oscillation experiments confirm neutrinos can have nonzero masses [14]. We, therefore, choose the lepton doublets such that the masses of neutrinos and mixings can be generated in the framework of SM[5]:

$$\begin{pmatrix} \nu'_e \\ e^- \end{pmatrix}, \begin{pmatrix} \nu'_\mu \\ \mu^- \end{pmatrix}, \begin{pmatrix} \nu'_\tau \\ \tau^- \end{pmatrix} \tag{1.26}$$

The violation of this universality in leptons is still not confirmed experimentally, though some hints from recent explorations exist [15–17]. With these updated primed fields, the spectrum of SM fields (referred to Tab 1.1) stands as follows:

$$Q^\alpha_{Li} = \begin{pmatrix} u^\alpha_L \\ d'^\alpha_L \end{pmatrix}, \begin{pmatrix} c^\alpha_L \\ s'^\alpha_L \end{pmatrix}, \begin{pmatrix} t^\alpha_L \\ b'^\alpha_L \end{pmatrix}, U^\alpha_{Ri} \equiv u^\alpha_{Ri} = \left(u^\alpha_R, c^\alpha_R, t^\alpha_R \right), D^\alpha_{Ri} \equiv d'^\alpha_{Ri} = \left(d'^\alpha_R, s'^\alpha_R, b'^\alpha_R \right),$$

$$L_{Li} = \begin{pmatrix} \nu'^e_L \\ e_L \end{pmatrix}, \begin{pmatrix} \nu'^\mu_L \\ \mu_L \end{pmatrix}, \begin{pmatrix} \nu'^\tau_L \\ \tau_L \end{pmatrix}, E_{Ri} = \left(e_R, \mu_R, \tau_R \right), \nu'_{Ri} = \left(\nu'^e_R, \nu'^\mu_R, \nu'^\tau_R, \right)$$

$$\tag{1.27}$$

From now on, we will be using these field definitions.

Mass generation of fermions

The mass terms for fermions are rendered following the same mechanism where the Higgs field interacts (Yukawa type) with the left- and right-handed fermions since it is not possible to write gauge-invariant mass terms for SM fermions. The gauge invariant Yukawa

---

[4]We can take the mixing for up-type or down-type quarks. It's just a convention to take the rotation for down-type quarks.

[5]If neutrinos are taken to be Majorana particles, the mass terms will have a form different from that of charged particles. In that case, mixings are generated only in the framework of the models beyond SM (BSM).

components can be written as

$$\mathcal{L}_{Yukawa} = \sum_{i,j=1}^{3} -y_{u_{ij}}\overline{Q}_{Li}^{\alpha}\Phi U_{Rj}^{\alpha} - y_{d_{ij}}\overline{Q}_{Li}^{\alpha}\widetilde{\Phi}D_{Rj}^{\alpha} - y_{e_{ij}}\overline{L}_{Li}\widetilde{\Phi}E_{Rj} + h.c., \; \widetilde{\Phi} = i\sigma_2\Phi'^* \quad (1.28)$$

where i and j denote three generations of leptons and quarks. Using the form of Φ' from Eq. (1.14) in Eq. (1.28) we get

$$\mathcal{L}_{Yukawa} = -\frac{1}{\sqrt{2}}(v+h)\left[y_{uij}\overline{u}_{Li}^{\alpha}u_{Rj}^{\alpha} + y_{dij}\overline{d}_{Li}'^{\alpha}d_{Rj}'^{\alpha} + y_{eij}\overline{e}_{Li}e_{Rj} + h.c.\right]. \quad (1.29)$$

The mass terms for the fermions are:

$$m_{ij}^e = \frac{y_{ij}^e v}{\sqrt{2}}, \quad m_{ij}^{d'} = \frac{y_{ij}^{d'} v}{\sqrt{2}}, \quad m_{ij}^u = \frac{y_{ij}^u v}{\sqrt{2}} \quad \text{(generation space)}$$
$$\Rightarrow m_f = y_f v/\sqrt{2} \quad \text{(mass basis)} \quad (1.30)$$

where f denotes the fermions in mass eigenstates and y_f are diagonal elements of arbitrary Yukawa matrices after diagonalization. Regardless of the Higgs VEV v, the constant y_f can be of any value to match the experimentally measured masses. The characteristic feature of Yukawa coupling is the proportionality of its strength with fermion mass, meaning that heavier particles interact more strongly with the Higgs. Since off-diagonal terms in the Yukawa matrices are non-zero, the weak eigenstates don't directly yield mass terms for fermions. Rather, it requires transformation into mass eigenstates to obtain their masses. For the leptons, no diagonalization is required since they do not have mixing due to massless neutrinos, whereas the matrices for quarks are not diagonal and need unitary transformations to transform from weak eigenstates to mass eigenstates in order to extract masses for them, which impacts the gauge interactions, discussed below.

1.1.3 CKM matrix

The coupling matrices Y_u and Y_d are diagonalized constructing four unitary matices $V_{u,d}^{L,R}$ as:

$$Y_u = V_u^L M_u V_u^{\dagger R}, \quad Y_d = V_d^L M_d V_R^{\dagger R} \quad (1.31)$$

where M_u and M_d are diagonalized Yukawa matrices with y_f in Eq. (1.30): $M_u = \text{Diag}(y_u, y_c, y_t)$ and $M_d = \text{Diag}(y_d, y_s, y_b)$. The corresponding field transformation from weak to mass

eigenstates ($q^{(M)}$) associated to up-type and down-type quarks is written as[6]

$$u_L^{(M)} = V_{uL}u_L, \quad u_R^{(M)} = V_{uR}^\dagger u_R,$$
$$d_L^{(M)} = V_{dL}d_L, \quad d_R^{(M)} = V_{dR}^\dagger d_R. \tag{1.32}$$

With the unitary transformations, the weak Lagrangian describing $W^\pm$ boson exclusively interacting with left-handed fields, expressed in the mass eigenstate basis as,

$$\mathcal{L}_W = \frac{-g}{\sqrt{2}} \begin{pmatrix} \overline{u}_L^{(M)} & \overline{c}_L^{(M)} & \overline{t}_L^{(M)} \end{pmatrix} \gamma^\mu W_\mu^+ V_{uL}V_{dL}^\dagger \begin{pmatrix} d_L^{(M)} \\ s_L^{(M)} \\ b_L^{(M)} \end{pmatrix} + h.c. \tag{1.33}$$

where

$$V_{CKM} \equiv V_{uL}V_{dL}^\dagger = \begin{pmatrix} V_{ud} & V_{us} & V_{ub} \\ V_{cd} & V_{cs} & V_{cb} \\ V_{td} & V_{ts} & V_{tb} \end{pmatrix} \Rightarrow \begin{pmatrix} d' \\ s' \\ b' \end{pmatrix} = \begin{pmatrix} V_{ud} & V_{us} & V_{ub} \\ V_{cd} & V_{cs} & V_{cb} \\ V_{td} & V_{ts} & V_{tb} \end{pmatrix} \begin{pmatrix} d \\ s \\ b \end{pmatrix} \tag{1.34}$$

Hence, the charge current interactions can change the flavour across three generations, and the probability of transition is expressed in terms of Cabibbo-Kobayashi-Maskawa (CKM) matrix (V_{CKM}) [18,19]. In a 2-generation approximation, we may identify from Eq. (1.25) $V_{ud} = \cos\theta_C, V_{us} = \sin\theta_C, V_{cd} = -\sin\theta_C, V_{cs} = \cos\theta_C$. The flavor-changing neutral currents (FCNC) are suppressed in SM and specially sensitive to beyond SM contributions. For neutral currents, $V_{uL/uR}V_{uL/uR}^\dagger$ or $V_{dL/dR}V_{dL/dR}^\dagger$ will be unity and no FCNC at tree level for SM.

The CKM matrix, a 3×3 unitary construct, can be parametrized using three mixing angles and a single CP-violating phase.[7] However, it is possible to select a real mass matrix in dimension two without compromising generality and V_{CKM} will be orthogonal. In that case, one angle would be sufficient to parameterize a real orthogonal matrix and there would be no scope of CP-violation. Out of many possible conversions, a standard choice yields [20]

$$V_{CKM} = \begin{pmatrix} c_{12}c_{13} & s_{12}c_{13} & s_{13}e^{-i\delta} \\ -s_{12}c_{23} - c_{12}s_{23}s_{13}e^{i\delta} & c_{12}c_{23} - s_{12}s_{23}s_{13}e^{i\delta} & s_{23}c_{13} \\ s_{12}s_{23} - c_{12}c_{23}s_{13}e^{i\delta} & -c_{12}s_{23} - s_{12}c_{23}s_{13}e^{i\delta} & c_{23}c_{13} \end{pmatrix} \tag{1.35}$$

---

[6]We are dropping the color indices of quarks (α) for simplicity.

[7]Total number of independent real parameters to parameterized a $n \times n$ mixing matrix is $N = n^2 - 2n + 1$, e.g. for $n = 2$, $N = 1$ (1 angle); $n = 3$ leads to $N = 4$ (3 angles, 1 phase) etc.

where $s_{ij} = \sin\theta_{ij}, c_{ij} = \cos\theta_{ij}$ and the phase factor δ accounts for all CP-violating effects in flavor-changing processes. Experimental findings suggest $s_{13} << s_{23} << s_{12} << 1$, which infers the first two generations mixing is maximum and smaller as we move further from first to third. Neutrino oscillations, as evidenced by the Super-Kamiokande experiment [21], imply non-zero neutrino masses. This necessitates the introduction of a leptonic mixing matrix, analogous to the quark mixing CKM matrix. This lepton mixing matrix is known as the Pontecorvo-Maki-Nakagawa-Sakata (PMNS) matrix [22]. However, in this thesis, we have not considered massive neutrinos and cling onto the established version of SM.

At this point, we have discussed the basic theoretical framework of the SM. Finally, the full SM Lagrangian can be represented by combining Eqs. (1.4), (1.9) and (1.28):

$$\mathcal{L}_{SM} = \mathcal{L}_{Gauge,Fermion} + \mathcal{L}_{Higgs} + \mathcal{L}_{Yukawa}. \tag{1.36}$$

which is invariant under the SM gauge symmetry. This is a good point to summarize the physical currents of the electroweak theory. Starting with the weak charged current (which is $V - A$ type), which can be obtained from kinetic terms of the fermion fields in Eq. (1.6):

$$J_\mu^+ = 2\left(\overline{\nu}_L^i\gamma_\mu e_L^i + \overline{u}_L^i\gamma_\mu V_{ij}d_L^j\right) \tag{1.37}$$

The complex conjugate of this will be $J_\mu^- = (J_\mu^+)^\dagger$. This current should be multiplied by $\frac{g}{2\sqrt{2}}$ when it couples to $W_\mu^\pm$. Here V_{ij} connects u- and d- type quarks of different generations. The neutral currents couples to W_μ^3 are:

$$J_\mu^3 = \frac{1}{2}\overline{\nu}_L^i\gamma_\mu\nu_L^i - \frac{1}{2}\overline{e}_L^i\gamma_\mu e_L^i + \frac{1}{2}\overline{u}_L^i\gamma_\mu u_L^i - \frac{1}{2}\overline{d}_L^{'i}\gamma_\mu d_L^{'i} \tag{1.38}$$

The electromagnetic current is purely vector-like, where each term is weighted with its charge:

$$
\begin{aligned}
J_\mu^{em} &= \sum_i q_i\overline{u}_{L,R}^i\gamma_\mu u_{L,R}^i + \sum_i q_i\overline{d}_{L,R}^{'i}\gamma_\mu d_{L,R}^{'i} + \sum_i l_i\overline{e}_{L,R}^i\gamma_\mu e_{L,R}^i \\
&= -\overline{e}_L^i\gamma_\mu e_L^i - \overline{e}_R^i\gamma_\mu e_R^i + \frac{2}{3}\left(\overline{u}_L^i\gamma_\mu u_L^i + \overline{u}_R^i\gamma_\mu u_R^i\right) - \frac{1}{3}\left(\overline{d}_L^{'i}\gamma_\mu d_L^{'i} + \overline{d}_R^{'i}\gamma_\mu d_R^{'i}\right)
\end{aligned}
\tag{1.39}
$$

The hypercharge current can be obtained from $J_\mu^Y = 2(J_\mu^{em} - J_\mu^3)$, and here the coefficient of each term is the hypercharge of the corresponding field:

$$J_\mu^Y = -\overline{\nu}_L^i\gamma_\mu\nu_L^i - \overline{e}_L^i\gamma_\mu e_L^i - 2\overline{e}_R^i\gamma_\mu e_R^i + \frac{1}{3}\overline{u}_L^i\gamma_\mu u_L^i + \frac{1}{3}\overline{d}_L^{'i}\gamma_\mu d_L^{'i} + \frac{4}{3}\overline{u}_R^i\gamma_\mu u_R^i - \frac{2}{3}\overline{d}_R^{'i}\gamma_\mu d_R^{'i} \tag{1.40}$$

The weak neutral current is given by:

$$
\begin{aligned}
J_\mu^Z = J_\mu^{NC} &= -\frac{1}{2}\frac{g'^2}{g'^2+g^2}J_\mu^Y + \frac{g^2}{g'^2+g^2}J_\mu^3 \\
&= -\frac{1}{2}\sin^2\theta_W J^Y + \cos^2\theta_W J^3 \\
&= J^3 - \sin^2\theta_W J^{em}
\end{aligned}
\tag{1.41}
$$

Inserting Eq. (1.38) and Eq. (1.39) in Eq. (1.41) the weak neutral current becomes

$$
\begin{aligned}
J_\mu^{NC} &= \frac{1}{2}\overline{\nu}_L^i\gamma_\mu\nu_L^i + \left(\sin^2\theta_W - \frac{1}{2}\right)\overline{e}_L^i\gamma_\mu e_L^i \\
&+ \left(\frac{1}{2} - \frac{2}{3}\sin^2\theta_W\right)\overline{u}_L^i\gamma_\mu u_L^i + \left(-\frac{1}{2} + \frac{1}{3}\sin^2\theta_W\right)\overline{d}_L'^i\gamma_\mu d_L'^i \\
&+ \sin^2\theta_W\overline{e}_R^i\gamma_\mu e_R^i - \frac{2}{3}\sin^2\theta_W\overline{u}_R^i\gamma_\mu u_R^i + \frac{1}{3}\sin^2\theta_W\overline{d}_R'^i\gamma_\mu d_R'^i
\end{aligned}
\tag{1.42}
$$

where this current should be multiplied by $g_Z = g/\cos\theta_W$ when it couples to Z_μ.

SM has around 19 free parameters: three coupling constants (g_s, g, g') of three gauge groups $(SU(3)_C, SU(2)_L, U(1)_Y)$ respectively, masses of nine charged fermions (or equivalently the Yukawa couplings), i.e. six quarks $(m_u, m_d, m_s, m_c, m_b, m_t)$ and three leptons (m_e, m_μ, m_τ), four parameters of the CKM matrix $(\theta_{12}, \theta_{23}, \theta_{13}, \delta)$, $v\&\lambda$ of the Higgs field and another strong phase θ_{QCD}. The SM has been tested and validated by experiments in terms of predicting masses of new particles: directly via its free parameters or indirectly by loop effect comparisons, several qualitative and quantitative predictions of physical observables like particle interactions and decay rates in high-precision measurements. We will briefly review them, focusing on the phenomenological aspects of SM Higgs boson.

1.1.4   Predictions and validations of the SM

Discovery of weak neutral current

Besides the charged current (CC) interactions via $W^\pm$ bosons, which were known to exist from β decays, the discovery of weak neutral currents (NC) in 1973 by the Gargamelle bubble chamber experiment at CERN [23, 24], both in hadronic and leptonic production affirms the evidence of weak neutral current. The electroweak model predicts weak neutral currents, which require the existence of Z boson. The discovery involved elastic scattering of neutrino and antineutrino (primarily ν_μ and $\overline{\nu}_\mu$) off nuclear targets in two types of processes:

one is neutrino scattering of hadrons (proton or neutron), and another is the interaction of a neutrino with a single electron in a pure leptonic process

$$\nu_\mu + N \to \nu_\mu + \text{hadrons}, \quad \overline{\nu}_\mu + N \to \overline{\nu}_\mu + \text{hadrons} \tag{1.43}$$

$$\overline{\nu}_\mu + e^- \to \overline{\nu}_\mu + e^-. \tag{1.44}$$

With $(O) \sim 166$ hadronic and one leptonic event, the experiment put a range on $sin^2\theta_W$ from the ratio of NC/CC. This confirms the presence of weak neutral current. Later, in 1983, the existence of the W and Z bosons was confirmed by the UA1 and UA2 experiments at CERN [25–28].

Observation of Charm quark

Recall the weak charged current vertex can alter the flavor not just within the same generation but also when $u-$type and $d-$type quark belong to two different generations (see Eqs. (1.24) and (1.25)) while the neutral current J_μ^{NC} in Eq. (1.42) does not induce transitions involving quarks from different generations with a same electrical charge. The similar is true for leptons, i.e. weak neutral currents do not couple, say, an e^- with a μ^-. Hence, in the electroweak model, the FCNC are naturally not present at the tree level. This led to the prediction of charm quark by Glashow, Iliopoulos and Maiani (GIM) in 1970 [29], some years before its discovery. This was envisioned by studying the decay of K^0 ($d\overline{s}$). Only non-leptonic final states were observed in the decay of K^0 mesons, e.g. $K_L^0 \to \mu^+\mu^-$ decay has an upper limit of branching ratio (BR) of 9×10^{-9}.

$$\frac{\Gamma(K_L^0 \to \mu\mu)}{\Gamma(K_L^0 \to \text{all modes})} = (9.1 \pm 1.9) \times 10^{-9} \tag{1.45}$$

The absence of any $u-d-Z$ vertex in J_μ^{NC} clarifies the absence of pure leptonic decays of K_L^0 via the weak neutral current. The weak neutral current ensures that SM fermions possessing identical electromagnetic charge and handedness are classified under the same EW gauge group. Thus, there should exist a quark $'c'$ with charge $Q_{em} = 2/3$ and a member of the isospin $T_3 = 1/2$ of a $SU(2)$ doublet containing the s quark. The existence of c quark alone is enough to achieve the observed suppression. Though decays by FCNC are forbidden at the tree level, they can take place through loop processes through the CC interactions. From the left diagram of Fig. 1.3 the decay would occur at a much higher rate than what
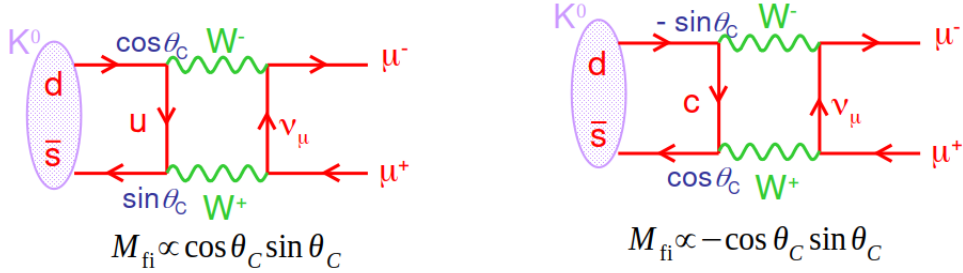
Figure 1.3: Two contributions to $K^0 \rightarrow \mu^+\mu^-$ process. Right Diagram is simply the left diagram with $u \rightarrow c$.

is observed with only $u \rightarrow d'$ transitions. However, due to introduction of the c quark, the right diagram occurs, which would exactly cancel the contribution from the left one if it were not for the mass difference of u and c quark. The range of the mass of the charm quark can be predicted through a comparative analysis of the process rate from computation and matching it with the observed suppression to less than one part in 10^9.

Precision measurements of SM

The precision tests of the SM refer to especially those experiments whose uncertainties are significantly smaller than the previous measurements. The first set of key predictions was in the 1970s with the observation of neutral currents and parity violation in atoms. In the 1980s, the value of $sin^2\theta_W$ was determined from mutually consistent predictions from many different processes. In this regard, the energy dependence of forward-backward asymmetry and that of the cross-section were analysed in $e^-e^- \rightarrow f\overline{f}$. The measurement of $\sin\theta_W$ helps the prediction of W, Z masses as well as their phenomenology, along with $\rho \simeq 1$ well before reaching the centre-of-mass energy ($\sqrt{s}$) of M_Z. In the 1990s, highly successful Z-factories were operating at the Large Electron-Position Collider (LEP) and Stanford Linear Collider (SLC), concentrating precision measurements to confirm the validity of the SM to the one-loop level [30]. With the testing of the ZWW vertex at LEP-II $SU(2)$ symmetry structure, and hence, the correctness of electroweak model predictions at the tree level was established. However, even with the relatively large uncertainties in measurements like W, Z

mass, $\sin\theta_W$, it is essential to include the loop corrections to various observables (primarily through t, b). These loop corrections provide an estimate of the top quark mass (M_t). In the 2000s, witness precise determination of - the mass and width of Z boson, ρ, $\sin^2\theta_W$ with radiative corrections [30], M_t from $p\bar{p}$ collision experiments at CDF and D0 [31, 32], M_W from W pair production at LEP-II [30], muon magnetic moment a_μ at BNL [33], Fermi constant at the MuLan experiment [34]. Along with these and asymmetry observables, a few other variables from polarised e-Deuterium scattering [35, 36], atomic parity violation [37] etc. are tested against a global fit of all these observables including the one loop electroweak radiative corrections in the framework of SM. The SM performs rather well and shows no large deviations. The $\Delta\chi^2$ at a finite nonzero mass gave an 'indirect' proof of the existence of the Higgs boson and its coupling with the gauge bosons and the t quark. The up-to-date global SM fit to electroweak precision data is maintained by the Gfitter group with new developments both in theory and experiment front [38, 39].

Discovery of Higgs boson

Since the proposal of Higgs mechanism, the search of Higgs boson has always been at the forefront of all collider searches. Though in the SM, there is no direct theoretical information on the Higgs mass since it is determined by an arbitrary parameter λ, electroweak precision measurements and in the theoretical front indirect bounds from: unitarity of $W^+W^- \to W^+W^-$ scattering [40], triviality bounds in terms of incorporating loop corrections to the scalar potential in Eq. (1.11) such that λ remains perturbative, which imply an upper bound on the higgs mass [41], opposite to that, the vacuum stability bound puts a lower limit on the M_h [42, 43]. Historically, LEP measurements put a lower bound on M_h, $M_h > 114.4$ GeV [44, 45], Tevatron excluded the mass regions [100-103] GeV and [147-180] GeV at 95% confidence level (CL) for Higgs detection [46]. Finally, the discovery of a spin-0 boson around 125 GeV was published in 2012 by ATLAS and CMS collaborations [1, 2], which has properties similar to the predicted SM Higgs boson. The probes cover different decay modes of Higgs boson including $\gamma\gamma, ZZ^*, WW^*, \tau^+\tau^-b\bar{b}$. It was discovered in two individual decay modes, $h \to \gamma\gamma$, and $h \to ZZ^* \to 4\ell$, independently by CMS and ATLAS with Run-1 data. These two are the cleanest channels in terms of background and identification efficiency. Fig. 1.4 shows the distributions of invariant masses in the two final states comprising di-photon (left plot) and four-lepton (right plot) by CMS. In both plots, a bump, i.e., an excess of events, is visible near the 125 GeV mass region over the SM prediction without the Higgs boson with
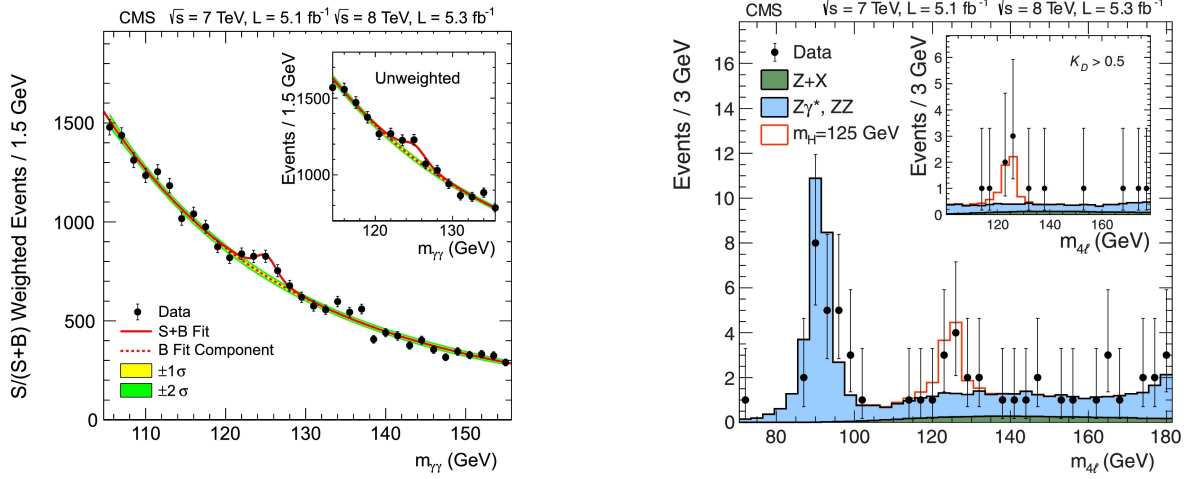
Figure 1.4: From initial CMS measurements, the distribution of *Left:* di-photon invariant mass with each event weighted by $S/S + B$ value of its category where S and B are the numbers of signal and background events to search $h \to \gamma\gamma$ channel. *Right:* four-lepton invariant mass to search $h \to ZZ^* \to 4\ell$ mode. The excess of events observed above the expected backgrounds around $\sim 125\,\text{GeV}$ in both plots with a local significance of 5σ confirms the existence of Higgs boson. The plots are taken from Ref. [2].

discovery level significance of 5σ.

We will now proceed to briefly review two important aspects relevant to this thesis: phenomenology of SM Higgs boson and top quark physics.

1.2 Phenomenology of SM Higgs boson: production and decay modes

Since the discovery of the Higgs-like boson, numerous tests have been performed to check the compatibility of the observed scalar with the SM Higgs boson. Significant efforts have been made to improve the theoretical prediction for Higgs boson production and decay rates, essential for studying its coupling with the fermions and gauge bosons.
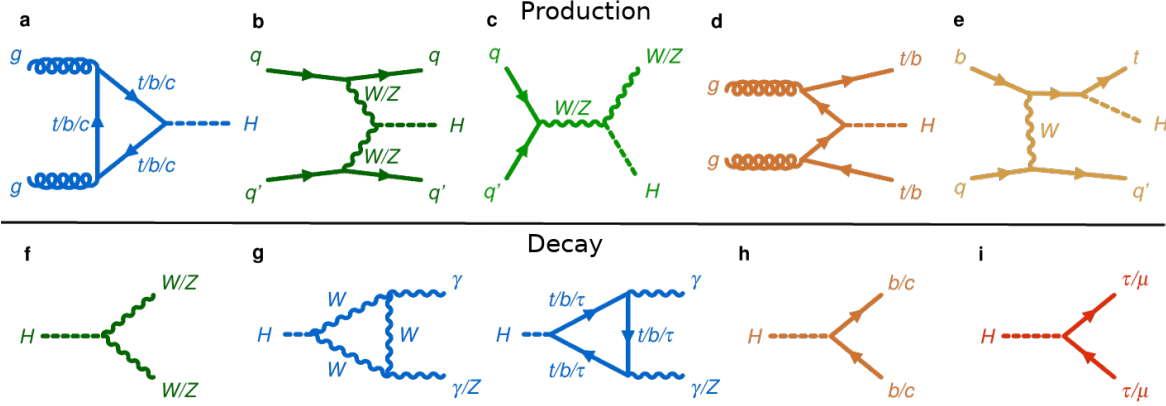
Figure 1.5: Feynman diagrams of different production and decay modes of Higgs boson: Higgs boson production in the Top row (a-e) via (a) gluon-gluon fusion (ggF) (b) vector boson fusion (VBF) (c) associated production with vector bosons (Vh) (d) associated production with top/bottom pair ($t\bar{t}h(b\bar{b}h)$) (e) associated production with single top (th). Bottom row (f-i) denotes the decay modes of Higgs to (f) a pair of vector bosons (g) a pair of photons or a Z boson and a photon (h) a pair of quarks (i) a pair of charged leptons. (Taken from Ref. [47], H in the figure is referred to as h in the text.)

Production of Higgs boson

The most dominant process of Higgs boson production at the LHC is the gluon–gluon fusion process (ggF), which accounts for $\sim 87\%$, shown in Fig. 1.5a. It is a heavy-quark loop-induced process, dominated by the top quark contribution, because of its large Yukawa coupling. Due to the dominance of gluons in the parton density function (PDF) of the colliding proton beams of $\sim$ TeV level energy, this mode has the largest cross-section. The latest precise cross-section of Higgs production via ggH at $\sqrt{s} = 13$ TeV for mass $M_h = 125$ GeV is calculated at N3LO QCD and NLO EW accuracies [48] to be $48.58^{+2.22(+4.56\%)}_{-3.27(-6.72\%)}$ (theory) $\pm$ $1.56(3.20\%)$ (PDF $+ \alpha_s$) pb. The second most dominant production mode is vector boson fusion (VBF) ($\sim 7\%$), in which two weak bosons, either Z or W, fuse to produce a Higgs boson (Fig. 1.5b). The characteristic signature of this process at colliders is the presence of two forward jets, separated in rapidity plane, with large invariant mass accompanying the Higgs decay products. The cross-section of Higgs production by VBF at $\sqrt{s} = 13$ up to NNLO QCD incorporating NLO EW accuracies [49] for $M_h = 125$ GeV is

$3.782^{+0.4\%}_{-0.3\%}$(QCD scale)$^{+2.1\%}_{-2.1\%}$ (PDF $+ \alpha_s$) pb. Next in rate is the production of a Higgs bo-
son in association with a vector boson ($V = W, Z$), which contributes to 4% (Fig. 1.5c).
There is a notable distinction between the Zh and Wh production since Zh can also be pro-
duced at the one-loop level by box diagram $gg \rightarrow Zh$. The total cross-section of Higgs
production by Wh with some approximation [49] at NNLO QCD and NLO EW reads as
$1.373^{+0.5\%}_{-0.7\%}$(QCD scale)$^{+1.9\%}_{-1.7\%}$ (PDF $+ \alpha_s$) pb while the same for Zh combining all the pro-
cesses ($pp \rightarrow Zh$) is $0.8839^{+3.8\%}_{-3.1\%}$(QCD scale)$^{+1.6\%}_{-1.6\%}$ (PDF $+ \alpha_s$) pb [50]. This process can offer
an efficient probe of hVV coupling. Another major higgs production process includes pro-
duction of the Higgs boson in association with a pair of top quarks ($t\bar{t}h$) or bottom quarks
($b\bar{b}h$), each contributes $\sim 1\%$ of the total rate (Fig. 1.5d). This process is of paramount
importance since it directly measures the top quark Yukawa coupling. Here, the cross-
section for the $b\bar{b}h$ mode is computed by combining contribution from 5 flavor scheme (at
NNLO) with 4 flavor scheme (at NLO) by Santander matching [51] without taking any
EW correction into account, which for 125 GeV Higgs at $\sqrt{s} = 13$ TeV turns out to be
$0.488^{+20.2\%}_{-23.9\%}$(QCD scale $+$ PDF $+ \alpha_s$) pb while the same for $t\bar{t}h$, calculated at NLO QCD with
NLO EW is $0.5071^{+5.8\%}_{-9.2\%}$(QCD scale)$^{+3.6\%}_{-3.6\%}$ (PDF $+ \alpha_s$) pb [49]. The contribution of other $q\bar{q}h$
processes is relatively small compared to other Higgs production mechanisms and is not
accessible at colliders. The smallest of all production modes is the associated production of
Higgs with a single top (th) which accounts for $\sim 0.05\%$ (Fig. 1.5e). Though this mode has
not been observed yet at the LHC, contrary to $t\bar{t}h$, it can measure the absolute value of top
Yukawa coupling.

Decay of the Higgs boson

In order to establish the mass generation of the fermions or bosons, it is of prime importance
to predict the Higgs partial decay widths and, hence, the branching ratios of all the decay
modes.

$h \rightarrow f\bar{f}$

Since the couplings of the Higgs boson to fermions are proportional to mass (see Eq. (1.30)),
the most prominent decay mode of the higgs is the heaviest kinematically accessible fermion.
Hence, keeping aside the $t\bar{t}$ mode because of its too off-shell production, the most impor-

tant fermion final states are $b\bar{b}, \tau^+\tau^-, c\bar{c}$ (Fig. 1.5h,i)[8]. The partial width of Higgs to a pair of fermions at tree level is given by

$$\Gamma(h \to f\bar{f}) = \frac{N_c}{8\pi} \frac{m_f^2}{v^2} m_h \left[1 - \frac{4m_f^2}{m_h^2}\right]^{3/2} \tag{1.46}$$

where, N_c is the color factor ($N_C = 3(1)$ for quarks(leptons)). The partial decay width is proportional to the square of the Yukawa coupling and m_h when the decay is well above the threshold (i.e. $m_h >> 2m_f$). Though the $b\bar{b}$ mode accounts for $\sim 57\%$ of the branching ratio, due to overwhelming background from multi-jet QCD process, it is not often favourable to probe until produced in associated production modes like VBF or $t\bar{t}h$. $h \to \tau^+\tau^-$ decays have more favourable circumstances for better signal-to-background ratio. The observation of direct coupling of the Higgs with the third-generation fermions, i.e. top-Higgs Yukawa coupling from observation of $t\bar{t}h$ production [52, 53], b quarks from $h \to b\bar{b}$ [54, 55], τ leptons from $h \to \tau^+\tau^-$ [56, 57] independently by ATLAS and CMS is one of the noteworthy achievements of the LHC experiment with Run-2 data.

$h \to W^+W^-, ZZ$

Higgs mass is not high enough to decay to W^+W^-/ZZ on-shell; one needs to calculate $h \to WW^*$ or ZZ^*. The tree-level Higgs decay width to vector bosons ($h \to W^+W^-/ZZ$) is also proportional to the square of the mass of the vector boson. The WW^* mode accounts for $\sim 21\%$ while branching ratio $BR(h \to ZZ^*) \sim 2.6\%$. Even the $ZZ*$ mode has a relatively low BR, $h \to ZZ^* \to 4\ell$ allows reconstruction of the Higgs boson mass with a sharp resonance (see Fig. 1.4).

$h \to gg, \gamma\gamma, Z\gamma$

Higgs boson does not couple to massless particles, i.e. $gg, \gamma\gamma$ directly, but does so through the loops of massive charged fermions or bosons. $h \to gg$ decay is dominated by the top quark loop with a small contribution from bottom quark loop. $h \to \gamma\gamma$, one of the two Higgs boson discovery channels is induced at one loop level by the W boson while there is a destructive interference by the top loop (bottom and tau lepton contribute little to the partial decay width). Though this channel contributes $\sim 0.2\%$ to the BR, the high resolution in the

---

[8]The QCD correction to $h \to b\bar{b}$ or $c\bar{c}$ is known up to N^4LO.

di-photon invariant mass peak makes it one of the efficient channels for Higgs searches at the LHC. In addition, a rare decay mode $h \to Z\gamma$ having very low branching ratio in the SM, has shown the first evidence at LHC [58].

1.3 Top quark physics

The top quark is the heaviest of all the fundamental particles discovered so far. Third-generation quarks, top and bottom, were predicted to explain the complex phase responsible for CP violation in electroweak decays [19]. The discovery of b quark from $b\bar{b}$ resonance in Y meson led to the conclusion of the top quark's existence in terms of an equal number of lepton and quark generations. The CDF and D0 collaborations at the Tevatron collider [31,32] achieved the groundbreaking discovery of the top quark in 1995. It has mass $\sim 175\,\text{GeV}$, close to the electroweak symmetry breaking scale, allowing it to show the effects of any new physics associated with the EWSB. Because of its extraordinarily large mass, it has a very short lifetime 5×10^{-25} s and hence decays before it can hadronize, which occurs on a time scale $1/\lambda_{QCD} \approx 10^{-24}$ s. Consequently, information regarding properties of the top quark, like its spin state, polarization, etc, are preserved and can be measured through its decay products. This provides a unique opportunity for measurements that are unattainable for light quarks since they can easily form bound states, enabling depolarization of spins via chromomagnetic interactions as in the case of QCD.

1.3.1 Top quark production and decay

Top quarks are predominantly produced in pairs ($t\bar{t}$ production), but single top production is also possible through charged-current interaction via tbW vertex. $t\bar{t}$ is produced via the strong (gluon fusion) and weak interaction ($q\bar{q}$ annihilation). Fig. 1.6 shows the leading order Feynman diagrams for top quark pair production (a-e) and single top production (f-i). Gluon fusion (Fig. 1.6(a-c)) is the dominant LHC process for top pair production because of the large parton distribution function (PDF) for gluons[9] in a proton-proton collision, which accounts for $\sim 80\%$. The other $\sim 20\%$ is form $q\bar{q}$ annihilation processes (Fig. 1.6(d)), which is disfavored with respect to gluon fusion because of the need for a sea-quark from one of the protons to fulfil the requirement of anti-quarks. On the other hand, single top is produced

---

[9]PDFs are a function of momentum transfer, Q^2, and x, the fraction of the incoming proton's longitudinal momentum carried by the parton. At small x, the gluon PDF dominates over anti-quark PDFs.

by electroweak interactions at leading order through three sub-processes: (a) associated production of the top with mostly a light quark by exchange of a virtual W boson in the t-channel (Fig. 1.6(f)) (b) s-channel production of the top with a bottom quark by exchange of a virtual W boson (Fig. 1.6(g)) (c) Wt channel, top in association with a on-shell W boson (Fig. 1.6(h-i)). For single top at LHC the t-channel is the dominant process, sub-leading processes are the gluon-initiated Wt channels, while the least contributing is the s-channel production.

Top quark almost 100% decays to W boson and down type quark within SM. Considering the values of the CKM matrix elements $V_{tb} >> V_{ts} > V_{td}$ the Ws and Wd final states are highly suppressed relative to Wb. The W boson further decays leptonically ($\sim 32.6\%$) into a charged lepton and a neutrino ($e\nu, \mu\nu, \tau\nu$) or hadronically ($\sim 67.4\%$) into two quarks ($q\bar{q}'$). The emitted W boson in top decay cannot be right-handed, i.e. positive helicity. Because of the vector-minus-axial-vector ($V - A$) charged-current weak interaction of top with all other fermions, the W boson only couples to b quark with left chirality, equivalent to left-handed helicity in the massless limit for b-quark. Hence, in the rest frame of the top, the W and b are emitted back-to-back and angular momentum conservation forces the W boson to be left-handed (negative helicity) or a longitudinal (zero helicity) depending on the orientation of the top quark spin.

1.3.2 Top Polarization

New physics (NP) can appear in the production or decay of the top quark when there is a deviation from the SM expectation, some of which includes polarization of the top quark, anomalous tbW-coupling [59, 60] which are being investigated at the LHC. The effective theory formalism to encapsulate the effect of NP in the top sector shows there can be higher dimensional operators [61], which contribute to the top quark vertices like tbW and $t\bar{t}g$. Also, higher-order effects in the SM can introduce corrections to the tree-level vertices [62–64].

The polarization of top quarks produced in hadron colliders, like the LHC, depends on the specific hard subprocesses responsible for their creation. Due to the vector nature of the strong interactions, which conserve parity, top quarks and anti-top quarks exhibit negligible polarization along any direction in the plane of production of $t\bar{t}$ pairs. The "longitudinal polarization" [10] of the top, defined along the direction of the top in the $t\bar{t}$ center of mass frame,

---

[10]The degree of longitudinal polarization ($\mathcal{P}$) is measured by the expectation value of the corresponding

(a) gg t-channel

(b) gg s-channel

(c) gg u-channel

(d) QCD $q\bar{q}$ s-channel

(e) EW $q\bar{q}$ s-channel

(f) t-channel

(g) s-channel

(h) Wt channel

(i) Wt channel
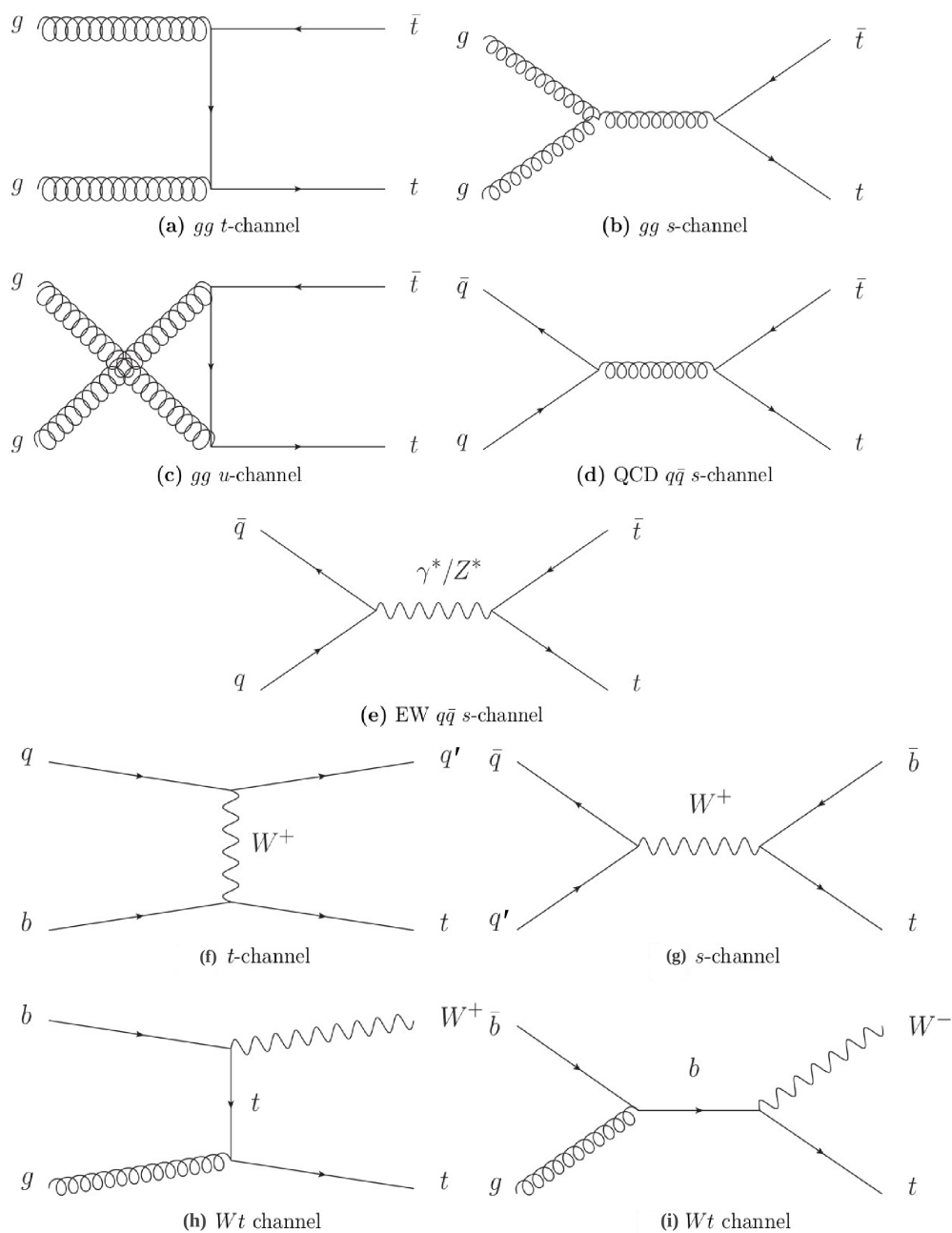
Figure 1.6: Leading order Feynman diagrams: (a-e) $t\bar{t}$ production and (f-i) single top quark production at LHC.
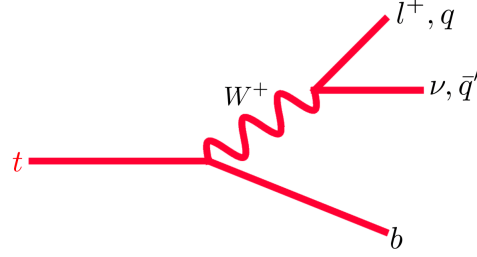
Figure 1.7: Feynman diagram of top quark decay via weak interaction with leptonic and hadronic decays from W boson.

is estimated to be less than 0.4% at LHC [65]. This slight contribution is due to one-loop, parity-violating electroweak radiative corrections [66–69] while SM predicts zero longitudinal polarization of the top quark in $t\bar{t}$ production. However, the top and the anti-top can have "transverse polarization"[11] characterised along the normal direction to the plain of production of $t\bar{t}$ pair. QCD absorptive parts in the strong production of $t\bar{t}$ (imaginary parts) contribute to this polarization. Hence, this occurs at one-loop and in higher orders while at tree-level, the amplitude is real, resulting in no transverse polarization at tree level [70–72]. The SM prediction of transverse polarization, including one loop EW and NLO QCD corrections at 14 TeV LHC is $\sim 0.57\%$. On the other hand, single top production via t-channel at LO is due to the same $(V - A)$ nature of tbW vertex. Therefore, the produced top quark is predicted to be highly polarised ($\sim 100\%$ left polarized), particularly along the direction of motion of the spectator quark [73, 74], i.e. the forward light quark denoted by q' in the process (f) of Fig. 1.6, in the rest frame of the top quark. Similarly, for subdominant t-channel top production, $\bar{d}b \rightarrow \bar{u}t$, the top spin direction is aligned in the direction of the incoming down-type antiquark. The opposite is true for single top-antiquark production. Here, the spin of $\bar{t}$ aligns in the direction opposite to that of the incoming down-type quark in the dominant process ($d\bar{b} \rightarrow u\bar{t}$) and opposite to that of the spectator antiquark in the

particle's helicity, $\mathcal{P} = \left\langle \vec{S}.\hat{p} \right\rangle$ where $\vec{S}$ and $\hat{p}$ denote the spin and momentum direction. Hence, under parity transformation, P: $P(\mathcal{P}) = -\mathcal{P}$.

[11]The degree of transverse polarization, $\mathcal{P}_\perp$ in $t\bar{t}$ production is defined as the average of the projection of the spin of top to the transverse direction of interaction plane: $\mathcal{P}_\perp = \left\langle \vec{S}. \left(\vec{p} \times \hat{k} \right) \right\rangle$ where $\vec{S}$ is the spin of the top, $\vec{p}(\vec{k})$ denotes the momenta of one of the incoming proton (top quark) in the $t\bar{t}$ center-of-mass frame. Under parity transformation: $P(\mathcal{P}_\perp) = \mathcal{P}_\perp$, which is a feature of strong interaction.

subdominant process ($\overline{ub} \rightarrow \overline{dt}$). Besides the choice of quantization axes, the degree of polarization for a sample containing t or $\bar{t}$ single production events depends on the mixture of dominant and subdominant production processes. The degree of polarization for $\bar{t}$ production is calculated at NLO in the spectator basis[12] to be -0.86, slightly smaller than the value of t production, 0.91 [74]. The other single top production processes via Wt channel or s-channel do not show a high degree of polarization in any basis.

We mention another important aspect of spin correlation in different $t\bar{t}$ production mechanisms. Although the t and $\bar{t}$ produced by strong interactions in hadron collisions are essentially unpolarized, their spins are correlated. For QCD production near the threshold, $t\bar{t}$ is produced in $^{1}S_{0}$ state with anti-parallel spins, i.e. opposite helicities for gluon-gluon fusion while for $q\bar{q}$ annihilation in a $^{3}S_{1}$ state with parallel spins, i.e. same helicities. The spin correlations are measured from the angular distributions of the decay products in $t\bar{t}$ decays. At LHC, the strength of spin correlation between t and $\bar{t}$ has been estimated in the di-lepton mode using $\Delta\phi$ observables, which is the difference in azimuthal angle between the charged leptons in the lab frame. At $\sqrt{s} = 7$ TeV, ATLAS reported this to be $A_{helicity}^{exp.} = 0.37 \pm 0.03 \pm 0.006$ [75] which agrees with SM NLO predictions of ~ 0.31 [76] in the helicity basis.

1.3.3 tbW **anomalous coupling**

Measurements of the top quark polarization and the spin observables of the associated W boson in t-channel single top quark production offer a powerful tool to study the tWb vertex in both the production and decay processes of the top quark. Deviations from the SM predictions in these observables could be indicative of new physics effects that modify this vertex. Within SM, the tWb coupling is purely left-handed at the tree level, whose strength is determined by the V_{tb} element of the CKM matrix. However, the presence of NP beyond the SM could alter the structure of the Wtb interaction, potentially leading to deviations from the SM prediction of $V_{tb} \simeq 1$. The most general model-independent Lagrangian describing the Wtb vertex can be written as follows:

$$\mathcal{L}_{tbW} = -\frac{g}{\sqrt{2}}\bar{b}\gamma^{\mu}\left(V_{L}P_{L} + V_{R}P_{R}\right)tW_{\mu}^{-} - \frac{g}{\sqrt{2}}b\frac{-i\sigma^{\mu\nu}}{M_{W}}q_{\nu}\left(g_{L}P_{L} + g_{R}P_{R}\right)tW_{\mu}^{-} + h.c. \quad (1.47)$$

---

[12]The top quark spin axis can be chosen either along the spectator quark momentum in the top quark rest frame, described as the spectator basis or along the top quark momentum in the center-of-mass frame, defined as the helicity basis.

where, g is the $SU(2)_L$ gauge coupling, q_ν and M_W are the four-momentum and mass of the W boson,respectively, $P_L(P_R)$ is left(right)-handed chiral projection operators. The constants $V_{L,R}$ and $g_{L,R}$ denote left- and right-handed vector and tensor couplings. In the SM, $V_{tb} \equiv V_L = 1$ and $V_R = g_{L,R} = 0$ at tree level. The coefficients $\delta V_L = V_L - 1, V_R, g_{L,R}$ are the "anomalous couplings". Anomalous couplings are often interpreted as coefficients of higher-dimension operators that are added to SM Lagrangian to account for potential new physics. Non-vanishing anomalous couplings in the top quark decay would provide hints of BSM physics. Additionally, complex-valued anomalous couplings would imply the presence of a CP-violating component in the decay process. The 95% CL exclusion limits on anomalous Wtb couplings are measured at CMS to be $V_R < 0.16, |g_L| < 0.057, -0.049 < g_R < 0.0048$ from single top quark events produced in the t-channel at $\sqrt{(s)} = 7$ and 8 TeV [77]. With the QCD and EW radiative corrections, these values computed at one-loop are not significantly different from SM prediction.

1.3.4 Measurement of top polarization

The top polarization can be analyzed through the angular distribution of its decay products. The differential decay rate of a decay product f with respect to spin direction $\hat{z}$ in the rest frame of the top quark is given by

$$\frac{1}{\Gamma}\frac{d\Gamma}{d\cos\theta_f} = \frac{1}{2}(1 + k_f \mathcal{P}_z \cos\theta_f) \tag{1.48}$$

where θ_f is the angle between the three-momentum of the decay product ($f = W, b, l, \nu, u, d$) in the top rest frame and the spin direction $\hat{z}$ for quantization of top spin [13]. The constant k_f is the spin analyzing power of the particle f, ($-1 \leq k_f \leq 1$) and $\mathcal{P}_z$ is the degree of top quark polarization along the $\hat{z}$ direction. k_f quantifies the degree of correlation between the spin of a top quark and f. Among the decay products of the top quark, the down-type quark produced in hadronic decays and the charged lepton produced in semileptonic decays of the top quark carry the maximal analyzing power ($k_{l^+} = k_{\bar{d}} = 1$ at tree level). Though the hadronic decay mode of the top, $t \rightarrow bjj$ has a higher branching ratio than the semileptonic, it is highly challenging to identify the jets originating from a $\bar{d}$ quark. There are a few proposals, like using the less energetic jet among the two light jets, a weighted

---

[13]For polarization measurements spectator basis is preferred than the helicity basis since it is the easier direction to reconstruct.

average of the directions of two light-quark jets where $50\% - 60\%$ correlation with top polarization can be achieved [78]. The decay product with the next highest analyzing power is the b-quark and one has $k_b = -k_W^+ = -0.41$ at tree level. Keeping in mind an impressive lepton identification at LHC and an efficient b-jets tagging, this thesis will focus on the study of top quark polarization using only charged leptons and b-jets from top decay. The spin analyzing powers associated with all the top decay products are summarized in Table 1.2. The QCD corrections to k_l, k_W, k_b at NLO are calculated for leptonically decaying top to be $< 5\%$ [79,80]. Moreover, k_l and k_d do not receive any corrections from the anomalous tbW coupling at LO [81], hence associated angular distributions are good probes of top polarization unaffected by new physics in decay.

Spin Analyzer	k_f at LO	k_f at NLO
W^+, b	-0.41	-0.39
ν_l	-0.32	-0.33
u, c	-0.32	-0.31
$\overline{d}, \overline{s}$	1	0.93
l^+	1	0.998

Table 1.2: Spin analyzing power of different top decay products calculated at LO and NLO. The sign of the value of k_f will be flipped from particle to its antiparticle.

The angular distribution of the decay lepton serves as the most effective probe of its polarization due to its exceptional sensitivity. However, for highly boosted top quarks, the collimation of decay products necessitates employing methods that also utilize the energy distribution of these products for polarization analysis [82]. Several proposals for new physics scenarios exist, including the production of single top quarks in a boosted scenario via interactions with novel particles. A few examples of this can be massive W-like boson, charged Higgs boson, Leptoquark, etc., where properties of the top quark and its coupling can be studied. We will discuss this in detail in Chapter 3.

1.4 Motivations of Physics Beyond the Standard Model

The SM has been extensively tested at facilities like LEP, the Tevatron, and the LHC, demonstrating remarkable agreement with experiments up to the energy scale of electroweak in-

teractions ($\Lambda_{EW} \sim 10^2$ GeV). However, the SM's inability to explain certain phenomena and inherent theoretical limitations suggest the existence of new beyond SM framework. We will discuss a few strong arguments why SM cannot be the ultimate theory for Particle Physics.

Neutrino masses

The SM spectrum contains three massless, neutral and left-handed neutrinos. However, the observation of neutrino oscillation between the three flavors in experiments like Super-Kamiokande [21] confirms that neutrinos must have a non-vanishing mass. In SM, a Dirac neutrino mass term can be generated by adding a right chiral neutrino in the spectrum and considering the usual kind of interaction of neutrinos with the SM Higgs field. Both cosmological [83,84] and terrestrial [85–88] experiments suggest the neutrinos are extremely light. Hence, they should have very small Yukawa couplings in order to achieve the tiny mass. A model of this nature would be inadequate in explaining the vast discrepancy in masses between charged leptons and neutrinos. Furthermore, the predicted right chiral neutrino would be sterile i.e singlet under $SU(2)_L \times U(1)_Y$. Consequently, they would not interact with the gauge bosons associated with these symmetries and will not participate in either charged current or weak neutral current weak interaction processes mediated by these bosons.

Neutrino oscillation experiments have demonstrated that the mixing behaviour of leptons, described by the PMNS matrix, deviates from the pattern observed in the CKM matrix for quark mixing and is quite large ($\theta_{12} \sim 33^0, \theta_{23} \sim 45^0, \theta_{13} \sim 9^0$)[14]. Many BSM models propose Majorana-type neutrino mass terms, constructed using only existing SM fields involving a higher-dimensional operator (dimension-5). This operator is inversely proportional to the energy scale of the new physics responsible for generating neutrino masses. A large energy scale for this new physics leads to a highly suppressed term, consequently explaining the small observed neutrino masses without requiring very small Yukawa couplings. This term infers neutrinos would be their own antiparticles violating the lepton number by 2 ($\Delta L = 2$). Experiments have focused on the possibility of neutrinoless double β-decay ($0\nu\beta\beta$), which can occur only if neutrinos are Majorana particles. From current knowledge

---

[14]Like CKM matrix PMNS matrix can also be parameterized in terms of the three angles $\theta_{12}, \theta_{23}, \theta_{13}$ and the CP phase δ_{CP}.

of neutrino masses, mixings and neutrino mass-squared differences[15] it is unclear whether the third eigenstate ν_3 is heavier (normal mass hierarchy (NH)) or lighter than the ν_1 and ν_2 (inverted mass hierarchy (IH)) neutrino mass eigenstates [89]. Therefore, whether neutrinos are Dirac or Majorana fermions, the neutrino mass hierarchy, the magnitude of the CP (charge and parity) phase, the absolute scale of the neutrino mass still remain open questions which point towards the possibility of new physics beyond its current description.

Baryon asymmetry

The universe exhibits a clear dominance of matter over antimatter [90]. This asymetry is quantified by the ratio of difference of baryon and anti-baryon number density to the photon number density. The measured value of this asymmetry is $\sim 10^{-10}$ from cosmic microwave background (CMB) [91] and big bang nucleosynthesis (BBN) [92]. To explain this asymmetry, a process known as Baryogenesis is believed to have occurred in the early universe. Andrei Sakharov proposed three necessary conditions for Baryogenesis [93]: (i) need a process that violates the baryon number (B), (ii) C and CP symmetry should be violated, (iii) there has been a moment of departure from thermal equilibrium in the universe. In SM, the Adler-Bell-Jackiw (ABJ) anomaly [94, 95] suggests a potential avenue through which baryon number violation can occur in the early Universe, contributing to the generation of the matter-antimatter asymmetry observed today. Electroweak baryogenesis, accommodate electroweak phase transition in first order, can driven the system away from the thermal equilibrium. For a Higgs boson mass around 125 GeV, as currently measured, this transition is predicted to be a smooth crossover rather than a first-order phase transition. This characteristic prevents the SM from supporting a mechanism known as electroweak Baryogenesis [96]. The violation of CP symmetry, which requires the underlying QFT describing the universe to possess sufficient sources of CP violation. While SM includes a potential source of CP violation through a complex phase in the CKM matrix, δ_{CP}, governing the mixing of quark flavors, the strength of this source appears insufficient to generate the observed matter-antimatter asymmetry [97].

---

[15]Two mass squared differences from neutrino oscillations are measured: $|\Delta m^2_{atm}| \sim 2.5 \times 10^{-3}$ eV^2, $\Delta m^2_{sol} \sim 7.5 \times 10^{-5}$ eV^2, but the sign of Δm^2_{atm} is still ambiguous.

Dark matter

Astrophysical observations such as rotation curves of galaxies [98] strongly suggest the existence of dark matter, a mysterious substance constituting roughly 26% [91] of the universe. Unlike ordinary matter, dark matter interacts with the SM of particles very weakly, if at all. This invisibility to light and most other interactions makes direct detection of dark matter extremely challenging. Several key properties are believed to characterize dark matter: no electric charge, weakly interacting with the SM particles, non-baryonic, massive, and stable in time scales of the universe. Dark matter is categorized as hot, warm, or cold based on particle velocity. Hot dark matter particles move at relativistic speeds, meaning their kinetic energy is comparable to or exceeds their rest mass. Conversely, cold dark matter particles have significantly lower kinetic energy than their rest mass, moving at non-relativistic speeds. Warm dark matter occupies the intermediate state between these two extremes. The SM can only account for the remaining 5% of the universe's matter, which is visible and baryonic. Interestingly, the only potential dark matter candidate within the SM framework is the neutrino. However, neutrinos fall under the category of Hot Dark Matter (HDM) [99–101]. This is because they are assumed to have been in thermal equilibrium with ordinary matter in the early universe, a state characterized by high temperatures and densities. Due to their minimal mass, neutrinos would have been highly relativistic at that time. Even as the universe expanded and cooled, neutrinos would have remained too fast to form the large-scale structures (galaxies and clusters of galaxies) observed today. Therefore, HDM theory, with neutrinos as the primary candidate, struggles to explain the observed galactic structure formation in the universe.

Cosmological observations [102, 103] indicate cold dark matter (CDM) must be a significant component of the universe to explain the growth of structures in the early universe to become galaxies and stars. Since the three flavors of neutrinos of the SM are relativistic, they do not contribute to this CDM. However, a weakly interacting massive particle (WIMP), an example of non-baryonic CDM candidate interacting via electroweak coupling with a mass around the electroweak scale, generates a correct relic density, the present-day cosmic density of DM particles left over from the early universe, which is measured to be $\Omega h^2 = 0.1184 \pm 0.0012$ at 68% C.L. [103]. This is referred to as the 'WIMP miracle' [104–106]. The absence of any dark matter candidate in the SM strongly suggests looking for possible BSM scenarios to explain the observed dark matter. A very well-motivated model, Supersymmetry, can provide a possible dark matter candidate, the lightest neutralino, within

R-parity conserved scenario. For a deeper exploration of dark matter, Sec. 1.10 discusses its thermal evolution in the early universe, potential DM candidates arising from Supersymmetric theories, and the diverse search strategies employed for its detection.

Strong CP problem

The strong CP problem is a conundrum in theoretical physics in case of QCD, governing strong interactions. The gauge invariance allows a term $\mathcal{L}_\theta$ in the QCD Yang-Mills Lagrangian of the following type

$$
\begin{aligned}
\mathcal{L}_{Full} &= \mathcal{L}_{QCD} + \mathcal{L}_\theta \\
&= \mathcal{L}_{QCD} + \theta \frac{1}{16\pi^2} \epsilon^{\mu\nu\alpha\beta} G^a_{\mu\nu} G^a_{\alpha\beta}
\end{aligned}
\tag{1.49}
$$

where, $G^a_{\mu\nu}, G^a_{\alpha\beta}$ denote the gluon field strength tensor. The term $\mathcal{L}_\theta$ violates CP if θ is non-zero and will contribute to the neutron electric dipole moment (NEDM). The experimental bounds on NEDM, $|d_n| < 1.8 \times 10^{10}$e.cm [107] puts a strong constraints on θ, $\theta \leq 10^{-10}$ [108]. SM itself predicts that θ should naturally take on a large value due to the way quark masses are generated. The lack of observed CP violation in strong interactions contradicts the theoretical prediction within the SM, known as the "strong CP problem". The discrepancy between the theoretical prediction and experiment points towards the limitations of the SM. This opens up the possibility of new physics mechanisms that suppress θ, like Peccei-Quinn mechanism [109,110] where a new psudoscalar field (the axion) is introduced that couples to θ.

Hierarchy problem and the fine-tuning problem

The hierarchy problem of the SM arises from the vast discrepancy between two energy scales: the EW scale ($\sim 10^2$ GeV), associated with the W and Z bosons, which mediate weak interactions and the Higgs mechanism, and the Planck scale ($M_{PL} = 1/\sqrt{G_N} \approx 10^{19}$ GeV, where G_N is the gravitational constant), where quantum effects of gravity are expected to become significant. The SM, at tree-level, doesn't predict the existence of the Planck scale. However, higher-order loop diagrams introduce a dependence on energies beyond the EW scale. While the SM allows for an arbitrary UV cutoff for these loops, setting it near the Planck scale would necessitate incorporating gravitational effects, which are absent in the SM. Therefore, within the SM, the UV cutoff can only be at most the Planck scale. This

creates a significant hierarchy problem - the ratio of the Planck scale to the EW scale is enormous, $M_{PL}/M_{EW} \approx 10^{17}$. The question remains: Why do these two vastly different energy scales exist without any intermediate scales evident in the SM? This is known as the hierarchy problem.

This hierarchy leads to another problem within SM, the 'fine-tuning problem', which arises from the radiative corrections to the Higgs boson mass. This includes contributions from self-interaction, gauge loops ($W^{\pm}, Z$), and fermion loops, where the most important one is coming from the top loop, due to the highest Yukawa coupling. Unlike gauge bosons and fermions, whose masses are protected by gauge and chiral symmetries respectively within the Standard Model, the Higgs mass lacks protection from any symmetry capable of preventing substantial radiative corrections. In other words, unlike other parameters in the SM, such as gauge couplings and fermion masses, which exhibit only logarithmic dependence on a high-energy cut-off scale Λ (e.g. in QED for electron mass at one loop $\delta m_e \sim (3\alpha/4\pi)m_e \log(\Lambda^2/m_e^2)$), the one-loop self-energy correction to the Higgs mass depends quadratically on Λ (leading Higgs mass correction $\delta m_h^2 = (3\Lambda^2/8\pi^2v^2)(-4m_t^2 + m_h^2 + 2m_W^2 + m_Z^2)$ [111]). While this quadratic divergence can be mathematically addressed by introducing a counterterm within the SM's framework of renormalizability, it leads to a situation where the counterterm must nearly cancel out the enormous correction term (at Plack scale, $\delta m_h^2 \sim 10^{38}$ GeV^2)to achieve the observed Higgs mass. This extreme cancellation means necessitates fine-tuning, especially when the high-energy cut-off scale is significantly larger than the EW scale.

This problem could be resolved by the existence of new particles and interactions at an intermediate energy scale closer to the EW scale, rather than the Planck scale, whose contributions to the Higgs boson's self-energy could cancel the quadratically divergent terms, alleviating the need for extreme fine-tuning. SUSY offers a similar possible solution by introducing a new symmetry between fermions and bosons, where for each SM particle, there would be a corresponding supersymmetric partner, superpartner with the opposite spin but similar mass. Crucially, loop corrections arising from bosonic and fermionic superpartners within a SUSY multiplet tend to have opposite signs. This inherent cancellation significantly reduces the dependence of the Higgs mass on the high-energy cut-off scale, leading to corrections proportional to a milder logarithmic dependence.

There are also other questions like: understanding the origin of the observed hierarchy in particle masses and mixing angles, known as flavour hierarchy, advocates for a

higher energy completion theories for a more unified explanation. Along with this, there are anomalies observed in B-meson decaying into τ/μs from various B physics experiments at Belle [112], Babar [113, 114] and LHCb [115, 116], which evidences for violation of lepton flavour universality in SM.[16]

These limitations of the SM inspire exploring frameworks beyond the SM and their signatures. In the next section, we discuss Supersymmetry, a well-established BSM model.

1.5 Supersymmetry

In 1967, Sidney Coleman and Jeffrey Mandula established a key limitation on how symmetries can be combined in QFT. Their no-go theorem [119] states that spacetime symmetries (Poincaré group) and internal symmetries (flavor, isospin etc.) can only be trivially combined – as a direct product. This assumes all symmetry generators are bosonic (scalar, vector, or tensor representations). Supersymmetry is a space-time symmetry that relates commuting, bosonic fields with anticommuting, fermionic fields. Since SUSY isn't an internal symmetry, its generators must necessarily mix with the existing transformations of the Poincaré group [120]. Rudolf Haag, Jan Lopuszński, and Martin Sohnius showed that if we give up the commutator bounds by introducing fermionic generators (only fermionic generators are capable of changing the spin), it allows for a non-trivial combination – *Lie-superalgebra* of supersymmetry. SUSY extends the Poincaré algebra by adding N anticommuting spin-$\frac{1}{2}$ operators, can be written as two Weyl spinors, denoted by Q_α, and $Q_{\dot\alpha}^\dagger$, which transform as left- and right-chiral under the Lorentz group, respectively. The indices α and $\dot\alpha$ differentiate between the left and right-chiral spinors, with both taking values $1, 2$. The Lie superalgebra involving the generators $Q_\alpha, Q_{\dot\alpha}^\dagger$ and the four-momentum generator of space-time translations P_μ for $N = 1$ SUSY reads as:

$$\left\{Q_\alpha, Q_{\dot\alpha}^\dagger\right\} = -2\sigma_{\alpha\dot\alpha}^\mu P_\mu \tag{1.50}$$

$$\{Q_\alpha, Q_\beta\} = \left\{Q_{\dot\alpha}^\dagger, Q_{\dot\beta}^\dagger\right\} = 0 \tag{1.51}$$

$$[Q_\alpha, P^\mu] = \left[Q_{\dot\alpha}^\dagger, P^\mu\right] = [P_\mu, P_\nu] = 0 \tag{1.52}$$

---

[16]Recent Dec, 22 LHCb $b \rightarrow sl^+l^-$ analysis decreed that the reanalysis supplants previous results and the corresponding R_K, R_{K^*} anomalies are actually compatible with SM [117], while there are still deviations from SM in lepton flavour universality measurements in $b \rightarrow c\tau\nu_\tau$ transitions [118].

where, $\sigma^\mu = (I, \vec{\sigma})$. The operators $Q_\alpha, Q_{\dot\alpha}^\dagger$ change the spin of the state by $1/2$ transforming from a bosonic state into a fermionic state and vice versa:

$$Q_{\dot\alpha}^\dagger|0\rangle = |\frac{1}{2}\rangle, \quad Q_{\dot\alpha}^\dagger|\frac{1}{2}\rangle = |1\rangle, \tag{1.53}$$

Accordingly, the spacetime is an 8-dimensional manifold, parametrised by the space-time co-ordinate x_μ and two Grassmann co-ordinates θ_α and $\overline{\theta}_{\dot\alpha}$ called "superspace". Fermions and bosons, related $Q_{\dot\alpha}^\dagger$ are termed as *superpartners* and they form an irreducible representation of the SUSY algebra, known as *supermultiplet*. A key consequence of the relation Eq.1.52 is that a particle and its superpartner share the same mass within a supermultiplet. Renormalizable SUSY theories allow for two main types of supermultiplets: Chiral supermultiplets (spin $(0, 1/2)$), made of a complex scalar & a Weyl fermion, e.g. a quark and Vector supermultiplets (spin$(1/2, 1)$), contain a (massless) Weyl fermion & a (massless) vector boson, like gauge bosons. To ensure equal numbers of bosonic and fermionic degrees of freedom (d.o.f.) even when particles are not actively interacting, i.e. off-shell, chiral (vector) supermultiplets include an auxiliary scalar field $F(D^a)$ that has no dynamical role. These auxiliary fields vanish when particles become actively interacting (on-shell) and are integrated out through the equations of motion from the Lagrangian. The decomposition of Chiral superfields in terms of their component fields in the chiral basis has the following form[17] [121]

$$\hat{\Phi}(x, \theta) = A(x) + \sqrt{2}\theta\psi(x) + \theta\theta F(x), \tag{1.54}$$

$$\hat{\Phi}^\dagger(\overline{x}, \overline{\theta}) = A^*(\overline{x}) + \sqrt{2}\overline{\theta\psi}(\overline{x}) + \overline{\theta\theta}F^*(\overline{x}). \tag{1.55}$$

The components $A(x)$, the complex scalar field, ψ, the fermion field and F, the auxiliary field, have the mass dimensions $1, 3/2, 2$ respectively. As we know, the left and right chiral fermions of SM transform differently under $SU(2) \times U(1)$; the SM fields can be elegantly extended to SUSY using one chiral superfield corresponding to each fermionic field in the SM. On the other hand, vector superfields which satisfy self-conjugation ($V^\dagger(x, \theta, \overline{\theta}) = V(x, \theta, \overline{\theta})$) in the Wess-Zumino gauge [120] have the following decomposition:

$$\hat{V} = \theta\overline{\sigma}^\mu\overline{\theta}A_\mu(x) + \theta\theta\overline{\theta\lambda}(x) + \overline{\theta\theta}\theta\lambda(x) + \frac{1}{2}\theta\theta\overline{\theta\theta}D(x), \tag{1.56}$$

---

[17]Any superfield, which is a function of x and θ ($\overline{x}$ and $\overline{\theta}$) only, would automatically be left-chiral (right-chiral).

where, A_μ, the gauge field, λ, the two-component fermion field, D, the auxiliary filed have the mass dimensions $1, 3/2, 2$ respectively.

In constructing the Lagrangian, we incorporate all gauge-invariant terms possessing a mass dimension of four. Given the definitions of the superfields, only specific types of SUSY-invariant functions can be formulated. The first category is the superpotential, a complex holomorphic function of the chiral supermultiplets, expressed in the following general form:

$$W = a_i \hat{\Phi}_i + b_{ij} \hat{\Phi}_i \hat{\Phi}_j + c_{ijk} \hat{\Phi}_i \hat{\Phi}_j \hat{\Phi}_k. \tag{1.57}$$

We focus on the coefficients of the $\theta\theta$ terms in the superpotential, Eq. (1.57), as the first term is of little interest due to describing a non-interacting theory while the second term generates mass terms for the scalars and fermions within the supermultiplets. The third term introduces Yukawa interactions between these fermions and scalars. The F-term, defined as the coefficient of $\theta\theta$ in Eq. (1.54), is given by:

$$F_i = \frac{\delta W}{\delta \hat{\Phi}_i} \tag{1.58}$$

A second type of invariant function exists alongside the superpotential: the Kähler potential, denoted by K. This function depends on the chiral superfields (denoted by $\hat{\Phi}$ and its conjugate $\hat{\Phi}^\dagger$) and is always real-valued: $K(\hat{\Phi}, \hat{\Phi}^\dagger) = \sum_i \hat{\Phi}^\dagger \hat{\Phi}$. Terms in the Kähler potential containing $\theta\theta\overline{\theta}\overline{\theta}$ determine the kinetic terms for both the fields A and ψ. The general form of the Kähler potential can be written as: $\sum_i \hat{\Phi}^\dagger e^{q\hat{V}}$, where V is the gauge supermultiplet and q signifies the charge of the chiral supermultiplet under the specific gauge symmetry. This term captures the kinetic energy contributions for both fermions and sfermions, and the interactions of these with the gauge field and gauginos (fermion-fermion-gauge, sfermion-sfermion-gauge, and fermion-sfermion-gaugino). Finally, the gauge kinetic term of the Lagrangian is written in terms of the field strength superfield $\mathcal{W}\alpha$ as $\frac{1}{4}\mathcal{W}_\alpha \mathcal{W}^\alpha$ where $\mathcal{W}_\alpha$ is defined as

$$\mathcal{W}_\alpha = -\frac{1}{4}\overline{\mathcal{D}}^2 \mathcal{D}_\alpha V \tag{1.59}$$

acts like a chiral superfield, with the covariant derivatives written as

$$\mathcal{D}_\alpha = \partial_\alpha + i\sigma^\mu_{\alpha\dot{\alpha}}\overline{\theta}^{\dot{\alpha}}\partial_\mu$$
$$\overline{\mathcal{D}}_{\dot{\alpha}} = -\overline{\partial}_{\dot{\alpha}} - i\theta^\alpha \sigma^\mu_{\alpha\dot{\alpha}}\partial_\mu \tag{1.60}$$

Summing up the three terms, we can now write the most generic $N = 1$ SUSY Lagrangian

$$\mathcal{L}_{SUSY} = \int d^2\theta \frac{1}{4} \mathcal{W}^\alpha \mathcal{W}_\alpha + \int d^2\theta d^2\overline{\theta} K\left(\hat{\Phi}^\dagger, \hat{\Phi}\right) + \int d^2\theta W\left(\hat{\Phi}\right) + \int d^2\overline{\theta} \overline{W}\left(\hat{\Phi}^\dagger\right) \quad (1.61)$$

The scalar potential $V(\hat{\Phi}^\dagger, \hat{\Phi})$, a function of the auxiliary fields F and D, is given by

$$V(\hat{\Phi}^\dagger, \hat{\Phi}) = |F|^2 + \frac{1}{2}|D|^2 = \frac{\partial W}{\partial \hat{\Phi}^i} \frac{\partial \overline{W}}{\partial \hat{\Phi}^\dagger_i} + \frac{1}{2}\sum_a g_a \sum_{ij} \left(\Phi^\dagger_i (T^a)_{ij} \Phi_j\right) \quad (1.62)$$

where T^a are the generators of the gauge group and g_a is the coupling strength and the sum over a implies a sum over all generators of all gauge groups. The F-terms in Eq. (1.62) guarantee that the four-vertex involving scalars has the same Yukawa coupling as the corresponding fermion, thus ensuring the cancellation of divergences arising from the fermion loop by the divergences due to the sfermion loop.

1.6 The Minimal Supersymmetric Standard Model

The Minimal Supersymmetric Standard Model (MSSM) is a well-studied extension of the SM that incorporates SUSY, maintaining the SM's gauge symmetry $SU(3)_C \times SU(2)_L \times U(1)_Y$ before EWSB. For a detailed review, ref. to [122–126]. SM fermions each gain a scalar superpartner, sfermion forming chiral multiples, while the SM gauge bosons become part of vector multiplets alongside their fermionic partners, gauginos. Unlike the single Higgs doublet in the SM, the MSSM introduces two complex Higgs doublets, H_d and H_u. This is driven by the fact that the Higgs becomes a chiral supermultiplet with a fermionic partner (higgsino); anomaly cancellation requires another fermion with the opposite hypercharge. Therefore, the MSSM Higgs sector features two complex Higgs doublets and four corresponding higgsinos. Table 1.3 illustrates the MSSM superfield spectrum.

The most general form of SM-gauge invariant superpotential, which gives the Yukawa terms, SM fermion masses and Higgsino masses, is given as

$$W_{MSSM} = W_1 + W_2 \quad (1.63)$$

$$W_1 = h^u_{ij}\hat{Q}^i_L\hat{U}^j_R\hat{H}_u + h^d_{ij}\hat{Q}^i_L\hat{D}^j_R\hat{H}_d + h^u_{ij}\hat{L}^i_L\hat{E}^j_R\hat{H}_d + \mu\hat{H}_d\hat{H}_u \quad (1.64)$$

$$W_2 = \lambda_{ijk}\hat{L}^i_L\hat{L}^j_L\hat{E}^k_R + \lambda'_{ijk}\hat{L}^i_L\hat{Q}^j_L\hat{D}^k_R + \lambda''_{ijk}\hat{U}^i_R\hat{D}^j_R\hat{D}^k_R + \epsilon_i\hat{L}^i_L\hat{H}_u. \quad (1.65)$$

Interestingly, gauge invariance allows terms with an odd number, either of quark or leptonic superfield specified by W_2, which violate lepton and baryon numbers. This arises

Name and Nature	Symbol	Spin 0	Spin 1/2	Spin 1	$(SU(3)_C, SU(2)_L, U(1)_Y)$
Quarks and squarks (Chiral)	$\hat{Q}_L^i$	$\left(\tilde{u}_L, \tilde{d}_L\right)$	(u_L, d_L)		$(3, 2, 1/6)$
	$\hat{U}_R^i$	$\tilde{u}_R^{C,i}$	$u_R^{C,i}$	-	$(\bar{3}, 1, 2/3)$
	$\hat{D}_R^i$	$\tilde{d}_R^{C,i}$	$d_R^{C,i}$		$(\bar{3}, 1, -1/3)$
Leptons and sleptons (Chiral)	$\hat{L}_L^i$	$\left(\tilde{\nu}_L^i, \tilde{e}_L^i\right)$	$\left(\nu_L^i, e_L^i\right)$	-	$(1, 2, -1/2)$
	$\hat{E}_R^i$	$\tilde{e}_R^{C,i}$	$e_R^{C,i}$		$(1, 1, -1)$
Higgs and higgsinos (Chiral)	$\hat{H}_u$	$\left(H_u^+, H_u^0\right)$	$\left(\tilde{H}_u^+, \tilde{H}_u^0\right)$	-	$(1, 2, 1/2)$
	$\hat{H}_d$	$\left(H_d^0, H_d^-\right)$	$\left(\tilde{H}_d^0, \tilde{H}_d^-\right)$		$(1, 2, -1/2)$
B boson and bino (Vector)	-	-	$\tilde{B}^0$	B^0	$(1, 1, 0)$
W bosons and winos (Vector)	-	-	$\tilde{W}^\alpha$	W_μ^α	$(1, 3, 0)$
Gluons and gluinos (Vector)	-	-	$\tilde{G}^a$	G_μ^a	$(8, 1, 0)$

Table 1.3: MSSM superfield content with the gauge transformation properties before electroweak symmetry breaking: $i, \alpha = 1, ., 3; a = 1, .., 8$

from the similar Lorentz structure of $\hat{L}_L^i$ and $\hat{H}_d$; both are chiral superfields with identical gauge charges. Experiments tightly constrain such terms due to rapid proton decay. To suppress these interactions, MSSM introduces an additional discrete symmetry - R-parity, that does not permit these additional terms. R-parity is defined as:

$$R_p = (-1)^{3(B-L)+2S} \tag{1.66}$$

where B, L and S are the baryon number, lepton number and spin of the particle, respectively. All the SM particles have $R_p = +1$ while all their superpartner have $R_p = -1$. R-parity is preserved if the product of the R_ps of all the interacting fields in each term in the Lagrangian is equal to 1, which in turn refers to $W_2 = 0$. If conserved, any interaction vertex must have an even number of particles, which leads to several phenomenologically interesting consequences. First, sparticles are produced in pairs. Second, sparticles decay to other sparticles, with the chain ending in the lightest supersymmetric particle (LSP) that provides a valid dark matter candidate. For MSSM, the Kähler potential is given by

$$\mathcal{L}_{kin} = \int d^2\theta d^2\bar{\theta}^2 \sum_{SU(3)_C, SU(2)_L, U(1)_Y} \hat{\Phi}_\beta^\dagger e^{qV} \hat{\Phi}_\beta \tag{1.67}$$

where $\hat{\Phi}_\beta = \hat{Q}_L^i, \hat{U}_R^i, \hat{D}_R^i, \hat{L}_L^i, \hat{E}_R^i, \hat{H}_d, \hat{H}_u$.

1.6.1 SUSY breaking

The lack of observed superpartners for SM particles within current collider experiments suggests that SUSY is broken at some scale, much higher than the EW scale, $\mathcal{O}$ (TeV). SUSY can be spontaneously broken if the auxiliary fields F or D acquire a VEV. This implies at least one (or more) F-components associated with one (or more) of the MSSM chiral (matter) superfields would develop a VEV. However, this approach to breaking SUSY proves problematic. It leads to the prediction of at least one superpartner being lighter than its corresponding SM particle. This contradicts experimental observations. One has to think of a different approach for SUSY breaking.

A popular approach to SUSY breaking involves a 'hidden sector'. This sector consists of superfields that don't interact with the SM forces. SUSY breaking happens spontaneously within this hidden sector. This message is relayed to the visible sector (MSSM) through a messenger sector. This messenger can be gravity (gravity mediation) or gauge interactions (gauge mediation). This communication results in SUSY breaking terms appearing in the MSSM Lagrangian. However, to maintain the benefit of mitigating the hierarchy problem, SUSY must be broken in a specific way that doesn't reintroduce the very quadratic divergences it aimed to cancel. This can be achieved by incorporating additional terms, called soft-breaking terms, into the Lagrangian and hence breaking SUSY *explicitly*, $\mathcal{L}_{MSSM} = \mathcal{L}_{SUSY} + \mathcal{L}_{soft}$. $\mathcal{L}_{soft}$ introduce mass splitting, making the SUSY particles heavier than their SM counterpart. Gauge invariant soft SUSY breaking terms are given by

$$
\begin{aligned}
\mathcal{L}_{soft} = & - M_{Q_{ij}}^2 \tilde{Q}_L^{i\dagger} \tilde{Q}_L^j - M_{u_{ij}}^2 \tilde{u}_R^{i\dagger} \tilde{u}_R^j - M_{d_{ij}}^2 \tilde{d}_R^{i\dagger} \tilde{d}_R^j - M_{L_{ij}}^2 \tilde{L}_L^{i\dagger} \tilde{L}_L^j - M_{e_{ij}}^2 \tilde{e}_R^{i\dagger} \tilde{e}_R^j \\
& - \frac{1}{2} \left(M_1 \tilde{B}\tilde{B} + M_2 \tilde{W}^\alpha \tilde{W}^\alpha + M_3 \tilde{G}^a \tilde{G}^a + h.c. \right) \\
& - M_{H_d}^2 H_d^\dagger H_d - M_{H_u}^2 H_u^\dagger H_u - (\mu H_d H_u + \text{ h.c. }) \\
& + A_{u,ij} \tilde{u}_R^i \tilde{Q}_L^j H_u + A_{d,ij} \tilde{d}_R^i \tilde{Q}_L^j H_d + A_{e,ij} \tilde{e}_R^i \tilde{L}_L^j H_d + h.c.
\end{aligned}
\tag{1.68}
$$

Here the first row of Eq. (1.68) corresponds to adding mass terms for squarks and sleptons, where $M_{Q_{ij}}, (M_{u_{ij}}, M_{d_{ij}}), M_{L_{ij}}$ and $M_{e_{ij}}$ denote the soft mass matrices for the left-chiral squarks, right-chiral squarks, left-chiral sleptons and right-chiral sleptons respectively. The generation indices i, j $(i, j = 1..3)$ need not be the same, implying possible flavour violation. The second row contains three gaugino mass terms, which are a part of vector superfield with M_1, M_2 and M_3 being the mass parameters for bino, winos and gluinos where index $\alpha = 1..3, a = 1..8$. The corresponding terms for the Higgs fields are given in the third row,

where the first two terms denote masses for the Higgs while the term $\mu H_d H_u$ is the only bilinear scalar coupling with μ identified as higgsino mass parameter. The scalar trilinear terms comprising of couplings between the squarks, sleptons, and Higgs fields are written in the fourth row with $A_{u,ij}, A_{d,ij}$ and $A_{e,ij}$ denote the trilinear couplings for the up-type squarks, down-type squarks and down-type sleptons.

The MSSM Lagrangian, when incorporating generation mixing and complex phases, introduces a significant challenge due to the large number of parameters required. These additional parameters, numbering 105, significantly increase the dimensionality of the parameter space, making comprehensive analysis difficult. To address this complexity, phenomenological studies typically focus on specific, lower-dimensional regions within the overall MSSM parameter space. These simplified models often rely on well-motivated symmetries and simplifying assumptions. Prime examples of such models are minimal supergravity (mSUGRA) [127] and the constrained MSSM (CMSSM) [128], pMSSM [129]. These models assume universal boundary conditions, reducing the number of free parameters to a more manageable set. For example, in the case of CMSSM the model is parametrized by universal scalar mass (m_0), gaugino mass ($m_{1/2}$), trilinear coupling at the GUT scale (A_0), higgsino mass (μ), and the ratio of the VEVs of the two Higgs doublets ($\tan\beta$). We now turn our focus to the Higgs sector within the MSSM. Following this, we will discuss the electroweakino sector of the MSSM.

1.6.2 Higgs sector of MSSM

The Higgs sector of MSSM is composed of two complex scalar Higgs doublets; the neutral components in both doublets get a VEV at EWSB.

$$H_d = \begin{pmatrix} H_d^0 \\ H_d^- \end{pmatrix}, \langle H_d^0 \rangle_0 = \frac{v_d}{\sqrt{2}} \tag{1.69}$$

$$H_u = \begin{pmatrix} H_u^+ \\ H_u^0 \end{pmatrix}, \langle H_u^0 \rangle_0 = \frac{v_u}{\sqrt{2}} \tag{1.70}$$

As we mentioned, the MSSM introduces two Higgs doublets: $H_u(H_u^+ : T_3 = +1/2, H_u^0 : T_3 = -1/2)$ doublet has the same structure as the original SM Higgs ($Y = +1$) and grants mass to all up-type sfermions, $H_d(H_d^0 : T_3 = +1/2, H_d^- : T_3 = -1/2)$ is the new doublet carries the opposite hypercharge ($Y = -1$) and provides mass to all down-type sfermions. After EWSB, three of the eight real degrees of freedom from both doublets are absorbed by

the $W^\pm$ and Z bosons, giving them mass. The remaining five real fields manifest as five Higgs bosons in the MSSM spectrum: two CP-even neutral Higgs bosons (h and H), one CP-odd neutral Higgs boson (A) and two charged Higgs bosons ($H^\pm$). The lighter CP-even Higgs boson (h) is believed to be the Higgs boson discovered at the LHC, often referred to as the SM-like Higgs boson due to its similarities to the SM Higgs.

In MSSM, the scalar potential for the Higgs fields arises from the combination of F-term, D-term, and terms for the soft SUSY breaking terms for the Higgs fields (third line of Eq. (1.68)) defined as:

$$V_H = V_F + V_D + V_{soft} \tag{1.71}$$

where,

$$V_F = \mu^2 \left(|H_d|^2 + |H_u|^2 \right) \tag{1.72}$$

$$V_D = \frac{g'^2}{8} \left(|H_u|^2 - |H_d|^2 \right)^2 + \frac{g^2}{8} \left[4|H_d^\dagger H_u|^2 - 2|H_d|^2|H_u|^2 + \left(|H_d|^2 \right)^2 + \left(|H_u|^2 \right)^2 \right] \tag{1.73}$$

$$V_{soft} = M_{H_d}^2 H_d^\dagger H_d + M_{H_u}^2 H_u^\dagger H_u + (\mu H_d H_u + \text{ h.c. }) \tag{1.74}$$

where g' and g denote $U(q)_Y$ and $SU(2)_L$ couplings respectively. The VEVs of the two Higgs doublets satisfy

$$v_u^2 + v_d^2 = v^2 \simeq (246\text{GeV})^2 \tag{1.75}$$

$$\tan \beta = \frac{v_u}{v_d} \tag{1.76}$$

Neutral components of the Higgs doublets are expanded around the respective VEVs in the following way:

$$H_u = \frac{1}{\sqrt{2}} \begin{pmatrix} H_u^+ \\ v_u + H_u^0 + iA_u^0 \end{pmatrix}, H_d = \frac{1}{\sqrt{2}} \begin{pmatrix} v_d + H_d^0 + iA_d^0 \\ H_d^- \end{pmatrix} \tag{1.77}$$

Following EWSB, the real neutral components, H_u^0 and H_d^0, mix resulting in two CP-even scalar Higgs states (h and H). Meanwhile, the imaginary components, A_u^0 and A_d^0, combine to form the CP-odd pseudoscalar Higgs (A) and one neutral Goldstone boson, absorbed by Z, granting it mass. Similarly, the charged complex scalars, H_u^+ and H_d^-, mix to form two physical charged Higgs states ($H^\pm$) and the two charged Goldstone bosons, absorbed by the $W^\pm$. The electroweak symmetry is spontaneously broken when the vacuum chooses one of the available minima of the Higgs potential, connected by gauge transformations. The

specific conditions that define this minimum of the Higgs potential can be mathematically expressed as $\partial V_H / \partial H_u^0 = 0$ and $\partial V_H / \partial H_d^0 = 0$. Using Eq. (1.6.2) and Eq. (1.76) this lead to two minimization conditions at tree level

$$\mu = \frac{\left(m_{H_1}^2 - m_{H_2}^2\right) \tan 2\beta + M_Z^2 \sin 2\beta}{2} \tag{1.78}$$

$$\mu^2 = \frac{m_{H_2}^2 \sin^2 \beta - m_{H_1}^2 \cos^2 \beta}{\cos 2\beta} - \frac{M_Z^2}{2} \tag{1.79}$$

The physical mass eigenstates of Higgs are given by rotation as following -

$$\text{Re}H_u^0, \text{Re}H_d^0 \xrightarrow{\alpha} h, H \quad \text{Im}H_u^0, \text{Im}H_d^0 \xrightarrow{\beta} A^0, G \quad H_u^\pm, H_d^\pm \xrightarrow{\beta} H^\pm, G^\pm \tag{1.80}$$

$$A = -\sin\beta A_d^0 + \cos\beta A_u^0, \tag{1.81}$$

$$H^\pm = -\sin\beta H_d^\pm + \cos\beta H_u^\pm, \tag{1.82}$$

$$\begin{pmatrix} h \\ H \end{pmatrix} = \begin{pmatrix} -\sin\alpha & \cos\alpha \\ \cos\alpha & \sin\alpha \end{pmatrix} \begin{pmatrix} H_u^0 \\ H_d^0 \end{pmatrix} \tag{1.83}$$

where α is the mixing angle between the two CP-even neutral states given by

$$\alpha = \frac{1}{2} \tan^{-1}\left(\tan 2\beta \frac{M_A^2 + M_Z^2}{M_A^2 - M_Z^2}\right), \quad -\frac{\pi}{2} \leq \alpha \leq 0 \tag{1.84}$$

The tree level Higgs masses read as

$$M_A^2 = -\mu\left(\tan\beta + \cot\beta\right), \tag{1.85}$$

$$M_{H^\pm} = M_A^2 + M_W^2 \tag{1.86}$$

$$M_{h,H}^2 = \frac{1}{2}\left(M_A^2 + M_Z^2\right) \mp \sqrt{\left(M_A^2 + M_Z^2\right)^2 - 4M_A^2 M_Z^2 \cos^2 2\beta} \tag{1.87}$$

Here the tree level CP-even Higgs mass h is bounded from above and cannot be greater than mass of Z.

$$m_h \leq M_Z |\cos 2\beta| \tag{1.88}$$

The experimentally observed 125 GeV Higgs mass suggests significant radiative corrections. The Higgs mass receives one-loop contributions from the top quark and its supersymmetric partner, the stop. In exact supersymmetry, these contributions would cancel. However, with broken supersymmetry, the stop's one-loop effect contributes to the Higgs mass as [130,131]:

$$\Delta M_{h,1-loop}^2 \simeq \frac{3m_t^4}{2\pi^2 v^2 \sin^2 \beta}\left[ln\frac{M_S^2}{m_t^2} + \frac{X_t^2}{2M_S^2}\left(1 - \frac{X_t^2}{6M_S^2}\right)\right], \tag{1.89}$$

where m_t denotes top quark mass, $M_S = (m_{\tilde{t}_1} + m_{\tilde{t}_2})/2$ with $m_{\tilde{t}_1,\tilde{t}_2}$ stands for mass ordered stop squarks and $X_t = A_t - \mu \cot \beta$ is stop mixing parameter with A_t being the soft supersymmetry-breaking stop trilinear coupling. The MSSM Higgs mass also receives substantial contributions from 2-loop and 3-loop. For a detailed review, refer to [132].

1.6.3 The electroweakino sector of MSSM

Because of the electroweak symmetry breaking, electroweak gauginos of the $SU(2)_L \times U(1)_Y$ gauge group mix with higgsinos of the same charge and result in mass eigenstates called electroweakinos, i.e. charginos and neutralinos. The neutral higgsinos $\tilde{H}_u^0$, $\tilde{H}_d^0$ mix with the neutral gauginos $\tilde{B}, \tilde{W}^0$ to form four neutralinos $\tilde{\chi}_{1,...4}^0$, while the charged higgsinos $\tilde{H}_u^+$, $\tilde{H}_d^-$ and charged winos $\tilde{W}^\pm$ combine into two charginos $\tilde{\chi}_{1,2}^\pm$. Conventionally masses of electroweakinos are in ascending order, i.e. $m_{\tilde{\chi}_1^0} < m_{\tilde{\chi}_2^0} < m_{\tilde{\chi}_3^0} < m_{\tilde{\chi}_4^0}$ and $m_{\tilde{\chi}_1^\pm} < m_{\tilde{\chi}_2^\pm}$. The lightest neutralino $\tilde{\chi}_1^0$ is usually the favoured LSP in MSSM in an R-parity conserving scenario (RPC), usually in DM models. Also, there are SUSY models with other particles being the LSP like stau, sneutrino, gravitino etc., both in RPC and R-parity violating (RPV) scenario.

In a gauge-eigenstate basis $\psi^0 = (\tilde{B}, \tilde{W}^0, \tilde{H}_d^0, \tilde{H}_u^0)^T$ the neutralinos has the Majorana mass term as

$$\mathcal{L}_{\text{nuentralino mass}} = -\frac{1}{2}(\psi^0)^T \mathbf{M}_N \psi^0 + c.c., \tag{1.90}$$

where 4×4 matrix $\mathbf{M}_N$ is given by

$$\mathbf{M}_N = \begin{pmatrix} M_1 & 0 & -M_Z \sin\theta_W \cos\beta & M_Z \sin\theta_W \sin\beta \\ 0 & M_2 & M_Z \cos\theta_W \cos\beta & -M_Z \cos\theta_W \sin\beta \\ -M_Z \sin\theta_W \cos\beta & M_Z \cos\theta_W \cos\beta & 0 & -\mu \\ M_Z \sin\theta_W \sin\beta & -M_Z \cos\theta_W \sin\beta & -\mu & 0 \end{pmatrix}. \tag{1.91}$$

$\mathbf{M}_N$ can be diagonalised by a unitary matrix $\mathbf{N}$, $\tilde{N}_i = \mathbf{N}_{ij}\psi_j^0$ to obtain the mass eigenstates, so that $\mathbf{N}^* \mathbf{M}_{\tilde{N}} \mathbf{N}^{-1} = \text{diag}(m_{\tilde{\chi}_1^0}, ..., m_{\tilde{\chi}_4^0})$. Neutralinos in the MSSM are a mixture of $(\tilde{B}, \tilde{W}^0, \tilde{H}_d^0, \tilde{H}_u^0)$ and the composition varies for each neutralino.

In the gauge-eigenstate basis $\psi^\pm = (\tilde{W}^+, \tilde{H}_u^\pm, \tilde{W}^-, \tilde{H}_d^-)$ the mass term of the charginos is given by

$$\mathcal{L}_{\text{chargino mass}} = -\frac{1}{2}(\psi^\pm)^T \mathbf{M}_C \psi^\pm + c.c., \tag{1.92}$$

where 2×2 $\mathbf{M}_C$ is given by

$$\mathbf{M}_C = \begin{pmatrix} 0 & \mathbf{X}^T \\ \mathbf{X} & 0 \end{pmatrix}, \text{ where } \mathbf{X} = \begin{pmatrix} M_2 & \sqrt{2}M_W \sin\beta \\ \sqrt{2}M_W \sin\beta & \mu \end{pmatrix} \tag{1.93}$$

The mass eigenstates are correlated to the gauge eigenstates by two unitary matrices $\mathbf{U}$ and $\mathbf{V}$ for positively and negatively charged left-handed fermions, respectively as

$$\begin{pmatrix} \widetilde{\chi}_1^+ \\ \widetilde{\chi}_2^+ \end{pmatrix} = \mathbf{V} \begin{pmatrix} \tilde{W}^+ \\ \tilde{H}_u^+ \end{pmatrix}, \quad \begin{pmatrix} \widetilde{\chi}_1^- \\ \widetilde{\chi}_2^- \end{pmatrix} = \mathbf{U} \begin{pmatrix} \tilde{W}^- \\ \tilde{H}_d^- \end{pmatrix} \tag{1.94}$$

The chargino mass eigenstates are obtained by diagonalizing the charging mass matrix as $\mathbf{U}^* \mathbf{X} \mathbf{V}^{-1} = \text{diag}\left(m_{\widetilde{\chi}_1^\pm}, m_{\widetilde{\chi}_2^\pm} \right)$.

1.6.4 Squarks and Sleptons

After EWSB, sfermions with the same electric charge mix. This suggests, with arbitrary soft terms, the mass eigenstates of squarks and sleptons are obtained by diagonalization of three 6×6 mixing matrices — one for up-type squarks ($\tilde{u}_L, \tilde{c}_L, \tilde{t}_L, \tilde{u}_R, \tilde{c}_R, \tilde{t}_R$), one for down-type squarks ($\tilde{d}_L, \tilde{s}_L, \tilde{b}_L, \tilde{d}_R, \tilde{s}_R, \tilde{b}_R$), and one for charged sleptons ($\tilde{e}_L, \tilde{\mu}_L, \tilde{\tau}_L, \tilde{e}_R, \tilde{\mu}_R, \tilde{\tau}_R$). The sneutrino sector have a 3×3 sneutrino mixing matrix for only left-handed fields ($\tilde{\nu}_{eL}, \tilde{\nu}_{\mu L}, \tilde{\nu}_{\tau L}$) since the SM does not contain right handed neutrinos.

The mass term of the sfermions reads as

$$\mathcal{L}_{Sfermion}^{mass} = -\phi_{\tilde{f}}^\dagger M_{\tilde{f}}^2 \phi_{\tilde{f}} \tag{1.95}$$

with $\tilde{f}$ spans over all the fermion flavors across the three generations. However, the presence of arbitrary mixings would cause very large FCNC effects, which have very strong experimental bounds. Hence, it is usually demanded that the squark mass eigenstates are entirely aligned with the quark mass eigenstates. Keeping this in mind, the squared mass matrix for a particular sfermion can be given as

$$M_{\tilde{f}}^2 = \begin{pmatrix} M_f^2 + M_{LL}^2 & M_f X_f \\ M_f X_f & M_f^2 + M_{RR}^2 \end{pmatrix} \tag{1.96}$$

with

$$M_{LL}^2 = M_{\tilde{f}_L}^2 + \left(T_3^f - Q_f \sin^2\theta_W \right) M_Z^2 \cos 2\beta \tag{1.97}$$

$$M_{RR}^2 = M_{\tilde{f}_R}^2 + Q_f \sin^2 \theta_W M_Z^2 \cos 2\beta \tag{1.98}$$

$$X_f = A_f - \mu \left(\tan \beta\right)^{-2T_3^f} \tag{1.99}$$

Here, M_f denotes the mass of the corresponding SM fermion, $M_{\tilde{f}L}$ and $M_{\tilde{f}R}$ represent the sfermion soft mass terms for the left-handed doublet and right-handed singlet respectively, T_3^f denotes the third component of weak isospin of left-handed fermions in left-handed doublet, Q_f is the electromagnetic charge of f. The mixing between the left and right sfermion of the same flavor is quantified by X_f, which originates from the trilinear coupling of the sfermion, the A-terms and Higgs-sfermion-sfermion couplings quantified by the higgsino mass parameter, and the ratio of VEVs of the two Higgs doublets. Since the mixing term in the squark mass matrices is proportional to the mass of the corresponding fermionic partner, significant squark mixing only occurs in the third generation, where the sfermions are much heavier.

1.7 Supersymmetry breaking mechanisms

Minimal Supergravity

In the minimal supergravity framework, gravitational interactions transmit this breaking from the hidden sector to the visible sector. The scale of SUSY breaking in this scenario is typically linked to the Planck scale leading to very massive superpartners. Here, the soft terms are $m_{\tilde{f}}^2 \approx M_S^2/M_{Planck}$ where M_S is the SUSY breaking scale. To have these masses at weak scale, $M_S \sim 10^{10}$ GeV. M_S^2 can be linked to the VEV of the F-term in the hidden sector. This mechanism of SUSY breaking is called supergravity (SUGRA) mediated supersymmetry breaking. However, flavour changing neutral current effects are usually problematic in SUGRA theories. A set of supergravity mediated supersymmetry breaking models, called "minimal" supergravity solves this by inducing boundary conditions and thus reducing the total number of free parameters. These models enforce specific equalities at the high scale: (i) equal gaugino masses (ii) equal scalar masses (iii) all the trilinear scalar interactions are equal (iv) all bilinear scalar interactions are equal. In literature, these models are also known as CMSSM, as pointed out previously.

Gauge-mediated supersymmetry breaking

In gauge-mediated SUSY breaking (GMSB) models [133], SUSY breaking is communicated from a hidden sector via messengers, which are charged under the SM gauge group. The soft SUSY breaking information is passed on to the visible sector via loop effects of gauge bosons and their fermionic partners. The SUSY breaking soft parameters in the MSSM sector are flavour diagonal as they are generated by gauge interactions, leading to similar gaugino and sfermion masses $\sim \frac{g_{SM}^2}{16\pi^2} \frac{F}{M_{mess}}$ where F is the SUSY-breaking VEV acquired by the fields in the hidden sector and M_{mess} is the messenger mass. Another important feature of the GMSB models is that the gravitino can be the LSP, with masses typically of the order of a few KeV.

1.7.1 Anomaly-mediated supersymmetry breaking

In anomaly-mediated supersymmetry breaking (AMSB) models, it is assumed that SUSY breaking in the hidden sector communicates with the MSSM through the auxiliary component of the supergravity multiple. The soft masses caused by gravity- or gauge-mediation are suppressed; hence, the soft masses arising from the superconformal anomaly become important [134, 135]. Anomaly mediation typically leads to relatively light gauginos compared to sfermions. However, these models face numerous phenomenological challenges, for instance, the presence of tachyonic sleptons.

1.8 The Next-to-MSSM

MSSM is a compelling theory that addresses some of the limitations of the SM and offers several theoretical advantages, although it has yet to be experimentally verified. SUSY proposes a solution to the hierarchy problem by loop corrections from superpartners, particularly the stop, which cancel out the large contributions from the top quark loop, stabilizing the Higgs mass and alleviating the need for fine-tuning. The MSSM, with its additional particles and interactions, shows some hints of potentially unifying the weak, electromagnetic, and strong couplings at a grand unification scale ($\Lambda_{GUT} \sim 10^{16}$ GeV). In the MSSM with R-parity neutralino, LSP offers many MSSM realisations as a valid WIMP candidate for DM. It allows mechanisms like the seesaw mechanism to introduce neutrino masses while maintaining consistency with other aspects of the theory.

However, the MSSM faces many challenges; one of the prominent is known as the "μ problem" [136]. This arises because a specific soft SUSY breaking term $\mu H_u^0 H_d^0$, in the Higgs potential, is needed for EWSB such that both the Higgs doublet get non-zero VEV. μ, being a dimensionful superpotential parameter, in principle, could take values as high as Plack scale, since it has no relation to the aforementioned soft terms. However, the minimisation conditions Eq. (1.78)-(1.79) infer that μ should be roughly at the same order of magnitude with the SUSY breaking scale to maintain M_Z. This inconsistency is the μ problem. The Next-to-Minimal Supersymmetric Standard Model (NMSSM) offers a solution by introducing a new singlet superfield ($\hat{S}$) that generates an effective μ-term through SUSY breaking. This mechanism elegantly solves the μ problem while preserving the successes of the MSSM. Additionally, the NMSSM provides a richer Higgs sector and electroweakino sector, potentially addressing limitations in the original MSSM.

The most general scale invariant NMSSM superpotential is given by [137],

$$W_{\text{NMSSM}} = W_{\text{MSSM}}|_{\mu=0} + \lambda \hat{S} \hat{H}_u . \hat{H}_d + \frac{\kappa}{3} \hat{S}^3, \tag{1.100}$$

where, $W_{\text{MSSM}}|_{\mu=0}$ denotes the MSSM superpotential without the $\mu-$term (Eq. (1.63)), $\hat{H}_u$ and $\hat{H}_d$ are the two doublet Higgs superfields similar to MSSM, and $\hat{S}$ is a gauge singlet Higgs superfield. The dimensionless parameters, "λ" and "κ", control the mixing between the doublet and singlet Higgs superfields and self-coupling of the singlet superfield, respectively. The superpotential in Eq. (1.100) provides a solution to the MSSM μ-problem by generating an effective μ-term, $\mu_{\text{eff}} = \lambda v_S$, when, $\hat{S}$ develops a vacuum expectation value v_S. Below, we write a short review of the Higgs and electroweakino sector of the NMSSM model, based on our work in [138].

1.8.1 Higgs sector of NMSSM

The Higgs scalar potential V_{Higgs} receives contributions from the soft SUSY breaking terms V_{soft} [137],

$$V_{soft} = m_{H_u}^2 |H_u|^2 + m_{H_d}^2 |H_d|^2 + m_S^2 |S|^2$$
$$+ \left(\lambda A_\lambda S H_u \cdot H_d + \frac{1}{3} \kappa A_k S^3 + \text{h.c.} \right), \tag{1.101}$$

where, m_{H_u}, m_{H_d}, m_S are the soft breaking Higgs masses and A_λ, A_κ are the trilinear couplings with dimensions of mass. The full scalar Higgs potential is obtained by combining

V_{soft} with the F and D terms, $V_{Higgs} = V_{soft} + V_D + V_F$, with,

$$V_F = |\lambda H_u \cdot H_d + \kappa S^2|^2 + \lambda^2 |S|^2 \left(H_u^\dagger H_u + H_d^\dagger H_d \right), \text{ and}$$

$$V_D = \frac{g_1^2 + g_2^2}{8} \left(H_u^\dagger H_u - H_d^\dagger H_d \right)^2 + \frac{g_2^2}{2} |H_d^\dagger H_u|^2. \tag{1.102}$$

In Eq. (1.102), g_1 and g_2 are the SM $U(1)_Y$ and $SU(2)_L$ gauge couplings, respectively. Expanding V_{Higgs} around the real neutral $vevs$ v_d, v_u and v_S, we obtain the physical neutral Higgs fields $\{H_d^0, H_u^0, S\}$,

$$H_d^0 = v_d + \frac{H_{dR} + iH_{dI}}{\sqrt{2}}, \quad H_u^0 = v_u + \frac{H_{uR} + iH_{uI}}{\sqrt{2}}, \quad S = v_S + \frac{S_R + iS_I}{\sqrt{2}}, \tag{1.103}$$

where, the subscripts R and I indicate the CP-even and CP-odd states of $\{H_d^0, H_u^0, S\}$, respectively. In the basis $\{H_{dR}, H_{uR}, S_R\}$, the 3×3 symmetric mass-squared matrix $\mathcal{M}_S^2$ for the CP-even neutral Higgs states is given by [137],

$$\mathcal{M}_S^2 = \begin{pmatrix} g^2 v_d^2 + \mu(A_\lambda + \kappa v_S)\tan\beta & (2\lambda^2 - g^2)v_u v_d - \mu(A_\lambda + \kappa v_S) & \lambda(2\mu v_d - (A_\lambda + 2\kappa v_S)v_u) \\ ... & g^2 v_u^2 + \mu(A_\lambda + \kappa v_S)/\tan\beta & \lambda(2\mu v_u - (A_\lambda + 2\kappa v_S)v_d) \\ ... & ... & \lambda A_\lambda \frac{v_u v_d}{v_S} + \kappa v_S(A_\kappa + 4\kappa v_S) \end{pmatrix}, \tag{1.104}$$

where $g^2 = (g_1^2 + g_2^2)/2$, $v_u = v\sin\beta$ and $v_d = v\cos\beta$ with $v^2 = v_u^2 + v_d^2 \approx (174 \text{ GeV})^2$, and $\tan\beta = v_u/v_d$. The CP-even Higgs mass eigenstates H_i $(i = 1, 2, 3)$ can be obtained by diagonalizing $\mathcal{M}_S^2$ by the matrix S, such that

$$H_i = \sum_{j=1}^{3} S_{ij} H_{jR}, \quad \text{with} \quad H_{jR} = \{H_{uR}, H_{dR}, S_R\}. \tag{1.105}$$

Assuming negligible mixing between the doublet and singlet components, the squared mass of the singlet-dominated CP-even state at the tree-level is given by the (3,3) element of $\mathcal{M}_S^2$,

$$m_{H_S}^2 \approx \mathcal{M}_{S33}^2 = \lambda A_\lambda \frac{v_u v_d}{v_S} + \kappa v_S(A_\kappa + 4\kappa v_S). \tag{1.106}$$

Under this assumption, one of the other two CP-even eigenstates must be consistent with the observed SM-like Higgs boson with a mass near 125 GeV, and the other one is a MSSM-like Higgs eigenstate with squared mass around

$$m_{H_3}^2 = 2\mu(A_\lambda + \kappa v_S)/\sin 2\beta \tag{1.107}$$

In this scenario, the CP-even Higgs bosons can be conveniently rotated to the basis $\{\widehat{h}, \widehat{H}, \widehat{s}\}$ [139, 140], such that $\widehat{h} = H_{dR}\cos\beta + H_{uR}\sin\beta$, $\widehat{H} = H_{dR}\sin\beta - H_{uR}\cos\beta$ and $\widehat{s} = S_R$, with $\widehat{h}$ and $\widehat{H}$ fields resembling the SM-like Higgs boson and the MSSM-like heavy Higgs bosons, respectively. The mass eigenstates in this basis can then be expressed as,

$$H_i = V_{h_i\widehat{h}}\widehat{h} + V_{h_i\widehat{H}}\widehat{H} + V_{h_i\widehat{s}}\widehat{s} \quad \text{where } (i = 1, 2, 3) \tag{1.108}$$

where V represents the 3×3 unitary matrix that diagonalizes the mass-squared matrix of CP-even Higgs boons in the rotated basis $\{\widehat{h}, \widehat{H}, \widehat{s}\}$.

The mass of SM-like Higgs boson H_{SM} at the one-loop level can be written as [141],

$$m_{H_{SM}}^2 = m_Z^2 \cos^2 2\beta + \lambda^2 v^2 \sin^2 2\beta + \Delta_{mix} + \Delta_{\text{rad.corrs.}} \tag{1.109}$$

Here, the second term implies that a large λ and low $\tan\beta$ is typically favorable to uplift $m_{H_{SM}}$ from $\sim m_Z$ and bring it closer to the observed mass of ~ 125 GeV at the tree-level, thus typically reducing the amount of radiative corrections required to generate the correct Higgs boson mass, when compared to MSSM. The third term in Eq. (1.109), Δ_{mix}, is the contribution arising from singlet-doublet mixing. In the limit where the mixing is not large, Δ_{mix} is given by [141],

$$\Delta_{\text{mix}} \simeq \frac{4\lambda^2 v_S^2 v^2 (\lambda - \kappa \sin 2\beta)^2}{(\overline{M_h}^2 - M_{SS}^2)}, \tag{1.110}$$

where, $\overline{M_h}^2 = m_{H_{SM}}^2$ (given by Eq. (1.109)) for $\Delta_{\text{mix}} \sim 0$, and $M_{SS}^2 \simeq \kappa v_S(A_\kappa + 4\kappa v_S)$ is the squared mass of CP-even singlet-like Higgs assuming a heavy singlet, $\kappa v_S >> A_\kappa, A_\lambda$ (see Eq. (1.106)). The contribution from this term can be positive or negative depending on the mass difference $\overline{M_h}^2 - M_{SS}^2$.

In the decoupling limit, $\lambda, \kappa \to 0$, the radiative corrections to $m_{H_{SM}}$, $\Delta_{\text{rad.corrs.}}$, become crucial to obtain the correct mass for the SM-like Higgs boson. The dominant radiative contributions at one-loop from the top/stop loops are given by,

$$\Delta_{\text{rad.corrs.}}^{1-\text{loop}} \simeq \frac{3m_t^4}{4\pi^2 v^2 \sin^2\beta} \left[ln\frac{M_S^2}{m_t^2} + \frac{X_t^2}{M_S^2}\left(1 - \frac{X_t^2}{12M_S^2}\right) \right], \tag{1.111}$$

where, m_t denotes top quark mass, $M_S = \sqrt{m_{\tilde{t_1}}m_{\tilde{t_2}}}$ with $m_{\tilde{t}_1, \tilde{t}_2}$ stands for mass ordered stop squarks and $|X_t| = A_t - \mu\cot\beta$ is stop mixing parameter with A_t being the soft supersymmetry-breaking stop trilinear coupling. Similar to Eq. (1.104), the mass squared

matrix $\mathcal{M}_{\mathcal{P}}'^2$ for the CP-odd states (H_{dI}, H_{uI}, S_I) from Eq. (1.103) can be defined as [137],

$$
\mathcal{M}_{\mathcal{P}}'^2 = \begin{pmatrix} \mu(A_\lambda + \kappa v_S)\tan\beta & \mu(A_\lambda + \kappa v_S) & \lambda v_u(A_\lambda - 2\kappa v_S) \\ ... & \mu(A_\lambda + \kappa v_S)/\tan\beta & \lambda v_d(A_\lambda - 2\kappa v_S) \\ ... & ... & \lambda(A_\lambda + 4\kappa v_S)\frac{v_u v_d}{v_S} - 3\kappa A_\kappa v_S \end{pmatrix}. \tag{1.112}
$$

Without any loss of generality, the mass matrix can be rotated to a new basis, $\{H_{dI}, H_{uI}, S_I\} \to \{A, G, S_I\}$,

$$
\begin{pmatrix} H_{dI} \\ H_{uI} \\ S_I \end{pmatrix} = \begin{pmatrix} \sin\beta & -\cos\beta & 0 \\ \cos\beta & \sin\beta & 0 \\ 0 & 0 & 1 \end{pmatrix} \begin{pmatrix} A \\ G \\ S_I \end{pmatrix}. \tag{1.113}
$$

Dropping the Goldstone mode G, the remaining 2×2 mass squared matrix in the basis of $\{A, S_I\}$ can be expressed as,

$$
\mathcal{M}_{\mathcal{P}}^2 = \begin{pmatrix} m_A^2 & \lambda(A_\lambda - 2\kappa v_S)v \\ \lambda(A_\lambda - 2\kappa v_S)v & \lambda(A_\lambda + 4\kappa v_S)\frac{v_u v_d}{v_S} - 3\kappa A_\kappa v_S \end{pmatrix}, \tag{1.114}
$$

with $m_A^2 = 2\mu(A_\lambda + \kappa v_S)/\sin 2\beta$, which represents the squared mass of the doublet-like CP-odd scalar A similar to that in the MSSM. Likewise, the squared mass of the singlet-like CP-odd scalar A_s, assuming negligible singlet-doublet mixing, is represented by the $\{2, 2\}$ element in $\mathcal{M}_{\mathcal{P}}^2$.

Overall, the scalar sector is characterized by six parameters:

$$
\lambda, \kappa, A_\lambda, A_\kappa, \mu, \tan\beta, \tag{1.115}
$$

as indicated by Eqs.(1.106), (1.109) and (1.114).

1.8.2 Electroweakino sector

The NMSSM electroweakino sector consists of the neutralinos and charginos that originate from the interaction of the fermionic superpartner of singlet field ($\widetilde{S}$) with the higgsinos and gauginos. This augments the electroweak sector to 5 neutralino and 2 chargino mass eigenstates. The neutralino sector in the basis $(\widetilde{B}, \widetilde{W}_3^0, \widetilde{H}_d^0, \widetilde{H}_u^0, \widetilde{S})$ is given by 5×5 symmetric

matrix as [137]

$$\mathcal{M}_{\widetilde{N}} = \begin{pmatrix} M_1 & 0 & -\frac{g_1 v_d}{\sqrt{2}} & \frac{g_1 v_u}{\sqrt{2}} & 0 \\ ... & M_2 & \frac{g_2 v_d}{\sqrt{2}} & -\frac{g_2 v_u}{\sqrt{2}} & 0 \\ ... & ... & 0 & -\mu_{eff} & -\lambda v_u \\ ... & ... & ... & 0 & -\lambda v_d \\ ... & ... & ... & ... & -2\kappa v_S \end{pmatrix} \tag{1.116}$$

where M_1 and M_2 are the bino and wino mass parameters, responsible for soft SUSY breaking of $U(1)_Y$ and $SU(2)_L$, respectively. The mass eigenstates of 5 neutralinos, $m_{\widetilde{\chi}_i^0}$(i=1,..5) can be obtained by diagonalizing the mass matrix $\mathcal{M}_{\widetilde{N}}$ by an orthogonal real matrix N as

$$\widetilde{\chi}_i^0 = N_{i1}\widetilde{B} + N_{i2}\widetilde{W}_3^0 + N_{i3}\widetilde{H}_d^0 + N_{i4}\widetilde{H}_u^0 + N_{i5}\widetilde{S}; \tag{1.117}$$

where the neutralino masses are ordered but not necessarily positive.

Similarly, the charged winos and higgsinos mix to generate the two charginos following the same mechanism as MSSM (see Sec 1.6.3). The input parameters that regulate the electroweakino sector at the tree level are $M_1, M_2, \mu_{eff}, \tan\beta, \lambda, \kappa$.

In the context of NMSSM, the LSP can be singlino-like, bino-like or higgsino-like. Since there is no tree-level coupling between the singlino and gauginos, the $\widetilde{\chi}_1^0$ will be singlino dominated if

$$2|\kappa|v_S << M_{1,2}, \mu \quad \text{with} \quad m_{\widetilde{\chi}_1^0} \approx 2\kappa v_S \equiv 2\kappa\mu/\lambda. \tag{1.118}$$

For singlino like LSP, $\kappa/\lambda << 1$ while for higgsino like LSP κ/λ ratio can be large along with $\lambda v >> \mu$. LEP2 put a lower bound on $\mu \geq 104$ GeV, where CMS and ATLAS experiments have excluded μ up to mass ~ 200 GeV with not so large mass splitting ~ 10 GeV [142,143]. Bino-like LSP needs $\mu >> M_1$. Implications of different compositions of LSP and their interactions with mainly singlet-like scalars are critical in the context of DM-annihilation, which we discuss in Chapter 4.

1.9 Long-Lived particles: a different look into BSM physics

We have already pointed out hints of physics beyond the SM. The search for physics beyond SM often prioritizes promptly decaying particles at the LHC. However, the lifetimes of SM particles vary greatly, as shown in Fig. 1.8. For simplicity, we'll use "lifetime" for the mean proper decay lifetime (τ) and "decay length" for the mean proper decay length ($c\tau$)
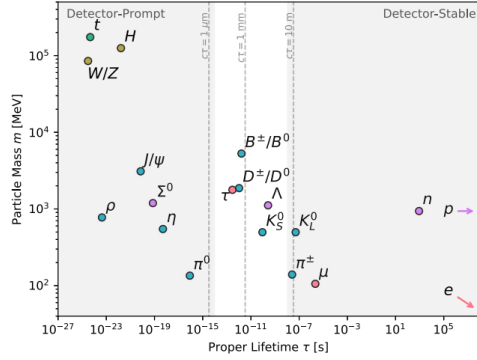
Figure 1.8: The SM particle spectrum is plotted against mass and proper lifetime. The regions where particles are detected promptly (Detector-Prompt) and remain stable within the detector (Detector-stable) are indicated by shaded areas, for a particle moving at near-light speed. The Fig. is taken from ref. [144].

unless otherwise specified. It's important to remember that the decay length observed in a detector's reference frame will be different due to a Lorentz boost, which will be,

$$d = \beta\gamma c\tau \tag{1.119}$$

with the boost factor of the particle is given by $\beta\gamma = \frac{p}{m}$ where p and m identify the particle's momentum in the collider and its mass, respectively. Typically, particles with a $c\tau$ greater than or around a few mm, which translates to $\tau \gtrsim \mathcal{O}(ps)$, are considered as "long-lived particle"s (LLP)s in the context of collider searches. In the middle region of Fig. 1.8 with lifetimes in the range of 10^{-12} s to 10^{-9} s lies the LLP hadrons of the SM, which are bound states containing s, c or b quarks.

A particle's long lifetime, or in other words, small decay width, can stem from several factors:

- Small matrix element: This can occur due to a combination of differing energy scales in the interactions mediating the decay, weak couplings between the particle and its decay products, or the presence of a massive propagator.

- Limited decay phase space: This happens when the mass difference between the decaying particle and its decay products is small, restricting the particle's ability to decay.

SM also contains examples of LLPs owing to the aforementioned reasons. Such as, the decay of b hadrons may involve off-diagonal terms of the CKM matrix inducing suppressed decay rates leading to a long lifetime. Neutron decays to a proton by emitting an electron and a neutrino via the exchange of a massive virtual W boson. It has a small decay width due to the very limited availability of the phase space and also because of the small mass difference between the proton and the neutron owing to isospin symmetry. Decays mediated by massive particles like the W boson may experience suppression. Muon decay is an example, where the large mass of the W boson compared to the muon significantly reduces the decay width $\left(\Gamma_\mu \propto \frac{M_\mu^3}{M_W^4}\right)$. Similarly, beyond the SM, many theories predict new particles with varying masses and lifetimes, including LLPs. Below, we discuss some scenarios of LLP in BSM and their signature at collider, which motivated the studies of Chapter 3.

1.9.1 LLP in BSM

As previously introduced, multiple mechanisms can prolong a particle's lifetime, therefore, a wide variety of BSM theories can produce LLPs. A brief overview of theories is given below.

Supersummetry

- In the MSSM or NMSSM, the LSP is often the neutralino $\widetilde{\chi}_1^0$, and the next-to-the lightest supersymmetric particle, NLSP can be long-lived if the mass difference between it and the LSP is small.

- In the RPV-SUSY models, LSPs are allowed to decay to SM particles, provided the RPV decays are hierarchically small. These tiny RPV interactions lead to very long lifetimes for the LSP, making it effectively long-lived. In principle, any superpartner could be the LSP in RPV models, and the decay products depend on the strongest RPV coupling.

- GMSB models include the SM particles, their superpartners, along with a goldstino which is absorbed by a gravitino, the superpartner of the graviton and also the LSP of the model. GMSB models are characterized by the effective mass scale of SUSY breaking Λ, which is proportional to the mass of the gravitino. The SM superpartners decay to SM particles and gravitino via high dimensional operators, and long lifetimes

may appear for the NLSP if the SUSY breaking scale is small enough to suppress the interaction of these operators.

Higgs-portal theories

In Higgs-portal theories, SM Higgs can couple to a new hidden sector of weakly interacting particles non-connected to the SM gauge group that are LLPs (like singlet under SM gauge group). The study of the unique properties of the SM Higgs boson provides a gateway to explore its interactions with BSM particles, establishing the Higgs portal as a compelling pathway for studying long-lived particles. The portal also offers a natural way to introduce new physics while maintaining a well-behaved renormalizable theory with potential solutions to the hierarchy problem. Some Hidden-Valley (HV) models [145] within this framework predict exotic decays like the Higgs splitting into two weakly interacting particles ($H \rightarrow XX$) with low mass. The Higgs boson stands out for its diverse production mechanisms beyond the prevalent gluon-fusion process. Vector-boson fusion (VBF) and Higgs-strahlung (VH) production offer unique ways to trigger Higgs events and reduce background noise, particularly for rare, exotic Higgs decays producing LLPs.

Gauge-portal theories

Gauge-portal theories propose new vector mediators that interact with LLPs [146] by extending the existing SM gauge group. These mediators (gauge bosons) can arise in models with a new charge and couple to both SM and LLPs, for example, Z' [147] in $p - p$ collision. Models with Abelian or non-Abelian forces (dark photons or dark Zs) that couple weakly to SM particles through kinetic mixing where the SM particles are not charged under the new gauge group are also included in this category.

Hevy neutral leptons

Neutrino portal theories introduce right-handed heavy neutral leptons (HNLs) [148]. With HNLs, the tiny neutrino mass can be explained via See-Saw mechanism [149] in terms of new gauge-invariant mass terms for the SM neutrinos. Stable HNLs could also be a dark matter candidate. HNLs are produced from their mixing with SM neutrinos, characterized by the coupling strength V_{Nl}. HNLs decay is mediated by $W^{\pm}$ or a Z^* boson. Its lifetime τ_N

depends on its mass m_N and the mixing strength $|V_{NL}|^2$. HNLs are long-lived if they have low mass and weak mixing parameters.

Dark-matter theories

There are considerable examples of LLPs occurring in DM-motivated models, like non-SUSY and hidden-sector DM scenarios where the cosmological DM is produced as a final state in the collider processes. Higgs-portal and gauge-portal models are some examples of this which we have already discussed. Other theories under this umbrella include multi-component DM like (a) models with new electroweak multiplates [150–152] where the LLP candidate can be the heavier components while the lightest component is the DM, (b) inelastic dark matter, [153–156] models with DM coannihilation partners [157–160] where LLPs appear in terms of Dark Photons, Scalar Mediators, etc., (c) strongly interacting massive particles (SIMPs) like in SIMPs models, axions could be produced through the decay of heavier SIMPs which can be long-lived, [161], (d) non-thermal "freeze-in" scenarios [162–168]. In general, these models postulate the existence of a DM candidate along with a LLP. This is an unique characteristic feature of these model, since it also introduces a detector-level signature for DM candidate, i.e. missing energy ($\not{E}_{\mathrm{T}}$) in the experiment phenomenology.

1.9.2 Collider signatures of LLP

LLPs, due to their extended lifetimes compared to typical collider particles, exhibit unique signatures in experiments. These signatures depend heavily on the specific model, its parameters, the LLP decay products, and their kinematics. Interestingly, even very different theories can produce the same experimental signature, enabling general searches independent of specific models. Before discussing the specific LLP signatures, let's recap the geometry of general purpose detectors like the CMS and ATLAS of LHC.

A collider detector is a cylindrical instrument with components arranged around a collision point (IP) where accelerated particles interact. Each detector layer is segmented by pseudorapidity (η) and azimuthal angle (ϕ). Fig. 1.9 shows the layers of a general purpose detector. Charged particles (electrons, muons, protons, pions) leave tracks in the silicon inner tracker within a uniform magnetic field. Track curvature in a magnetic field reveals particle type (particle vs anti-particle) and momentum. Next, light particles (electrons, photons) shower and have their energy measured in the electromagnetic calorimeter (ECAL) by
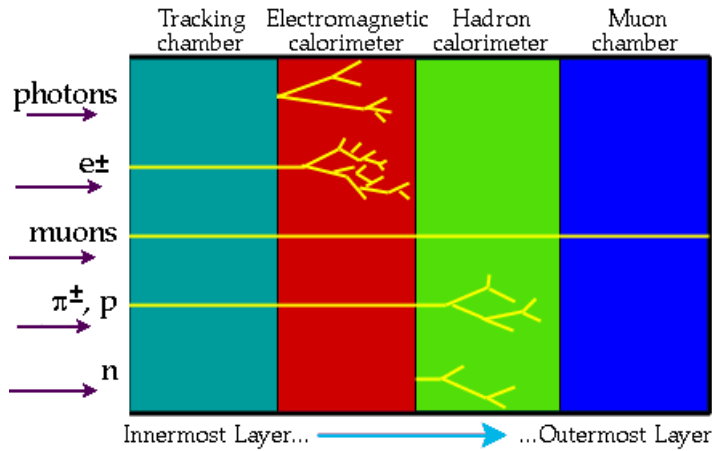
Figure 1.9: Illustration of layers of a general purpose detector and signatures of different objects in them.

stopping them, also within the uniform magnetic field created by the surrounding solenoid magnet. CMS uses homogeneous, fine-grained lead tungstate crystals, while ATLAS utilizes liquid argon for this purpose. The outer detector, with a separate toroidal magnetic field, houses the hadronic calorimeter (HCAL) where the energy of both charged can neutral hadrons are measured which fly through the ECAL and are stopped by its high dense material made of primarily brass and scintillators. Finally, the outermost muon spectrometer (MS), with its own magnetic field, detects and measures the precise momentum of muons by their track curvature and combining information from the tracker. MS comprised of gaseous detectors, like drift tubes (DT), resistive plate chambers (RPC), cathode strip chambers (CSC), and gas electron multiplier chambers (GEM).

Fig. 1.10 summarizes the most common signatures studied in LLP analyses. In general, the long lifetime, being a unique signature, helps differentiate the LLPs from the SM background. Backgrounds mimicking LLP signals often involve non-standard effects themselves capable to mimic that signature. Electrically charged LLPs leave behind hits in the silicon tracker layers if their lifetime allows them to travel through multiple layers before decaying. Hence, its trajectory can potentially be reconstructed from these hits. For LLPs that decay to undetected particles before reaching the end of the tracker, a "disappearing track" [170] signature might be observed, where a track seemingly vanishes within the detector. For extremely long-lived or stable LLPs, their tracks could potentially be reconstructed in the
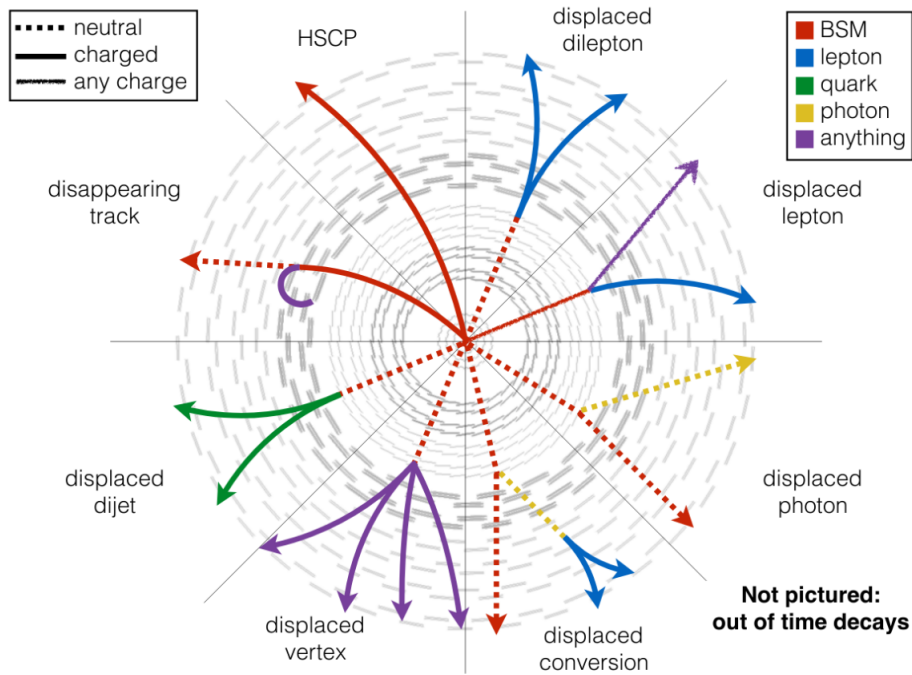
Figure 1.10: Schematic view of a variety of unconventional signatures arising from the decay of LLPs. The figure is taken from a presentation in 38th ICHEP conference [169].

muon chamber and a global track is fitted in the whole detector. This applies particularly to Heavy Stable Charged Particles (HSCPs) [171,172]. Due to their high mass, HSCPs typically have low velocity ($\beta = v/c$) and manifest as high-momentum global tracks with significant energy loss through ionization (dE/dx) [171]. Other stable or quasi-stable heavy LLPs with fractional electric charge would also leave global tracks, but with anomalously low dE/dx [173].

Indirect detection of LLPs relies on inferring their presence from their decay products, not their direct energy deposit in a detector. Unlike most SM processes where particles originate from the interaction point (detector centre), the particles produced from an LLP's decay will appear from a vertex displaced from the interaction point. The interaction point creates a beam spot of multiple vertices. The vertex with the highest total transverse momentum (sum of p_T^2) of all the tracks is identified as the "primary vertex" (PV), while the

vertex for a neutral LLP leads to a "secondary vertex" (SV), sufficiently displaced from the PV. "Displaced vertex" searches [174–177] address these kind of scenarios.

For hadronically decaying LLPs, the resulting quarks hadronize (form hadrons) at a distance from the collision point (beamspot). This leads to displaced jets, with tracks originating from a potentially reconstructable displaced vertex. At larger decay distances, some tracks might not be reconstructed, resulting in incomplete displaced jets with fewer tracks. Similarly, if LLPs decay di-leptonically into either electrons or muons, both displaced lepton tracks (usually have fewer hits) could also be fitted to identify the displaced dilepton vertex.

While targeting unconventional signatures that may uncover BSM physics, it is often necessary to develop dedicated triggers and object reconstruction algorithms. Additionally, these signatures are more susceptible to background contamination from misidentified objects and detector noise, making Monte Carlo simulations less reliable and sometimes impossible for background estimates.

We limit the discussion of the LLP at this point. Since a considerable portion of the thesis focuses on evaluating the prospects of dark matter in the framework of NMSSM (Chapters 2, 3) we briefly review the mechanisms of DM detection in the next section.

1.10 Detection of Dark Matter

The nature of DM still remains a major unsolved problem. Its elusive nature stems from a vast possible mass range (10^{-22} eV [178] to $100\,M_\odot$ [179,180] masses) and limited knowledge of its interactions. In Sec. 1.4, we discussed the 'WIMP miracle', suggesting WIMPs as a popular DM candidate since it predicts the correct observed DM relic density when the DM particle has a mass of around 100 GeV and interaction strength with SM particles, similar to electroweak interactions. As pointed out, many SUSY theories offer potential dark matter candidates in the form of the lightest supersymmetric particle, LSP, when it is neutral, stable and behaves as a WIMP. There are two main mechanisms for achieving the correct LSP relic density in SUSY:

- **Thermal Freeze-Out**: In the early universe's hot, dense environment, LSPs could have been abundantly produced and annihilated with other particles. As the universe expanded and cooled, this annihilation process became less frequent. At a certain point, called "freeze-out", the rate of LSP production fell below the annihilation rate, leaving behind a specific relic density of LSPs. The specific SUSY model and the LSP's

properties determine the details of this freeze-out process.

- **Non-Thermal Processes**: In some SUSY models, LSPs might not have participated significantly in thermal interactions in the early universe. Instead, they could have been produced non-thermally through the decay of heavier particles or other mechanisms [181, 182]. This could lead to a different relic density compared to the thermal freeze-out scenario.

Non-thermal processes offer more flexibility in achieving the correct LSP relic density compared to thermal freeze-out, which can be sensitive to the LSP's mass and interaction strength. In our investigation of possible avenues of BSM physics, we turn to a well-explored phenomenological enriched SUSY model, the NMSSM, where the LSP is singlino-dominated. Chapter 3 deals with the scenario of non-thermal singlino-like DM where the relic density predicted by the model can be as large as $\Omega h^2 \approx 10^6$ requiring additional DM candidate or nonstandard evolution of the Universe to satisfy the relic. On the other hand, Chapter 4 is based on the under-abundant singlino-dominated LSP viz. with predicted relic density has a value below the measured value. For decades, a global and intensive effort has been underway to detect the WIMPs. These searches include three primary detection methods, based on the different ways SM and DM interact as shown in Fig. 1.11, these are:
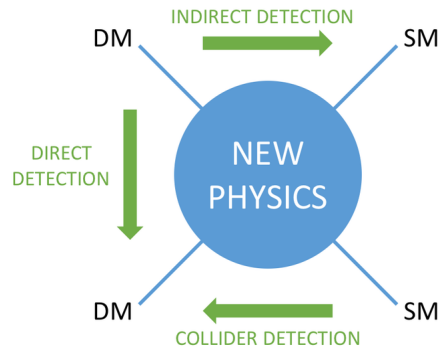
Figure 1.11: A visual illustration of the three main DM detection methods: direct detection seeks DM-SM scattering (top to bottom), indirect detection targets DM annihilation products (left to right), while collider experiments aim to produce DM particles (right to left).

1.10.1 Direct Detection

DM Direct detection (DD) relies on elastic scatting of WIMPs off a target nucleus within a shielded underground detector (to reduce the cosmic-ray backgrounds significantly). These searches hinge on measuring the energy deposited by a dark matter particle scatters off a nuclei. The scattering rate between the WIMP and target nucleus (dN/dE) can be written as [183–186],

$$\frac{dR}{dE}(E,t) = \underbrace{N_T}_{Target\,Dependence} \overbrace{\frac{\rho_{DM}}{m_{DM}}}^{Number\,density} \int_{v_{min}} \underbrace{\frac{d\sigma}{dE}(v,E)}_{Diff.\,Cross\,Section} v \overbrace{f_E(\vec{v},t)}^{veloc.\,distribution} d^3\vec{v},$$

(1.120)

where N_T is the number of the target nuclei per kilogram of the detector, ρ_{DM} and m_{DM} are the local DM density and DM mass, $\vec{v}$ is the velocity of the DM particle relative to the Earth, $f_E(\vec{v}, t)$ is the velocity distribution of the dark matter in the frame of the Earth, $v_{min} = \sqrt{m_N E/2\mu^2}$ is the minimum velocity of the dark matter, required to cause a detectable recoil energy withing a detector, with $\mu = m_{DM} m_N/(m_{DM} + m_N)$ being the reduced mass of the DM-nucleus system, $d\sigma/dE(v, E)$ is the differential DM-nuclei scattering cross-section given by,

$$\frac{d\sigma}{dE} = \frac{m_N}{2\mu^2 v^2}(\sigma_{SI} F^2(q) + \sigma_{SD} S(q))$$

(1.121)

with σ_{SI} and σ_{SD} denote the spin-independent (SI) and spin-dependent (SD) DM-nucleon interaction cross-sections, respectively, along with $F^2(q)$ and $S(q)$ being their respective form factors [187]. We show the current upper limit on the spin-independent WIMP-nucleon cross-section in the *Left* panel of Fig. 1.12 where the best limit is from LUX-ZEPLIN (LZ) [188] collaborations in the WIMP mass range of 10 GeV to 1 TeV. The *Right* panel shows the projected limits of σ_{SI} expected from the complete data of ongoing experiments and proposals of future experiments. Additionally, axial-vector structure of WIMP-nucleon coupling leads to the spin-dependent interactions which describe the WIMP coupling to unpaired nuclear spins in terms of WIMP-neutron (σ_{SD}^n) and WIMP-proton (σ_{SD}^p) cross-sections. We show the current limit on the σ_{SD}^n (σ_{SD}^p) in *Left* (*Right*) panel of Fig. 1.13 where the most sensitivity is from LZ [188] and PICO-60 [191]. The unprecedented precision in probing both SI and SD DM-nucleon scatterings without any evidence of DM, implies the feeble nature interaction of DM-nucleon which will eventually reach a point where the neutrino background becomes the dominant source of noise, known as ν-floor. This necessitates another
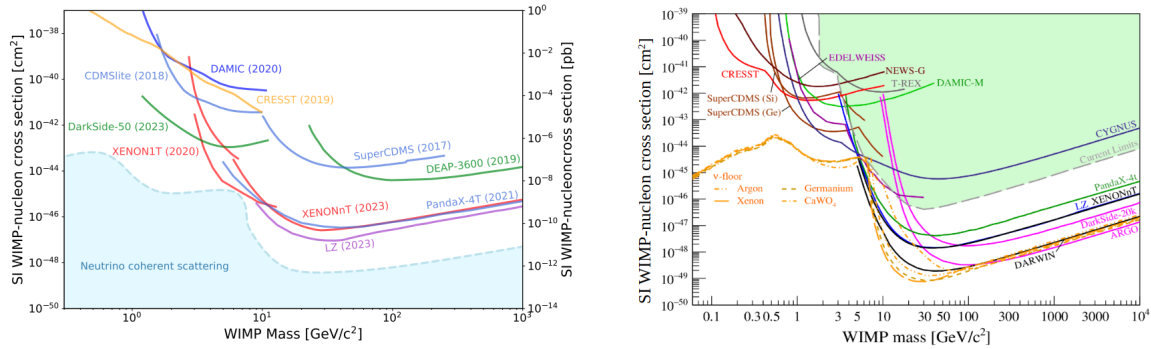
Figure 1.12: Upper limits on the SI DM-nucleon cross-section as a function of DM mass in *Left* plot, and sensitivity projections for the same from ongoing experiments and future projects in *Right* plot. Figures are taken from [189, 190].

kind of search for DM, like colliders.
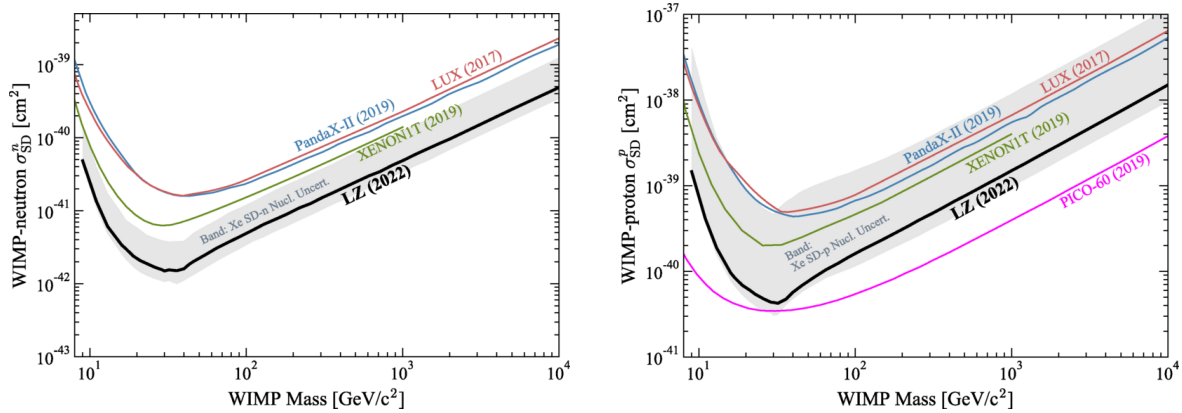
Figure 1.13: Current upper limits of spin-dependent cross-sections vs WIMP mass for WIMP-neutron (*Left*) and WIMP-proton (*Right*). The figures are from [188].

1.10.2 Collider searches

Dark matter particles, being electrically neutral and cosmologically stable, manifest as missing energy at colliders. At LHC, since the momentum of incoming partons can't be measured along the beam line, i.e. z direction, one defines the missing energy in the trans-

verse direction (MET) as negative vector sum of the transverse momenta of all particles: $\slashed{E}_T = \sqrt{(-\sum_{vis} p_x)^2 + (-\sum_{vis} p_y)^2}$. Collider searches for dark matter are based on the detection of the visible counterpart of the signal, such as a jet and charged leptons. One such kind is "Mono-X +MET", in decay like SM $\rightarrow$ mediator $\rightarrow$ DM, where X accounts for initial state radiations of SM particles like $\gamma, W/Z$ and quark/gluons [192–194]. Another way is to look for a resonant signature in decays like SM $\rightarrow$ mediator $\rightarrow$ SM where the mediator mass is within the collider reach. An important point to remember regarding collider searches of DM is that it can only offer complementary insights but cannot definitively identify the universe's dark matter. This is because any neutral particle escaping detection can manifest as missing energy, complicating definitive identification.

1.10.3 Indirect Detection

Indirect dark matter detection searches for SM particles produced by the decay or annihilation of DM already present in the cosmos. These annihilations, though rare today, could still occur in dense DM regions due to gravitational collapse in the centre of gravitationally bound objects, like galaxies or clusters of galaxies. In these regions, the aforementioned processes can produce flux of gamma-rays, charged cosmic rays, neutrinos, etc., which can appear as an excess over the expected background. The flux originating from dark matter annihilation within a solid angle should be proportional to the annihilation cross-section of DM particles, the energy spectrum (e.g. the number of photons produced per annihilation in case of gamma-rays) of annihilation process, squared number density of DM particles, dark matter density profile along the line of sight between the source and the observer. Some experiments exploring the DM indirect detection signals are: space-based instruments like the Fermi Gamma-ray Space Telescope [195–197] and ground-based telescopes like HESS [198,199] and MAGIC [200,201] investigate gamma-ray signals, large-scale neutrino detectors like IceCube [202,203] ANTARES [204,205], cosmic ray measurements in instruments like the Alpha Magnetic Spectrometer (AMS) [206,207] etc.

We conclude the current chapter here and outline the remaining chapters of this thesis. The rest of the thesis is organized as follows. In Chapter 2, we discuss a strategy to tag boosted top jets decaying semi-leptonically with tau in the final state in a model-independent framework and later identify variables to discriminate tagged top jets with left and right polarization. In Chapter 3, we shift to the NMSSM framework and study the prospect of probing long-lived decays with singlino LSP from cascade decay of elec-

troweakinos at the HL-LHC. The current status of the singlino dark matter in the NMSSM is scrutinized in Chapter 4, where we evaluate the prospect of probing light BSM Higgs boson in electroweakino pair production at the HL-LHC.

CHAPTER 2

BOOSTED TOP QUARK WITH A τ LEPTON IN THE FINAL STATE

This chapter is based on my work [208] done in collaboration with Amit Chakraborty, Rohini M. Godbole, Monoranjan Guchait.

2.1 Introduction

Top quark [209], the heaviest fermion in the SM, has a large coupling with the Higgs boson. Hence, it plays an important role in many of the suggested ideas BSM physics, as most of these try to address the issue of radiative stability of the Higgs mass. The top, being the heaviest, dominates these radiative corrections. Its coupling with the Higgs boson holds the promise of testing the Higgs sector of the SM and beyond (see e.g. [210–213]) as well as of probing different suggestions/formalisms of BSM physics. Many of these models have a heavy top partner or resonances whose decays involve top quarks, and thus, they provide opportunities to probe these BSM ideas by studying top quark production at the LHC.

Top quarks are, of course, produced copiously at the hadron colliders, in pairs or singly, respectively, *predominantly* through strong and weak interactions (see sec. 1.3.1 for more details). As mentioned above, another source of t-quarks produced at colliders is the decay of

hypothetical heavier particles, predicted in various BSM scenarios, to final states containing the top quark. Examples of such BSM models are supersymmetry (SUSY) [123,125,214–216] or little Higgs model [217,218]. Both of these are, in fact, models which address the hierarchy problem. Models with extra space dimension [219] also predict exotic heavy resonances, which would decay to a final state containing one or more top quarks. In all cases, the decay vertices are likely to carry an imprint of the BSM in their strength and chiral structure. Hence, studying the production and decay of the top quarks at colliders provides an excellent avenue to explore BSM physics [220, 221]. The produced t-quark can be successfully tagged in all its decay modes: pure hadronic as well as the semi-leptonic ones, where the W in $t \to bW^+$ decays hardonically or leptonically, respectively.

In the context of the study of t-quarks at colliders, knowledge of the polarization of the produced top quark can provide an additional important handle to get information on the interaction vertex. The information of its spin can be studied in the angular distribution of the decay products with respect to the spin direction of the decaying top as well as their energy distributions, which depends on the t-polarization [222–224]. Since t-quark polarization is an important probe of BSM physics and the aforementioned correlations follow from the chiral structure of the SM tbW vertex, the effect of anomalous tbW couplings in Eq. (1.47), on these correlations also has to be investigated for them to be useful probes of polarization. Such investigations [81,225–234] have shown that the angular distributions of the down type fermion (ℓ, d), in the decay of the W coming from the top, are particularly robust probes of the t-polarization.

With the ever-increasing lower limits on the masses of the BSM particles, the top quarks, expected to be produced in their decays, will necessarily have higher transverse momenta and, hence, will be highly boosted. This large boost causes the decay products to be highly collimated, appearing in the detector as a single jet in both the hadronic and semi-leptonic decay modes. Tagging these boosted top quarks at the LHC has been an active field of research for more than a decade now. The opening angle between the decay products depends inversely on the top decay Lorentz factor $\gamma \sim E/m$. The jet, which includes all the decay products of the decaying boosted top quark, tends to have a larger radius than a typical QCD jet, which owes its structure to the light parton radiations. The jet corresponding to a boosted top quark is thus a 'large-R jet' [235]. A number of tagging algorithms have been proposed corresponding to hadronic top quark decays using large-R jet analysis. These range from those based on substructure [236–238] to the recent ones which include

state-of-the-art deep learning methods [239–243]. The jet substructure-based taggers use the identification of W-boson and top quark through its mass reconstruction while working with jet constituents. The strategies based on jet images have been the main thrust in the deep learning algorithms (for more details, see Ref. [244, 245]).

Tagging of a boosted top quark decaying semi-leptonically referred to as leptonic top jet, suffers due to the presence of the neutrinos in the final state, which hinders complete reconstruction of the top quark mass. One can, of course, resort to the transverse mass variables such as M_T and extract the mass of the decaying top quark from the edge of the M_T distribution. Alternatively, it is also possible to use the presence of hard tracks originating from the leptons inside a large-R jet, to tag [242] a leptonically decaying boosted top quark. The authors in [246] have shown that it is possible to construct kinematic quantities, which can discriminate between a boosted leptonic top-jet containing non-isolated electrons/muons and a QCD large-R jet where light jets are mistagged as leptons.

In this Chapter, we focus on devising a tagging method to identify boosted top quarks decaying semi-leptonically with a tau-lepton in the final state, taking into account decays of the τ both in its leptonic and hadronic channels. In addition to the ν_τ from the W decay, the final state contains one more neutrino coming from the τ decay as well. This complicates the tagging process. It should be noted that since the τ-leptons are heavier than other leptons, their couplings and, hence, polarization are also sensitive to new physics effects. Hence, having a top-tagger for a t decaying with a τ in the final state can open up further possibilities of BSM studies using the polarization of the τ [247–250] as well. The major challenge in identifying a τ-jet (τ_h), which arises due to the hadronic decay mode of the τ inside a large-R jet, is to distinguish it from quark and gluon-initiated QCD jets. The proposed top tagger relies on efficiently identifying an energetic b-jet and a τ-jet within the top-candidate jet. We benchmark the performance of our proposal by using simulated events, corresponding to the production of a heavy W' followed by its decay $W' \to tb$ and further the decay of the t into a $b\tau\nu_\tau$ final state, applying the jet substructure technique and constructing a few discriminating kinematic observables. We demonstrate that these are very useful in eliminating QCD jets faking as τ-jets and thus facilitate tagging the top jet. We achieve an efficiency of $\sim 77\%$ for tagging the semi-leptonic top quark jet with taus in the final state, while keeping the mistagging efficiencies of backgrounds from light flavour QCD jets to $\sim 3\%$ level.

Even though the main focus of this study is to identify top quark jets with τ-leptons in

the final state, the proposed methodology can be applied to any large-R jet, which includes a b quark and a τ. For example, a light charged Higgs boson with $m_{H^\pm} < m_{top}$, is an example. In this case, the top quark can decay to a bottom quark and a charged Higgs boson, which then subsequently dominantly decays through $\tau \nu_\tau$ mode. Our proposed methodology can also probe decays of the third-generation squark, namely the top squark, in RPV scenarios. In RPV SUSY model, both bi-linear (LH) and tri-linear (LLE, LQD) re-normalizable lepton number violating operators are allowed in the superpotential [123,251] by gauge invariance and Supersymmetry. In this scenario, RPV decay of top squark $\tilde{t} \to b\tau$, can occur for both the bilinear and trilinear RPV terms. See, for example, [252] and [253], respectively. Clearly, our methodology can be used to tag the top squark decaying in this fashion. A third generation Leptoquark of electric charge of +4/3 unit can also have decays to a final state containing a b and a τ similar to the top quark jet. In these cases, the absence of neutrinos from W decay implies that, unlike the top quark mass, it is possible to reconstruct the mass of Leptoquark or top squark in a straightforward way once we tag the b- and τ-subjets efficiently.

The content of this Chapter is organized as follows. In sec. 2.3, we introduce the methodology used for tagging top quarks with taus in the final state and discuss the identification strategy for the b- and τ- subjets which are the first steps in this study. In sec. 2.4, we introduce several variables which have the power to discriminate the signal from the background. The results of the multivariate analysis are presented in sec. 2.5. In sec. 2.6, we construct a few polarization sensitive observables to explore the ability of our top-tagger to differentiate between left- and right-polarized top quarks. Finally, we conclude this Chapter in sec. 2.7.

2.2 W' model and calculation of top polarization

For the purpose of simulation of boosted top quark signal, we generate events for the production of a heavy W' boson with its subsequent decay $W' \to tb$ and further the decay of the t into a $b\tau \nu_\tau$ final state. We do this for the LHC center of mass energy $\sqrt{s} =$13 TeV. Henceforth, we refer to these as W' events. The generated process is indicated in Eq. (2.1). Even though the Eq. (2.1) and the Feynman diagram correspond only to W'^+ we have of course generated events for W'^- as well.

$$pp \longrightarrow W'^+ \longrightarrow t\,\bar{b}$$
$$\downarrow \qquad\qquad (2.1)$$
$$\tau^+ \nu_\tau b,$$

The corresponding leading order (LO) Feynman diagram is shown in Fig. 2.1.
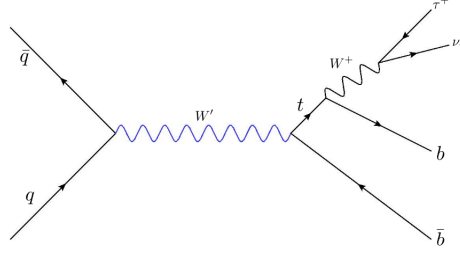
Figure 2.1: Feynman diagram at leading order for the signal process $pp \rightarrow W'^+ \rightarrow t\bar{b} \rightarrow \tau^+ \nu_\tau b\bar{b}$.

We consider the W' effective model [254] to generate the signal events setting $m_{W'} = 1$ TeV. This model is an extension of the SM incorporating a W' boson with arbitrary vector and axial-vector couplings to the SM quarks. Following [254], the relevant part of the Lagrangian can be written as,

$$\mathcal{L} = \frac{g}{\sqrt{2}} V_{f_i f_j}^{CKM} \overline{f}_i \gamma_\mu (k_R P_R + k_L P_L) W' f_j + h.c. \; , \qquad (2.2)$$

where $k_R(k_L)$ are the right-handed (left-handed) W' boson gauge couplings to quarks f_i and f_j, $V_{f_i f_j}^{CKM}$ are the CKM matrix elements, and $P_{R,L} = (1 \pm \gamma_5)/2$, g is the SM $SU(2)_L$ coupling. For a SM W boson, $k_R = 0$, $k_L = 1$. Relative values of k_L and k_R determine the polarization of the produced top quark. Its value $\mathcal{P}_0$ in the rest frame of W' can be calculated easily by computing $\Gamma^\pm$, the partial decay widths of the $W' \rightarrow t_\Lambda \bar{b}$ with helicity $\Lambda = \pm$ and is given by,

$$\mathcal{P}_0 = \frac{\Gamma^+ - \Gamma^-}{\Gamma^+ + \Gamma^-}. \qquad (2.3)$$

The helicity amplitudes for the decay $W'_\lambda \rightarrow t_{\lambda_1} \bar{b}_{\lambda_2}$ (i.e.$|1, \lambda > \rightarrow |\frac{1}{2}, \lambda_1|, |\frac{1}{2}, \lambda_2|$) can be categorized into $M(\lambda, \lambda_1, \lambda_2)$, where the helicity for the boson $\lambda = \pm 1$ and for the fermion $\lambda_{1/2} = \pm 1/2$. If the form of the decay vertex is taken as $\overline{f}_1 \gamma^\mu (k_R P_R + k_L P_L) f_2 W_\mu$ the helicity amplitudes in the rest frame of W' are listed below [255] ($M(+,+,+) = M(1, +\frac{1}{2}, +\frac{1}{2})$ etc.).

$$M(+,+,+) = \left[-i\frac{k_R p_t^+ p_b^- + k_L p_t^- p_b^+}{2} \right] e^{+i\phi} \left(\frac{-1}{\sqrt{2}} \sin\theta \right)$$

$$M(+,+,-) = \left[+i\frac{k_R p_t^+ p_b^+ + k_L p_t^- p_b^-}{\sqrt{2}} \right] e^{+i\phi} \left(\cos^2\frac{\theta}{2} \right)$$

$$M(+,-,+) = \left[-i\frac{k_R p_t^- p_b^- + k_L p_t^+ p_b^+}{\sqrt{2}} \right] e^{+i\phi} \left(\sin^2\frac{\theta}{2} \right)$$

$$M(+,-,-) = \left[+i\frac{k_R p_t^- p_b^+ + k_L p_t^+ p_b^-}{2} \right] e^{+i\phi} \left(\frac{-1}{\sqrt{2}} \sin\theta \right)$$

$$M(0,+,+) = \left[-i\frac{k_R p_t^+ p_b^- + k_L p_t^- p_b^+}{2} \right] (\cos\theta)$$

$$M(0,+,-) = \left[+i\frac{k_R p_t^+ p_b^+ + k_L p_t^- p_b^-}{\sqrt{2}} \right] \left(\frac{+1}{\sqrt{2}} \sin\theta \right) \qquad (2.4)$$

$$M(0,-,+) = \left[-i\frac{k_R p_t^- p_b^- + k_L p_t^+ p_b^+}{\sqrt{2}} \right] \left(\frac{-1}{\sqrt{2}} \sin\theta \right)$$

$$M(0,-,-) = \left[+i\frac{k_R p_t^- p_b^+ + k_L p_t^+ p_b^-}{2} \right] (\cos\theta)$$

$$M(-,+,+) = \left[-i\frac{k_R p_t^+ p_b^- + k_L p_t^- p_b^+}{2} \right] e^{-i\phi} \left(\frac{+1}{\sqrt{2}} \sin\theta \right)$$

$$M(-,+,-) = \left[+i\frac{k_R p_t^+ p_b^+ + k_L p_t^- p_b^-}{\sqrt{2}} \right] e^{-i\phi} \left(\sin^2\frac{\theta}{2} \right)$$

where the polar angle θ and azimuthal angle ϕ are measured with respect to this quantization axis. The masses and momentum of top(bottom) is given as $m_t(m_b)$ and $p_t(p_b)$ respectively. For top(bottom) with energy $E_t(E_b)$ the symbols $p_t^\pm, p_b^\pm$ are defined as,

$$p_t^\pm = \frac{E_t + m_t \pm p}{\sqrt{E_t + m_t}}, \quad p_b^\pm = \frac{E_b + m_b \pm p}{\sqrt{E_b + m_b}} \qquad (2.5)$$

with

$$E_t = \frac{m_{W'}^2 + m_t^2 - m_b^2}{2m_{W'}}, \quad E_b = \frac{m_{W'}^2 + m_b^2 - m_t^2}{2m_{W'}},$$

$$p = \frac{\sqrt{((m_{W'} + m_b)^2 - m_t^2)((m_{W'} + m_t)^2 - m_b^2)}}{2m_{W'}} \qquad (2.6)$$

72

Inserting the amplitudes of Eq. (2.4) in Eq. (2.3), the polarization of top is given by,

$$
\begin{aligned}
\mathcal{P}_0 &= \frac{\left(\begin{smallmatrix} M(+,+,+)^2+M(+,+,-)^2+M(0,+,+)^2 \\ +M(0,+,-)^2+M(-,+,+)^2+M(-,+,-)^2 \end{smallmatrix}\right) - \left(\begin{smallmatrix} M(+,-,+)^2+M(+,-,-)^2+M(0,-,+)^2 \\ +M(0,-,-)^2+M(-,-,+)^2+M(-,-,-)^2 \end{smallmatrix}\right)}{\left(\begin{smallmatrix} M(+,+,+)^2+M(+,+,-)^2+M(0,+,+)^2 \\ +M(0,+,-)^2+M(-,+,+)^2+M(-,+,-)^2 \end{smallmatrix}\right) + \left(\begin{smallmatrix} M+,-,+)^2+M(+,-,-)^2+M(0,-,+)^2 \\ +M(0,-,-)^2+M(-,-,+)^2+M(-,-,-)^2 \end{smallmatrix}\right)} \\
&= \frac{\left(k_R^2 - k_L^2\right)\left(2 - x_t^2 + x_b^2\right)\sqrt{1 + \left(x_t^2 - x_b^2\right)^2 - 2\left(x_t^2 + x_b^2\right)}}{12 k_R k_L x_t x_b + \left(k_R^2 + k_L^2\right)\left(2 - \left(x_t^2 - x_b^2\right)^2 - \left(x_t^2 + x_b^2\right)\right)},
\end{aligned}
$$

(2.7)

where $x_t = m_t/m_{W'}, x_b = m_b/m_{W'}$. The value of $\mathcal{P}_0$ in the plane of $k_L - k_R$ is shown in Fig. 2.2. If we were to neglect the t, b masses, then the produced t will be always left-handed for $k_L = 1, k_R = 0$ and right-handed for $k_L = 0, k_R = 1$. If we use Eq. (2.7) to calculate $\mathcal{P}_0$, for $m_{W'} = 1$ TeV, $m_t = 172$ GeV and $m_b = 4.7$ GeV, and $k_R = 1, k_L = 0$ and $k_R = 0, k_L = 1$ we get $\pm 0.97 (\sim \pm 1)$, respectively. Thus the large mass of the W' implies that the polarization of the produced t-quark will be decided completely by values of k_L and k_R. We will have unpolarized t-quarks for $k_L = k_R$. To develop the tagging methodology, we generate unpolarized boosted top quarks from W' decay by setting $k_L = k_R$. For the polarization study, we set $k_R (k_L)$ to zero to produce left (right) -polarized top quarks.
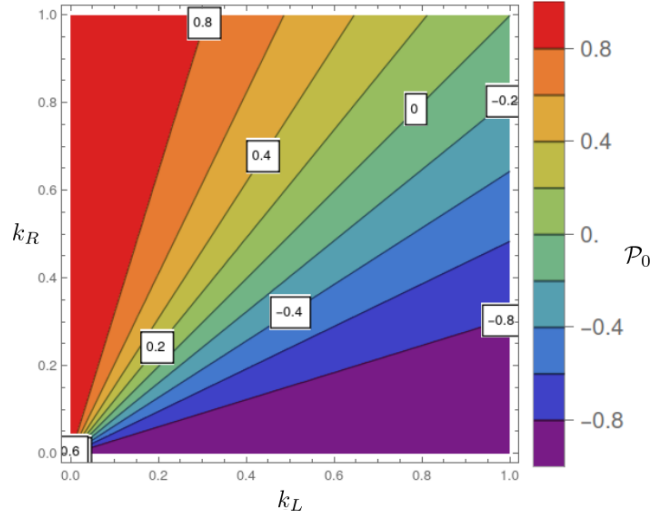
Figure 2.2: Polarization of top in W' decay for different values of k_L and k_R. The values of W', t, b masses used for the calculation are $1000, 172, 4.7$ GeV respectively.

2.3 Methodology : b and τ-jet identification

The challenging part of tagging a boosted top quark in the $t \rightarrow b\tau^+\nu_\tau$ decay mode is to identify the b- and τ-like subjets inside the top fatjet. In this section, we describe this strategy very systematically.

The W' events ($pp \rightarrow W'^+ \rightarrow t\bar{b}$) are generated using MadGraph-aMC@NLO [256]. It is necessary to take into account the effect of the spin correlations as well as the finite width of the decaying top quark in the decay $t \rightarrow b\tau^+\nu_\tau$. We do this by employing the MADSPIN [257] method. Next, W' events are passed through PYTHIA8 [258] for parton shower and hadronization. In order to consider detector effects, those events are passed through DELPHES-v3.4 [259] with Compact Muon Solenoid (CMS) card setting.

Jet formation

The process of identifying boosted top jets begins with the construction of fatjets, setting jet radius parameter R = 1.5 and anti-k_T jet clustering algorithm [260] as implemented in FastJet-v3.2.1 [261]. Jets produced by the anti-k_T algorithm exhibit collinear and infrared safety. This means the set of hard jets remains unaffected when collinear particles are merged or split, or when soft radiation is introduced. We select only those fatjets which pass the threshold of transverse momentum, $p_{T_J}^{min} = 200$ GeV. The boosted fatjets are contaminated by several sources, such as soft radiation, underlying events and multi-particle interactions. The jets are cleaned by applying the SoftDrop technique [262] to remove soft wide-angle radiation. This process mitigates the impact of uninteresting interactions like initial state radiation (ISR), underlying event (UV), and pile-up, which occur alongside the primary hard-scattering interaction. To illustrate, for a jet composed of two subjets, the softer constituent is discarded unless

$$\frac{min(p_{T,1}, p_{T,2})}{p_{T,1} + p_{T,2}} > z_{cut} \left(\frac{\Delta R_{1,2}}{R}\right)^\beta, \tag{2.8}$$

where, $p_{T,1}$ and $p_{T,2}$ are the transverse momenta of the two subjets, z_{cut} is the soft-drop threshold, $\Delta R_{1,2}$ is the distance between the two subjet, R is the jet radius, and β is an angular exponent. We set the free parameters β and z_{cut} to their values for the standard CMS choice [263], viz. $\beta = 0$ and $z_{cut} = 0.1$. The constituents of the soft-dropped fatjet are further re-clustered with jet radius parameter R = 0.5 using anti-k_T algorithm to form subjets with a minimum $p_{T_j}^{min} = 20$ GeV.

In principle, W' is produced at almost rest; hence W' decay to b and t will produce two back-to-back fatjets. For the above mentioned choices of various parameters, we find that for $m_{W'} = 1$ TeV about 58% events contain two back-to-back fatjets whereas the fraction of these events rises to $\sim 79\%$ for $m_{W'} = 3$ TeV. To ensure that a fatjet is indeed a topjet, it is necessary to identify the subjets in it as b- and τ-jets. We will describe our strategy for identification of the b- and τ- like subjets after describing the different event samples we generate for the backgrounds as well.

High p_T QCD jets can fake as top jets. Hence, we need to study the impact of jets produced via QCD processes while developing the strategy to tag top jets in the semi-leptonic channel. The kinematics of the top decay looks similar to QCD parton splitting when its boost factor y_t is $\sim 1/\alpha_s$. Therefore, at high p_T, the subjets of the QCD fatjet, are very likely will be misidentified as b- or τ- jets. Hence, efficient identification of the subjets as b- and τ- jet is necessary to suppress the number of QCD events significantly. Various properties of the QCD jets differ significantly from the top-fatjet and the idea is to exploit these differences to reduce the QCD contamination. One such property is the average mass of the jet, which is affected mainly by the sharing of energy among different members of the jet. For a QCD fatjet this average mass increases with the p_T of jets. It has been shown that for QCD jets with p_T more than ~ 300 GeV, the corresponding mean jet invariant masses lie within the window of 30-160 GeV [236]. This mass range, covering the semi-leptonic top mass, is precisely the one that is important for our analysis which aims to tag a top quark.

QCD jets have a steeply falling p_T distribution, but due to the much larger production cross-section of the jets, there is a significant number of jets even after the requirement of large minimum p_T of 200 GeV for the jet. The steeply falling p_T spectrum of these jets means that one has to take extra care to generate appropriately large number of events. QCD events from $pp \rightarrow jj$ are generated in three p_T^{bins}: [200-300, 300-600, > 600] GeV where p_T corresponds to the transverse momentum of hard scattered particles in the final state. The number of simulated events is determined by keeping in mind that we perform our analysis for a luminosity of 10 fb^{-1} and we need to pay particular attention to the region [300-600] GeV, since the QCD jets in this p_T^{bin} contribute dominantly to a window in jet mass which is populated by the signal from semi-leptonic decay of the top quark. We have simulated 10M, 7M and 3M events in these three p_T^{bins}, respectively. We also need to simulate the hadronically decaying top-antitop quark pair ($t_h \bar{t}_h$) events which is a potential background. The list of generated events used for simulation is presented in Table 2.1 along with the

range of p_T^{bins} for the dijet QCD events as well as for the $t_h\bar{t}_h$ events. Next, we proceed to discuss the identification of the subjets as τ- and b- subjets, which, as mentioned above, is very important so as to be able to handle the background from QCD jets.

Process	p_T^{bins} (GeV)	Cross Section (pb)
	200–300	$\approx 4.9 \times 10^4$
Dijet QCD	300–600	$\approx 7.9 \times 10^3$
	> 600	$\approx 2.0 \times 10^2$
t$\bar{\text{t}}$ Hadronic($t_h\bar{t}_h$)	> 150 GeV	≈ 208.2
W$' \to t\bar{b} \to \tau b\bar{b}\nu$	Mass of W$' = 1$ TeV	≈ 0.6

Table 2.1: List of the signal and background samples used with their kinematics.

2.3.1 τ- jet identification

The τ-lepton decays hadronically with a probability of 65% producing charged (mainly $\pi^{\pm}$) and neutral hadrons (π^0). Hence the multiplicity of decay products, particularly charged tracks, is low in numbers and they are highly collimated in a cone with $\Delta R = \sqrt{\Delta\eta^2 + \Delta\phi^2} <<$ 1.5, where $\Delta\eta$ and $\Delta\phi$ are the differences of pseudo rapidities and azimuthal angles respectively between two particles. In collinear approximation, i.e. if $p_T^{\tau} >> m_{\tau}$, the decay products are collimated even more so as to be contained in a jet of even smaller radius, say $R < 0.5$. Among the τ decay products, the neutral pions deposit a considerable fraction of electromagnetic energy in the calorimeters through photon. This is accompanied by one or three-prong low p_T charged track multiplicity observed in the tracker, which are the characteristics of a τ-jet. Currently, ATLAS and CMS have developed very sophisticatedly dedicated algorithms for the identification of τ-jets using attributes of τ decay, such as energy difference in calorimeter cells, lifetime and mass, track multiplicities etc. [264–266]. However, those techniques are beyond the scope of our present analysis. Instead, we use a naive track-based isolation algorithm to identify τ-like subjets.

   In this procedure [264]; first, we identify the tracks which are within the jet-track matching cone with radius $R_m = 0.1$ calculated using the candidate τ-jet axis, and then select those tracks with minimum p_T of 2 GeV (see Fig. 2.3). Among these tracks, we identify the leading track (or the seed track) with minimum $p_T > 6$ GeV and $|\eta| < 2.5$. Other tracks are
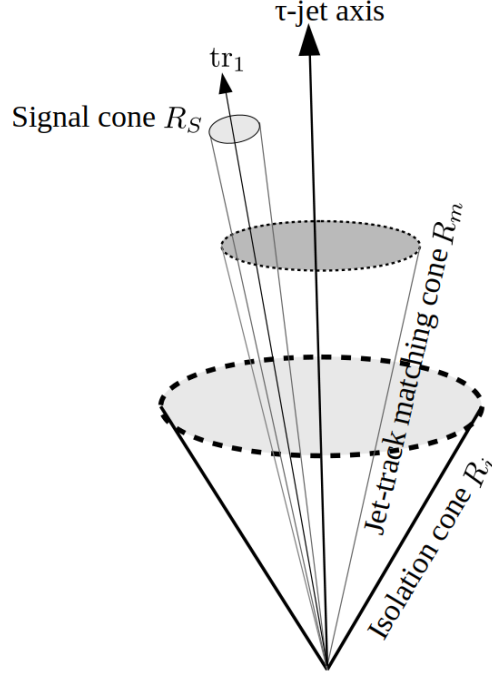
Figure 2.3: Basic principle of τ-jet identification with charged track isolation.

accumulated in a narrow region around the seed track with a cone radius $R_s = 0.07$, and we demand that the difference of the z-impact parameter Δz_{tr} between the leading track and these selected tracks (signal cone) is smaller than 2 mm. This additional requirement ensures that all the tracks in the signal cone are coming from the same τ-lepton decay. Furthermore, we adopt a track isolation method, where isolated tracks are reconstructed in a larger cone size $R_i = 0.45$ around the candidate τ jet axis with minimum transverse momentum p_T^i of 1 GeV. The isolation criterion is satisfied when the number of tracks (1 or 3) in the isolation region is the same as in the signal cone. Following this naive technique, we achieve τ-identification efficiency $\epsilon_\tau \sim 60\%$ for a moderate range of $p_T = 20 - 60$ GeV of τ-jets. In case of QCD, the misidentification rate as τ-jets is $\sim$ 5-6%. The effectiveness of the τ identification method is demonstrated in Fig. 2.4 in distributions of multiplicity of the charged tracks ($\mathrm{N_{trk}}(\tau_h)$), mass (m_{τ_h}) for the identified τ-jets. The left plot of charge track multiplicity shows a clear tendency to one and three prong structures for identified τ-jets, as expected. QCD jets acquire mass through multiple splitting and the EM clusters
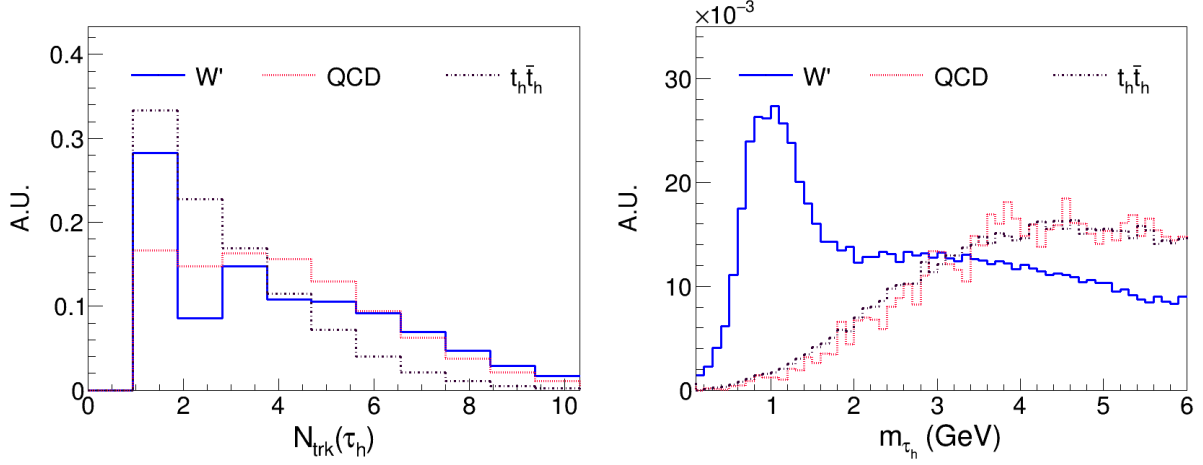
Figure 2.4: Distribution of the number of charged tracks inside the τ-subjet (left) and mass of the τ-subjet (right) for signal (W') and background events. The solid blue line shows the distribution for the signal while the same for QCD and $t_h\bar{t}_h$ are shown in red dotted and black dash dotted lines, respectively.

are far away from the jet axis than that of signal, therefore, a smeared distribution is more likely. While a clear peak structure is visible in the mass distribution for the signal events, shown by the solid blue line (right plot in Fig. 2.4), the invariant mass distribution for the misidentified τ-jet shows a long tail, for the QCD jets as well as the jets from $t_h\bar{t}_h$, displayed in the same plot by red dotted and black dash dotted lines respectively. It is true that the invariant mass distribution for the signal events does have a somewhat long tail. However, it is possible to reduce it further by using isolation criteria in addition to the single one that we have used [267].

2.3.2   b-jet identification

A subjet inside the candidate top fatjet is identified as a b-jet, if the angular distance ΔR between the jet and the nearest B-hadron satisfy $\Delta R < 0.5$. For signal events, B-hadrons dominantly arise from the b-quarks, which are produced through the decay of W' and the t. Intuitively, the B hadrons, which come from the b quark originating from the top quark

$\mathrm{p_T}$ of the b-jet (GeV)	b tagging Efficiency
upto 60	60%
[60,200]	80%
[200,400]	60%
400 -	50%

Table 2.2: b-tagging efficiencies for different p_T range of the jets following the performance of ATLAS b-identification algorithms with Run2 data [268].

decay, are likely to satisfy the above matching condition viz. $\Delta R < 0.5$. On the other hand, for QCD multijet events, B hadrons mostly originate due to a gluon splitting into a $b\bar{b}$ pair and hence unlikely to be close to the fatjet axis. In b-jet identification strategy, we also take into account the impact of detector effects by incorporating the b-tagging efficiencies and mistag rates reported in [268] and which are summarized in Table 2.2. Following the CMS analysis, we have used a mistag rate to be 2% for a light jet to be identified as a b-jet, irrespective of p_T of the jet [269]. In our simulation, we correct the b identification probability by applying all these efficiencies. We get $\sim 77\%$ identification efficiency for b.

Fig. 2.5 shows distributions in the invariant mass of the fatjets containing b- and τ-like subjets, identified to be so, using the above procedure for all the three types of events (Table 2.1) that have been generated, viz. W' and hadronic top and QCD events. For the sake of comparison, the same invariant mass constructed out of the total four-momentum of b-quark and the visible decay products of the τ-lepton (τ^{vis}), referred to as $b - \tau^{vis}$ system is shown. At the truth level, mass of $b - \tau^{vis}$ system $m_{b\tau^{vis}}$ is expected to be bounded by $m_{b\tau^{vis}} < \sqrt{m_t^2 - m_W^2} \approx 152$ GeV in the limit $m_b \to 0$. A clear peak is visible in the distribution for parton level events around ~ 75 GeV. The reconstructed top jet mass distribution from W' event is found to have a peak too around the same value and the distribution is smeared due to the hadronization of the b-quark and consequent decay of the B-meson as well as the decay of the τ lepton and the detector effects. Notice that the distribution does not show any peak-like structure for the $t_h \bar{t}_h$ and QCD events. This indicates to us that a window in the distribution of invariant mass of the b- and τ-subjets, i.e. $M_{b_j \tau_h}$, say between 60 to 160 GeV, could be chosen optimally to tag a semi-leptonic t-fatjet.
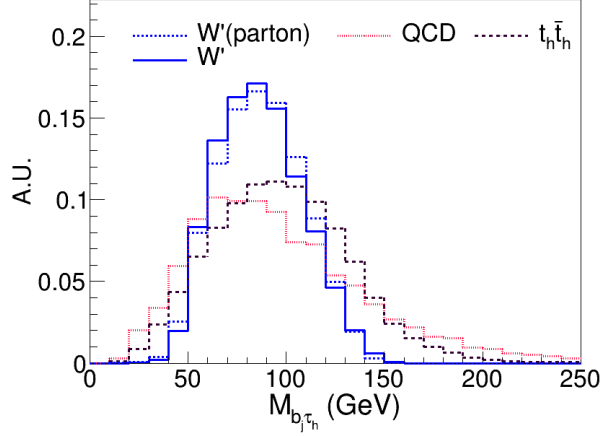
Figure 2.5: Distribution of invariant mass of $b - \tau$ jet system for signal and background events. The parton level (blue dotted line) curve for W' is constructed out of momenta of the b-quark and visible decay products of τ. The color code for all the other curves is the same as in Fig. 2.4.

2.4 Top jet identification

In this section, we construct a number of observables that can be used to identify top jets. We do this by exploiting the features of the b- and τ-like subjets that we observed in the earlier section.

- **Transverse Mass**

  The dominant source of missing transverse energy (MET) in the signal is due to the presence of two neutrinos: one from decay of W and the other from the decay of the τ as can be seen from Eq. (2.1). The presence of two neutrinos makes it difficult to reconstruct the mass of the top fatjet, compared to the case of the hadronically decaying t, where such reconstruction plays an important role in its tagging. However, the direction of MET can help to do the job in the present case because of the boosted nature of the t and the W. In fact, as a result of the boosted nature of the t, W and τ, the direction of MET is expected to be collinear to τ decay products. This feature can be utilized to get an additional handle to identify top jets and also to reduce background. Keeping the above kinematics in mind, we require the ΔR between MET and the candidate top

jet to be < 3. We construct a transverse mass observable, combining the momenta of the identified b- and τ-jet, along with the MET given by,

$$m_T^2 = m_{b\tau^{vis}}^2 + 2(E_T^{b\tau^{vis}} \not{E}_T^{\nu} - \mathbf{p}_T^{b\tau^{vis}}.\not{p}_T), \tag{2.9}$$

where $m_{b\tau^{vis}}$ and $\mathbf{p}_T^{b\tau^{vis}}$ denote the invariant mass and transverse momentum of the $b - \tau^{vis}$ system respectively. The transverse mass m_T of b-τ jet, displayed by the solid blue curve in Fig. 2.6 is expected to have an endpoint at t mass which is smeared due to difference in correlation of MET coming from two neutrinos with top jet as well as other effects mentioned in the previous section. We can use this feature of the m_T distribution to select the candidate fatjet after requiring an invariant mass of $M_{b_j\tau_h}$ in the aforementioned mass window of [60-160] GeV, which removes a good fraction of background events.
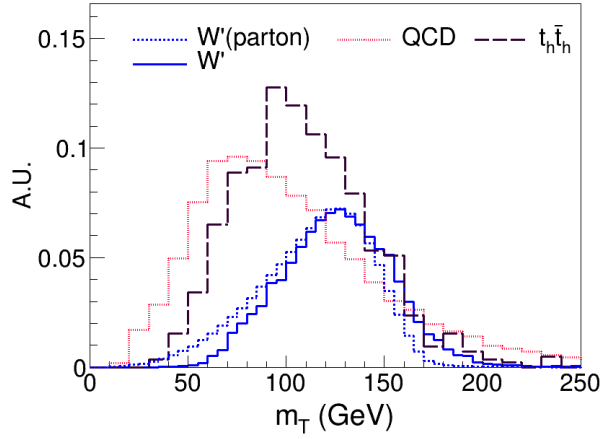
Figure 2.6: Distribution of the transverse mass constructed out of b-subjet (b_j), τ-subjet (τ_h) and MET for the signal and background events. The color code is the same as in Fig. 2.5.

- **Energy sharing of subjets**

  The pattern of energy sharing of subjets is very different for the signal and backgrounds. This facilitates the construction of an observable which offers good separation between boosted top jets from the signal and the background. The fraction of

energy carried by a subjet (j) of a fatjet (J) as

$$Z_j = \frac{E_j}{E_J}. \tag{2.10}$$
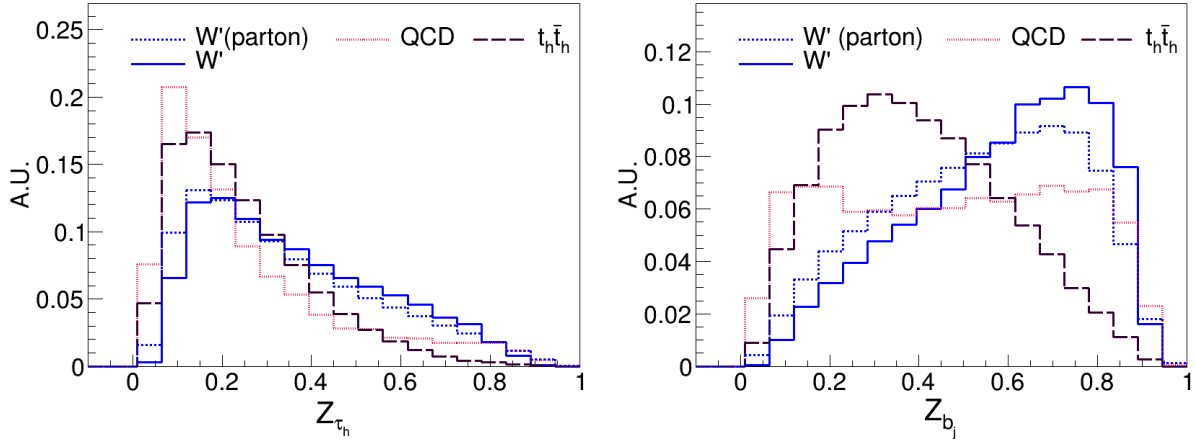
Figure 2.7: Distribution of energy fraction of τ_h (left) and b_j (right) in top jet for signal and background events. The color code is same as Fig. 2.5.

In Fig. 2.7, we show the Z_j distribution for τ_h(left panel) and b-like(right panel) subjets corresponding to both signal and background events. For one-to-one correspondence with the jet level, the energy fractions at the parton level are defined as the ratio of the energy of the b quark or energy of the visible decay products of the τ to the sum of the two ($E_b + E_{\tau^{vis}}$). For signal events, it is expected that the b-subjet will carry a large fraction of energy while τ_h will share comparatively a smaller fraction of energy of the top system since a fraction is taken away by MET which contains the neutrino from the τ decay. One can see that Z_{τ_h} peaks around 0.2. However, for background events, these energy fractions of the b- and τ- like jets are uncorrelated. In fact, Z_{b_j} in QCD, the dotted red line in the right plot of Fig. 2.7, shows a flat distribution, whereas Z_{τ_h} for a QCD jet mimicking a $\tau-$ like subjet is dominantly distributed to much lower values. The peculiar sharing of energies, particularly for Z_{b_j} in QCD events, can be attributed to additional components the subjet contains due to soft radiation, which could not be removed even after the application of soft drop method [262].

We exploit this characteristic of background sub jets by defining a new variable, $\Delta X_{b_j \tau_h}$ which includes the ratio of the mass of the b- and τ- subjet system ($M_{b_j \tau_h}$) with respect to the mass of the corresponding identified candidate top jet (M_J),

$$\Delta X_{b_j \tau_h} = 1 - \frac{M_{b_j \tau_h}}{M_J}. \tag{2.11}$$

Clearly, for signal events, it is expected to peak around $\Delta X_{b_j \tau_h} \sim 0$ as shown in the blue line of Fig. 2.8. For the backgrounds, as explained above, b-jets are contaminated by soft components and hence are much flatter and extend to larger values. We find that this variable helps improve the top tagging efficiency.
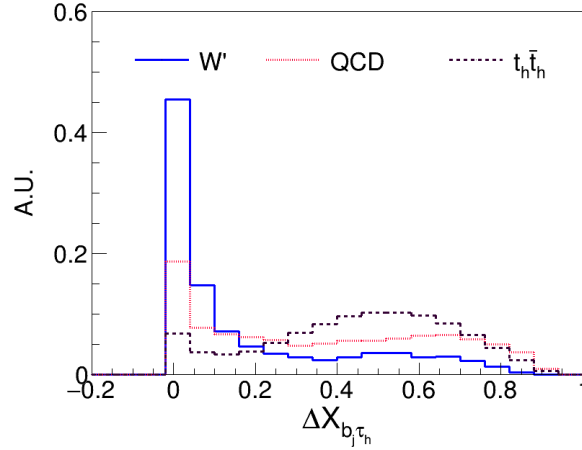
Figure 2.8: Distribution of variable $\Delta X_{b_j \tau_h}$ (Eq. (2.11)) for signal and background events. Colour code is the same as in Fig. 2.4.

- **N-subjettiness**

  Another very useful variable in the jet substructure technique, which helps to improve our study is N-subjettiness. Subjettiness [270] takes advantage of the different energy flow in the different particles present within the fatjet. It effectively counts the number of subjets in a given jet. If there are N candidate subjets in a specific jet, one calculates subjettiness as,

  $$\tau_N = \frac{1}{\sum_k p_{T,k} R_{Jet}} \sum_k p_{T,k} \min\{\Delta R_{1,k}, \Delta R_{2,k}, ..., \Delta R_{N,k}\}. \tag{2.12}$$

Here k runs over all the constituents of a jet of momentum $p_{T,k}$ and $\Delta R_{J,k} = \sqrt{(\Delta\eta)^2 + (\Delta\phi)^2}$ is the distance in $\eta - \phi$ plane between a candidate subjet j and a constituent k. The normalization factor is taken to be the jet p_T multiplied by its radius. In the limit $\tau_N \to 0$, the jet must have $\Delta R_{N,k} = 0$ i.e all the radiation is perfectly aligned along the candidate subjets, and therefore the jet has exactly N subjets. In case of $\tau_N \to 1$, the jet must have a large fraction of its energy distributed away from the candidate subjet direction, therefore it has at least N + 1 subjets i.e the minimization missed some subjet axes.
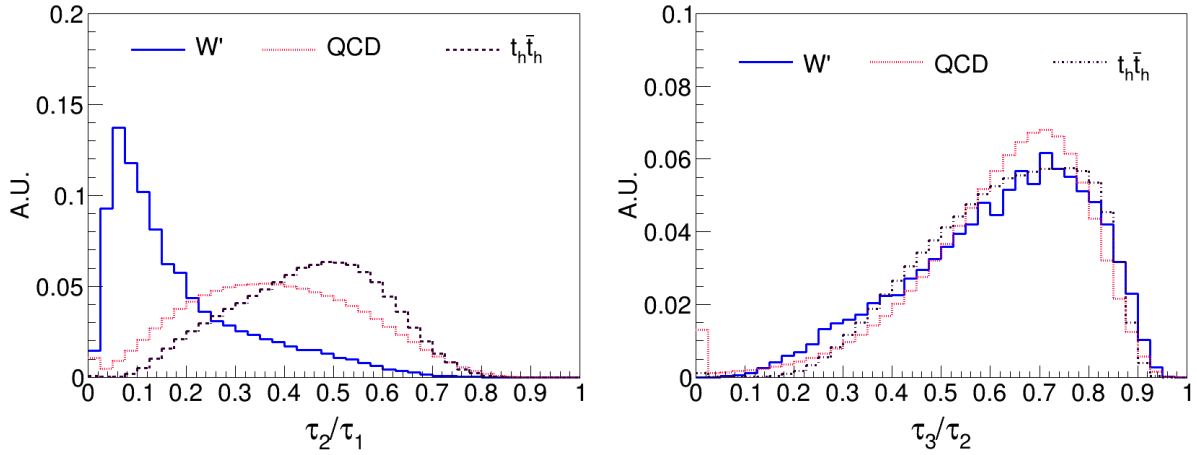
Figure 2.9: Distribution of τ_2/τ_1 (left) and τ_3/τ_2 (right) for leptonic top and background jets. Discriminators like τ_2/τ_1 measure the relative alignment of the jet energy along the individual subjet directions. Colour code is the same as Fig. 2.4.

Therefore, jets with smaller τ_N are said to be N-subjetty, whereas larger τ_N have more than N subjets. QCD jets can have larger values of subjetiness variables due to diffuse spray of large angle radiation, and hence individually τ_1 or τ_2 can not provide much distinction between signal and background events. The ratio τ_2/τ_1, however, is a different story and can be effective in discriminating the different two-prong objects. Similarly, τ_3/τ_2 is a better choice while probing three-prong objects. We show the distribution of these two variables viz., τ_2/τ_1 and τ_3/τ_2 in the left and right panel of Fig. 2.9 respectively. For the leptonically decaying t-quark the fatjet is essentially a two prong object and hence τ_2/τ_1 is found to be a good discriminating observable.

Based on the various observations in the discussion above we list the steps to be followed systematically to identify a boosted top jet in its decay channel, $t \to \bar{b}\tau^{+}\nu_{\tau}$.

1. Cluster the final state hadrons of the events to jets with a minimum p_T, say $p_T \sim 200$ GeV or larger, setting the jet size parameter R = 1.5. Then apply a jet grooming technique (e.g., SoftDrop) and remove the soft and wide angle radiation contamination. Select the fatjet mass with a window of the range 60-160 GeV. It is likely to be a top candidate jet.

2. Recluster the constituents of the candidate fat top jet to a smaller radius ($R \sim 0.5$), and select those events where the candidate jet consists of at least two subjets.

3. Identify b- and τ- like subjets following the procedure as described in Sec 2.

4. Finally, if at least two different subjets in close proximity originating from the candidate fatjet pass the b and τ jet identification, the fatjet can be considered as a top-fatjet if the invariant mass lies in the window 60-160 GeV.

5. Furthermore, construct the following discriminating observables to reduce possible backgrounds.
   (a) Transverse mass(m_T), constructed from the b-τ subjet system and MET following Eq. (2.9).
   (b) Energy Fractions of the b- and τ- subjets inside the top fatjet. One can then utilize the difference in the template of energy sharing between the subjets (Z_{b_j}, Z_{τ_h}).
   (c) The fraction of mass carried by the $b - \tau$ jet, Eq. (2.11) ($\Delta X_{b_j \tau_h}$). In defining this observable one has used the excess of softer contamination to subjets in backgrounds as compared to the signal.
   (d) N-subjettiness variable such as, τ_2/τ_1 and τ_3/τ_2 etc. (cf. Eq. (2.12))

Fig. 2.10 shows the efficiency ϵ_t of topjet identification obtained after following the above procedure (steps 1-4) for a moderate range of boosted top jet p_T of 200-450 GeV. Here ϵ_t is defined as the ratio of number of candidate fatjet which has b- and τ- subjets, to the corresponding total number of candidate top fatjets within matching cone of 1.5 of t-quark, running on all fatjets in an event. The corresponding top like jet misidentification efficiency for QCD jets is ~1-2%. An important observation is that ϵ_t decreases with the increasing p_T

of the top jet. It is due to the fact that for large values of p_T for the fatjet, the subjets are no longer distinguishable. The tagging efficiency also depends on the radius of the fatjet. We
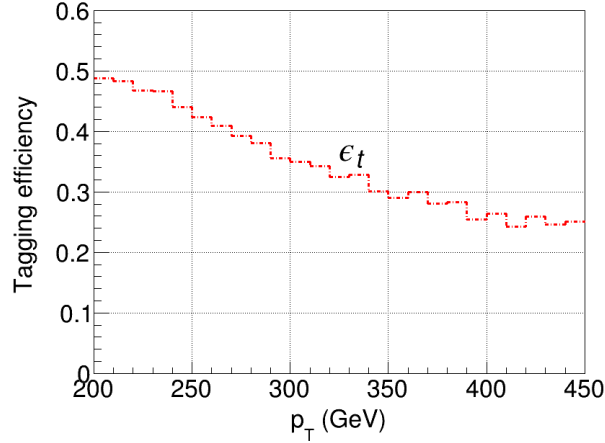
Figure 2.10: The efficiencies for identification of the top jet (ϵ_t) in the p_T range of 200-450 GeV.

have checked that by changing ΔR from 1.5 to 1.0 and the subjet radius from 0.5 to 0.3, the tagging efficiency increases by 5-6%.

We compute the efficiency of rejecting the backgrounds with the following set of cuts as described in Eq. (2.13) on the discriminators mentioned in last step above.

$$50 < m_T < 200, \quad 0.3 < Z_{b_j} < 0.9, \quad 0.15 < Z_{\tau_h} < 0.9,$$
$$0 < \tau_2/\tau_1 < 0.45, \quad 0.2 < \tau_3/\tau_2 < 0.9, \quad \Delta X_{b_j\tau_h} < 0.3 \tag{2.13}$$

With the variables mentioned in Eq. (2.13), the signal efficiency integrated over the p_T range of t-fatjet turns out to be 63.5% where the corresponding mistagging efficiency due for QCD jets is 3.1% and for $t_h\bar{t}_h$ it is 5.9%.

2.5 MVA Analysis: Unpolarized top

The standard cut-based strategy often rejects a significant fraction of signal events while reducing the background events that mimic the signal events. This situation can be improved

further by employing a Multivariate analysis (MVA) [271] technique which increases the background rejection rates.

We use the Boosted Decision Tree (BDT) method for the optimization purpose with the TMVA framework [271]. A decision tree takes a set of input features and splits input data recursively based on those features to classify events as either signal-like or background-like. To increase the stability in the training sample with respect to statistical fluctuations, we adopt the *Adaboost* [272] technique. The decision trees are constructed using half of the signal and background events, while the other half is utilized to test the performance of the trained model. We choose the relevant hyperparameters of this method as follows: Number of trees `NTree` = 850, maximum depth of the decision tree `MaxDepth` = 5, and minimum percentage of training events in each leaf node is given by `MinNodeSize` = 2.5%; other parameters are set to its default values [272].

Events are selected when the candidate fatjet includes a b- and a τ-identified subjet inside it. A number of kinematic variables are constructed out of the momenta of these objects, as discussed in the previous section, and eventually 10 input variables are used for BDT training. In Table 2.3, the set of input variables are shown, ranking them according to the importance in the BDT analysis for $m_{W'} = 1$ TeV at $\sqrt{s} = 13$ TeV. The importance here means the effectiveness of those variables in suppressing backgrounds while maintaining better signal purity.

In a typical BDT analysis, a few things need to be taken care of, such as instability, bias and overtraining. To that end first and foremost one has to ensure that a sufficient number of events for both signal and backgrounds are generated such that the importance or ranking of the variables is stabilized. To remove any bias coming from a particular QCD process because of the kinematical features of the background, we optimize the number of generated events. For instance, QCD events for low p_T bins, such as 200-300 GeV regime, 10M events are simulated, while for 300-600 GeV and for > 600 GeV regime, approximately 7M and 3M events are generated, respectively. We have simulated 1.3M signal events for W' mass = 1 TeV. In order to verify that there is no overtraining of the trees, the sample size of both training and testing data sets are optimised so that no deviation is observed in the final outcome. The goodness of fit is also checked with the Kolmogorov-Smirnov (KS) test, and observed that the KS value is within the permissible range of [0,1] and closer to the mean 0.5.

Rank	Variable	Description
1	m_T	Transverse mass of $b - \tau$ jets and MET of the system
2	$M_{b_j \tau_h}$	Fatjet Mass distribution in the mass range [60,160] GeV
3	$\Delta X_{b_j \tau_h}$	1 - Invariant mass of $b - \tau$ jet/Fatjet mass
4	τ_2/τ_1	Ratio of subjetiness of the Soft dropped Top-jet τ_2/τ_1
5	Z_{b_j}	Fraction of energy carried by the identified b-jet of Soft-Dropped Top Fatjet
6	Z_{τ_h}	Fraction of energy carried by the identified τ-jet of Soft-Dropped Top Fatjet
7	τ_3/τ_2	Ratio of subjetiness of the Soft dropped Top-jet τ_3/τ_2
8	m_{b_j}	Mass of identified b- jet
9	m_{τ_j}	Mass of identified τ- jet
10	$N_{\mathrm{trk}}(\tau_h)$	Charged track multiplicity of identified τ- jet

Table 2.3: List of the variables used to train W' signal, QCD and $t_h \bar{t}_h$ events.

After the classifier has been trained, it gives the output in terms of a single variable, the BDT response. Applying a cut on the BDT output variable, the signal-to-background ratio is optimised and can be presented as the Receiver Operative Characteristic (ROC). In Fig. 2.11, we display the ROC for our proposed tagging technique. The figure estimates the tagger performance at different background rejection rates $(1 - \epsilon_b)$, where ϵ_b is the background acceptance efficiency. For this classifier the signal-to-noise ratio is maximized at a cut value of > -0.05 where the signal efficiency is $\sim 77\%$ against a QCD jet mistag rate of $\sim 3\%$. The figure also shows it is possible to get a good separation against the background due to hadronic top jets, with the same discriminators.

Note that, a method to identify boosted top jets consisting of electrons was studied in [246]. The final outcome of our study is found to be comparable with the same as obtained in [246]. We thus see that our proposed top tagger has acceptable efficiency and can be used to study boosted objects consisting of b quark and τ lepton in the decays involving BSM particles in the context of BSM searches.

2.6 Tagging a polarized top

In the SM the $t/\bar{t}$ quarks produced via QCD are essentially unpolarized due to the vector nature of QCD whereas for the single t production in association with a W, the V-A nature
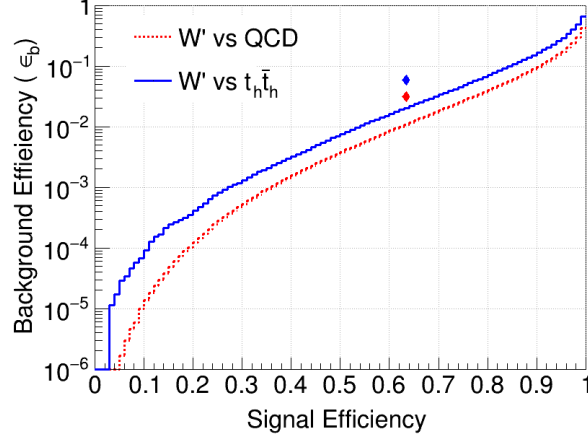
Figure 2.11: The Signal and background efficiencies for $m_{W'} = 1\,\text{TeV}$ against QCD (red dotted) and $t\bar{t}$ (blue solid). The two points in red and blue color represent the corresponding efficiencies for QCD and $t_h\bar{t}_h$ from a cut based analysis with the choice of cuts mentioned in Eq. (2.13).

of the tbW coupling completely determines the polarization of the produced t. Top quarks produced from BSM sources, either in pair or singly, may have a polarization different from the predictions of the SM depending on the chiral structure of the BSM vertices responsible for its production. Hence the polarization of the produced t is a good probe of many a BSM physics scenarios (see for example [210–213, 242, 250, 273–278]). As already pointed out, in the rest frame of the top quark, the angular distribution of the decay products carries information about the initial top spin direction [222–224]. The angular distribution of the decay product (f) in the rest frame of the top with polarization $\mathcal{P}_z$, $(-1 \leq \mathcal{P}_z \leq 1)$, expressed as Eq. (1.48) is a function of the spin analyzing power k_f and the angle of the decay product f with respect to the top spin direction in the top rest frame, θ_f. Note that the down-type quark and charged lepton, originating from the decay of W-boson in hadronic and leptonic top decay, respectively, have the maximum power ($k_{\ell+} = k_{\bar{d}} = 1$). This makes the leptonic decay mode of the t-quark particularly suited for t-polarization measurements.

In the boosted regime, the finite angular resolution of the detector reduces the effectiveness of the angular distributions of the decay products. Luckily one can construct polarization sensitive observables like energy fractions unambiguously without the requirement

of W reconstruction inside the top jet [82, 279] to study the polarization of top quark. To this end one can exploit the kinematic features of the top decay products [82, 242, 246, 277, 279, 280]. Here in this section, we explore the feasibility of distinguishing between the left-, right- and un- polarized, boosted semi-leptonic top quarks using polarization sensitive observables. For that, we repeat the procedure of top tagging, i.e steps 1-5 mentioned in the later part of sec. 2.4 and construct a few polarization sensitive variables constructed out of the energies and momenta of the tagged top jet and its subjets.

- <u>Energy Fractions:</u>

The different angular distributions of the decay products in the rest frame of the t get translated into different energy distributions of the decay products in the lab-frame for the boosted t-quark and hence of course to different distributions in energy fractions of the decay t that these carry. The difference in the distributions in these energy fractions (at the parton level this is just the ratio of the lepton or b quark energies to the energy of the t) for the left and right polarized top quarks was first pointed out in [82] and then used for tagging the polarized top jet in [279]. The left and right panels of Fig. 2.12 show the behavior of energy fraction variables (Z_j) defined in Eq. (2.10) for both the τ_h- and b- like jets respectively, for the case of left-handed top quarks (t_L), right-handed top quarks (t_R) and unpolarized top quarks (t_{LR}) originating from W' decay. The corresponding expected distributions at the parton level are shown by dotted lines for comparison. For a more realistic comparison with the jet level plots, one uses the visible energy from τ-lepton to determine Z_{τ_h} as described in Sec. 2.4.

We do see the same difference, as seen in Fig. 2.7, between the energy fractions carried by the b-jets and τ_h-jets. Further, we note that b-like jets from t_L are more boosted compared to those from the t_R whereas for the τ_h, exactly opposite is the case. This can be of course understood in terms of the opposite signs of the spin analysing powers of the b quark and the τ^+. Due to the negative sign of κ_b according to Eq. 1.48, b quarks are preferentially emitted opposite to the spin direction in the rest frame of the t. For the t_L, this means that they are emitted preferentially in the direction of motion of the t in the laboratory. This, in turn, means that the boost from the rest frame of the t to the laboratory frame makes these b quarks more energetic than would be the case with b quarks coming from the decay of t_R or unpolarised t-quarks. For the τ^+ the positive nature of κ_τ implies exactly the opposite. As can be seen from the left panel of Fig. 2.12, the τ-jet energy fraction (Z_{τ_h}) peaks ~ 0.15

for t_L, taking relatively larger values (~ 0.3 or more) for t_R. The right plot of Fig. 2.12, displays the characteristics of the b-jet that it takes away more energy for t_L than t_R. The distributions Z_{b_j} shown in the right panel of Fig. 2.12 peak at ~ 0.8 & 0.4 for t_L and t_R respectively. For comparison, we have included the distributions of energy fractions (Z_{τ_h} and Z_{b_j}) for t_{LR} which we have previously discussed in Fig. 2.7. Thus, we see that even though the full reconstruction of the τ momentum is not possible at the jet level (due to the presence of neutrinos in the final state), the energy fractions can act as a good polarimeter for differentiating left-handed, right-handed and unpolarized boosted top quarks decaying to final state containing τ leptons.
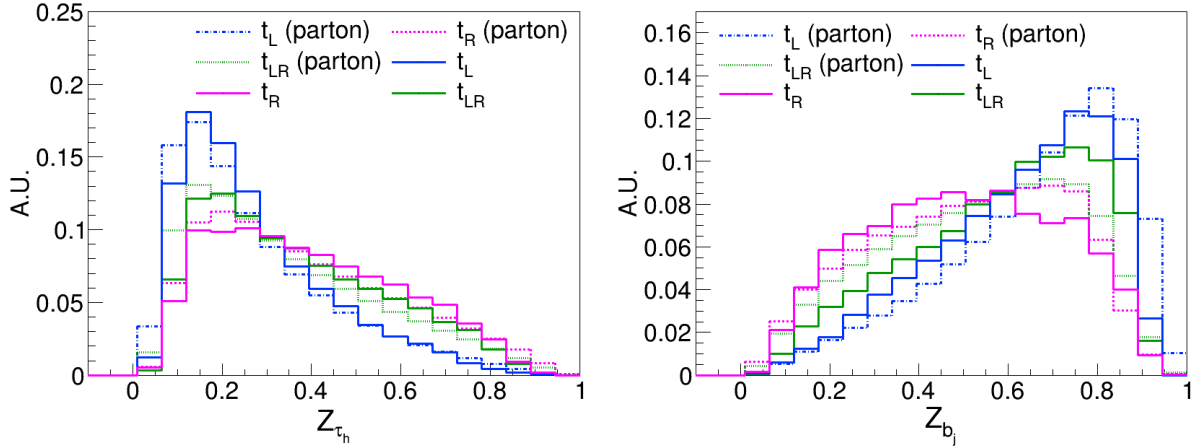
Figure 2.12: Distribution of energy fraction (Eq. (2.10)) of τ_h- (left panel) and b- (right panel) like subjets for left-, right- and un- polarized top. Blue solid (dotted) lines denote the distribution for left-handed reconstructed (parton level) top and magenta solid (dotted) is for right-handed reconstructed (parton level) top. Similarly, the green solid (dotted) distributions are for reconstructed (parton level) unpolarized top.

● Angular variable ($\cos\theta_j$):

Eq. 1.48 gives the distribution in the angle of the decay product with the spin direction of the decaying t, in the rest frame of the t. Since for the t-quark of a given helicity, the spin direction is related to the direction of the t three-momentum vector; we can instead look at the correlation of the decay product momentum in the rest frame of the t, with the

original t direction in the laboratory. In case of the hadronic topjet, the topjet direction in the laboratory is of course a very good proxy for the momentum of the t-quark in laboratory. This was used to good effect in [277] to discriminate boosted topjets with different helicities. In the present case due to the presence of missing momentum, we consider sum of the reconstructed momentum of the $b - \tau$ jet system in the laboratory frame, viz. $(\vec{b_j} + \vec{\tau_h})$ system as a proxy for the t momentum (and hence top-spin) direction. We then define

$$\cos\theta_{\mathrm{J}}\big|_{J=b_j,\tau_h} = \frac{(\vec{b_j} + \vec{\tau_j}).\vec{j'}}{\left|(\vec{b_j} + \vec{\tau_j})\right|\left|\vec{j'}\right|}. \tag{2.14}$$

Here j' is the momentum of the subjet (either b-jet or τ-jet) in the rest frame of the b-τ jet system.

For left-handed top quark, the direction of the top quark spin is in the opposite direction with respect to the top quark momentum in the laboratory frame. Eq. 1.48 and the values of $\kappa_{\ell^+}, \kappa_b$, tell us then that the $\tau_h(b)$ from t_R would be preferentially emitted along (opposite) the direction of the $(\vec{b_j} + \vec{\tau_h})$, i.e. the proxy t momentum direction. Exactly opposite will be the case for t_L, and for t_{LR} it will be in between t_L and t_R. This is borne out by the left plot in Fig. 2.13, which shows that the $\cos\theta_{\tau_h}$ is preferentially positive (negative) for right (left) handed top quarks. As seen in the right plot in Fig. 2.13, the b-jet exhibits a behavior exactly opposite to the τ-case i.e., $\cos\theta_{b_j}$ takes preferentially negative (positive) values for right (left) handed top quark.

Using only these two sets of variables, namely the energy fractions (Z_{b_j} and Z_{τ_h}) and angular correlation discriminator ($\cos\theta_j$) of the top decay products, we can achieve a good separation between the left-handed, right-handed and unpolarized top quarks. Note that the top tagging efficiencies for left and right polarized top quark do differ only slightly $\sim 2-3\%$. In Fig. 2.14, we display the ROC curve obtained by training the BDT with two polarization sensitive observables along with the other variables of Table 2.3, for left, right and unpolarized top samples. The blue (magenta) curve shows the efficiency of t_L (t_R) against t_{LR}, while the yellow line represents the same for t_R against t_L. It can be seen from Fig. 2.14 that t_R is identified more efficiently than t_L against an unpolarized top background. This can be understood by looking at kinematic regions where one of the t_L or t_R differs distinctly from t_{LR}. In this case, the b-jet energy fraction seems to be a better discriminator between the polarized top and unpolarized sample for the right polarized top. As we pointed out previously, because a fraction of the energy of top is carried out by the MET in τ decay, Z_{b_j}
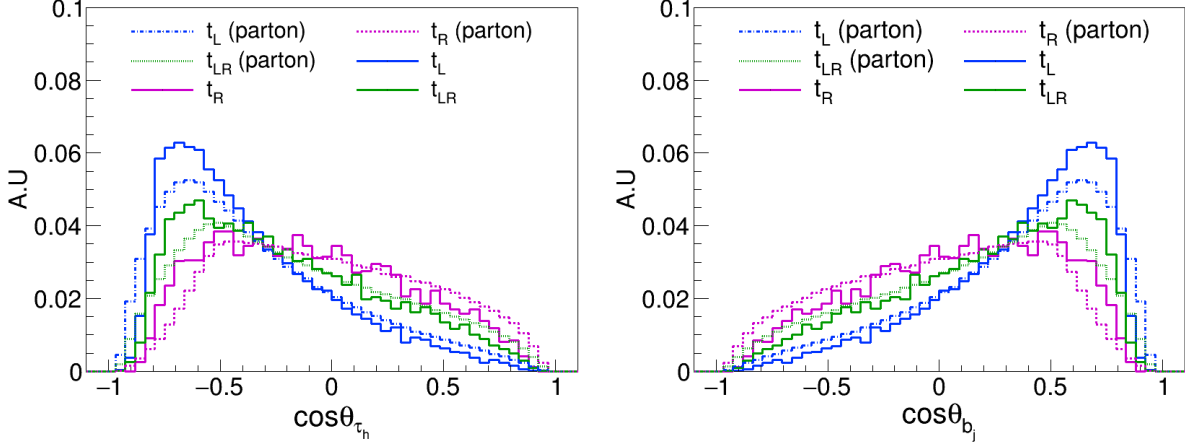
Figure 2.13: The angular distribution of τ_h (left) and b_j (right) in the rest frame of $(b_j + \tau_h)$ system for t_L, t_R and t_{LR} following Eq. 2.14. The color code is similar to Fig. 2.12.

peaks at higher values than Z_{τ_h} for t_{LR}. Hence, t_R for which the b quark from t decay is less energetic than that of t_L, has a higher chance of discrimination against t_{LR}. We find that right-handed top jets can be tagged with $\sim 65\%$ efficiency (ϵ_{t_R}) with a mis tagging rate of $\sim 25\%$ for left-handed top jets (ϵ_{t_L}) and $\sim 35\%$ against unpolarized top ($\epsilon_{t_{LR}}$) jets. If we reduce ϵ_{t_L} to $\sim 1 - 2\%$, ϵ_{t_R} comes out to be around $15 - 20\%$.

2.7 Summary and Outlook

In this Chapter, we investigated the performance of a boosted top tagger when the top quark decays in the leptonic channel with the τ lepton in the final state. The proposed top tagger relies on the identification of an energetic b-jet and a τ-jet within the top fatjet and its energy profile with respect to the parent particle. This methodology focuses on the distribution of energy between two subjets within the fatjet and constructs kinematic variables relevant to the final state topology. This in turn helps to discriminate the signal from SM backgrounds. Some of the variables that are found to be useful in identifying and classifying the semi-leptonic boosted tops are (a) the energy fraction of the identified b- and τ- subjets of the total fatjet energy, (b) the difference of the masses of the b-τ system and top fatjet (cf. Eq. (2.11)), (c) the ratios of the N-subjettiness variables (d) transverse mass of the b-τ subjet.
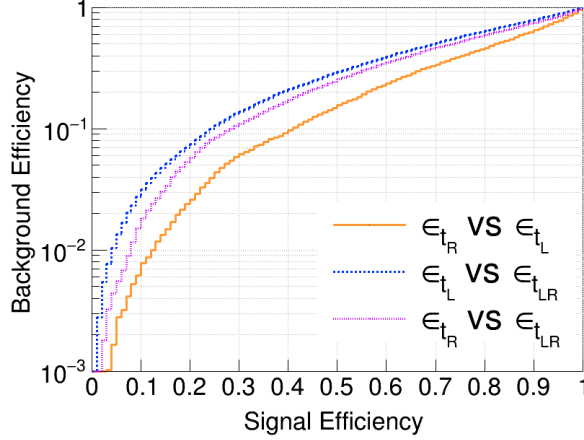
Figure 2.14: The ROC curve estimates the performance of the BDT classifier of distinguishing the (a) right vs left (b) left vs unpolarized (c) right vs unpolarized top jets.

We analyze the performance of the proposed tagger by using simulated signal and background events and then constructing observables based on the jet substructure technique. Through a BDT analysis, we obtain a signal efficiency of around 77% while keeping the mistagging rate of the QCD jets (consists of quark and gluon initiated jets) to 3% level. The hadronically decaying top quark initiated jets can also play the role of a potential background. We find that with a signal efficiency of around 77%, the mistagging rate of the hadronic top quark jet is around 5-6%. It is noteworthy that even though the main focus of this study is to develop a toptagger when top quark decays through τ-lepton in the final state, however, this tagger can be applied to any fatjet, which includes a b-jet and a τ-jet. For example, decays of a 3rd generation Leptoquark, top squark decay in R-parity violating supersymmetric models etc. can all lead to a final containing a b- and a τ- subjet inside a fatjet due to the boosted nature of the parent particle. Absence of a ν in the primary decay in the signal ought to make the tagging using this strategy even easier.

Another important aspect of developing a toptagger for this leptonic final state, is that we can analyze and estimate the sensitivity of the tagger with respect to top quark polarization. The couplings of the top quark with fermions and bosons in various BSM scenarios can have different implications for the top quark polarization. This polarization in turn modifies the distribution of various kinematic observables involving its decay products.

We study the sensitivity of these distributions to t-polarization in two extreme cases of top polarization, namely purely left-handed and purely right-handed top quarks. We use the same method of top-tagging as described above. We indeed find that using the observables based on the energy profile of subjets of the boosted top jet, namely the b- and τ- tagged jets along with the angular correlations measured in the rest frame of b-τ system, one can differentiate between the left and right-handed top quarks quite efficiently. A detailed exploration of some of the interesting applications of our proposed top tagger is left for future investigations.

CHAPTER 3

LONG LIVED NLSP IN NMSSM

This chapter is based on my work [281] done in collaboration with Amit Adhikary, Rahool Kumar Barman, Biplob Bhattacherjee, Rohini M. Godbole and Suchita Kulkarni

3.1 Introduction

Observations of the existence and measurements of DM [91,282] of matter-antimatter asymmetry and non-zero neutrino masses, [282] as well as theoretical considerations such as the hierarchy problem [283–285], point to the existence of new physics beyond that in the SM. Among the extensions of the SM, those involving SUSY still remain one of the most appealing because they address multiple shortcomings of the SM at once [120, 121, 286–288]. Depending on the exact realization, SUSY can present numerous DM candidates such as the lightest neutralino, sneutrino, or gravitino [121, 289–291]. The SUSY DM candidate, viz. the Lightest Supersymmetric Particle (LSP), is stabilized by means of an external symmetry, such as R-parity; see, for example, [121, 288].

The interactions of the DM with the particles in the SM or those within the dark sector affect its exact evolution and hence subsequently, the prediction for the amount re-

maining today, dubbed as relic density. This has been now accurately measured to be $\Omega h^2 = 0.120 \pm 0.001$ [91] where h is Hubble constant in units of $100 \text{ km s}^{-1}\text{Mpc}^{-1}$. In case of the neutralino LSP, the relic density is often generated utilizing the popular thermal freeze-out process [292–294], while for gravitino, the suppressed couplings with the SM necessitate a non-thermal relic density generation mechanism [181, 182]. Apart from the particle physics aspect, the relic density also depends on the details of the early Universe evolution. For example, late-time entropy production can substantially dilute the relic density while keeping the particle physics details unchanged. In the absence of precise knowledge of DM interactions and the evolution of the early Universe, it is thus important to consider both over-abundant and under-abundant (viz. with predicted relic density has a value above (below) the measured value) regions of SUSY DM parameter space [291, 295–300].

Dark matter can be searched for in several experiments. Due to model-independent search strategies, the results are applicable to SUSY and a variety of other beyond the SM scenarios. The primary detection strategies are via detection of missing energy at the LHC, via scattering off nuclei at underground direct detection experiments, or via detection of decay or annihilation products through cosmic rays in the Universe today at indirect detection experiments. Among these, the direct detection experiments already rule out left-handed sneutrino DM arising in the minimal supersymmetric Standard Model [301]. Out of the thermal candidates, this leaves the lightest neutralino – a linear combination of the bino, wino, and higgsino – as a viable DM candidate, whose compatibility with the experimental searches needs to be checked in detail.

In the MSSM, the lightest neutralino is a part of the system of electroweakinos, which consists of four neutralinos and two charginos. The electroweakino sector, and in particular, light neutralinos, have been a topic of intense phenomenological and experimental investigations in the past decade. Some of the latest LHC results for electroweakino searches are summarized below. A CMS search for electroweakinos through chargino-neutralino production ($\widetilde{\chi}_1^\pm \widetilde{\chi}_2^0$) with on-shell decays to Wh final state rules out wino-like chargino masses up to 700 GeV, for bino-like LSP mass $M_{\widetilde{\chi}_1^0} < 350$ GeV [302]. This search was performed at the centre-of-mass energy of 13 TeV with an integrated luminosity of 137 fb^{-1}. Another search from the ATLAS collaboration considers pair production of neutralinos at 13 TeV with 139 fb^{-1} integrated luminosity in fully hadronic final states mediated by WW, WZ or Zh [303]. This search excludes wino (higgsino) mass up to 1060 (900) GeV for bino-like LSP up to 400 (200) GeV. These searches imply a relatively heavier electroweakino sector.

It should, however, be noted that these results assume a simplified model framework with 100% branching ratios, which should be reinterpreted in the context of specific SUSY models, e.g., pMSSM or NMSSM. As a result, lighter electroweakinos can still be allowed despite the stringent LHC limits, and the exact limits are model dependent.

Some generic conclusions about the MSSM neutralino dark matter in light of recent collider and astrophysical constraints are available now. For example, the neutralino masses in phenomenological MSSM (pMSSM) have a lower limit of $M_{\widetilde{\chi}_1^0} > 34\ \mathrm{GeV}$ in order to avoid over-abundant relic density [300, 304–307]. In the general-MSSM scenario, higgsinos are favoured to have mass $\sim 1\ \mathrm{TeV}$ to obtain the correct DM abundance for a single component thermal DM [308–310]. Within the MSSM, relic density compliant regions require either heavy DM or rely on a co-annihilation mechanism, which demands a small mass splitting between DM and its co-annihilating partner. Such small mass gaps can lead to long-lived particles (LLP), which can then be investigated, for example, by looking for displaced vertices or heavy stable charged particles. It is worth noting that relaxing the DM relic density requirement does not necessarily lead to additional LLP parameter space within the MSSM. This is because the only way to obtain LLPs is through small mass splitting, as the SUSY couplings are related to those of SM and hence can not be suppressed.

Although the MSSM can successfully provide a DM candidate, a drawback of this most commonly used SUSY realization is the "μ-problem" which arises as an artifact of the common mass term for two Higgs doublets. This introduces a fine-tuning, which requires an electroweak scale μ parameter rather than the expected Planck scale [311]. An alternative can be considered as a singlet extension of the MSSM, the next-to-minimal supersymmetric standard model (NMSSM) [312–314] with a singlet Higgs field in addition to two Higgs doublets of the MSSM. For this additional scalar, the effective μ term can be generated dynamically, alleviating the fine-tuning of μ. The fermionic component of the singlet superfield provides an additional neutralino without violating the existing constraints. In such cases, the LSP can be pure singlino dominated or a mixture of higgsino-singlino. Such LSP can be lighter than the corresponding MSSM counterpart [315–319]. We have already discussed the details of this model in sec .1.8.

The phenomenology of such extended sectors can open up interesting new avenues for DM phenomenology as well as experimental searches. In this work, we revisit the neutralino sector of the NMSSM, focusing on the LSP with a significant singlino fraction [320–323]. Such singlino has suppressed couplings with the rest of the SUSY spectrum and thus

can lead to a long-lived next-to-the lightest supersymmetric particle (NLSP) neutralino. We investigate this possibility and suggest a displaced vertex search relying on tracks originating through NLSP decays. It should be noted that the region of the LLP parameter space in the NMSSM considered in this work has two distinct features. First, the long-lifetime of the NLSP neutralino results from suppressed couplings and small mass differences with the singlino-dominated LSP neutralino, and secondly, it leads to over-abundant relic density for the LSP neutralino DM.

The LLPs are intriguing since they lead to characteristic collider signatures. The charge and color-neutral LLPs travel a macroscopic distance before decaying into SM particles at a secondary vertex, resulting in a displaced vertex signature. The LLPs can be realized either with scenarios involving suppressed couplings or small mass splittings. Depending on the LLP lifetime, its decay may take place either in the tracker, in calorimeters and muon system, or even outside the detector. The pivotal advantage is having an almost negligible background, thanks to the existence of displaced vertices. A variety of theory scenarios, including SUSY, little Higgs [324], twin Higgs [325], dark sector models [326–330] etc, predict LLPs. In SUSY, LLPs are usually featured in R-parity violating models [331]. Besides, in many R-parity conserving (RPC) scenarios gauge-mediated SUSY (GMSB) [332, 333], anomaly-mediated SUSY (AMSB) [334], particles with long lifetime can appear.

The long-lived NLSP neutralino within the NMSSM is thus an exciting prospect, and a potential discovery could lead to a renewed understanding of the behaviour of dark matter in the early Universe. We, therefore, present a detailed search strategy for such parameter space in this work. The rest of the Chapter is organized as follows. In Sec. 3.2 we describes the pertinent range of parameters for numerical scan, along with the current phenomenological constraints. The characteristic features of the parameters to achieve long-lived neutralinos are discussed in Sec. 3.3. In Sec. 3.4 we present a signal-to-background study via searches of displaced vertices from decays of long-lived neutralinos and explore the reach of such searches for direct production of electroweakinos at the HL-LHC. Finally, we summarize in Sec. 4.6.

3.2 Parameter space scan and constraints

Our primary focus is the region in the parameter space of the RPC NMSSM, featuring a long-lived neutralino while being consistent with the current collider and direct/indirect

detection constraints. The lightest neutralino $\widetilde{\chi}_1^0$ naturally provides a DM candidate in R-parity conserving NMSSM. *A priori*, the LSP $\widetilde{\chi}_1^0$ can be pure gaugino, higgsino, singlino, or an admixture of these states. Such an LSP can lead to the correct DM relic density either if it is purely higgsino or wino-like with masses up to $2.8\,\mathrm{TeV}$ [335,336] or if it is bino or singlino like which can annihilate through co-annihilation or resonant annihilation through Higgs or Z boson. Such resonant annihilation conditions can only be realized for $m_{\widetilde{\chi}_1^0} \sim m_{H/Z}/2$, subject to non-negligible $\widetilde{\chi}_1^0 \widetilde{\chi}_1^0 Z/H$ couplings. In this work, however, we do not impose any relic density requirements and the allowed parameter space points of our interest are all over-abundant. For these scenarios, the relic density can be fulfilled either by requiring additional DM candidates or by requiring non-standard evolution of the Universe, as argued in Sec 3.1.

We consider a dominantly singlino-like LSP $\widetilde{\chi}_1^0$ and bino-like NLSP $\widetilde{\chi}_2^0$. Since there are no tree-level couplings between the bino and singlino, the bino-like NLSP $\widetilde{\chi}_2^0$ decays to the singlino-like LSP $\widetilde{\chi}_1^0$ only through their mutual higgsino admixtures. This leads to a suppressed coupling between LSP and NLSP states. An additional phase space suppression can be achieved if the mass difference between the two states is smaller than the Z mass. In such scenarios, the bino-like $\widetilde{\chi}_2^0$ can be LLP. The heavier neutralinos $\widetilde{\chi}_3^0, \widetilde{\chi}_4^0, \widetilde{\chi}_5^0$, and charginos $\widetilde{\chi}_1^\pm, \widetilde{\chi}_2^\pm$ can be either higgsino-like, wino-like, or admixtures of both and decay promptly. In this analysis, we consider a moderately mixed scenario with $\mu < M_2$, which implies a relatively large higgsino admixture in $\widetilde{\chi}_3^0, \widetilde{\chi}_4^0$, and $\widetilde{\chi}_1^\pm$.

Our choice for $\mu < M_2$ is motivated by three factors. First, LHC constraints for higgsinos are weaker compared to winos [302, 303]. Second, higgsinos have tree-level couplings with both singlino and bino, while no such interactions exist for wino-bino or wino-singlino. Therefore, winos can decay into bino or singlino only by virtue of its mixing with higgsinos. Third, both bino-like $\widetilde{\chi}_2^0$ and singlino-like $\widetilde{\chi}_1^0$ are required to have non-zero higgsino admixtures in order to generate a tractable decay width for $\widetilde{\chi}_2^0$ such that they can be probed at the LHC through track-based LLP searches. Concretely, we choose $500\,\mathrm{GeV} \lesssim \mu \lesssim 1000\,\mathrm{GeV}$, $M_2 \geq 2\,\mathrm{TeV}$ such that $\widetilde{\chi}_3^0, \widetilde{\chi}_4^0$, and $\widetilde{\chi}_1^\pm$ have a dominant higgsino admixture with appreciable production rates at HL-LHC, compatible with existing LHC constraints from direct electroweakino searches, discussed in Sec. 4.2.

In the NMSSM superpotential as given in Eq. (1.100), we observe that interactions between the singlet superfield $\hat{S}$ and the MSSM Higgs superfields $\hat{H}_u, \hat{H}_d$ is controlled by λ. In the limit, $\lambda \to 0$ (for a fixed $\mu = \lambda v_S$), the singlet-like scalar, singlet-like pseudoscalar, and

the singlino can no longer interact with the MSSM sector. This consideration leads to the possibility of a pure singlino-like neutralino LSP with a tree level mass $\sim 2\kappa v_S$. In this case, the NLSPs would be composed of bino/wino/higgsinos, similar to that in MSSM. Furthermore, in the $\lambda \to 0$ limit, the LSP has no interaction with NLSPs, however, keeping a finite but small λ leads to suppressed interactions between singlino LSP and MSSM-like neutralino NLSPs. This suppression leads to long-lived NLSPs, which is the focus of this work. In particular, we consider bino-like $\tilde{\chi}_2^0$. In the limit, $\mu \gg 2\kappa v_S$, the mass of the singlino-like neutralino $m_{\tilde{\chi}_1^0}$ can be approximated as:

$$m_{\tilde{\chi}_1^0} \sim 2\kappa v_S \simeq 2\frac{\kappa}{\lambda}\mu. \tag{3.1}$$

We, therefore, observe that a singlino-like LSP with a typical mass of $\mathcal{O}(100)$ GeV and $\mu \sim \mathcal{O}(500)$ GeV leads to $\kappa/\lambda \sim \mathcal{O}(0.1)$. In order to maintain a similar mass hierar-
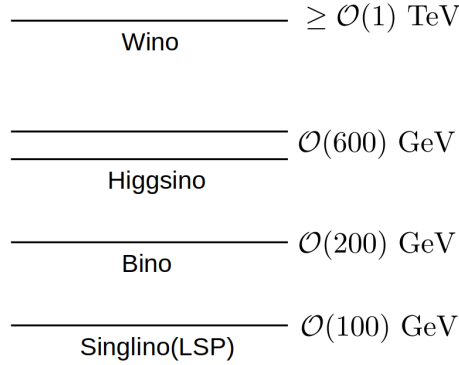
Figure 3.1: Mass hierarchy in the electroweakino sector.

chy between the higgsino-like neutralinos and the singlino-like $\tilde{\chi}_1^0$, we restrict ourselves to $\kappa/\lambda \leq 0.15$ with $10^{-5} \leq \lambda \leq 10^{-1}$. Correspondingly, for the sake of simplicity, we restrict ourselves to the parameter space where singlino-like LSP mass is $\mathcal{O}(100)$ GeV. We are thus left with the bino mass parameter, M_1, the only remaining parameter in the electroweakino mass spectrum, which is not fixed. Since we are interested in a bino-like $\tilde{\chi}_2^0$, it must fall between the singlino- and higgsino-like neutralinos. Correspondingly, we vary M_1 over the range $150\,\text{GeV} \leq M_1 \leq 550\,\text{GeV}$. We illustrate the mass hierarchy between the electroweakinos in Fig. 3.1. The other input parameters that are relevant to the present study are: A_λ, A_κ, the gluino mass parameter M_3, squark mass parameters M_{U_R,D_R}^i, $M_{Q_L}^i$ (i=1,2,3), the

tri-linear couplings A_t, A_b, A_τ, the slepton mass parameters M_E^i, M_L^i. We set A_b, A_τ, squark and slepton mass parameters to 2 TeV. In order to maximize the one-loop top/stop contributions to the lightest CP-even Higgs mass, the tri-linear soft coupling A_t is varied over a wide range [-10,10] TeV. To respect the constraints on the parameter space from charge and color breaking minima [337, 338], we exploit the maximum mixing scenario (c.f. Ref. [131]) and require that the ratio of stop mixing parameter $|X_t|$ ($= A_t - \mu \cot\beta$) to average stop mass M_T ($M_T^2 = m_{\tilde{t}_1} m_{\tilde{t}_2}$, where $m_{\tilde{t}_1, \tilde{t}_2}$ are the stop masses) to satisfy $|X_t/M_T| < 2.5$ [338, 339].

3.2.1 Scan range

We utilize the `NMSSMTools-5.5.3` [340, 341] package to perform a random scan over the parameter space. The particle masses, couplings, branching ratios, and decay widths are also computed using `NMSSMTools-5.5.3`. We perform a flat random scan over 10^8 points. The efficiency for obtaining allowed parameter space consistent with the current collider and astrophysical data (discussed in Sec. 4.2) is 0.001 %. The scan is performed over the following range of input parameters:

$$
\begin{aligned}
&10^{-5} < \lambda < 0.1, \ \left|\frac{\kappa}{\lambda}\right| \leq 0.15, \ M_1 = (150, 550) \text{ GeV}, \\
&M_2 = (2000, 3000) \text{ GeV}, \ M_3 = (3000, 10000) \text{ GeV}, \\
&\mu = (500, 1000) \text{ GeV}, \ \tan\beta = (1, 40), \\
&A_\lambda = (-100, 10000) \text{ GeV}, \ A_\kappa = (-1000, 100) \text{ GeV}, \\
&A_t = (-10000, 10000) \text{ GeV}
\end{aligned}
\tag{3.2}
$$

3.2.2 Constraints

In our analysis, the lightest CP-even Higgs boson H_1 plays the role of the observed SM-like Higgs boson. In this regard, H_1 is required to be consistent with the Higgs mass constraints and Higgs signal strength constraints coming from the LHC. The heavier CP-even Higgs bosons H_2, H_3 and the CP-odd Higgs bosons A_1, A_2 can be an admixture of singlet and doublet components and can be constrained by heavy Higgs searches at the LHC. The constraints from heavy Higgs searches are subject to the doublet content and get weaker with increasing singlet admixture. Furthermore, the NMSSM parameter space of our interest is also constrained by limits from LEP searches, flavor physics, direct and indirect detection

experiments, and direct electroweakino searches at the LHC. We discuss various constraints below.

- **Mass of SM-like Higgs boson:** The mass of the observed Higgs boson has been measured to be within 124.4-125.8 GeV at 3σ uncertainty [342]. Acknowledging the theoretical uncertainties in Higgs mass computation [343–345], and adopting a conservative approach, we allow m_{H_1} to lie within the range $122 \text{ GeV} \leq m_{H_1} \leq 128 \text{ GeV}$.

- **Limits from LEP**: We impose a lower limit on the chargino mass $M_{\widetilde{\chi}_1^\pm} > 103.5$ GeV which implies a lower bound of $\mu, M_2 \gtrsim 100$ GeV [346]. Searches at LEP have also derived an upper limit of 0.1 pb on the production cross-section of $e^+e^- \rightarrow (\widetilde{\chi}_2^0 \rightarrow q\widetilde{q}\widetilde{\chi}_1^0)\widetilde{\chi}_1^0$ for $|m_{\widetilde{\chi}_2^0} - m_{\widetilde{\chi}_1^0}| > 5$ GeV [347]. We also require $\Gamma_{Z_{\text{inv}}} < 2$ MeV [348], where $\Gamma_{Z_{\text{inv}}}$ is the invisible decay width for the Z boson excluding neutrinos. These constraints have been imposed using the `NMSSMTools-5.5.3` package.

- **Constraints from Higgs signal strength measurements:** Measurements by the ATLAS and CMS collaborations of the couplings of the 125 GeV Higgs boson with SM particles are encoded via signal strength parameters μ_i^f defined as,

$$\mu_i^f = \frac{\sigma_i \times \text{BR}^f}{(\sigma_i)_{\text{SM}} \times (\text{BR}^f)_{\text{SM}}}. \tag{3.3}$$

Here, i represents the various production modes of the Higgs boson viz gluon fusion (ggF), vector boson fusion (VBF), associated production with vector bosons (VH ($V = W^\pm, Z$)), while f denotes the various decay modes of the Higgs viz $b\bar{b}, \gamma\gamma, \tau^+\tau^-, ZZ^*, W^+W^{*-}$. In the present analysis, signal strength measurements for $\{i = ggF, f = \gamma\gamma, W^+W^-, b\bar{b}, \tau\tau, ZZ\}$, $\{i = VBF, f = \gamma\gamma, \tau\tau\}$, and $\{i = VH, f = W^+W^-, b\bar{b}\}$ [55, 349–353], have been implemented through a global χ^2 fit assuming 2σ uncertainty following the strategy in Ref. [354].

- **Constraints from flavor physics:** The flavor physics constraints are imposed through bounds on the branching ratios of relevant rare processes viz $Br(b \rightarrow s\gamma)$, $Br(B_s \rightarrow \mu^+\mu^-)$ and $Br(B^+ \rightarrow \tau^+\nu_\tau)$, which are sensitive to SUSY contributions. For example, the loop-mediated $b \rightarrow s\gamma$ process is sensitive to modifications from loops involving charged Higgs-top, neutral Higgs-bottom, and electroweakino-squark. Contributions from the latter decouple since the squark masses have been fixed at a rather high

value ~ 2 TeV. The $B_s \to \mu^+\mu^-$ process is mediated through penguin and box diagrams at one loop. Both contributions are sensitive to a loop containing scalar or pseudoscalar heavy Higgs and a down quark. The contributions from the penguin diagram are also sensitive to modifications from loops containing charged Higgs-up quark, higgsino-up quark, and gaugino-up quark, while loops from up quark-charged Higgs-neutrino, up squark-charged higgsino-sneutrino and up squark-charged wino-sneutrino can induce modifications to the box diagram contributions. Recent measurements are: $Br(B \to X_s\gamma) = (3.32 \pm 0.15) \times 10^{-4}$ [355], $Br(B_s \to \mu^+\mu^-) = (2.69^{+0.37}_{-0.35}) \times 10^{-9}$ [356, 357], $Br(B^+ \to \tau^+\nu) = (1.06 \pm 0.19) \times 10^{-4}$ [355]. We use `micrOMEGAs-5.0.8` [358–360] to compute the corresponding branching ratios for points in our allowed parameter space and require them to fall within 2σ uncertainty of the current best-fit values. We also include a theoretical uncertainty of 10% while computing the 1σ ranges. Constraints on ΔM_D, ΔM_S, the mass differences between $B^0_d, \overline{B}^0_d$ and $B^0_s, \overline{B}^0_s$ respectively, are also imposed through the `NMSSMTools-5.5.3` package.

- **Constraints from LHC searches:** The composition of heavy Higgs bosons H_2 and A_1 in the parameter space of interest are presented in Fig. 3.2 (left) and (right), respectively. In Fig. 3.2, $S^2_{21} + S^2_{22}$ and S^2_{23} represents the doublet and singlet content in H_2. Similarly, the doublet and singlet admixture in A_1 is denoted by P^2_{11} and P^2_{12}, respectively. We observe that both H_2 and A_1 have a dominant singlino composition ($\gtrsim 90\%$), leading to immunity from heavy Higgs search limits. We would like to note that the heaviest neutral Higgses H_3 and A_2 have a dominant doublet composition and have masses above $\gtrsim 2$ TeV, thereby remaining outside the direct reach of current LHC. Searches for long-lived particles at the LHC can also potentially constrain the allowed parameter space. We discuss their impact for some benchmark scenarios in Sec. 3.4.4.

Searches for pair-produced electroweakinos in the hadronic final state by the ATLAS collaboration using LHC Run-II data collected at $\mathcal{L} = 139$ fb^{-1} have excluded winos (higgsinos) up to a mass of 1060 GeV (900 GeV) given $m_{\widetilde{\chi}^0_1} \leq 400$ GeV (240 GeV) and the mass difference between the decaying wino (higgsino) and the LSP is larger than 400 GeV (450 GeV) at 95% CL [303]. However, these searches assume a simplified framework where the heavier wino/higgsino-like electroweakinos $\widetilde{\chi}^0_i$ directly
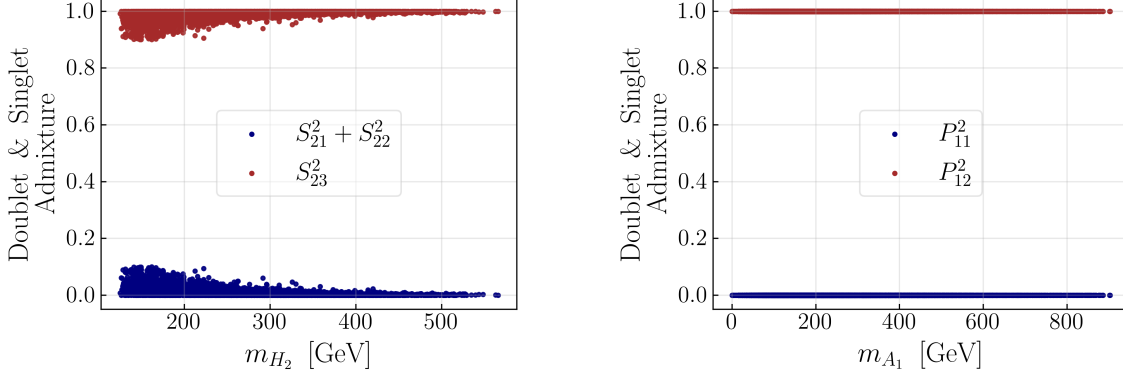
Figure 3.2: Singlet and doublet admixtures in H_2 (left panel) and A_1 (right panel) for parameter space allowed by light Higgs mass constraints, LEP limits, Higgs signal strength constraints and bounds from flavor physics. $S_{21}^2 + S_{22}^2$ and S_{23}^2 correspond to the doublet and singlet admixtures, respectively, in H_2. P_{11}^2 and P_{12}^2 represent the doublet and singlet admixture, respectively, in A_1.

decay into the LSP $\widetilde{\chi}_1^0$ with $Br(\widetilde{\chi}_i^0 \to \widetilde{\chi}_1^0 + Z) + Br(\widetilde{\chi}_i^0 \to \widetilde{\chi}_1^0 + h_{125}) = 100\%$. Let us analyze the implications of these constraints on the parameter space considered in this work. Within the parameter space of our interest, $\widetilde{\chi}_3^0, \widetilde{\chi}_4^0$ and $\widetilde{\chi}_1^\pm$ have dominant higgsino composition with masses ranging from $\sim$500 GeV to 2 TeV, while the wino-like $\widetilde{\chi}_5^0$ and $\widetilde{\chi}_2^\pm$ are decoupled $m_{\widetilde{\chi}_5^0/\widetilde{\chi}_2^\pm} \gtrsim 2$ TeV. In principle, $\widetilde{\chi}_3^0, \widetilde{\chi}_4^0$ and $\widetilde{\chi}_1^\pm$ have two potential pathways for decay, either through the intermediate bino-like $\widetilde{\chi}_2^0$ or directly into the singlino-like $\widetilde{\chi}_1^0$. The partial decay width for $\widetilde{\chi}_3^0/\widetilde{\chi}_4^0 \to \widetilde{\chi}_1^0 Z^*$ is determined by the higgsino admixture in $\widetilde{\chi}_1^0$, which is directly proportional to λ. The partial decay width for $\widetilde{\chi}_3^0/\widetilde{\chi}_4^0 \to \widetilde{\chi}_1^0 H$ also has a similar λ-dependence by virtue of the second term in the NMSSM superpotential in Eq. (1.100). Therefore, the partial decay widths for both channels through which $\widetilde{\chi}_3^0/\widetilde{\chi}_4^0$ can directly decay into $\widetilde{\chi}_1^0$ are $\mathcal{O}(\lambda^2)$ [361]. Thus, they are far smaller relative to the partial decay widths for $\widetilde{\chi}_3^0/\widetilde{\chi}_4^0$ decaying into the bino-like $\widetilde{\chi}_2^0$. Similar arguments can also be extended to the higgsino-like $\widetilde{\chi}_1^\pm$. Consequently, in the present scenario, directly produced $pp \to \widetilde{\chi}_3^0\widetilde{\chi}_1^\pm + \widetilde{\chi}_4^0\widetilde{\chi}_1^\pm$ will dominantly undergo cascade decay via $(\widetilde{\chi}_3^0/\widetilde{\chi}_4^0 \to (\widetilde{\chi}_2^0 \to \widetilde{\chi}_1^0 Z^{(*)}/H^{(*)})Z/H)(\widetilde{\chi}_1^\pm \to (\widetilde{\chi}_2^0 \to \widetilde{\chi}_1^0 Z^{(*)}/H^{(*)})W^\pm)$ leading to final states that are markedly different from those considered in the ATLAS search [303]. Furthermore, the allowed points in the parame-

ter space with $m_{\widetilde{\chi}_3^0, \widetilde{\chi}_4^0, \widetilde{\chi}_1^\pm} \lesssim 1$ TeV and a dominant higgsino admixture in $\widetilde{\chi}_3^0, \widetilde{\chi}_4^0$ and $\widetilde{\chi}_1^\pm$ ($\gtrsim 90\%$), correspond to mass differences between $\{\widetilde{\chi}_3^0 / \widetilde{\chi}_4^0 / \widetilde{\chi}_1^\pm\}$ and $\widetilde{\chi}_2^0$, which are very close to the ATLAS search threshold ~ 400 GeV [303], leading to low efficiencies. Overall, the parameter space of our interest is rather weakly constrained by all the direct electroweakino searches at the LHC.

- **Constraints from direct detection:** We apply the most recent upper limits on SI WIMP-nucleon interaction cross-section σ_{SI} from Xenon-1T [362] and PandaX [363], on SD WIMP-proton interaction cross-section σ_{SD_p} from PICO-60 [191] and SD WIMP-neutron interaction cross-section σ_{SD_n} from Xenon-1T [364]. We impose these direct detection (DD) limits after all the constraints discussed till now and find that these direct detection searches do not lead to any additional constraints on the parameter space. In fact, the predicted SI DD cross-sections fall below the neutrino floor for the entirety of the currently allowed points in the scanned parameter space. Hence, these would be inaccessible to future DD experiments based on σ_{SI} measurements. We also examine the projected sensitivity at the future σ_{SD} based experiments. For the range of $m_{\widetilde{\chi}_1^0}$ in the parameter space of our interest, the most stringent projected sensitivities for σ_{SD_p} and σ_{SD_n} are furnished by PICO-250 [365] and LZ [366], respectively. However, we observe that neither of them would be sensitive to any of the currently allowed points in the parameter space. We will discuss the aspects of direct detection in our next exploration mentioned in Sec. 4.2.

Having discussed the implications of the relevant current constraints, we move on to discuss the features of the currently allowed parameter space in the next section.

3.3 Features of the allowed parameter space

In this section, we examine the features of the allowed parameter space. We would like to emphasize again that our objective is to delineate the NMSSM parameter space that contains a long-lived bino-like $\widetilde{\chi}_2^0$ with mass $\sim \mathcal{O}(100)$ GeV and is also allowed by the current experimental constraints. In Fig. 3.3, we present the fraction of singlino content in $\widetilde{\chi}_1^0$ (upper-left), bino content in $\widetilde{\chi}_2^0$ (upper-right) and higgsino contents in $\widetilde{\chi}_3^0$ (lower-left) and $\widetilde{\chi}_4^0$ (lower-right) for the allowed points. We observe that the singlino admixture in $\widetilde{\chi}_1^0$ is $\gtrsim 99\%$ while $\widetilde{\chi}_2^0$ has a dominant bino content. Similarly, the heavier neutralinos $\widetilde{\chi}_3^0$ and $\widetilde{\chi}_4^0$ have a dominant
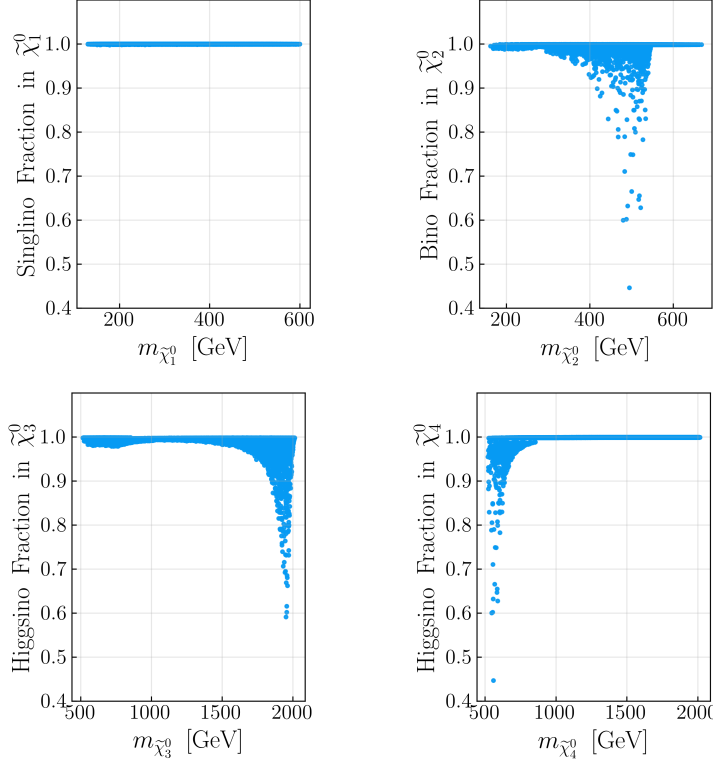
Figure 3.3: Singlino content N_{11}^2 in $\widetilde{\chi}_1^0$, bino content N_{21}^2 in $\widetilde{\chi}_2^0$, higgsino content $(N_{33}^3 + N_{34}^2)$ in $\widetilde{\chi}_3^0$ & higgsino content $(N_{43}^2 + N_{44}^2)$ in $\widetilde{\chi}_4^0$ is shown for currently allowed parameter space.

higgsino composition.

As noted in Eq. (4.1), we consider $|\kappa|/\lambda < 0.15$ besides 500 GeV $\leq \mu \leq 1$ TeV and 2 TeV $\leq M_2 \leq 3$ TeV in order to obtain a dominantly singlino-like LSP. We illustrate the allowed points in the k/λ vs μ plane in the left panel of Fig. 3.4. The color palette represents the mass of $\widetilde{\chi}_1^0$. We observe that $m_{\widetilde{\chi}_1^0}$ increases moderately with μ for a fixed value of κ/λ. At a given κ/λ, κ also increases with μ since $\mu \sim \lambda v_S$. This leads to an increment in the mass of singlino-like $\widetilde{\chi}_1^0$ since $m_{\widetilde{\chi}_1^0} \sim 2\kappa v_S$. For a fixed μ, the points with the smallest values of $|\kappa|/\lambda$ correspond to lowest, $m_{\widetilde{\chi}_1^0}$ as implied from Eq. (3.1)[1]. Considering $\mu \sim 1$ TeV and our assumption of $|\kappa|/\lambda < 0.15$, $m_{\widetilde{\chi}_1^0}$ is restricted to $m_{\widetilde{\chi}_1^0} \lesssim 300$ GeV, which is consistent with

---

[1]Eq. (3.1) can be adapted to $|\kappa|/\lambda \sim 0.5 \times m_{\widetilde{\chi}_1^0}/\mu$, which shows a direct correlation between $m_{\widetilde{\chi}_1^0}$ and $|\kappa|/\lambda$ at a given μ.
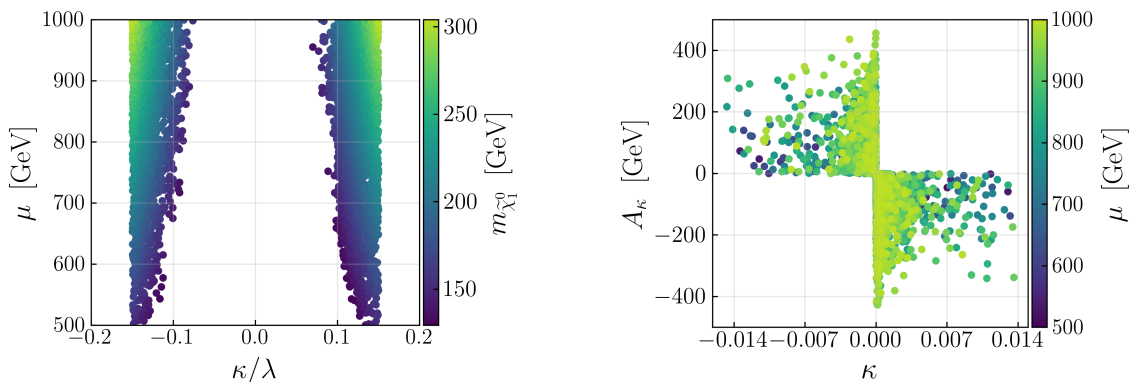
Figure 3.4: *Left panel:* Allowed parameter space points in the plane of κ/λ vs. μ. The color palette represents the mass of the singlino-like LSP neutralino. *Right panel:* Allowed parameter space in the k vs. A_κ plane. The color palette represents the higgsino mass parameter μ.

the observations in Fig. 3.4 (left). Similarly, at $\mu \sim 1$ TeV, the lowest value of $m_{\widetilde{\chi}_1^0}$, $m_{\widetilde{\chi}_1^0} \sim$ 125 GeV, implies a lower limit of $|\kappa|/\lambda \gtrsim 0.063$. As we move towards smaller values of μ, the lower limit on $|\kappa|/\lambda$ gets stronger, for instance at $\mu \sim 500$ GeV, we obtain $|\kappa|/\lambda \gtrsim 0.125$ for $m_{\widetilde{\chi}_1^0} \sim 125$ GeV, as also observed in Fig. 3.4 (left). We also present the allowed points in the κ vs A_κ plane in the right panel of Fig. 3.4. While both κ and A_κ can take positive or negative values, their product is required to be $\lesssim 0$. This requirement is implied by Eq. (1.114) where a positive value of $M_{P,22}^2$ at small λ is guaranteed only if $\kappa A_\kappa < 0$. One of the most exciting aspects of the parameter space is the presence of a long-lived neutralino. In Fig. 3.5, we present the decay width of $\widetilde{\chi}_2^0$ ($\Gamma_{\widetilde{\chi}_2^0}$) as a function of the mass difference between $\widetilde{\chi}_2^0$ and $\widetilde{\chi}_1^0$, $\Delta m(\widetilde{\chi}_2^0 - \widetilde{\chi}_1^0)$. We concentrate on the region highlighted by pink with $\Gamma_{\widetilde{\chi}_2^0} \leq 10^{-13}$ GeV. A decay width of $\Gamma \sim 10^{-13}$ GeV roughly translates to $c\tau \sim \mathcal{O}(0.1)$ mm. We observe that $\Gamma_{\widetilde{\chi}_2^0}$ can be smaller than $\lesssim 10^{-13}$ GeV when $\Delta m(\widetilde{\chi}_2^0 - \widetilde{\chi}_1^0) < m_Z$. In this region, only three body decays of $\widetilde{\chi}_2^0$ are viable [367]. We observe that $\Gamma_{\widetilde{\chi}_2^0}$ can be as small as $\sim 10^{-19}$ GeV for relatively smaller mass differences $\Delta m(\widetilde{\chi}_2^0 - \widetilde{\chi}_1^0) \lesssim 40$ GeV. Most notably, this mass difference is still large enough to produce energetic final states as $\widetilde{\chi}_2^0$ decays. Such configurations are not possible in MSSM with neutralino LSP and are a unique feature of the NMSSM scenario we consider.

Thus, the allowed points can have long-lived bino-like $\widetilde{\chi}_2^0$ with decay widths up to
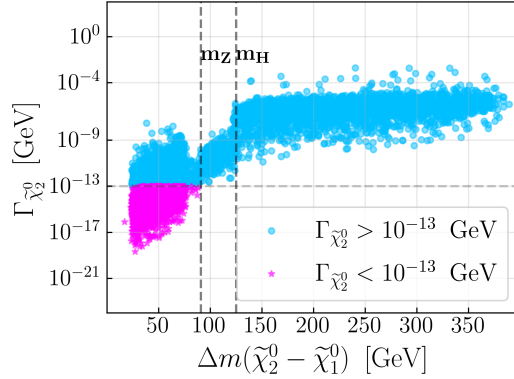
Figure 3.5: Allowed parameter space are presented in the plane of mass difference between $\widetilde{\chi}_2^0$ and $\widetilde{\chi}_1^0$ $\Delta m(\widetilde{\chi}_2^0 - \widetilde{\chi}_1^0)$ vs the decay width of $\widetilde{\chi}_2^0$ $\Gamma_{\widetilde{\chi}_2^0}$. The vertical black dashed lines represent the Z and H_{125} on-shell conditions. Parameter space with $\Gamma_{\widetilde{\chi}_2^0} \leq 10^{-13}$ GeV and $\Gamma_{\widetilde{\chi}_2^0} > 10^{-13}$ GeV are illustrated in pink and cyan colors, respectively.

$\sim 10^{-19}$ GeV. Furthermore, the heavier neutralinos $\widetilde{\chi}_3^0, \widetilde{\chi}_4^0$ and the lightest chargino $\widetilde{\chi}_1^\pm$ have a dominant higgsino admixture while $\tilde{\chi}_5^0$ and $\widetilde{\chi}_2^\pm$ are wino-like. We have set M_2 to be above $\gtrsim 2$ TeV, thus, decoupling $\tilde{\chi}_5^0$ and $\widetilde{\chi}_2^\pm$ from the rest of the electroweakinos. Since the LSP $\widetilde{\chi}_1^0$ has a dominant singlino content, the higgsino-like $\widetilde{\chi}_3^0, \widetilde{\chi}_4^0$ mostly decays through the intermediate bino-like $\widetilde{\chi}_2^0$, $\widetilde{\chi}_3^0/\widetilde{\chi}_4^0 \to \widetilde{\chi}_2^0 + H_1/Z$, instead of decaying directly into $\widetilde{\chi}_1^0 + X$ states. In Fig. 3.6, we present the branching ratios $Br(\widetilde{\chi}_3^0 \to \widetilde{\chi}_2^0 + H_1/Z)$ (upper-left panel) and $Br(\widetilde{\chi}_4^0 \to \widetilde{\chi}_2^0 + H_1/Z)$ (upper-right panel) for the allowed parameter space. We observe that $\widetilde{\chi}_3^0$ ($\widetilde{\chi}_4^0$) can decay via $\widetilde{\chi}_2^0 + H_1$ ($\widetilde{\chi}_2^0 + Z$) with branching fractions as large as ~ 0.9. The $\widetilde{\chi}_2^0$'s can eventually undergo three-body decay,

$$\widetilde{\chi}_2^0 \to \widetilde{\chi}_1^0 + Y \tag{3.4}$$

where $Y = b\bar{b}, \tau^\pm\tau^\mp, \ell^\pm\ell^\mp, j\bar{j}$, mediated through off-shell Z or Higgs boson if $\Delta(\widetilde{\chi}_2^0 - \widetilde{\chi}_1^0) < m_Z$. Here ℓ represents electrons and muons. The correlations among the three-body branching ratios of $\widetilde{\chi}_2^0$ in various decay modes for the allowed parameter space points are shown in Fig. 3.6 (lower panel). Points with $\kappa > 0$ and $\kappa < 0$ are represented in blue and red colors, respectively. In the $\kappa < 0$ scenario, the three-body decays of $\widetilde{\chi}_2^0$ are dominantly mediated through Z^*, resulting in generation universal branching fractions in leptonic decay modes. The Z mediated coupling $g_{Z\widetilde{\chi}_i^0\widetilde{\chi}_j^0}$ is governed by the higgsino admixtures $g_{Z\widetilde{\chi}_i^0\widetilde{\chi}_j^0} \sim$

Figure 3.6: *Upper panel:* Branching fractions for the dominant decay modes of $\widetilde{\chi}_3^0$ (*left*) and $\widetilde{\chi}_4^0$ (*right*) are shown for allowed parameter space. The green and purple colored points represent the branching ratio of $\widetilde{\chi}_3^0/\widetilde{\chi}_4^0$ into $\widetilde{\chi}_2^0 + Z$ and $\widetilde{\chi}_2^0 + H_1$, respectively. *Lower panel:* Correlations among the branching fractions for $\widetilde{\chi}_2^0$, $\{BR(\widetilde{\chi}_2^0 \to \widetilde{\chi}_1^0 + b\bar{b}), BR(\widetilde{\chi}_2^0 \to \widetilde{\chi}_1^0 + \tau\tau)\}$ (*left*) and $\{BR(\widetilde{\chi}_2^0 \to \widetilde{\chi}_1^0 + \text{jets}), BR(\widetilde{\chi}_2^0 \to \widetilde{\chi}_1^0 + \ell^\pm \ell^\mp/\nu\bar{\nu})\}$ (*right*), are shown for the allowed parameter space points with $\kappa > 0$ (blue) and $\kappa < 0$ (red).

$(N_{i3}N_{j3} - N_{j4}N_{k4})$. In the parameter space of our interest, we observe that the higgsino fractions in $\widetilde{\chi}_1^0$ are typically larger by $1 - 3$ orders of magnitude in the $\kappa < 0$ scenario compared to that in the $\kappa > 0$ case, giving more precedence to Z over h mediated decays.

3.4 Discovery potential of LLP decays at the HL-LHC

3.4.1 Electroweakino pair production rates at the HL-LHC

As discussed previously, directly produced chargino-neutralino pairs at the HL-LHC can lead to interesting final state topologies involving long-lived $\widetilde{\chi}_2^0$ in addition to several promptly
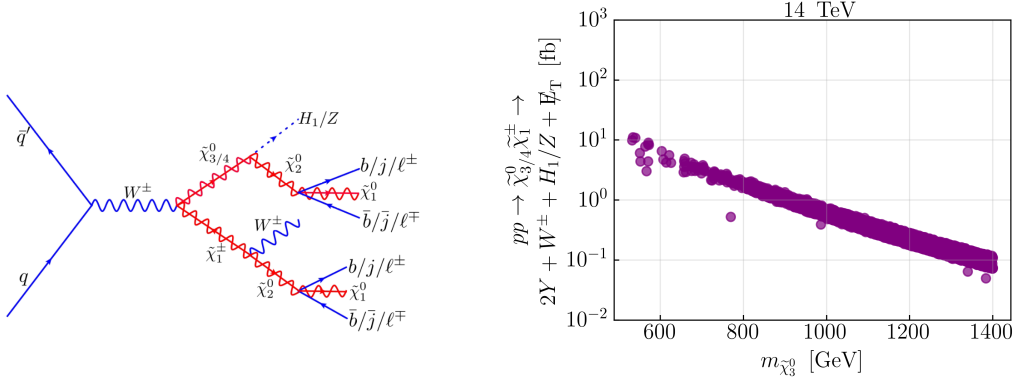
Figure 3.7: *Left panel:* Feynman diagram at the leading order for the signal process $\widetilde{\chi}_1^\pm \widetilde{\chi}_3^0/\widetilde{\chi}_4^0 \to (\widetilde{\chi}_1^\pm \to \widetilde{\chi}_2^0 + W^\pm, \widetilde{\chi}_2^0 \to \widetilde{\chi}_1^0 + Y)(\widetilde{\chi}_3^0/\widetilde{\chi}_4^0 \to \widetilde{\chi}_2^0 + H_1/Z, \widetilde{\chi}_2^0 \to \widetilde{\chi}_1^0 + Y)$. *Right panel:* Leading order cross-section for the process $pp \to \widetilde{\chi}_1^\pm \widetilde{\chi}_3^0/\widetilde{\chi}_4^0 \to (\widetilde{\chi}_1^\pm \to \widetilde{\chi}_2^0 + W^\pm, \widetilde{\chi}_2^0 \to \widetilde{\chi}_1^0 + Y)(\widetilde{\chi}_3^0/\widetilde{\chi}_4^0 \to \widetilde{\chi}_2^0 + H_1/Z, \widetilde{\chi}_2^0 \to \widetilde{\chi}_1^0 + Y) \to 2Y + WH_1/Z + \not{E}_T$ at $\sqrt{s} = 14$ TeV for the allowed parameter space with $\Gamma_{\widetilde{\chi}_2^0} < 10^{-13}$ GeV. Here, Y corresponds to all visible decays of $\widetilde{\chi}_2^0$, *viz.* $Y = b\bar{b}, \tau^\pm\tau^\mp, \ell^\pm\ell^\mp, j\bar{j}$.

decaying candidates. Such typical cascade decay chain can be written as follows,

$$\begin{aligned} pp \to &\widetilde{\chi}_1^\pm \widetilde{\chi}_3^0 + \widetilde{\chi}_1^\pm \widetilde{\chi}_4^0, \\ &\widetilde{\chi}_1^\pm \to \widetilde{\chi}_2^0 + W^\pm, \widetilde{\chi}_2^0 \to \widetilde{\chi}_1^0 + Y, \\ &\widetilde{\chi}_3^0/\widetilde{\chi}_4^0 \to \widetilde{\chi}_2^0 + Z/H_1, \widetilde{\chi}_2^0 \to \widetilde{\chi}_1^0 + Y. \end{aligned} \quad (3.5)$$

where Y represents all possible visible final states produced from the decay of $\widetilde{\chi}_2^0$ i.e $Y = b\bar{b}, \tau^\pm\tau^\mp, \ell^\pm\ell^\mp, j\bar{j}$. Since the $\widetilde{\chi}_2^0$ is long-lived, the final states contain displaced jets or leptons along with $W + Z/H_1 + \not{E}_T$. Henceforth, we refer to all possible visible decay modes of $\widetilde{\chi}_2^0$ as Y. For illustration, we show a typical leading order (LO) Feynman diagram in Fig. 3.7 (left).

The direct production of a chargino-neutralino pair is a pure electroweak process and is controlled by the $W^\pm \widetilde{\chi}_i^\pm \widetilde{\chi}_j^0$ coupling. We obtain the production cross-sections $\sigma(pp \to \widetilde{\chi}_1^\pm \widetilde{\chi}_3^0 + \widetilde{\chi}_1^\pm \widetilde{\chi}_4^0)$ for configurations of our interest by rescaling the NLO MSSM production cross-sections computed using `Prospino` [368] for a pure higgsino-like $\widetilde{\chi}_i^\pm \widetilde{\chi}_j^0$ by the respective reduced squared $W^\pm \widetilde{\chi}_i^\pm \widetilde{\chi}_j^0$ coupling [2]. The reduced squared coupling has the following

---

[2]The multiplicative factor corrects for any electroweakino admixture contributes to the desired production mode.

form,

$$C^2_{W\widetilde{\chi}^\pm_1 \widetilde{\chi}^0_j}\Big|_{j=3,4} = \left\{ \left(N_{j3}V_{12} - \sqrt{2}\,N_{j2}V_{11} \right)^2 + \left(N_{j4}U_{12} + \sqrt{2}\,N_{j2}U_{11} \right)^2 \right\}. \tag{3.6}$$

Here, $N_{j3/j4}$ represents the higgsino component while N_{j2} denotes the wino component in the jth neutralino. The higgsino and wino admixtures in $\widetilde{\chi}^\pm_1$ are represented by V_{12}/U_{12} and V_{11}/U_{11}, respectively. The NMSSM parameter space considered in the present study characterizes a dominant higgsino composition in $\widetilde{\chi}^0_3/\widetilde{\chi}^0_4$ and $\widetilde{\chi}^\pm_1$. Correspondingly, both $N^2_{33} + N^2_{34}$ and $N^2_{43} + N^2_{44} \sim 1$. Similarly, U_{12} and V_{12} are ~ 1. On the other hand, N_{32}, N_{42}, V_{11} and U_{11} are $\ll 1$. Therefore, from Eq. (3.6) $(N_{j3}V_{12})^2$ and $(N_{j4}U_{12})^2$ are the only relevant terms to compute $\sigma(pp \to \widetilde{\chi}^\pm_1 \widetilde{\chi}^0_3 + \widetilde{\chi}^\pm_1 \widetilde{\chi}^0_4)$. The scaled production cross-section is then multiplied by the relevant branching ratios for $\widetilde{\chi}^0_2$, H_1/Z and $W^\pm$. In Fig. 3.7 (right), for all the allowed points featuring a long-lived $\widetilde{\chi}^0_2$ (Fig. 3.5, pink points) we present cross-section $(\sigma(pp \to \widetilde{\chi}^\pm_1 \widetilde{\chi}^0_3 + \widetilde{\chi}^\pm_1 \widetilde{\chi}^0_4) \times Br(\widetilde{\chi}^\pm_1 \to \widetilde{\chi}^0_2 + W^\pm, \widetilde{\chi}^0_2 \to \widetilde{\chi}^0_1 + Y) \times Br(\widetilde{\chi}^0_3/\widetilde{\chi}^0_4 \to \widetilde{\chi}^0_2 + H_1/Z, \widetilde{\chi}^0_2 \to \widetilde{\chi}^0_1 + Y))$ at $\sqrt{s} = 14$ TeV as a function of $m_{\widetilde{\chi}^0_3}$. This cross-section of the entire cascade chain can be as large as $\mathcal{O}(1)$ fb and $\mathcal{O}(0.1)$ fb at $m_{\widetilde{\chi}^0_3} \sim 500$ GeV and ~ 1 TeV, respectively. Considering the large production rates at the HL-LHC, we perform a detailed collider study to explore the projected sensitivity for some benchmark scenarios selected from the allowed parameter space. We focus on direct electroweakino production with the final state containing $WZ/H_1 + \not{E}_T$ + displaced objects. Before moving to a discussion of the details of the collider analysis, let us examine some generic features of long-lived particles that are relevant to the present study.

3.4.2 Kinematic features of LLP decays

In Fig. 3.8 (left), we illustrate allowed parameter space with $\Gamma_{\widetilde{\chi}^0_2} \leq 10^{-13}$ GeV (Fig. 3.5, pink points) in the plane of mean proper decay length, $c\tau^0_{\widetilde{\chi}^0_2}$ vs. mass of the LLP $\widetilde{\chi}^0_2$. Here, $\tau_{\widetilde{\chi}^0_2}$ represents the mean proper lifetime of $\widetilde{\chi}^0_2$, and c is the speed of light. For convenience, we refer to the mean proper decay lifetime (τ^0) as just "lifetime" and the mean proper decay length ($c\tau^0$) as "decay length" unless stated otherwise. The decay length for $\widetilde{\chi}^0_2$ is relatively large, $c\tau^0_{\widetilde{\chi}^0_2} \gtrsim 10$ cm, for a considerable fraction of the allowed parameter space. The decay length of $\widetilde{\chi}^0_2$ in the laboratory frame is given by

$$l_{\widetilde{\chi}^0_2} = \beta\gamma c\tau^0_{\widetilde{\chi}^0_2} \tag{3.7}$$
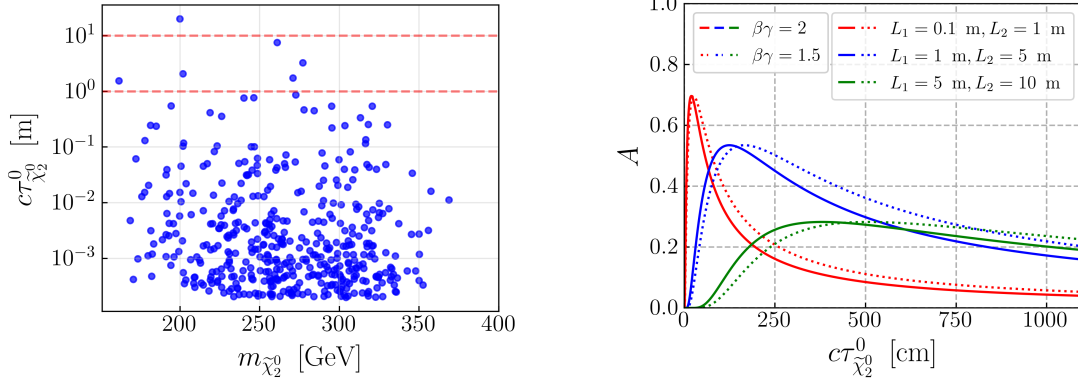
Figure 3.8: *Left panel:* Decay length of the LLP as a function of its mass. The top and bottom red horizontal lines correspond to a decay length of 10 m and 1 m, respectively. This shows that the SM decay products of LLP can reach ECAL and can also traverse a few meters in HCAL. For lengths $\geq \mathcal{O}(10)$ m, they can even reach the muon-detectors. *Right panel:* Acceptance probability of an LLP with constant boost, A in Eq. (3.11) vs. decay length of that LLP $\widetilde{\chi}_2^0$, $c\tau_{\widetilde{\chi}_2^0}$ for three choices of $\{L_1, L_2\}$: $\{0.1$ m, 1 m$\}$, $\{1$ m, 5 m$\}$, and $\{5$ m, 10 m$\}$, assuming a hypothetical scenario with $\beta\gamma = 2$ and 1.5. Here, L_1 and L_2 are the inner and outer radii of the LLP sensitive detector volume.

where $\gamma = (1 - \beta^2)^{-1/2}$ is the relativistic factor, $\beta = |\vec{p}|/E = v/c$ is the boost, v is the velocity, E is the energy and $|\vec{p}|$ is the momentum of the particle in the laboratory frame. The acceptance probability of a single LLP $\widetilde{\chi}_2^0$ decaying within distance $L_1 < L < L_2$ inside the detector can be then expressed as,

$$\mathcal{P}_1(L_1, L2, \sqrt{s}) \simeq \int db\, f(\sqrt{s}, b) \left[\exp\left(\frac{-L_1}{bc\tau_{\widetilde{\chi}_2^0}} \right) - \exp\left(\frac{-L_2}{bc\tau_{\widetilde{\chi}_2^0}} \right) \right], \qquad (3.8)$$

where $b = \beta\gamma$, $f(\sqrt{s}, b)$ is the probability density function of b, L_1 and L_2 are the inner and outer radii of the detector volume that are sensitive to the LLP decay. The signal considered in the present analysis involves the decay of two long-lived $\widetilde{\chi}_2^0$'s. The probability that one

decay within (L_1, L_2) and other within (L_3, L_4) is given by [369]

$$\mathcal{P}_2(L_1, L_2, L_3, L_4, \sqrt{s}) = 2 \int db_1 db_2 \ f(\sqrt{s}, b_1, b_2) \left[\exp\left(\frac{-L_1}{b_1 c\tau^0_{\widetilde{\chi}^0_2}}\right) - \exp\left(\frac{-L_2}{b_1 c\tau^0_{\widetilde{\chi}^0_2}}\right) \right]$$
$$\left[\exp\left(\frac{-L_3}{b_2 c\tau^0_{\widetilde{\chi}^0_2}}\right) - \exp\left(\frac{-L_4}{b_2 c\tau^0_{\widetilde{\chi}^0_2}}\right) \right] \tag{3.9}$$

Correspondingly, the number of observed LLP decays is given by,

$$N_{LLP} = \mathcal{L} \times \sigma_{\text{signal}} \times BR^n \times \mathcal{P}_n \times \epsilon^n_{\text{reco}}, \tag{3.10}$$

where n is the number of LLPs in the decay chain, $\mathcal{P}_n$ represents their decay probability, as given in Eq. (3.8) for one DSV and Eq. (3.9) in case of two DSVs. $\mathcal{L}$ represents the integrated luminosity, $\sigma_{signal} \times BR^n$ refers to the event rate and ϵ^n_{reco} corresponds to the signal efficiency. To have an idea of what detector volume is optimal for a given decay length, we consider a hypothetical scenario by setting the boost factor, b, to a constant value. Eq. (3.8) with constant b reduces to

$$A = \mathcal{P}|_{b=\text{const.}} \simeq exp(-L_1/bc\tau^0_{\widetilde{\chi}^0_2}) - exp(-L_2/bc\tau^0_{\widetilde{\chi}^0_2}) \tag{3.11}$$

We illustrate the variation of acceptance probability (A) with $c\tau^0_{\widetilde{\chi}^0_2}$ in Fig. 3.8 (right), for three different choices of $\{L_1, L_2\}$: $\{0.1 \, \text{m}, 1 \, \text{m}\}$, $\{1 \, \text{m}, 5 \, \text{m}\}$, and $\{5 \, \text{m}, 10 \, \text{m}\}$, assuming a constant $\beta\gamma = 2$ and 1.5. For $\{L_1 = 0.1 \, \text{m}, L_2 = 1 \, \text{m}\}$, the highest acceptance probability is observed for $c\tau^0_{\widetilde{\chi}^0_2} \sim 20$ cm. Keeping this in mind, in the analysis, we restrict the choice of decay lengths of the LLP up to $\mathcal{O}(10^1)$ cm for the benchmark points as discussed below.

The momentum resolution at the tracker is better than the energy resolution at the calorimeters for charged tracks [259]. Hence, the tracker enables more efficient identification of the charged tracks from LLP decays and reconstruction of the displaced secondary vertex (DSV). Keeping this in mind, in the present work, we restrict our analysis to the tracker region using single/di-lepton triggers and missing energy. In both CMS and ATLAS detectors, the tracker region extends to a radius of $L_2/L_4 \sim 1$ m. Therefore, we consider only such signal benchmark points where the decay length of $\widetilde{\chi}^0_2$, $c\tau^0_{\widetilde{\chi}^0_2} \lesssim 1$ m, such that the majority of $\widetilde{\chi}^0_2$ decays occur inside the tracker region (c.f. Fig. 3.8 (right)). Considering these observations, we identify 3 benchmark points with $\Gamma_{\widetilde{\chi}^0_2}(\text{in GeV}) \sim 10^{-14}$ (BP1), $\sim 10^{-15}$ (BP2) and $\sim 10^{-16}$ (BP3). In Table 3.1, we present the input parameters, along with masses, decay
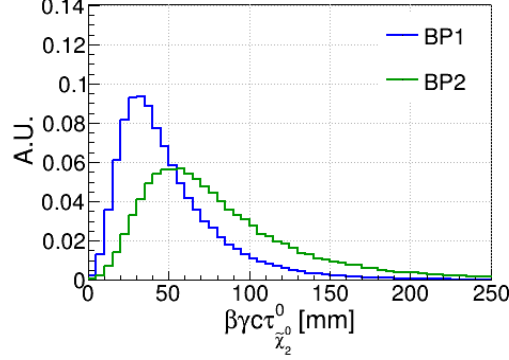
Figure 3.9: Distributions for decay length of one of the LLPs $\widetilde{\chi}_2^0$ produced via $pp \to (\widetilde{\chi}_3^0 \to \widetilde{\chi}_2^0 h)\widetilde{\chi}_1^\pm$ at $\sqrt{s} = 14$ TeV for signal benchmark BP1$\{m_{\widetilde{\chi}_3^0} = 760$ GeV$, m_{\widetilde{\chi}_2^0} = 217$ GeV$, c\tau_{\widetilde{\chi}_2^0} = 17.5$ mm$\}$ and BP2$\{m_{\widetilde{\chi}_3^0} = 791$ GeV$, m_{\widetilde{\chi}_2^0} = 193$ GeV$, c\tau_{\widetilde{\chi}_2^0} = 26$ mm$\}$ are shown as blue and green solid lines, respectively.

widths, and branching rates of the relevant electroweakinos and Higgs bosons for BP1, BP2, and BP3.

It is worth noting that the $\widetilde{\chi}_2^0$'s in our signal benchmarks can undergo decays in different segments of the detector depending on the boost (β) and decay length ($\tau_{\widetilde{\chi}_2^0}$) where the latter is inversely correlated to $\Gamma_{\widetilde{\chi}_2^0}$. For illustration, we present the distributions for $l_{\widetilde{\chi}_2^0}$, where $\widetilde{\chi}_2^0$ is produced via $pp \to (\widetilde{\chi}_3^0 \to \widetilde{\chi}_2^0 H_1)\widetilde{\chi}_1^\pm$, for BP1 (blue solid) and BP2 (green solid), in Fig. 3.9. These benchmarks have $c\tau_{\widetilde{\chi}_2^0} = 17.5$ mm (BP1) and 26 mm (BP2), respectively, thereby furnishing a relatively large acceptance probability in the tracker volume. We would like to note that particles with larger decay lengths can also undergo decay within the tracker region. However, the fraction of such decays would be small and warrant a separate study of its own (c.f. [370]), which is beyond the scope of the present work.

As discussed previously, the decay of $\widetilde{\chi}_2^0$ to visible final states within the tracker region leads to charged tracks that originate from displaced secondary vertex (DSV) corresponding to the LLP $\widetilde{\chi}_2^0$. An important parameter relevant for the reconstruction of DSV is the transverse impact parameter $|d_0|$,

$$|d_0| = \frac{\left|x_d^{track}p_y^{track} - y_d^{track}p_x^{track}\right|}{p_T^{track}}, \tag{3.12}$$

where, $\{x_d^{track}, y_d^{track}\}$ are the track coordinates in the transverse plane passing through the

primary interaction vertex (PIV), p_x^{track} and p_y^{track} are the x- and y-components of the track momentum and $p_T^{track} = \sqrt{p_x^{track\,2} + p_y^{track\,2}}$. In the present scenario, the displaced charged tracks from $\widetilde{\chi}_2^0$ decays in BP1, BP2 and BP3 can feature a typically large $|d_0| \gtrsim \mathcal{O}(1)$ cm, which is indicative of a DSV.

Note that the analysis strategy considered in this work requires separate tackling of the prompt and long-lived objects. Motivated by studies from the ATLAS and CMS collaboration in Refs. [371, 372], we consider final state objects with transverse impact parameter $d_0 \gtrsim 2$ mm to be long-lived while those with $d_0 \lesssim 2$ mm as prompt.

3.4.3 Benchmark points and analysis setup

Having discussed the generic features of the LLP $\widetilde{\chi}_2^0$ in a collider environment, we will move on to study the projected capability of the HL-LHC to probe the NMSSM parameter space of interest through LLP searches in direct electroweakino production of Eq. (3.5). As discussed previously, to this end, we perform a detailed collider study of three different benchmark points BP1, BP2, and BP3 (Table 3.1), chosen from the current allowed parameter space. We use PYTHIA8 [373, 374] to simulate the signal process in Eq. (3.5). The signal process is mediated through a promptly decaying WZ/WH_1 in addition to the late decaying $\widetilde{\chi}_2^0$'s, leading to a variety of prompt SM objects in the final state, which could be potentially triggered upon. The list of dominant backgrounds would vary according to the trigger choice. The different viable triggers and the associated backgrounds will be discussed in detail in Sec. 3.4.5. We use the Madgraph5-aMC@NLO-2.7.3 [256] framework to simulate the background events at the parton-level, with subsequent showering and hadronization being performed using PYTHIA8. The HL-LHC detector response is simulated using Delphes-3.5.0 [259] using the default HL-LHC detector card [375].

As our analysis relies on tracks originating from the LLP, we do not cluster jets but rather use Delphes collections both for generator and reconstructed level objects within our analysis. We separate out the prompt objects like leptons, which are primarily used for event selection. The main analysis deals with displaced 'particle-flow' tracks. The generator-level charged particles, estimated with a good resolution, have a finite probability of being reconstructed as tracks. We have checked that there is no overlap between reconstructed leptons and displaced tracks with $|\eta| < 4$ and $p_T > 10$ GeV in our analysis. At the stage of particle propagation, only smearing on the norm of the transverse momentum vector is applied, as-

suming a perfect angular resolution on tracks. In the mentioned updated Delphes module, a dedicated filter is used [376] to enhance the tracking performance along with momentum resolution. This tackles inefficiencies in boosted, dense environments. We would like to note that displaced vertex selection efficiencies for HL-LHC are not available yet and, hence, could not be applied to our analysis. Therefore, our results are optimistic estimates and should be treated as such.

	BP1	BP2	BP3
λ	5.15×10^{-3}	5.85×10^{-3}	1.67×10^{-4}
κ	6.12×10^{-4}	5.854×10^{-4}	2.07×10^{-5}
A_λ [GeV]	5279	2110	9705
A_κ [GeV]	-32	-510	-21
μ [GeV]	743.05	775.05	688.05
$\tan\beta$	25.098	36.32	44.67
M_1 [GeV]	218.39	194.4	238.8
M_2 [GeV]	3909	3709	2789
M_3 [GeV]	4219	4371	5465
$m_{\widetilde{\chi}_1^0}$ [GeV]	180.17	158.08	173.76
$m_{\widetilde{\chi}_2^0}$ [GeV]	216.76	193.00	236.93
$m_{\widetilde{\chi}_3^0}$ [GeV]	759.62	790.67	703.55
$m_{\widetilde{\chi}_4^0}$ [GeV]	760.42	791.80	704.94
$m_{\widetilde{\chi}_1^\pm}$ [GeV]	758.43	789.72	702.37
m_{H_1} [GeV]	126.31	122.52	124.54
m_{H_2} [GeV]	168.43	143.11	164.7
m_{A_1} [GeV]	92.0	108.90	73.19
$\Gamma_{\widetilde{\chi}_2^0}$ [GeV]	1.11×10^{-14}	7.69×10^{-15}	3.85×10^{-16}
$\Gamma_{\widetilde{\chi}_3^0}$ [GeV]	0.4847	0.5002	0.4367
$\Gamma_{\widetilde{\chi}_4^0}$ [GeV]	0.4571	0.4755	0.4088
σ_{NLO} [fb]	1.56	1.15	2.15
$\mathrm{BR}(\widetilde{\chi}_2^0 \to \widetilde{\chi}_1^0 b\bar{b})$	0.528	0.63	0.34
$\mathrm{BR}(\widetilde{\chi}_2^0 \to \widetilde{\chi}_1^0 j\bar{j})$	0.1834	0.074	0.3602
$\mathrm{BR}(\widetilde{\chi}_2^0 \to \widetilde{\chi}_1^0 \tau^+\tau^-)$	0.12	0.177	0.0969
$\mathrm{BR}(\widetilde{\chi}_2^0 \to \widetilde{\chi}_1^0 \lambda^+\lambda^-)$	0.085	0.014	0.176
$\mathrm{BR}(\widetilde{\chi}_3^0 \to \widetilde{\chi}_2^0 H_1)$	0.79	0.704	0.816
$\mathrm{BR}(\widetilde{\chi}_3^0 \to \widetilde{\chi}_2^0 Z)$	0.204	0.24	0.184
$\mathrm{BR}(\widetilde{\chi}_4^0 \to \widetilde{\chi}_2^0 Z)$	0.7834	0.74	0.811
$\mathrm{BR}(\widetilde{\chi}_4^0 \to \widetilde{\chi}_2^0 H_1)$	0.215	0.24	0.189
$\mathrm{BR}(\widetilde{\chi}_1^\mp \to \widetilde{\chi}_2^0 W)$	0.994	0.995	0.999

Table 3.1: The input parameters, Higgs boson and electroweakino mass spectrum, branching ratios of electroweakinos, decay width and decay length of the LLP $\widetilde{\chi}_2^0$, and the production cross-section for the process $pp \to \widetilde{\chi}_3^0 \widetilde{\chi}_1^\pm + \widetilde{\chi}_4^0 \widetilde{\chi}_1^\pm$ at $\sqrt{s} = 14$ TeV, for BP1, BP2, and BP3.

3.4.4 Sensitivity from displaced vertex searches at the LHC

Several searches for long-lived particles with displaced vertices have been performed in the literature. For example, in Refs. [377,378], searches are performed for long-lived particles decaying into displaced jets plus missing energy. Both analyses consider gauge-mediated supersymmetry breaking (GMSB) scenario with long-lived gluinos ($\tilde{g}$), focusing on the $pp \rightarrow \tilde{g}\tilde{g} \rightarrow \cancel{E}_{\mathrm{T}} + \mathrm{jets}$ channel, requiring one or more displaced jets and missing transverse energy in the final state. The decay topology considered in Ref. [378] can be realized in the parameter space of our interest in all electroweakino pair production modes with at least one $\tilde{\chi}_2^0$ in the cascade decay chain, $pp \rightarrow \tilde{\chi}_i^0 \tilde{\chi}_j^0 / \tilde{\chi}_1^\pm \tilde{\chi}_i^0 \rightarrow \geq 1 \; \tilde{\chi}_2^0 + X + \cancel{E}_{\mathrm{T}} \; (i = \{2,3,4\}, j = \{1,i\}$ and X represents other promptly decaying candidates in the decay chain), provided one or more $\tilde{\chi}_2^0$ decays into the hadronic final state resulting in displaced jets plus missing energy. Let's examine the case of BP3 where $\tilde{\chi}_2^0$ has the largest proper decay length among the three representative benchmarks (see Table 3.1) and closest to the decay lengths considered in the above reference. For BP3 ($m_{\tilde{\chi}_2^0} = 237$ GeV), the production rate in the channel containing at least one displaced jet and $\cancel{E}_{\mathrm{T}}$ is ~ 1.435 fb at $\sqrt{s} = 13$ TeV. Adopting the analysis strategy from Ref. [378], we require the signal events to satisfy: a) $\cancel{E}_{\mathrm{T}} > 300$ GeV, and b) at least one displaced vertex with an invariant mass of ≥ 10 GeV. Only 3% of signal events satisfy the aforementioned cuts, resulting in an effective signal production rate of $\sigma_{BP3}^{\mathrm{eff.}} = 1.435 \, \mathrm{fb} \times 3\% = 0.04 \, \mathrm{fb}$. The search in Ref. [378] excludes gluinos up to $m_{\tilde{g}} \sim 2.1$ TeV with proper decay length between 0.3 m and 30 m. The most stringent upper limit on the long-lived gluino pair production cross-section times efficiency from this search is ~ 0.09 fb at 95% CL for $m_{\tilde{g}} = 2.4$ TeV given the proper decay length is roughly 1 m. Similarly, the search in Ref. [377] has excluded $\sigma(pp \rightarrow \tilde{g}\tilde{g})$ up to ~ 0.2 fb for $m_{\tilde{g}} = 1.4$ and 2 TeV, at 95% CL, with the best signal efficiency for a proper decay length of 1 m. These upper limits could be conservatively extended to smaller masses of long-lived particles. In the case of BP3, despite a smaller mass of the long-lived candidate, the production rate times signal efficiency is several factors below the current upper limit in Refs. [377,378].

It is also worth noting that extrapolating the reach of long-lived searches to the HL-LHC presents additional complexities due to challenges in devising efficient triggers for the online level (L1) and High-Level trigger (HLT) amidst the high pile-up environment. Though there are not many detailed studies for dedicated LLP triggers at HL-LHC [379], CMS has explored two L1 triggers; including tracking information upto $|d_0| = 8$ cm and ECAL barrel timing [380]. For a lighter LLP and hence with less energetic hadronic decay products, these

additional advancements become more useful. Applications of these triggers in different LLP models are still developing for both L1 and the HLT [379, 381] at the HL-LHC. We opt for a standard L1 trigger, like the single lepton, in our analysis because of the advantages of similar thresholds at the L1 trigger and the HLT, inclusiveness, and less susceptibility to pile-up effects. We discuss this in detail in Sec 3.4.5.

ATLAS and CMS collaborations have also searched for exotic decays of the Higgs boson to long-lived neutral scalars (S) in the Higgs-strahlung channel, for $m_S < m_h/2$ [382, 383]. The production process is $pp \to ZH \to (Z \to \ell^+\ell^-)(H \to SS \to b\bar{b}b\bar{b})$ [382] and $pp \to ZH \to (Z \to \ell^+\ell^-)(H \to SS \to 4j)$ [383]. We will mainly discuss the analysis strategy in Ref. [382] in the present discussion. Event selection requires the same flavor opposite sign (SFOS) lepton pair from Z boson and multi-jets from resonant Higgs decay. Ref. [382] requires at least two tracks associated with the displaced vertex, and a lower bound is imposed on the reduced mass $m/\Delta R_{\max} > 3$ GeV of the displaced vertex in order to veto the displaced vertices resulting from the random crossing of unrelated tracks. Here, m is the reconstructed invariant mass of the vertex ($\sim m_S$), and $\Delta R_{\max}$ is the maximum ΔR separation between the track momentum and the combined momentum of other tracks associated with the displaced vertex. Within the parameter space of our interest, and considering the LLP signal process considered in our work, m could be roughly approximated to $m_{\widetilde{\chi}_2^0} - m_{\widetilde{\chi}_1^0} \sim [25, m_Z]$ GeV, which overlaps with the region of m probed in Ref. [382]. However, for m_S much larger than $2m_b$, the tracks associated with the displaced vertex corresponding to $S \to b\bar{b}$ decay would be collimated, leading to smaller $\Delta R_{\max}$. On the other hand, $\Delta R_{\max}$ would be relatively larger when the long-lived candidate $\widetilde{\chi}_2^0$ undergoes $3-$body decay while also involving a missing particle, resulting in smaller reduced masses, which may not pass the selection cut considered in Ref. [382]. We note that the Ref. [382] excludes $\sigma(pp \to ZH) \times \mathrm{BR}(H \to SS)$ up to ~ 40 fb at 95% CL at the $\sqrt{s} = 13$ TeV LHC with $\mathcal{L} = 139$ fb^{-1} from searches in the SFOS dilepton plus at least two displaced b jets. A similar final state could be realized in the parameter space of our interest via the processes $pp \to \widetilde{\chi}_1^\pm \widetilde{\chi}_3^0/\widetilde{\chi}_4^0 \to (\widetilde{\chi}_1^\pm \to \widetilde{\chi}_2^0 + W^\pm, \widetilde{\chi}_2^0 \to \widetilde{\chi}_1^0 + b\bar{b})(\widetilde{\chi}_3^0/\widetilde{\chi}_4^0 \to \widetilde{\chi}_2^0 + Z, \widetilde{\chi}_2^0 \to \widetilde{\chi}_1^0 + b\bar{b}/jj)$ with Z decaying via leptonic modes, and W decaying hadronically. For BP1, the production rate for $pp \to \widetilde{\chi}_1^\pm \widetilde{\chi}_3^0/\widetilde{\chi}_4^0 \to (\widetilde{\chi}_1^\pm \to \widetilde{\chi}_2^0 + W^\pm)(\widetilde{\chi}_3^0/\widetilde{\chi}_4^0 \to \widetilde{\chi}_2^0 + Z)$ at $\sqrt{s} = 13$ TeV is 0.616 fb, which is more than an order of magnitude smaller than the current upper limits in Refs. [382, 383], thus, escaping these constraints.

Searches have also been performed in multi-jet final states [384], which could arise from

pair-produced gluinos or neutralinos in the R-parity violating SUSY scenario. The search in Ref. [384] triggers on high values of H_T ($H_T > 1050$ GeV), where H_T is the scalar p_T sum of the final state jets. The LLP signal realized within the parameter space of our interest comprises two $\widetilde{\chi}_1^0$'s, which results in missing energy signatures, with mass $\gtrsim 100$ GeV. The H_T distribution for the LLP signal for our benchmark points typically peaks at lower values. Correspondingly, the signal efficiency in the signal region considered in Ref. [384] is smaller, leading to weaker constraints. The above discussion suggests the need for designing a strategy optimized for the final state of our interest. We will detail it in the following.

3.4.5 Signal trigger and background

Before moving on to discuss the strategy to reconstruct the DSV's associated with $\widetilde{\chi}_2^0$, let us examine the prompt components in the signal process. The WZ/WH_1 pair produced through $pp \to (\widetilde{\chi}_1^\pm \to W^\pm \widetilde{\chi}_2^0)(\widetilde{\chi}_3^0/\widetilde{\chi}_4^0 \to Z/H_1 \widetilde{\chi}_2^0)$ decay promptly and can lead to various different SM final states which could be triggered upon. In Fig. 3.10, we present the multiplicity n_ℓ of isolated prompt leptons ℓ ($= e, \mu$) that can originate from the decay of WZ/WH_1 pair in the signal process in Eq. (3.5) at truth level (red, dotted line) and detector level (solid blue line). At the detector level, an isolated lepton is required to satisfy,

$$I(P) = \frac{\sum\limits_{i \neq l} p_{\mathrm{T}}(i)^{\Delta R < 0.3}}{p_{T,l}} < 0.1, \quad l = e, \mu \tag{3.13}$$

where, $\sum\limits_{i \neq l} p_{\mathrm{T}}(i)^{\Delta R < 0.3}$ represents the sum of transverse momenta of all objects (excluding the lepton candidate) with $p_T > 2$ GeV within a cone of radius $\Delta R < 0.3$ centred around the candidate lepton, $\Delta R = \sqrt{\Delta \eta^2 + \Delta \phi^2}$ where $\Delta \eta$ and $\Delta \phi$ are the pseudorapidity and azimuthal angle differences and $p_{T,l}$ is the transverse momentum of the candidate lepton. We would like to note that these isolated leptons are also required to satisfy $d_0 < 2$ mm.

The single prompt lepton final state in Fig. 3.10 can originate when the W decays leptonically, $W \to \ell' \nu$ ($\ell' = e, \mu, \tau$) while the Z/H_1 decays hadronically. Similarly, the final state with two prompt leptons can arise when W decays hadronically ($W \to jj$) while the Z/H_1 decays via leptonic modes. The scenario with $n_\ell = 3$ can arise when (a) $W \to \ell' \nu, Z \to \ell' \ell'$ (b) $W \to \ell' \nu, H_1 \to \ell' \ell'$ (c) $W \to \ell' \nu, H_1 \to (W \to \ell' \nu)(W^* \to \ell' \nu)$ (d) $W \to \ell' \nu, H_1 \to (Z \to \ell' \ell')(Z^* \to jj)$ etc. Accordingly, we consider two different analysis categories corresponding to different signal triggers, $n_\ell = 1$ and $n_\ell = 2$. The $n_\ell = 3$
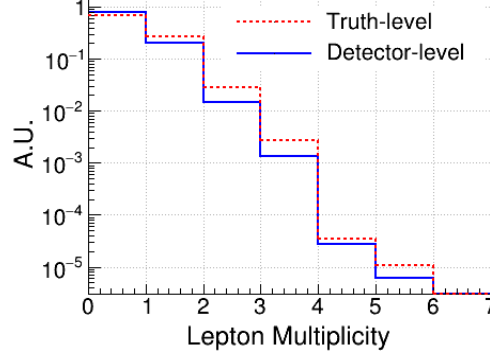
Figure 3.10: Distribution for lepton multiplicity n_ℓ ($\ell = e, \mu$) from promptly decaying WZ/WH_1 pair produced in the process $pp \to (\widetilde{\chi}_1^\pm \to W^\pm \widetilde{\chi}_2^0)(\widetilde{\chi}_3^0/\widetilde{\chi}_4^0 \to Z/H_1 \widetilde{\chi}_2^0)$ at the HL-LHC. The truth level and detector level distributions are shown in solid red and solid blue, respectively.

signal category is ignored due to smaller production rates relative to the other two. For $n_\ell = 1$, we require the isolated prompt lepton to satisfy $p_{T,\ell} > 30$ GeV. Recall that the signal final state contains two long-lived $\widetilde{\chi}_2^0$. Therefore, in addition to prompt leptons, we will have displaced objects ($b\bar{b}, \tau^\pm \tau^\mp, \ell^\pm \ell^\mp, j\bar{j}$) + $\not{E}_T$. The dominant backgrounds in this signal category are semileptonic $t\bar{t}$ and W + jets. In the $n_\ell = 2$ signal category, we impose $p_{T,\ell_1} > 30$ GeV and $p_{T,\ell_2} > 20$ GeV where $p_{T,\ell_1} > p_{T,\ell_2}$. The dominant backgrounds are dileptonic $t\bar{t}$ and $2\ell + jets$, where $jets$ mainly include b and c jets. We also require the isolated leptons to lie within $|\eta| < 4.0$ and impose a lower threshold on the missing transverse energy $\not{E}_T > 50$ GeV at the event selection stage. In principle, a stricter cut on the $\not{E}_T$ can be imposed, the implications of which we have discussed later in Sec. 3.4.7. Alternatively, jet triggers can be used instead of lepton triggers since the WZ/WH_1 pair in the signal can predominantly decay via hadronic modes. Choosing an optimized event triggering criteria for the online trigger systems viz the Level-1 (L1) trigger and the HLT is among the most critical steps in any analysis (c.f. Refs. [379, 381] and references therein). The choice of efficient triggers is more pertinent for the L1 to ensure that the events of interest (viz the LLPs in the present analysis) are not lost forever. The event selection rates at the HLT are, on average, an order of magnitude smaller than at the L1 system. Therefore, typically stronger thresholds are applied to the HLT system to ensure consistent event rates. In this regard,

triggering on leptons is advantageous due to similar thresholds at the L1 trigger and the HLT, inclusiveness, and less susceptibility to pile-up effects. For the case of a single isolated muon (electron), the values of L1 trigger seed of $p_T > 22$ GeV (28 GeV) and $|\eta| < 2.4$, are pretty similar to the threshold at the HLT viz. $p_T > 24$ GeV (32 GeV) [385, 386]. On the other hand, HLT thresholds on p_T and the sum of transverse momenta H_T for the jet(s) are harder compared to their L1 counterparts. Therefore, jet-triggered events are vulnerable to considerable efficiency loss at the HLT. Furthermore, the jet thresholds are also strongly sensitive to the level of pile-up, and the high pile-up environment at the HL-LHC can degrade jet energy resolution leading to depleted trigger efficiencies [385]. Optimal jet trigger rates require the implementation of dedicated pile-up mitigation techniques, which is beyond the scope of our work. Therefore, for simplicity, we adhere to lepton triggers only. The signal triggers and the corresponding selection cuts are summarized in Table 3.2.

Signal triggers	
$|d_0| < 2$ mm	
$n_\ell = 1$	$n_\ell = 2$
$p_{T,\ell_1} > 30$ GeV	$p_{T,\ell_1} > 30$ GeV
	$p_{T,\ell_2} > 20$ GeV
$\displaystyle{\not}E_T > 50$ GeV	

Table 3.2: Summary of signal triggers and the basic selection cuts. These triggers are only applied to prompt objects. Tracks with $|d_0| < 2$ mm are classified within the prompt category.

Besides the SM backgrounds, additional background contributions can arise from instrumental effects, such as hadronic interactions with the detector and misidentification or misreconstruction in tracking to produce high mass DSV with large track multiplicities. The instrumental background effects can be largely mitigated by imposing a lower threshold on the invariant mass of the tracks and requiring a high track multiplicity [377]. It is also worthwhile to note that it is rather challenging to simulate the instrumental background sources and can only be estimated through measured data. Hence, the inclusion of instrumental effects is beyond the scope of quasi-realistic collider studies such as the present analysis. The only exception is the usage of signal regions for which the instrumental effects are estimated by the experimental collaborations. We adopt such a 'realistic' signal region in addition to

other 'optimistic' signal regions (where instrumental background estimations are unavailable) in Sec. 3.4.7.

3.4.6 Reconstructing the displaced secondary vertex from LLP $\widetilde{\chi}_2^0$

As discussed earlier, the cascade decay channel for the directly produced $\widetilde{\chi}_3^0\widetilde{\chi}_1^\pm/\widetilde{\chi}_4^0\widetilde{\chi}_1^\pm$ pair results into two $\widetilde{\chi}_2^0$'s in addition to other prompt SM candidates. The two LLP candidates can, in principle, lead to two displaced secondary vertices. In the signal, the tracks with larger transverse impact parameters are expected to originate from these two displaced secondary vertices. To reconstruct the final DSVs, we retrace the tracks with $d_0 \geq 2\,\mathrm{mm}$.
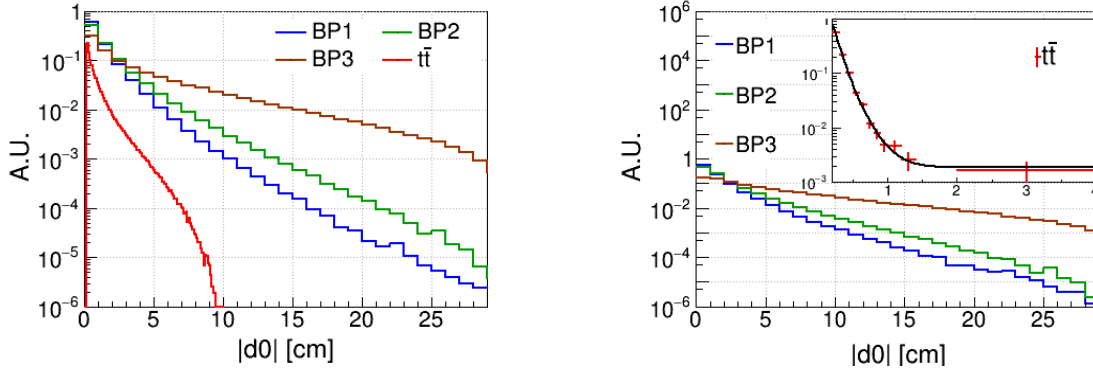
Figure 3.11: Distribution of transverse impact parameter $|d_0|$ for all tracks with $\mathrm{p_T} > 1\,\mathrm{GeV}$ and $|\eta| < 4$ corresponding to BP1 (blue), BP2 (green) and BP3 (brown), at the HL-LHC. *Left panel:* Events pass the trigger choice $n_\ell = 1$. The corresponding distribution for the semileptonic $t\bar{t}$ background is shown in red color. *Right panel:* Events pass the trigger choice $n_\ell = 1$ and have at least one displaced secondary vertex. The distribution for the semileptonic $t\bar{t}$ background is shown in red color in the figure inset.

In Fig. 3.11 (left), we present the distributions for d_0 for the signal benchmarks BP1, BP2, and BP3. Here, we include all tracks with $\mathrm{p_T} > 1\,\mathrm{GeV}$ and $|\eta| < 4.0$ in events that pass the selection cuts corresponding to the signal trigger $n_\ell = 1$. The corresponding distributions for the dominant semileptonic $t\bar{t}$ background are also illustrated in the same figure. We observe from Fig. 3.11 (left) that the tail of the distributions for the signal process shifts to larger $|d_0|$ values with decreasing $\Gamma_{\widetilde{\chi}_2^0}$. For BP3 the fraction of events (n_{frac}) above $|d_0| > 10$ cm, $n_{\mathrm{frac}} \sim 0.02$. In this range of $|d_0|$ the fraction is considerably low for BP1 ($n_{\mathrm{frac}} \sim 0.001$) and

BP2 ($n_{\text{frac}} \sim 0.005$). Interestingly, the $|d_0|$ distributions for the semileptonic $t\bar{t}$ background extends all the way up to $|d_0| \sim 10$ cm. This happens due to long-lived mesons like K_s^0, Λ, D etc. produced from b hadrons. Therefore, it is essential to explore other features of the LLP-specific topology which can reduce the backgrounds. One such entity that is largely exclusive to the phenomenology of long-lived decay is the displaced secondary vertex. As such, our next objective is to reconstruct the secondary vertices associated with the LLP $\widetilde{\chi}_2^0$. We will also explore various observables that are contingent on the reconstructed DSVs, optimizing the selection cuts on them, and revisit the $|d_0|$ distributions afterwards.

In an ideal scenario, tracks that arise from the same secondary vertex are expected to share a common point of origin $\{x_0, y_0, z_0\}$. Correspondingly, we allocate tracks with $d_0 \geq 2$ mm whose point of origin are within $\{|\Delta x| < 1$ mm, $|\Delta y| < 1$ mm, $|\Delta z| < 1$ mm$\}$ of each other, to a reconstructed vertex. Among them, the ones that contain at least 3 tracks are classified as a DSV. Having reconstructed the DSVs, let us revisit the distributions for $|d_0|$. We redraw the distributions for $|d_0|$ in Fig. 3.11 (right), similar to that in Fig. 3.11 (left), except now with only those events which have at least one reconstructed DSV.

Let us also note the following important fact about the $t\bar{t}$ background. Imposing the requirement for a reconstructed DSV leads to a major depletion in the d_0 distributions for the semileptonic $t\bar{t}$ background. It falls sharply before it reaches $|d_0| \sim 2$ cm and suffers from substantial statistical uncertainty in the tail. Therefore, we extrapolate the shape of $|d_0|$ for semileptonic $t\bar{t}$ background using 5M t$\bar{\text{t}}$ events in Fig. 3.11 (right) and is shown by the solid black line. To ensure consistency, we generate additional 6.5 M $t\bar{t}$ events, and the extrapolated function derived in the previous step matches with the $|d_0|$ distributions drawn for this new sample. Note that the long tail for the $|d_0|$ distribution in case of the $t\bar{t}$ background is an artifact of rarity of events with large decay length in SM.

3.4.7 LLP-specific observables at the detector level, cut flow and signal significance

With an enhanced tracking algorithm, ATLAS shows a good reconstruction efficiency even for displaced tracks produced at a large radius within 30 cm from the primary interaction vertex [387]. In order to reconstruct a displaced vertex, first, the tracks from that vertex need to be successfully reconstructed. Tracks originating far from the center of the detector tend to have higher values of d_0. Standard track reconstruction has low efficiency for large d_0 values. In the following, we construct a few variables without solely relying on d_0 to

eliminate the background.
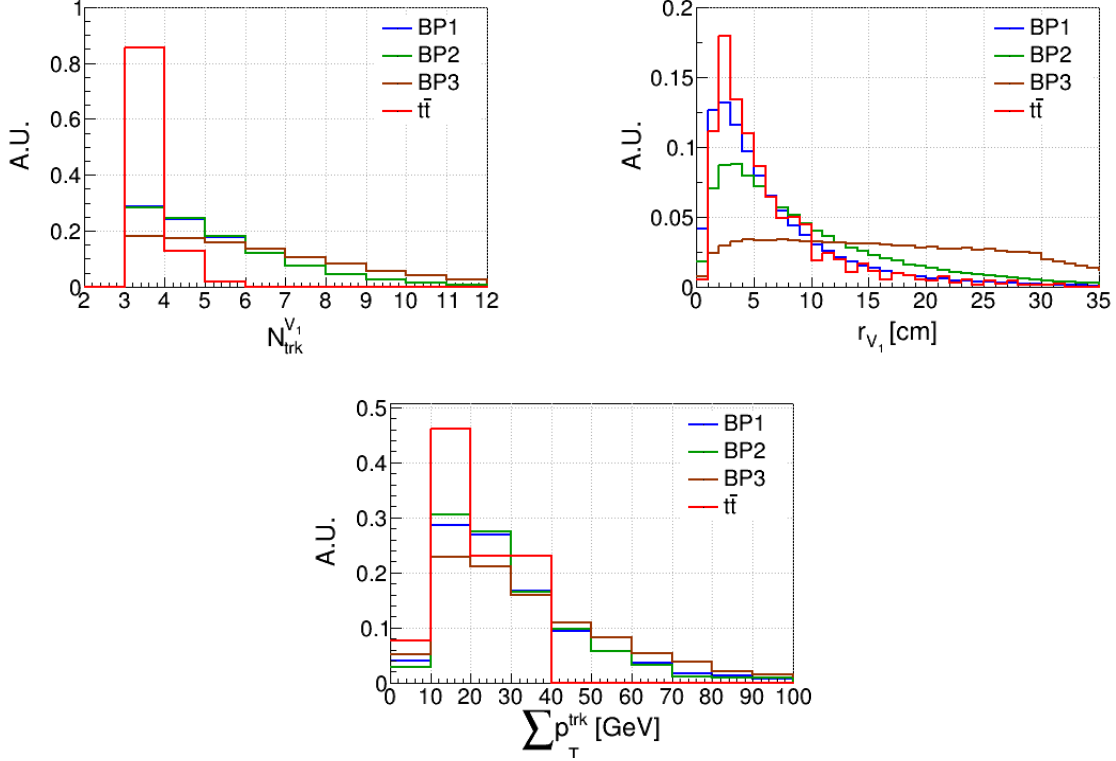
Figure 3.12: Distributions for track multiplicity of DSV V_1, $N_{\mathrm{trk}}^{V_1}$ (upper-left panel), radial distance of V_1 from the primary interaction vertex, r_{V_1} (upper-right panel), and sum of transverse momentum of all tracks in V_1, $\sum \mathrm{p}_{\mathrm{T}}^{\mathrm{trk}}$ (lower panel), in the $pp \to \widetilde{\chi}_1^{\pm} \widetilde{\chi}_3^0 / \widetilde{\chi}_4^0 \to$ $(\widetilde{\chi}_1^{\pm} \to \widetilde{\chi}_2^0 + W^{\pm}, \widetilde{\chi}_2^0 \to \widetilde{\chi}_1^0 + Y)(\widetilde{\chi}_3^0 / \widetilde{\chi}_4^0 \to \widetilde{\chi}_2^0 + Z/H_1, \widetilde{\chi}_2^0 \to \widetilde{\chi}_1^0 + Y)$ channel corresponding to BP1 (blue), BP2 (green) and BP3 (brown) at the HL-LHC. Here Y signifies all possible visible decay modes of $\widetilde{\chi}_2^0$, as mentioned earlier. Distributions for the semileptonic $t\bar{t}$ background are shown in red.

We refer to DSVs with the highest and 2nd highest track multiplicity as V_1 and V_2, respectively. For illustration, we show the track multiplicity of V_1, referred to as $N_{\mathrm{trk}}^{V_1}$, for BP1, BP2, and BP3, in Fig. 3.12 (upper-left). These distributions are presented for the $n_\ell = 1$ signal trigger region, summarized in Table 3.2. We observe that $N_{\mathrm{trk}}^{V_1}$ can reach up to $\sim 5 - 6$ for a considerable fraction of signal events in all three benchmark points. On the other

hand, $N_{\mathrm{trk}}^{V_1}$ reaches only up to ~ 3 in the semileptonic $t\bar{t}$ process, which is the dominant background when the signal trigger is $n_\ell = 1$. Accordingly, we optimize $N_{\mathrm{trk}}^{V_1}$ to improve signal-to-background discrimination. Another parameter of interest is r_{V_1}, which represents the radial distance of V_1 from the PIV. r_{V_1} is computed as $r_{V_1} = \sqrt{X_{V_1}^2 + Y_{V_1}^2 + Z_{V_1}^2}$, where $\{X_{V_1}, Y_{V_1}, Z_{V_1}\}$ are the coordinates of the reconstructed DSV V_1 in a reference frame centered at PIV $= \{0, 0, 0\}$. In Fig. 3.12 (upper-right), we illustrate r_{V_1} for the signal benchmarks and semileptonic $t\bar{t}$ background, considering the $n_\ell = 1$ signal trigger. The radial distance of the DSV from PIV is inversely proportional to the decay width of LLP in addition to the effect of Lorentz factor $\beta\gamma$. This behaviour is illustrated in Fig. 3.12 (upper-right) where the distributions for r_{V_1} get flattened, and the tail shifts to larger values as the decay length of $\widetilde{\chi}_2^0$ are increased. In the case of BP1, where $\Gamma_{\widetilde{\chi}_2^0} \sim 10^{-14}$ GeV, r_{V_1} peaks roughly at 2 cm. As we move to BP2, where $\Gamma_{\widetilde{\chi}_2^0}$ is smaller by an order of magnitude, the peak position shifts noticeably, however, the overall distributions get flatter. At further lower values of $\Gamma_{\widetilde{\chi}_2^0} \sim 10^{-16}$ GeV corresponding to BP3, we observe a considerable alteration in the distribution. The corresponding distribution for the semileptonic $t\bar{t}$ background peaks at a much lower value $r_{V_1} \sim 3$ cm. Overall, this observable demonstrates potential not only as a background discriminator but also as an excellent identifier of variations in the decay width of the LLP. Consequently, we optimize the selection cuts on r_{V_1} such that the signal significance $S/\sqrt{B}$ is maximized, where S and B are the signal and background yields at the HL-LHC. In addition to $N_{\mathrm{trk}}^{V_1}$ and r_{V_1}, we also optimize the selection cut on the sum of transverse momentum of all tracks associated with V_1, represented as $\sum \mathrm{p_T^{trk}}$. We present the distributions for $\sum \mathrm{p_T^{trk}}$ in Fig. 3.12 (bottom). The $\sum \mathrm{p_T^{trk}}$ distributions for both signal and the $t\bar{t}$ background peaks in the same region of 15 GeV, however, the background falls sharply compared to the signal. While the backgrounds become negligible at $\sum \mathrm{p_T^{trk}} \gtrsim 40$ GeV, the signal tail extends far beyond. Correspondingly, we optimize the upper limit on $\sum \mathrm{p_T^{trk}}$ in our cut-based analysis.

We first present the signal and background yields at the HL-LHC in the 1ℓ and 2ℓ signal categories in Table 3.3, considering the selection cuts for the '*Prompt sector*' ($|d_0| < 2$ mm) as discussed in Sec 3.4.5. The S/B ratio, where S and B are the signal and background yields at the HL-LHC, is $\sim \mathcal{O}(10^{-6})$ after the application of prompt category cuts for all signal benchmarks and signal categories. Next, we discuss the implications of different DSV sensitive observables in the '*Displaced sector*' of the analysis where at least one DSV must be reconstructed. We have segregated this displaced sector into three broad regions

		Prompt sector ($|d_0| < 2$ mm)		
		$\left\|d_0^\ell\right\|, \left\|d_Z^\ell\right\|$ < 2 mm	$p_T^{\ell_{1,2}} >$ 30, 20 GeV	$\not{E}_T$ > 50 GeV
1ℓ	BP1	2590	2150	2088
	BP2	2004	1683	1638
	BP3	3646	3073	2975
	$t_h t_\ell$	2.4×10^8	1.6×10^8	1.15×10^8
2ℓ	BP1	399	280	273
	BP2	300	215	210
	BP3	519	379	368
	$t_\ell t_\ell$	6.02×10^7	4.5×10^7	3.5×10^7

Table 3.3: Selection cuts on lepton $\left|d_0^\ell\right|, \left|d_Z^\ell\right|$, p_T (i=1,2) and $\not{E}_T$ for prompt candidates are applied successively. These selection cuts tabulated under the prompt sector are common to all signal regions which are discussed later in each signal category. Signal and background rates are presented for $\sqrt{s} = 14$ TeV LHC assuming $\mathcal{L} = 3000$ fb^{-1}.

based on $|d_0|$. The first signal region SR1 focuses on displaced tracks with $|d_0| \geq 2$ mm. Two additional signal regions are considered where displaced objects are required to satisfy a more stringent $|d_0|$ criteria viz $|d_0| \geq 4$ mm (SR2) and $|d_0| \geq 8$ mm (SR3).

It is worth noting that backgrounds from SM processes are negligible in the displaced vertex searches. It was shown by the LHC collaboration that in this type of analysis, the background contribution is largely instrumental in nature [377,378]. We reiterate that the instrumental backgrounds can only be estimated from measured data. Hence, we first adopt a signal region defined in the ATLAS analysis [177,377] for which the instrumental background has been estimated. We refer to this 'realistic' signal region as SR$_A$. It considers displaced charged tracks with $|d_0| \geq 4$ mm, requires at least one DSV with $N_{trk} \geq 5$ and the invariant mass of the tracks associated with the DSV must be greater than $m_{trk} > 10$ GeV. A considerable fraction of events for our signal benchmarks can pass these thresholds, as shown in Fig. 3.13, where we display the number of signal events for BP1 at the HL-LHC as a function of m_{trk} and N_{trk}. We notice from Fig. 3.13 that ~ 99 signal events pass the selection cuts mentioned above at the HL-LHC for BP1. The ATLAS collaboration has esti-
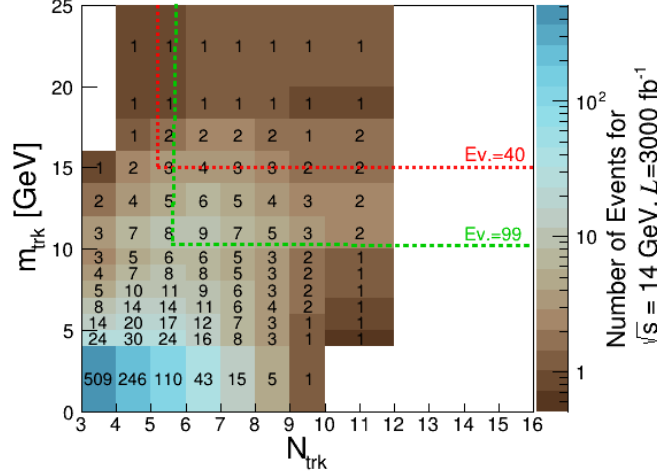
Figure 3.13: Number of signal events at the HL-LHC for the representative benchmark BP1 as a function of the invariant mass of the tracks m_{trk} and the number of tracks N_{trk} for at least one displaced secondary vertex with $|d_0| \geq 4$ mm. The green and red dotted line corresponds to the boundary of $|d_0| \geq 4$ mm, $N_{\text{trk}} \geq 5$ signal region with $m_{\text{trk}} > 10$ and 15 GeV, respectively. The signal yield for both regions is shown for HL-LHC.

mated the instrumental background rate for SR_A to be ~ 5 at the $\sqrt{s} = 13$ TeV LHC with $\mathcal{L} \sim 139$ fb^{-1} [177]. We extrapolate the background estimate B to the HL-LHC through the luminosity scaling and triple the background estimates further to incorporate the effects of high pile up at the HL-LHC, $B \sim 5 \times (3000/139) \times 3.0 \sim 324$. We have shown the signal

	BP1	BP2	BP3
$m_{\geq 5trk} > 10$ GeV, $N_{\text{trk}} \geq 5$ ($\mathcal{L} = 3$ ab^{-1})	99	70	422
SM Background	-	-	-
Instrumental Background ($\mathcal{L} = 139$ fb^{-1})	5	5	5
$\frac{S}{\sqrt{B}}$ ($3 \times$ Ins. BG, $\mathcal{L} = 3$ ab^{-1})	5.5	3.9	23

Table 3.4: Signal rates for region SR_A at HL-LHC are presented. The background is estimated from instrumental effect for this signal region from ATLAS analysis [177]. Signal significance corresponding to three times this background is estimated.

significance computed as $S/\sqrt{B}$ in Table 3.4 for the three benchmark points. With this background estimation, the signal significance for BP1, BP2, and BP3, turns out to be $\sim 5.5,\ 3.9$, and $23\ \sigma$, respectively. Thus, our results indicate that it should be possible to probe the LLP signature from the representative benchmark point BP1 and BP3 at the HL-LHC even after folding in considerations of instrumental backgrounds.

While SR_A considers displaced tracks with $|d_0| > 4$ mm, it is worth exploring other signal regions with different choices for $|d_0|$. For example, the CMS analysis in Ref. [174] considers signal regions with $|d_0| > 2$ mm. In this regard, we consider three different signal regions SR1, SR2 and SR3 with $|d_0| > 2$ mm, $|d_0| > 4$ mm and $|d_0| > 8$ mm, respectively, with optimized selection cuts on $N_{trk}^{V_1}$, $\sum p_T^{trk}$, r_{V_1} and $N_{trk}^{V_2}$ (Number of tracks from vertex V_2). We present the optimized selection cuts in the displaced sector for SR1, SR2 and SR3 for the $n_\ell = 1$ (2) signal category in Table 3.5. The event rates at the HL-LHC for the three signal benchmarks (BP1, BP2, BP3) and the dominant $t\bar{t}$ background are also shown.

| | | SR1 | | | | | SR2 | | SR3 | |
| | | $|d_0| \geq 2$ mm | | | | | $|d_0| \geq 4$ mm | | $|d_0| \geq 8$ mm | |
		N_{trk}^{V1} ≥ 3	N_{trk}^{V1} ≥ 5	$\sum p_T^{trk}$ < 30 GeV	r_{V_1} ≥ 4 cm	N_{trk}^{V2} ≥ 5	N_{trk}^{V1} ≥ 3	N_{trk}^{V1} ≥ 5	N_{trk}^{V1} ≥ 3	N_{trk}^{V1} ≥ 5
1ℓ	$t_h t_\ell$	109453	1937	1210	484	0	2422	0	242	0
	BP1	1348	635	428	226	27	1087	459	741	271
	BP2	1204	569	389	272	38	1047	447	809	301
	BP3	1198	770	430	390	40	1154	723	1078	648
2ℓ	$t_\ell t_\ell$	35712	624	406	281	0	812	0	62	0
	BP1	174	82	55	30	4	140	59	96	35
	BP2	152	71	49	35	5	132	56	102	38
	BP3	147	93	52	47	5	142	87	132	78

Table 3.5: Selection cuts on the displaced candidates and the cut flow for SR1, SR2, and SR3 are shown. The selection cuts shown here have been applied in succession to the selection cuts on the prompt candidates shown in Table 3.3. We note that the instrumental background estimates are unavailable for SR1-3.

We observe from Table 3.5 that the requirement for at least one DSV with $N_{trk}^{V_1} \geq 3$ using displaced tracks with $|d_0| > 2$ mm improves S/B from $\sim \mathcal{O}(10^{-6})$ (after imposing selection

cuts from the prompt sector) to $\sim \mathcal{O}(10^{-3})$. Furthermore, this requirement leads to negligible event rates for $W + \text{jets}$ and $Z + \text{jets}$ in both $n_\ell = 1$ and $n_\ell = 2$ signal categories, respectively. In this light, we ignore these backgrounds in our analysis. The subsequent imposition of $N_{\text{trk}}^{V_1} \geq 5$ in SR1 reduces the SM background rates further by a factor of ~ 50 while the signal rates for the three benchmarks reduces only by a factor of ~ 2. For SR1, the SM background further reduces to negligible values on imposing $\sum p_T^{\text{trk}} < 30$ GeV, $r_{V_1} \geq 4$ cm and $N_{\text{trk}}^{V_2} \geq 5$ in both the $n_\ell = 1$ and $n_\ell = 2$ signal categories. For SR2 and SR3, the SM backgrounds are suppressed on applying $N_{\text{trk}}^{V_1} \geq 5$. However, the results presented in Table 3.5 are rather conservative estimates since the instrumental background rates are unavailable for SR1-3 and, therefore, could not be considered. While it is true that the instrumental backgrounds, which are not available for SR1, SR2 and SR3, might imply that we overestimate the efficacy of our analysis to remove the background events entirely, it is worth noting that one gets encouraging values for significance at the last but one step in the analysis where the SM background is not yet completely absent. For example, for BP3 in 1ℓ channel for the signal regions [SR1, SR2, SR3], these significance values are [17.7, 23.4, 69] σ. Similarly, for 2ℓ channel, the σ_ss for BP3 in the three signal regions are 2.8, 5.0 and 16.8 σ. Hence SR1-3 show promising prospects to further perform a realistic collider analysis with instrumental backgrounds.

Another area of optimization can be the $\not{E}_T$ selection criteria. In SR1, we imposed $\not{E}_T > 50$ GeV as baseline selection. We performed a similar analysis with a stronger lower bound on $\not{E}_T$. The HL-LHC rates are shown in Table 3.6 for the 1ℓ channel in SR1 with $\not{E}_T > 120$ GeV. This stronger $\not{E}_T$ cut reduces the background in the prompt sector by almost an order of magnitude, while the signal reduces roughly by 10% when compared with the yields of Table 3.5. This leads to improved signal-vs-background ratios at successive stages of the analysis. However, in both cases, the kinematic variables for the displaced vertex completely remove the SM background. It is worth noting that we considered a weaker cut on $\not{E}_T$ ($\not{E}_T > 50$ GeV) in SR1 to emphasize the relevance of observables related to the DSV. Our goal was to highlight that despite a weaker selection cut on $\not{E}_T$, the variables associated with the reconstructed displaced vertex efficiently reduce the SM background.

		Prompt sector			SR1				
		$\lvert \mathrm{d}_0 \rvert < 2$ mm			$\lvert \mathrm{d}_0 \rvert \geq 2$ mm				
		$\mathrm{D}_0^\ell, \mathrm{D}_Z^\ell$ < 2 mm	$\mathrm{p}_T^\ell >$ 30 GeV	$\not{E}_T$ > 120 GeV	$\mathrm{N}_{\mathrm{trk}}^{\mathrm{V1}}$ ≥ 3	$\mathrm{N}_{\mathrm{trk}}^{\mathrm{V1}}$ ≥ 5	$\sum \mathrm{p}_T^{\mathrm{trk}}$ < 30 GeV	$\mathrm{r}_{\mathrm{V}_1}$ ≥ 4 cm	$\mathrm{N}_{\mathrm{trk}}^{\mathrm{V2}}$ ≥ 5
	BP1	2590	2150	1837	1183	557	377	198	23
	BP2	2003	1683	1456	1068	504	346	242	33
1ℓ	BP3	3646	3073	2561	1021	655	368	333	33
	$\mathrm{t}_\mathrm{h}\mathrm{t}_\ell$	2.4×10^8	1.6×10^8	1.9×10^7	14771	726	484	242	0

Table 3.6: Signal and background rates are presented for $\sqrt{s} = 14$ TeV LHC assuming $\mathcal{L} = 3000$ fb^{-1} for the selection cuts corresponding to signal region SR1 (Table 3.5) except for a stronger lower bound on missing transverse energy $\not{E}_T > 120$ GeV.

3.5 Outlook and conclusion

In this Chapter, we focus on the case of singlino-like light neutralino DM in the NMSSM framework. Implications from current collider and astrophysical constraints have been analyzed, and the allowed parameter space has been scrutinized in light of projected sensitivities in the future direct detection experiments. We consider an electroweakino mass spectrum where $\widetilde{\chi}_2^0$ has a dominant bino admixture, $\widetilde{\chi}_3^0, \widetilde{\chi}_4^0, \widetilde{\chi}_1^\pm$ have a dominant higgsino composition, and $\widetilde{\chi}_5^0, \widetilde{\chi}_2^\pm$ are wino-like. In the allowed region of parameter space, there exists long-lived bino-like NLSP $\widetilde{\chi}_2^0$. The small decay width of this $\widetilde{\chi}_2^0$ being caused for, $\Delta M = m_{\widetilde{\chi}_2^0} - m_{\widetilde{\chi}_1^0} < m_Z$ which allows only 3 body decay for $\widetilde{\chi}_2^0$. Within the scope of the allowed parameter space of interest, the long-lived $\widetilde{\chi}_2^0$ can decay through $\widetilde{\chi}_2^0 \to \widetilde{\chi}_1^0 b\bar{b}$, $\widetilde{\chi}_2^0 \to \widetilde{\chi}_1^0 \tau^+\tau^-$, $\widetilde{\chi}_2^0 \to l^+l^-$, $\widetilde{\chi}_2^0 \to \widetilde{\chi}_1^0 j\bar{j}$ or $\widetilde{\chi}_2^0 \to \widetilde{\chi}_1^0 \gamma$. The $\widetilde{\chi}_2^0$'s can appear in direct electroweakino searches at the LHC via cascade decays of heavier electroweakinos, and lead to displaced secondary vertices, which can be reconstructed in the tracker region of the LHC. In this work, we study the projected sensitivity for direct electroweakino production $pp \to \widetilde{\chi}_3^0/\widetilde{\chi}_4^0 \widetilde{\chi}_1^\pm \to (\widetilde{\chi}_3^0/\widetilde{\chi}_4^0 \to Z/H_1 \widetilde{\chi}_2^0)(\widetilde{\chi}_1^\pm \to W^\pm \widetilde{\chi}_2^0)$ with $\widetilde{\chi}_2^0 \to \widetilde{\chi}_1^0 Y$ at the HL-LHC. We choose three different signal benchmarks BP1, BP2, and BP3, from the currently allowed parameter space that features a long-lived $\widetilde{\chi}_2^0$. We perform a detailed collider analysis using the cut-and-count methodology while including signal and relevant backgrounds at the detector level.

We consider two different signal categories, $n_\ell = 1, 2$ as discussed in Sec. 3.4. To separate the signal from the background effectively, we use selection cuts on separate sets of observables in case of prompt and long-lived objects. Objects with transverse impact parameter $|d_0| < 2$ mm are classified as prompt, while those with $|d_0| \geq 2$ mm are categorized as long-lived. Prompt objects are used to trigger the events, while the displaced objects play the major role in discriminating against the backgrounds. We identify the signal regions SR1 with optimized selection cuts on $N_{\text{trk}}^{V_1}$, the track multiplicity of V_1, $\sum p_T^{\text{trk}}$, sum of transverse momentum of all tracks associated with V_1, r_{V_1}, radial distance between V_1 and PIV, and $N_{\text{trk}}^{V_2}$, track multiplicity for the second DSV. SR2 and SR3 are defined by optimizing the cuts on $|d_0|$, the minimum transverse impact parameter, and $N_{\text{trk}}^{V_1}$. We show that with the choice of the three signal regions, SR1, SR2, and SR3, one can completely suppress the SM background. However, considering a purely instrumental background for the signal region SR_A as estimated in Ref. [177], scaling it to the HL-LHC luminosity and additionally tripling this scaled background to account for the effect of difficulties of the HL-LHC environment, we found that BP1, BP2, and BP3 can be probed with a signal significance of $\sigma_S \gtrsim 5.5, 3.9$, and 23σ in SR_A (cf. Table 3.4). Similar analysis can be extended to other points in the allowed parameter space of our interest to evaluate their exclusion/discovery at the high luminosity LHC.

CHAPTER 4

EXPLORING THE SINGLINO-DOMINATED THERMAL NEUTRALINO DARK MATTER IN THE Z_3 INVARIANT NMSSM

This chapter is based on an ongoing work [138] done in collaboration with Amit Adhikary, Rahool Kumar Barman, Biplob Bhattacherjee and Rohini M. Godbole.

4.1 Introduction

The nature of Dark Matter (DM) remains a central mystery in contemporary particle physics, particularly within the realm of Beyond Standard Model (BSM) physics. Unveiling the properties of DM candidates is a key objective, driving extensive experimental efforts that employ direct, indirect [388,389] and collider searches [390,391]. Among the proposed DM candidates, a Weakly Interacting Massive Particle (WIMP), an example of non-baryonic Cold Dark Matter (CDM) candidate interacting via electroweak coupling with a mass around the electroweak scale, can naturally predict a relic density that aligns very closely to the measured value of $\Omega h^2 = 0.120 \pm 0.001$ in the PLACK experiment at 68% C.L. [91]. WIMPs are one of the favourable DM candidates since they can be produced at the thermal equilibrium conditions prevailing in this surprising agreement, referred to as the 'WIMP mir-

acle' [104–106]. The non-relativistic nature and weak interactions of WIMPs lead to two primary categories for DM-nucleon scattering: spin-independent (SI) and spin-dependent (SD). The recent LUX-ZEPLIN (LZ) experiment has reported the most stringent limit of DM-nucleon SI elastic scattering cross-section (σ_{SI}) at 9.2×10^{-48} cm^2 at the 90% C.L. corresponding to DM particle mass at 36 GeV [188]. While the SD WIMP-nuclear cross-section has the minimum limit for 30 and 25 GeV WIMPs at 1.49×10^{-42} and 3.2×10^{-41} cm^2 from LZ and PICO-60 C_3F_8 experiments for SD WIMP-neutron (σ_{SD_n}) and SD WIMP-proton (σ_{SD_p}) cross-sections [188, 191]. LZ for 1000 live day run has projected an increase by around an order of magnitude in these cross-sections [392]. These strong limits on SI and SD DM-nucleon scattering indicate the feeble nature of the DM and nucleon interactions, which poses significant experimental challenges [393]. This necessitates exploring alternative avenues for DM detection, such as searching for missing energy signatures in experiments at the LHC.

The absence of any DM candidate in the SM strongly suggests looking for possible BSM scenarios to explain the observed dark matter. A very well-motivated model, Supersymmetry, can provide a possible dark matter candidate, the lightest neutralino, within R-parity conserved scenario [121, 288]. The neutralino sector in Minimal Supersymmetric Standard Model (MSSM) involves the mixing of Bino ($\tilde{B}$), Wino ($\tilde{W}$), and neutral Higgsinos ($\tilde{H}_u$ and $\tilde{H}_d$), to produce four neutralinos. The lightest neutralino ($\tilde{\chi}_1^0$), denoted as the lightest supersymmetric particle (LSP), a Majorana spin 1/2 particle, is usually the most popular candidate for DM. In phenomenological MSSM (pMSSM), LSP mass must exceed 34 GeV to avoid over-abundant relic density [300, 304–307]. For single-component thermal DM in the general MSSM, Higgsinos are favoured to be massive ($\gtrsim 1$ TeV) to achieve the correct DM abundance [308–310]. This avoids an overly large annihilation rate unless stops are very heavy [394, 395] or the Higgsino mass parameter (μ) is negative [396]. In the low-mass limit ($\lesssim 1$ TeV), a Bino-dominated LSP with significant co-annihilation from Wino-like neutralinos is preferred to match the observed relic density. The parameter μ receives constraints from both theory and experimental front. Moreover, a large value of Higgsino mass parameter μ far above the value of M_Z is disfavored in the MSSM since it is not *natural* and can introduce a "little fine-tune problem" [397–399]. This can be evaded in a model featuring a singlet extension of the MSSM, the Next-to-Minimal Supersymmetric Standard Model (NMSSM) [137, 314, 400], which introduces a singlet Higgs field in addition to two Higgs doublets of the MSSM. In NMSSM, the μ parameter is generated dynamically when the singlet field develops a vacuum expectation value (*vev*) v_S, with Z_3 symmetry in the NMSSM,

$\mu = \lambda v_S$ at the electroweak scale.

The NMSSM introduces an extended Higgs sector with seven Higgs bosons: three CP-even, two CP-odd neutrals, and two charged ones. Interestingly, this allows for a light singlet-dominated scalar (H_1) or singlet-dominated pseudoscalar Higgs (A_1) potentially lighter than the SM-like Higgs (H_{SM}) satisfying the collider constraints [323,401–405]. Likewise, the Singlino, fermionic superpartner of singlet field, expands the neutralino sector to five states, where the lightest of these neutralinos remains a viable candidate for DM [281, 320, 321, 406–411]. The singlet-like light scalars (H_1/A_1) are important to our current study, where along with it, a Singlino-dominated LSP containing critical amount of Higgsino admixture for moderate values of μ [361, 412–414] can provide under-abundant relic. In exceedingly low mass regions, this scenario offers new annihilation funnels via light Higgs along with correct Singlino admixture in LSP to satisfy the limits of DM DD, which was not possible in MSSM [361, 413]. In the relatively high mass regions, the usual co-annihilation mechanism dominates where Higgsino admixture allows the LSP to efficiently annihilate in the early universe and, in turn, increase the interaction strength of LSP, making it more detectable in DM DD experiments. Moreover, considering a slight Bino content in the LSP for suitably small M_1, could provide us with a viable Singlino-dominated DM candidate, which allows funnels featuring SM Higgs boson, Z-boson and even the light singlet-like Higgs [404, 415]. Given a low-mass Singlino-like DM candidate, we primarily aim to study if this type of scenario is still compatible with the DM DD and collider searches. Then, look for possible interesting channels involving decays to Singlino-like LSP and their sensitivity of detection at high luminosity LHC in the framework of NMSSM.

Usually, the interesting channels involve cascade decays of MSSM-like NLSPs to Singlino-like LSP where the decays of heavier neutralinos and charginos proceed via the emission of on/off shell gauge and Higgs bosons $Z/W^{\pm}/H_{SM}/H_1/A_1$ when the sparticles in the model are heavy, and the electroweakinos do not form a compressed spectrum. Particularly, the condition $m_{LSP} < M_1 < \mu$ in NMSSM facilitate typical decays $\widetilde{\chi}_1^{\pm} \rightarrow \widetilde{\chi}_1^0/\widetilde{\chi}_2^0 \, W^{\pm}, \tilde{\chi}_i^0 \rightarrow Z/H_{SM}/H_1/A_1 \, \widetilde{\chi}_1^0$. In this work, we only include the triple-boson channels [416–419] from the Higgsino-like chargino-neutralino production, which is otherwise not native to MSSM. These triple-bosons are usually detected via their leptonic decays, leading to a signal final state consisting of $\not{E}_T$ and leptons. Some specific consequences of such possibilities incorporate light singlet Higgs producing collimated decays to $b\bar{b}/\tau\tau/W^{\pm}W^{\pm}/\gamma\gamma$. We study one such possibility where H_1 decays to $b\bar{b}$ and appears as a single fatjet. A few studies

have been performed at the LHC to search light scalar in decays $\tau\tau$ [420], $b\bar{b}$ [323, 421], $\gamma\gamma$ [407, 422, 423]. To summarize, we look for a signal final state consisting of a Higgs fatjet, leptons plus $\not{E}_\mathrm{T}$ and predict the sensitivity at HL-LHC.

This Chapter is organized as follows. We discuss the range of parameters for our scan, relevant collider and astrophysical constraints, and their impact on the parameter space of our interest in Sec. 4.2. We examine the different DM annihilation modes responsible for effective DM dilution in the early universe, through which consistency with relic density constraints is achieved in Sec. 4.3. In Sec. 4.4, we discuss the benchmark scenario adopted for analyzing the HL-LHC potential for direct electroweakino pair production in the triple boson $+\not{E}_\mathrm{T}$ final state. The details of the collider search are presented in Sec. 4.5. We conclude in Sec. 4.6.

4.2 Parameter space scan and constraints

In this work, we concentrate on the region of Z_3-invariant NMSSM parameter space that leads to Singlino-dominated LSP $\widetilde{\chi}_1^0$ with under-abundant relic density. In the $\lambda \to 0$ limit, the singlet superfield decouples from the MSSM Higgs superfields, as indicated by Eq. (1.100). In this decoupled regime, the mass of the Singlino-like neutralino at the tree-level is approximately $\sim 2\kappa v_S$. Given the effective Higgsino mass parameter $\mu = \lambda v_S$, and our region of interest being the parameter space with a Singlino-dominated LSP $\widetilde{\chi}_1^0$, we require $2\kappa v_S \lesssim \lambda v_S$. Accordingly, we impose $|\kappa/\lambda| < 0.5$ in our scans to ensure Singlino dominance in the LSP $\widetilde{\chi}_1^0$. Values of $\kappa, \lambda < 10^{-3}$ are avoided as to ensure beyond-the-MSSM scenario. It is also worth noting that perturbativity of the theory up to the GUT scale requires both $\lambda, \kappa < 0.7$. Based on initial results from our scan, we restrict λ to less than 0.4 to increase the likelihood of generating points with Singlino-dominated LSP. Our scan considers a wide range for the Bino, Wino and Higgsino mass parameters: $70\,\mathrm{GeV} < M_1 < 2\,\mathrm{TeV}$, $200\,\mathrm{GeV} < M_2 < 3\,\mathrm{TeV}$ and $100\,\mathrm{GeV} < \mu < 900\,\mathrm{GeV}$, respectively. M_2 is varied from a higher minimum value due to more stricter constraints on Winos. This choice of M_1, M_2, and μ allows the study of a diverse electroweakino sector within the NMSSM, involving various admixtures from Bino, Wino, and Higgsinos in the Singlino-dominated LSP. A small value of A_κ tends to favor a singlet-dominated light Higgs bosons, which could be crucial for resonant DM annihilation at low LSP masses, $m_{\widetilde{\chi}_1^0} \lesssim m_Z/2$. Therefore, we vary it in the [0-1000] GeV range. Other key input parameters required to characterize the Higgs

and electroweakino sectors at the tree level are A_κ and $\tan\beta$, which have been varied in the [-10,10^4] GeV and [1,40] ranges, respectively. The third-generation squark mass parameters MQ_3, MU_3, MD_3 are varied in the range [500-10^4] GeV, while the third-generation slepton mass parameters are fixed at 3 TeV. The second-generation squark and slepton mass parameters are also fixed at 3 TeV. Lastly, we vary the stop trilinear coupling A_t in the range [-10,10] TeV, while the bottom and stau trilinear couplings are fixed at $A_b = A_\tau = 2$ TeV.

We perform a random scan over the parameter space, considering the previously discussed scan range, utilizing the `NMSSMTools-v6.0.0` [367, 424, 425] package. The masses and relevant branching ratios of the Higgs bosons and the SUSY particles are computed using `NMSSMTools-v6.0.0` [367, 424, 425]. We use `MicrOmegas` [426–428] to compute the observables constrained by LEP, B-physics experiments, and DM measurements. We initially perform a flat random scan over 10^8 points. Roughly $10^{-4}\%$ of the scanned points pass the relevant collider and astrophysical constraints. The range of input parameters considered in the scan is summarized below:

$$0.0001 < \lambda < 0.4, \ \left|\frac{\kappa}{\lambda}\right| \leq 0.5, \ M_1 = (70, 2000) \text{ GeV},$$

$$M_2 = (200, 3000) \text{ GeV}, \ M_3 = (2000, 5000) \text{ GeV},$$

$$\mu = (100, 900) \text{ GeV}, \ \tan\beta = (1, 40),$$

$$A_\lambda = (-10, 10000) \text{ GeV}, \ |A_\kappa| = (0, 1000) \text{ GeV},$$

$$A_t = (-10000, 10000) \text{ GeV} \tag{4.1}$$

$$A_b = A_\tau = 2000 \text{ GeV}$$

$$ML_3 = ME_3 = 2000 \text{ GeV}$$

$$MQ_3 = MU_3 = MD_3 = (0.5, 10) \text{ TeV}$$

Constraints from collider experiments

The NMSSM parameter space of our interest is constrained by various collider and astrophysical measurements. We first discuss the relevant collider constraints. Adhering to LEP measurements, we require the mass of the charginos to be $M_{\widetilde{\chi}_1^\pm} > 103.5$ GeV [347] and the production rate of the process $e^+e^- \to \widetilde{\chi}_2^0\widetilde{\chi}_1^0$ in the jets+$\not{E}_T$ final state with $|M_{\widetilde{\chi}_2^0} - M_{\widetilde{\chi}_1^0}| < 5$ GeV to be below ≤ 0.1 pb at 95% C.L. Limits from searches in the ZH_j and A_iH_j processes are imposed through `NMSSMTools-v6.0.0` [367, 424, 425]. In the left panel of Fig. 4.1, we display the parameter space in the $m_{\widetilde{\chi}_1^0}$-Ωh^2 plane, consistent with the LEP limits. The color
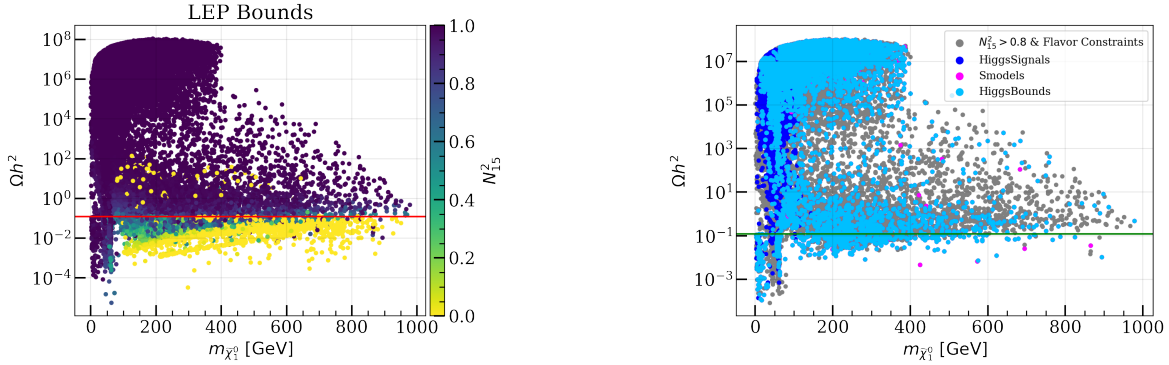
Figure 4.1: *Left:* Parameter points allowed by the theoretical constraints and LEP limits are shown in the $m_{\widetilde{\chi}_1^0}$-Ωh^2 plane. The color palette represents the Singlino admixture N_{15}^2 in the LSP $\widetilde{\chi}_1^0$. *Right:* Parameter points allowed by the successive application of flavor constraints and the requirement of a Singlino-dominated $\widetilde{\chi}_1^0$ ($N_{15}^2 > 0.8$) (shown in grey), Higgs signal-strength constraints imposed through `HiggsSignals-v2.6.2` [429, 430] (blue), bounds from electroweakino, gluino, squark, stop and sbottom searches at the LHC applied through `SModels-v2.3.2` [431, 432] (pink) and the limits from BSM Higgs searches at the LHC implemented via `HiggsBounds-v5.10.0` [429, 433–435] (skyblue), are shown in the same plane.

axis represents the amount of Singlino admixture, N_{15}^2 in $\widetilde{\chi}_1^0$. The imposed upper limit on the relic density $\Omega_{\widetilde{\chi}_1^0} h^2 < 0.122$ is indicated as a solid red line in Fig. 4.1 (left). The region above $\Omega_{\widetilde{\chi}_1^0} h^2 > 0.122$ is dominantly populated by purple colored points, which are mostly Higgsino-dominated. Furthermore, for these over-abundant points, it is typically observed that $|\kappa|/\lambda > 0.3$ in the higher $m_{\widetilde{\chi}_1^0} \gtrsim 100$ region. Such points typically lead to an MSSM-like scenario with Higgsino-like dark matter. Notably, around 24% of points below $\Omega_{\widetilde{\chi}_1^0} h^2 < 0.122$ are Singlino-domimated with $N_{15}^2 > 0.8$, which are the primary focus on this analysis.

The parameter space of interest is also constrained by flavor physics observables, especially through measurements of the rare decay of B-mesons. Updated constraints from flavor physics are also imposed from `NMSSMTools-v6.0.0` [367, 424, 425] in terms of $BR(b \to s\gamma)$, $BR(B_s \to \mu^+\mu^-)$, $BR(B^+ \to \tau^+\nu_\tau)$, $BR(B \to X_s\mu^+\mu^-)$. Additionally constraints from $\Upsilon(1s) \to H/A\gamma$, ΔM_s, ΔM_d, $\eta_b(1s)$ mass difference are imposed.

Among the three CP-even Higgs bosons, we require either H_1 or H_2 to be consistent

with the properties of the observed SM-like Higgs boson H_{SM}. The mass of H_{SM} has been measured at 125.28 ± 0.14 GeV through combined measurements by the ATLAS and CMS collaborations at the LHC [1,2]. To account for the theoretical uncertainties in the Higgs boson mass calculation [342], we adopt a conservative approach, and require the mass of the Higgs boson consistent with H_{SM} to be within 122-128 GeV. Its couplings with $t\bar{t}$, $b\bar{b}$, $\tau^+\tau^-$, $\gamma\gamma$, W^+W^-, ZZ and gg are also required to be consistent with the signal strength measurements within 2σ uncertainty, imposed through the `HiggsSignals-v2.6.2` [429,430] package. The heavier and/or lighter scalar and pseudoscalar Higgs bosons can be an admixture of doublet and singlet states and are primarily constrained by BSM Higgs searches at the LEP, Tevatron and the LHC. We impose these constraints using `HiggsBounds-v5.10.0` [429,433–435]. Limits from the searches for supersymmetric particles at the LHC, especially electroweakinos, are implemented using `SModels-v2.3.2` [431,432] interfaced with `NMSSMTools-v6.0.0` [367,424,425].

Constraints from relic density of dark matter and direct detection

As discussed previously, our main focus is the region of parameter space where the Singlino-dominated LSP $\widetilde{\chi}^0_1$ serves as the thermal DM candidate. In this scenario, the Dark Matter relic abundance of $\widetilde{\chi}^0_1$ is required to be within $\Omega_{\widetilde{\chi}^0_1}h^2 < 0.122$, allowing a 2σ uncertainty around the best-fit of $\Omega^{obs.}_{DM}h^2 = 0.120 \pm 0.001$ as measured by the PLANCK collaboration [91].

The parameter space points that survive the previously discussed constraints are further subjected to the most recent upper limits on the spin-independent DM-nucleon cross-sections σ_{SI}, from LZ [188]. We also impose the upper limits from SuperCDMS [436], which is sensitive in the lower m_{DM} regime, $100\,\text{MeV} \lesssim m_{DM} \lesssim 5\,\text{GeV}$. We rescale σ_{SI} with ξ, the ratio of the DM relic density predicted by the model to the observed upper limit on $\Omega^{obs.}_{DM}h^2$ allowing 3σ uncertainty, $\xi = \Omega h^2/0.122$. In Fig. 4.2, we illustrate the parameter points allowed by the previously discussed constraints in the plane of $\xi\sigma_{SI}$ and $m_{\widetilde{\chi}^0_1}$. Among them, approximately 70% of points are excluded by LZ SI limits. We also illustrate the projected sensitivity of ARGO [437], DARWIN [438,439], and LZ-1000 [392], in probing σ_{SI} in the same plot. It is observed that a sizeable fraction of currently allowed points are within the reach of these future experiments. Several of these currently allowed points also fall beneath the neutrino scattering floor shown in yellow, thus will remain outside the reach of any σ_{SI}-based future direct detection experiments.
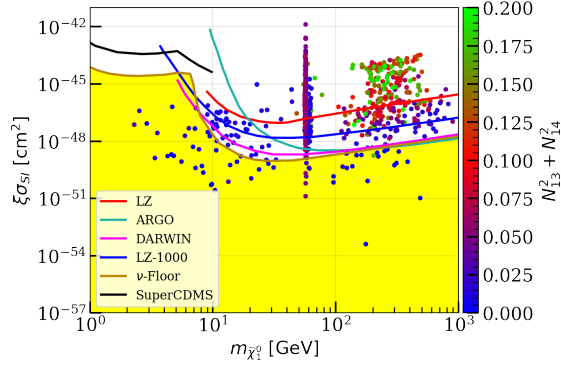
Figure 4.2: Parameter space points with a singlino-dominated LSP, and allowed by searches at the LEP, rare B-meson decay, Higgs signal strength, and BSM Higgs, electroweakino and other particle searches at the LHC (sky-blue points from thr right panel of Fig. 4.1) are shown in the $\xi\sigma_{SI}-m_{\widetilde{\chi}_1^0}$ plane. The color palette represents the Higgsino fraction in the LSP. The red lines denote the current upper limit of σ_{SI} from the LZ results at 90% C.L [188]. Projected limits on σ_{SI} from future experiments, ARGO [437], DARWIN [438,439], and LZ-1000 [392] are also presented.

The spin-independent DM-nucleon interaction is largely mediated through the t-channel exchange of CP-even Higgs bosons, where σ_{SI} can be expressed as [408],

$$\sigma_{SI} = \frac{4\mu_R}{\pi}\left|f\right|^2, \quad f \approx \sum_{i=1}^{3} f_{H_i} = \sum_{i=1}^{3} \frac{g_{H_i\widetilde{\chi}_1^0\widetilde{\chi}_1^0}g_{H_iNN}}{2m_{H_i}^2}, \quad (4.2)$$

where N denotes the nuclear states, μ_R is the reduced mass of the DM particle and the nucleon, and $g_{H_i\widetilde{\chi}_1^0\widetilde{\chi}_1^0}$ and g_{H_iNN} denotes the coupling of the ith CP-even Higgs bosons with the DM particle and the nucleons, respectively. For a Singlino-dominated $\widetilde{\chi}_1^0$, characterized by $N_{15}^2 \sim 1$, the couplings with H_i are given by [139],

$$g_{H_i\widetilde{\chi}_1^0\widetilde{\chi}_1^0}\Big|_{\{\widehat{h},\widehat{H},\widehat{s}\}} \approx \sqrt{2}\lambda\big[V_{H_i\widehat{h}}N_{15}(N_{13}\sin\beta + N_{14}\cos\beta) + V_{H_i\widehat{H}}N_{15}(N_{14}\sin\beta - N_{13}\cos\beta)$$
$$+ V_{H_i\widehat{s}}(N_{13}N_{14} - \frac{\kappa}{\lambda}N_{15}^2)\big], \quad (4.3)$$

where we have retained N_{15} or $V_{H_i\hat{S}}$ dependent terms only. The Singlino-like $\widetilde{\chi}_1^0$ couples with the CP-even Higgs bosons through its mixing with the Higgsinos. Additionally, it can

couple with the singlet component on its own accord, with the coupling strength proportional to κ/λ, as indicated by Eq. (4.3).

The coupling of the ith CP-even scalar with the nucleons is given by [440]

$$g_{H_iNN}\Big|_{\{\widehat{h},\widehat{H},\widehat{s}\}} = \frac{m_N}{\sqrt{2}v}\Big[V_{H_i\widehat{h}}(F_d^{(N)} + F_u^{(N)}) + V_{H_i\widehat{H}}\big(\tan\beta F_d^{(N)} - \frac{1}{\tan\beta}F_u^{(N)}\big)\Big] \qquad (4.4)$$

where m_N denotes the mass of the nucleon and $F_{d,u}^{(N)}$ are the combined form factors associated with the atomic nuclear states. The coupling g_{H_iNN} is primarily determined by the doublet-admixtures in the CP-even Higgs bosons and would be highly suppressed for a singlet-like Higgs boson.

Overall, for a Singlino-dominated $\widetilde{\chi}_1^0$, a higher spin-independent DM-nucleon interaction rate is typically associated with greater Higgsino mixing, as suggested by Eqs. (4.3) and (4.4). To illustrate this, we show the amount of Higgsino admixture in the LSP $\widetilde{\chi}_1^0$, $N_{13}^2 + N_{14}^2$, as a color palette in Fig. 4.2. It is observed that for higher DM masses, $m_{\widetilde{\chi}_1^0} \gtrsim 100$ GeV, where consistency with the upper limit on relic density is achieved through co-annihilation (further discussed in Sec. 4.3), the parameter points excluded by the recent LZ limits are associated with a relatively larger Higgsino admixture. In contrast, in the lower $m_{\widetilde{\chi}_1^0}$ regime, a large Higgsino admixture is not required for large σ_{SI} due to s-channel resonant annihilation mediated through a light Higgs boson.

It is important to note that there could be several conditions that result in a diminished value of σ_{SI}, falling below the neutrino floor. This could potentially arise from "blind spots" in the parameter space [139]. One such example is when coupling of SM-like Higgs with the Singlino-like $\widetilde{\chi}_1^0$'s, $g_{H_{SM}\widetilde{\chi}_1^0\widetilde{\chi}_1^0}$, vanishes for either small lambda or $m_{\widetilde{\chi}_1^0}/\mu \simeq \sin 2\beta$ [411]. This SM-Higgs exchange process only applies when other CP-even Higgs bosons, H_s and H are decoupled and $H_s >> H_{SM}$. Another important case related to our present study is the possibility of destructive interference from the CP-even singlet-like Higgs and the SM-like Higgs, $\sigma_{SI} \propto \Big[V_{SM,\widehat{h}}\, g_{H_{SM}\widetilde{\chi}_1^0\widetilde{\chi}_1^0}/m_{H_{SM}}^2 + V_{SM,\widehat{S}}\, g_{H_s\widetilde{\chi}_1^0\widetilde{\chi}_1^0}/m_{H_s}^2\Big]^2$. This is critical for $m_{H_s} < m_{H_{SM}}$ with the MSSM like Higgs boson, H being decoupled for both cases of Singlino-dominated LSP having large λ and small $\tan\beta$ and Higgsino-Singlino scenario. We refer the reader to Ref. [440] for further details. Also, it must be noted that a relatively light Bino/Wino-like state, characterized by $m_{\widetilde{\chi}_1^0} < M_1 < \mu < M_2$ or $m_{\widetilde{\chi}_1^0} < M_1 < M_2 < \mu$, can induce gaugino-admixtures (gaugino is referred to Bino and Wino combinedly) in the Singlino-dominated LSP, which can potentially modify the usual blind spot condition for Z_3 symmetric NMSSM, revealing new parameter space for low σ_{SI} [404, 441].
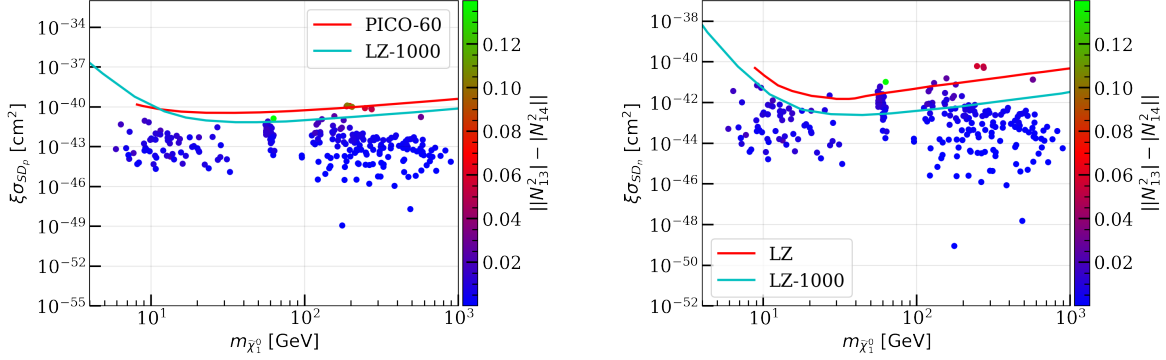
Figure 4.3: *Left*: The parameter space points allowed by the latest LZ SI limits in Fig. 4.2 are plotted in the $\xi\sigma_{SD_p} - m_{\widetilde{\chi}_1^0}$ plane. The red line represents the latest upper limits on σ_{SD_p} from PICO-60 [191]. *Right*: The allowed parameter points from the *Left* panel are plotted in the $\xi\sigma_{SD_n} - m_{\widetilde{\chi}_1^0}$ plane. The current upper limits on σ_{SD_n} from LZ [188] are presented in red. The future sensitivity from LZ-1000 [392] on SD_p and SD_n is also projected in both panels. The color palette in both panels represents the coupling $g_{Z\widetilde{\chi}_1^0\widetilde{\chi}_1^0} \propto |N_{13}^2 - N_{14}^2|$.

The parameter space of interest can also be probed through spin-dependent DM-nucleon interactions. In this regard, we impose the most recent upper limits on the spin-dependent DM-neutron σ_{SD_n} and DM-proton σ_{SD_p} cross-sections from LZ [188] and PICO-60 [191], respectively, on the parameter points allowed by the previously discussed constraints, including the upper limits on $\xi\sigma_{SI}$. We show our results in Fig. 4.3. It is observed that only a few parameter space points are excluded by the upper limits on the spin-dependent interaction rate. Future projections for σ_{SD_n} and σ_{SD_p} for LZ-1000 [392] are also shown in the respective figures. The points allowed by the current upper limits on SD DM-neutron and DM-proton interactions will be henceforth referred to as the currently allowed parameter points.

The DM SD interactions are typically induced by t-channel exchange of Z boson. Their cross-section can be expressed as,

$$\sigma_{SD_{n/p}} \simeq C^{n/p} \times \left(\frac{g_{Z\widetilde{\chi}_1^0\widetilde{\chi}_1^0}}{0.01}\right)^2, \tag{4.5}$$

where n (p) denotes neutron (proton), with the nuclear form factor C^n $(C^p) \sim 10^{-41}$ cm^2,

and the coupling $g_{Z\widetilde{\chi}_1^0\widetilde{\chi}_1^0}$ is determined by the Higgsino admixtures in the LSP $\widetilde{\chi}_1^0$,

$$g_{Z\widetilde{\chi}_1^0\widetilde{\chi}_1^0} = \frac{m_Z}{\sqrt{2}v}(N_{13}^2 - N_{14}^2). \qquad (4.6)$$

We illustrate the dependency of DM SD cross-sections on $||N_{13}|^2 - |N_{14}^2||$ in Fig. 4.3 through the color palette. It is observed that the parameter points excluded by PICO-60 and LZ, through upper limits on σ_{SD-p} and σ_{SD-n}, respectively, are mostly in red, which corresponds to a relatively larger $||N_{13}|^2 - |N_{14}^2||$. We would like to mention that all the allowed parameter points shown in Fig. 4.3 survive the constraints from DM indirect detection experiments [195], as shown in Appendix A.1 .

4.3 Annihilation processes with Singlino LSP

In this section, we examine the primary DM annihilation modes at different LSP masses. As discussed previously, our focus in this work is the region of parameter space where the LSP $\widetilde{\chi}_1^0$ is Singlino-dominated, is consistent with the upper limit on the relic density $\Omega h^2 < 0.122$, and passes the relevant experimental constraints discussed in Sec. 4.2. The parameter space of interest contains points where the mass of the LSP spans from approximately 4 GeV to 1 TeV. Different DM annihilation modes ensure complicity with the relic density constraint at different LSP masses.

Within our parameter space of interest, the DM annihilation mechanisms include resonant s-channel annihilation via the exchange of singlet-like Higgs bosons A_1/H_1, the Z boson, and the SM-like Higgs boson H_{SM}, t-channel annihilation via the exchange of a chargino or neutralino, and co-annihilation with the NLSP. For LSP masses below the Z-funnel, $m_{\widetilde{\chi}_1^0} \lesssim m_Z/2$, it is observed that DM annihilation primarily proceeds via the s-channel exchange of a singlet-like Higgs boson A_1/H_1 with mass $m_{A_1/H_1} \sim 2m_{\widetilde{\chi}_1^0}$. This is depicted in the left panel of Fig. 4.4, where we show the currently allowed parameter space points in the $m_{\widetilde{\chi}_1^0}$-m_{A_1} plane, with the z-axis representing m_{H_1}. The black-dashed line represents the condition $m_{A_1} = 2m_{\widetilde{\chi}_1^0}$, indicating that a major fraction of points align with the criteria. For points in the lower LSP mass regime that are farther away from the $m_{A_1} = 2m_{\widetilde{\chi}_1^0}$ line, it is observed that the lightest CP-even scalar H_1 is singlet-like, with mass $m_{H_1} \sim 2m_{\widetilde{\chi}_1^0}$, indicating that DM annihilation proceeds through the exchange of resonant H_1 in the s-channel. Resonant annihilation predominantly proceeds via the exchange of the
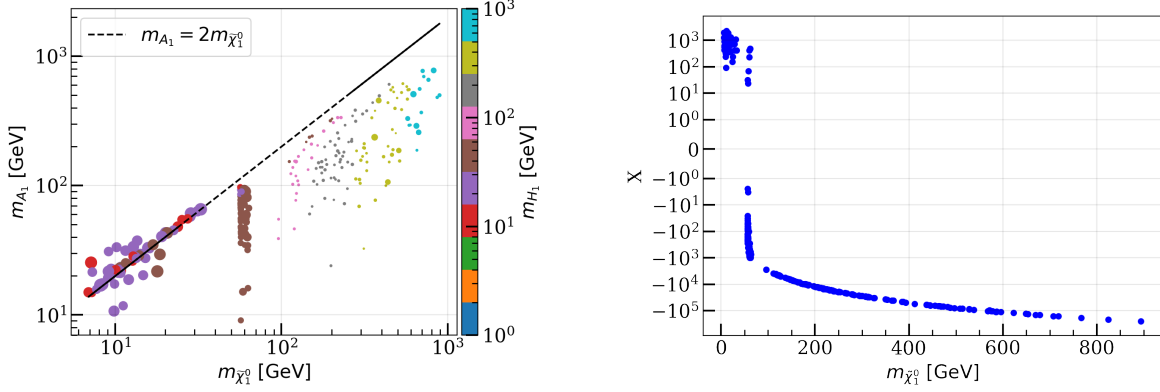
Figure 4.4: *Left:* The currently allowed parameter points are presented in the plane of $m_{\widetilde{\chi}_1^0}$ and the mass of the singlet-dominated pseudoscalar Higgs boson A_1. The color palette represents the mass of the singlet-dominated scalar Higgs boson H_1. The diagonal black-dashed line corresponds to the condition: $m_{A_1} = 2m_{\widetilde{\chi}_1^0}$. *Right:* The variation of X in Eq. (4.8) with the mass of the Singlino-dominated LSP $\widetilde{\chi}_1^0$ is shown for the currently allowed parameter space points.

Z boson and the SM-like Higgs boson H_{SM} as we approach the Z and H_{SM}-funnel thresholds, corresponding to $m_{\widetilde{\chi}_1^0} \sim m_Z/2$ and $m_{H_{SM}}/2$, respectively.

For the scenario involving a Singlino-like $\widetilde{\chi}_1^0$ and the singlet-like Higgs bosons with negligible doublet-admixture, using Eqs. (1.106), (1.114) and (1.116), the mass-rule connecting the two can be approximated as [361, 404],

$$
\begin{aligned}
\mathcal{M}^2_{\widetilde{N},55} \equiv 4\kappa^2 v_S^2 &= M^2_{S_R,S_R} + \frac{1}{3}M^2_{S_I,S_I} - \frac{4}{3}v_u v_d \left(\lambda^2 \frac{A_\lambda}{\mu} + \kappa\right) \\
&\approx \mathcal{M}^2_{\mathcal{S},33} + \frac{1}{3}\mathcal{M}^2_{\mathcal{P},22} - \frac{4}{3}v_u v_d \left(\lambda^2 \frac{A_\lambda}{\mu} + \kappa\right).
\end{aligned}
\tag{4.7}
$$

Considering the singlet-like pseudoscalar Higgs mass twice the mass of the Singlino-like LSP $\widetilde{\chi}_1^0$, $\mathcal{M}^2_{\mathcal{P},22} = 4\mathcal{M}^2_{\widetilde{N},55} = 4m^2_{\widetilde{\chi}_1^0}$, the condition necessary for resonant DM annihilation, Eq. (4.7) leads to,

$$
\mathcal{M}^2_{\mathcal{S},33} = -\frac{1}{3}m^2_{\widetilde{\chi}_1^0} + \frac{4}{3}v_u v_d \left(\lambda^2 \frac{A_\lambda}{\mu} + \kappa\right) \equiv X.
\tag{4.8}
$$

We illustrate the variation of X in Eq. (4.8) with the mass of Singlino-like LSP in the right panel of Fig. 4.4. Within the parameter space of our interest, X attains positive values only

in the region $m_{\widetilde{\chi}_1^0} \lesssim 50$ GeV. Eq. (4.8) and Fig. 4.4 (right) indicates that it is impossible to simultaneously achieve a physical mass for the singlet-like CP-even Higgs boson, $\mathcal{M}_{S,33}^2 > 0$, given $\mathcal{M}_{\mathcal{P},22}^2 \sim m_{A_1}^2 \geq 4\mathcal{M}_{\widetilde{N},55}^2 \sim m_{\widetilde{\chi}_1^0}^2$ for the Singlino-like $m_{\widetilde{\chi}_1^0} \gtrsim 50$ GeV. This implies that within our parameter space, resonant DM annihilation through the exchange of a singlet-like Higgs boson in the s-channel is not viable for LSP masses above $\gtrsim 50$ GeV.

As indicated in Eq. (4.3), the coupling of the Singlino-dominated neutralinos with the singlet-dominated Higgs bosons relies on κ, which is typically smaller $\lesssim 0.1$ within our parameter space. Alternatively, it couples with the singlet-dominated Higgs bosons through its Higgsino admixture. At higher LSP masses, $m_{\widetilde{\chi}_1^0} \gtrsim 100$ GeV, co-annihilation processes are required to comply with the relic density upper limits. This includes co-annihilation of Singlino-dominated LSP $\widetilde{\chi}_1^0$ with the near-degenerate NLSP neutralino $\widetilde{\chi}_2^0$ or chargino $\widetilde{\chi}_1^\pm$ containing a non-trivial Higgsino admixture, LSP + NLSP $\rightarrow$ SM and the NLSP-NLSP 'assisted' co-annihilation, NLSP + NLSP $\rightarrow$ SM. Typically, when $m_{\mathrm{LSP}} \sim m_{\mathrm{NLSP}}$, the thermal equilibrium between the LSP and the NLSP in the early universe can be maintained by the process LSP + $X \leftrightarrows$ NLSP + X', where X and X' are SM fermions. This interaction is mediated via the t-channel exchange of gauge bosons or Higgs bosons, with interaction rates governed by $n_{\mathrm{LSP}} n_X \langle \sigma v \rangle$, where n_{LSP} is the number density of the LSP and $\langle \sigma v \rangle$ represents the thermally-averaged cross-section times velocity [442]. The Higgsino admixture in the LSP $\widetilde{\chi}_1^0$, although small but non-negligible, typically boosts these interactions within our parameter space of interest. Likewise, the rate of NLSP-NLSP annihilation process, NLSP + NLSP $\rightarrow$ SM, scales as $\sim (n_{\mathrm{NLSP}}^2 \langle \sigma v \rangle)$, where n_{NLSP} is the number density of the NLSPs. Near the freeze-out temperature, where the number density of SM fermions is several orders of magnitude larger than the NLSP, the interaction rate for the process LSP + $X \rightarrow$ NLSP + X' is typically larger than NLSP + NLSP $\rightarrow$ SM. This allows the Singlino-dominated LSP $\widetilde{\chi}_1^0$ to annihilate at a rate roughly comparable to that of the Higgsino-dominated NLSP, resulting in the observed under-abundant relic density. In the left panel of Fig. 4.5, we show the allowed parameter points in the $m_{\widetilde{\chi}_1^0}$-$m_{\widetilde{\chi}_1^\pm}$ plane. The red dashed line represents the mass degeneracy condition required for co-annihilation, $m_{\widetilde{\chi}_1^0} = m_{\widetilde{\chi}_1^\pm}$, and it is observed that the parameter points with $m_{\widetilde{\chi}_1^0} \gtrsim 100$ GeV mostly lie along this line. In the z-axis, we show the minimum of the mass difference between the $\widetilde{\chi}_1^0$ and $\widetilde{\chi}_2^0/\widetilde{\chi}_1^\pm$.

As discussed in Sec. 4.2, the chargino mass limits from LEP exclude Winos and Higgsinos up to 103.5 GeV [347]. The Higgsinos can be further constrained by direct searches at the
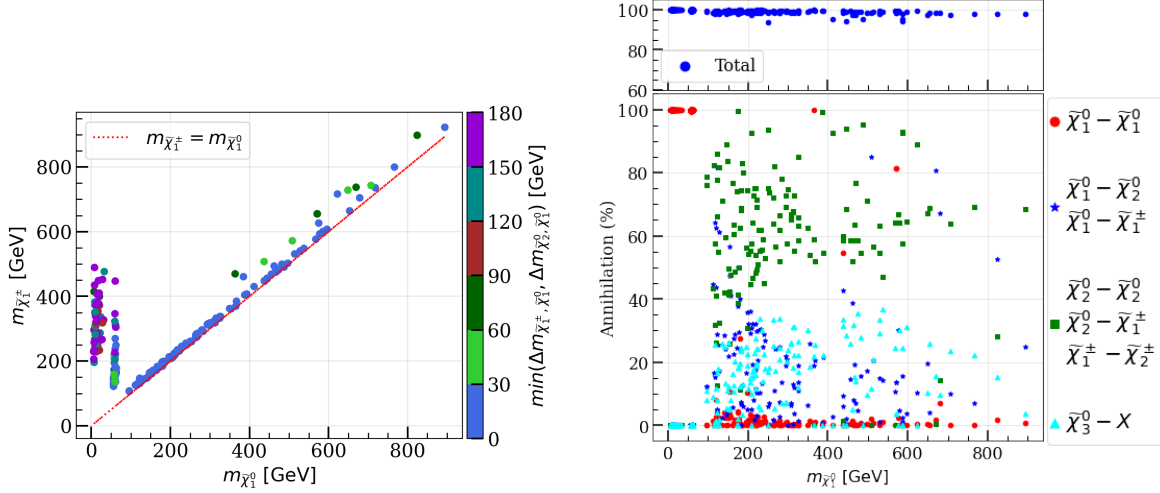
Figure 4.5: *Left*: Currently allowed parameter points are depicted in the $m_{\widetilde{\chi}_1^\pm}$ versus $m_{\widetilde{\chi}_1^0}$ plane. The z-axis represents the minimum of the mass difference between the singlino-dominated $\widetilde{\chi}_1^0$ and the NLSP $\widetilde{\chi}_2^0/\widetilde{\chi}_1^\pm$, $\min(\Delta m_{\widetilde{\chi}_1^\pm, \widetilde{\chi}_1^0}, \Delta m_{\widetilde{\chi}_2^0, \widetilde{\chi}_1^0})$. *Right:* The contribution percentage from the different DM annihilation modes in the early universe is shown for the allowed parameter points as a function of $m_{\widetilde{\chi}_1^0}$. The points in red represent the contribution from $\widetilde{\chi}_1^0 - \widetilde{\chi}_1^0$ annihilation, including the resonant s-channel and t-channels. Contributions from co-annihilation with the $\widetilde{\chi}_2^0$ or $\widetilde{\chi}_1^\pm$ are shown in blue, while those from NLSP-NLSP-assisted co-annihilation are shown in green. The contribution from co-annihilation with the heavier neutralinos $\widetilde{\chi}_3^0$ is depicted in sky-blue. The top panel represents the sum of contributions from the DM annihilation modes depicted in the lower panel.

LHC and direct detection experiments. However, within our parameter space of interest, due to mixing with the gauginos and depending on the relative values of M_1 and M_2, the lower bounds on Higgsinos are significantly weakened. As a result, we obtain allowed points with Higgsino-dominated charginos and neutralinos as low as 110 GeV, with $m_{\widetilde{\chi}_1^0}$ around the same mass, the criterion required for co-annihilation. It is worth noting that a sub-dominant contribution to the DM annihilation rate arises from $\widetilde{\chi}_1^0 \widetilde{\chi}_1^0$ annihilation into a pair of singlet-like light Higgs bosons: $\widetilde{\chi}_1^0 \widetilde{\chi}_1^0 \to H_1 H_1$ when $m_{\widetilde{\chi}_1^0} > m_{H_1}$ and $m_{A_1} + m_{H_1} > 2m_{\widetilde{\chi}_1^0}$, $\widetilde{\chi}_1^0 \widetilde{\chi}_1^0 \to A_1 A_1$ when $m_{\widetilde{\chi}_1^0} > m_{A_1}$ and $m_{A_1} + m_{H_1} > 2m_{\widetilde{\chi}_1^0}$, and $\widetilde{\chi}_1^0 \widetilde{\chi}_1^0 \to H_1 A_1$ when $m_{H_1} + m_{A_1} < 2m_{\widetilde{\chi}_1^0}$. These annihilation channels can involve the s-channel exchange of the Z, H_1, or A_1 bosons, or the t-channel exchange of $\widetilde{\chi}_1^0$ and other heavier neutralinos.

We present the relative contribution (in %) from the different DM annihilation modes for our allowed parameter space points in the right panel of Fig. 4.5. The relative contribution from $\widetilde{\chi}_1^0 - \widetilde{\chi}_1^0$ annihilation in the s- or t-channels are shown in red, $\widetilde{\chi}_1^0$-$\widetilde{\chi}_2^0/\widetilde{\chi}_1^\pm$ co-annihilation is shown in blue, and NLSP-NLSP assisted co-annihilation is shown in green. The contribution from co-annihilation processes involving $\widetilde{\chi}_3^0$ is shown in sky-blue. As discussed previously, resonant s-channel $\widetilde{\chi}_1^0 - \widetilde{\chi}_1^0$ annihilation is the dominant mode for DM dilution in the early universe for $m_{\widetilde{\chi}_1^0} < m_{H_{SM}}/2$. At higher $\widetilde{\chi}_1^0$ masses, co-annihilation with and assisted co-annihilation plays a crucial role in achieving consistency with the relic density limits.

4.4 Benchmark Scenario

Building on our understanding of the currently allowed parameter space, we now focus on examining the potential of probing these regions at the upcoming HL-LHC. One of the most promising modes to probe the electroweakinos at the LHC is through their direct production, as suggested by a plethora of studies such as [302,443–447]. However, our approach diverges from the traditional decay topologies, emphasizing NMSSM-specific scenarios aimed at exploring discovery prospects at the HL-LHC.

For our collider analysis, we examine a scenario from the allowed parameter region where the NLSP and LSP have non-degenerate masses, allowing the NLSP to decay promptly into the LSP. This configuration is observed in the low LSP mass regime, $m_{\widetilde{\chi}_1^0} \lesssim m_Z/2$, where the primary DM dilution mode is characterized by resonant s-channel annihilation through a singlet Higgs boson with roughly twice the mass of the LSP. It is worth noting that in the co-annihilation regime with mass degenerate NLSP and LSP, the NLSPs may become long-lived, as previously explored in [281].

Within our parameter space of interest, featuring gaugino and Higgsino-dominated heavier neutralinos and charginos, appreciable pair production rates are expected at the LHC. With the Singlino-dominated state serving as the LSP DM, heavier electroweakino states will decay into it in a cascading manner, involving more steps compared to the MSSM scenario. The final state may also involve a light singlet-like Higgs boson, which is a characteristic feature in the NMSSM scenarios. The extended decay chain opens the possibility for probing these scenarios via final states involving triple-boson plus missing energy, $pp \rightarrow VVV + \not{E}_{\mathrm{T}}$ ($V = Z, W^\pm, H_{SM}, H_1, A_1$), which can be challenging to achieve in the

BPs	Parameters (GeV wherever applied)	Masses (GeV)	Cross-sections at 14 TeV (fb)	Interesting Processes & B.F.s(%)
BP	$\lambda = 0.174, \kappa = 0.007$, $A_\lambda = 1384, A_\kappa = -70$, $\tan\beta = 5.15, \mu = 229$, $A_t = -6348, A_b = A_\tau = 2000$, $A_\mu = 0, M_1 = 131.4$, $M_2 = 965.8, M_3 = 3663$, $N_{15} = 0.99, N_{21} = 0.95$, $N_{23} = 0.26, N_{24} = 0.16$, $N_{33} = N_{34} = 0.7$, $N_{41}=0.3, N_{43} = N_{44} = 0.66$ $N_{52} = 0.99, \Gamma_{A_1} = 4.41 \times 10^{-5}$, $\Gamma_{H_1} = 9.47 \times 10^{-7}$	$m_{\widetilde\chi_1^0} = 20.5, m_{\widetilde\chi_2^0} = 123.9$ $m_{\widetilde\chi_3^0} = 243, m_{\widetilde\chi_4^0} = 244$, $m_{\widetilde\chi_5^0} = 1028, m_{\widetilde\chi_1^\pm} = 233$, $m_{\widetilde\chi_2^\pm} = 1028, m_{H_1} = 14.2$, $m_{H_2} = 125.1, m_{H_3} = 1169$, $m_{H^\pm} = 1170, m_{A_1} = 43.8$, $m_{A_2} = 1168$	$\widetilde\chi_3^0\widetilde\chi_1^\pm = 194.4$ $\widetilde\chi_1^\mp\widetilde\chi_1^\pm = 116.4$ $\widetilde\chi_4^0\widetilde\chi_1^\pm = 163.0$ $\widetilde\chi_3^0\widetilde\chi_4^0 = 85.04$ $\widetilde\chi_2^0\widetilde\chi_1^\pm = 50.62$	$H_1 \to b\bar{b} = 82.4$, $\quad H_1 \to \tau^+\tau^- = 10.6$, $H_3 \to \widetilde\chi_2^0\widetilde\chi_3^0 = 13.8$, $\quad A_2 \to \widetilde\chi_2^0\widetilde\chi_4^0 = 12.0$, $\widetilde\chi_1^\pm \to \widetilde\chi_1^0 W = 52.3$, $\widetilde\chi_1^\pm \to \widetilde\chi_2^0 W = 47.7$, $\widetilde\chi_2^\pm \to \widetilde\chi_1^\pm Z = 25.6$, $\widetilde\chi_2^\pm \to \widetilde\chi_3^0 W = 24.8$, $\widetilde\chi_2^\pm \to \widetilde\chi_1^\pm H_2 = 24.1$, $\widetilde\chi_2^0 \to \widetilde\chi_1^0 H_1 = 50.4$, $\widetilde\chi_2^0 \to \widetilde\chi_1^0 Z = 46.3$, $\quad \widetilde\chi_3^0 \to \widetilde\chi_1^0 Z = 31.4$, $\widetilde\chi_3^0 \to \widetilde\chi_2^0 Z = 48.9$, $\widetilde\chi_3^0 \to \widetilde\chi_1^0 H_2 = 16.4$, $\widetilde\chi_4^0 \to \widetilde\chi_1^0 Z = 45.3$, $\quad \widetilde\chi_4^0 \to \widetilde\chi_2^0 Z = 14$, $\widetilde\chi_4^0 \to \widetilde\chi_1^0 H_2 = 20.4, \widetilde\chi_4^0 \to \widetilde\chi_2^0 H_1 = 17.2$, $\widetilde\chi_5^0 \to \widetilde\chi_3^0 Z = 21.4$, $\widetilde\chi_5^0 \to \widetilde\chi_1^\pm W = 50.4$, $\widetilde\chi_5^0 \to \widetilde\chi_4^0 H_2 = 19.5$

Table 4.1: The input parameters, neutralino admixtures, masses and branching ratios of the electroweakinos and Higgs bosons, decay length of the light singlet-dominated Higgs bosons, and the cross-section of electroweakino pair production at $\sqrt{s} = 14$ TeV, for benchmark point BP.
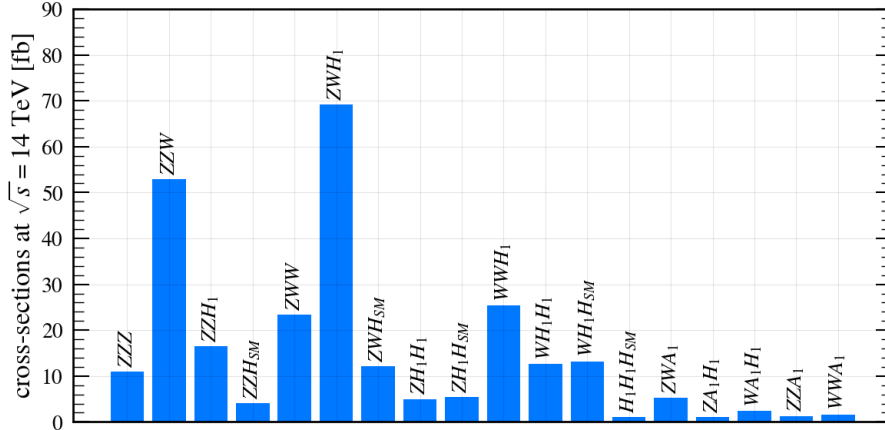

Figure 4.6: Production rates at the HL-LHC for all possible triple-boson channels from cascade decays of electroweakino pair production corresponding to benchmark point BP (see Table 4.1). Final states with a production rate of < 1 fb have been ignored.

MSSM framework.

We consider a benchmark point BP from the low LSP mass regime, $m_{\widetilde{\chi}_1^0} \lesssim m_{H_{SM}}/2$, in the allowed parameter space. The details of model parameters and the masses of electroweakinos and Higgs bosons are presented in Table 4.1. The branching ratios of the heavier charginos and neutralinos are also given, showing $\widetilde{\chi}_2^0$ with mass $m_{\widetilde{\chi}_2^0} = 123.9$ GeV as Bino-dominated with significant Higgsino admixture, while $\widetilde{\chi}_3^0, \widetilde{\chi}_4^0$ and $\widetilde{\chi}_1^\pm$ being Higgsino-dominated with masses 243.2, 244.7 and 233.6 GeV, respectively. This configuration results in $\widetilde{\chi}_1^\pm \widetilde{\chi}_3^0 + \widetilde{\chi}_1^\pm \widetilde{\chi}_4^0$ having the highest production cross-section at the HL-LHC among all possible chargino-neutralino pair production channels. Alternatively, a benchmark point with a Higgsino-dominated NLSP $\widetilde{\chi}_2^0$ could potentially lead to higher production rates for $\widetilde{\chi}_1^\pm \widetilde{\chi}_2^0$ and larger branching rates into final states with a singlet-like Higgs boson. However, it would preclude the triple-boson $+\not{E}_T$ final state. We proceed to analyze the production rates of potential triple-boson $+\not{E}_T$ final states arising from $pp \to \widetilde{\chi}_1^\pm \widetilde{\chi}_3^0 + \widetilde{\chi}_1^\pm \widetilde{\chi}_4^0$ for BP. We display our results in Fig. 4.6. Interestingly, the triple-boson final state with the highest production cross-section for BP is ZWH_1, featuring a light singlet-dominated Higgs boson unique to NMSSM-specific scenarios. We consider this decay channel for our collider analysis in the next section.

4.5 Direct Electroweakino searches in the ZWH_1 channel

We perform a detailed collider analysis to probe the electroweakinos at the HL-LHC through searches in the $pp \to \widetilde{\chi}_1^\pm \widetilde{\chi}_3^0 + \widetilde{\chi}_1^\pm \widetilde{\chi}_4^0 \to ZWH_1 + \not{E}_T$ channel, considering the benchmark point BP. As highlighted in Sec. 4.9, we choose the ZWH_1 channel due to its higher production rate among all potential triple-boson final states arising from the cascade decay of directly produced $\widetilde{\chi}_1^\pm \widetilde{\chi}_3^0$ or $\widetilde{\chi}_1^\pm \widetilde{\chi}_4^0$ pairs. The cascade decay chain for the ZWH_1 channel is outlined as follows,

$$\begin{aligned}
pp \to \widetilde{\chi}_1^\pm \widetilde{\chi}_3^0 &\to (\widetilde{\chi}_1^\pm \to W^\pm \widetilde{\chi}_1^0)(\widetilde{\chi}_3^0 \to Z(\widetilde{\chi}_2^0 \to H_1 \widetilde{\chi}_1^0)) \to ZW^\pm H_1 + \not{E}_T, \\
&\to \widetilde{\chi}_1^\pm \widetilde{\chi}_4^0 \to (\widetilde{\chi}_1^\pm \to W^\pm(\widetilde{\chi}_2^0 \to H_1 \widetilde{\chi}_1^0))(\widetilde{\chi}_4^0 \to Z\widetilde{\chi}_1^0) \to ZW^\pm H_1 + \not{E}_T.
\end{aligned} \tag{4.9}$$

At benchmark point BP, the tree-level cross-section for the process $pp \to \widetilde{\chi}_1^\pm \widetilde{\chi}_3^0 + \widetilde{\chi}_1^\pm \widetilde{\chi}_4^0$ is approximately 358 fb at the $\sqrt{s} = 14$ TeV LHC, as detailed in Table 4.1. The cascade decay chain in Eq. 4.9 results in a production rate of approximately 43 fb for the ZWH_1 final state. For the analysis, we consider the dominant decay mode of H_1: $H_1 \to b\bar{b}$, with a
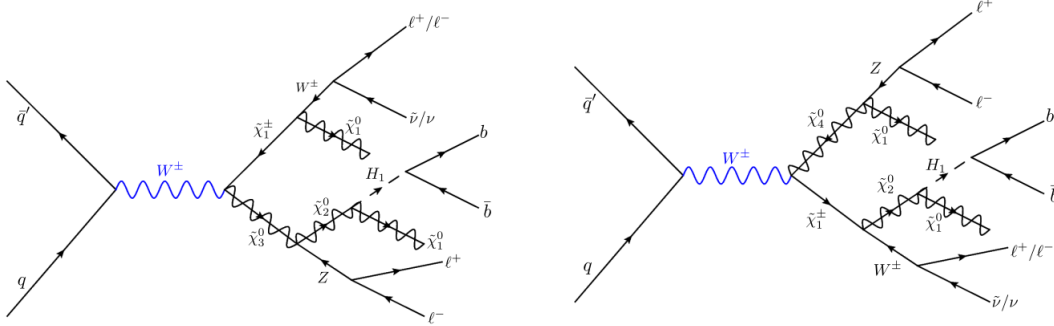
Figure 4.7: The leading order Feynman diagram for the signal process: $pp \to \widetilde{\chi}_1^\pm \widetilde{\chi}_3^0 + \widetilde{\chi}_1^\pm \widetilde{\chi}_4^0 \to ZW^\pm H_1 \to 3\ell + b\bar{b} + \slashed{E}_T$ ($\ell = e^\pm, \mu^\pm, \tau^\pm$).

branching ratio of $Br(H_1 \to b\bar{b}) \sim 82.4\%$. Furthermore, we exclusively focus on the leptonic decay modes of the Z and W bosons due to their cleaner signatures at the detector and to avoid large QCD backgrounds. Thus, the signal process features a final state with three charged leptons, two bottom quarks, along with missing energy owing to the LSP $\widetilde{\chi}_1^0$'s: $pp \to \widetilde{\chi}_1^\pm \widetilde{\chi}_3^0 + \widetilde{\chi}_1^\pm \widetilde{\chi}_4^0 \to ZW^\pm H_1 \to 3\ell + b\bar{b} + \slashed{E}_T$ ($\ell = e^\pm, \mu^\pm, \tau^\pm$). The leading order Feynman diagrams for the signal are presented in Fig. 4.7.

Dominant contributions to the background arise from top-pair production in association with the gauge bosons, $pp \to t\bar{t}W, t\bar{t}Z$, associated production with the SM Higgs boson, $t\bar{t}H_{SM}$, $ZWb\bar{b}$, VVV, $VV + \mathrm{jets}$, and VH_{SM} processes, where $V = W^\pm, Z$. We consider all possible decay topologies in the background processes that lead to the $3\ell + b\bar{b} + \slashed{E}_T$ final state. Furthermore, sub-dominant contributions from tH_{SM} and $t\bar{t}VV$ processes are also included in the analysis.

The signal and background events are generated at the parton-level with `MG5aMC@NLO v2.9.16` [256] utilizing the `NNPDF23LO` parton distribution function [448] with the `A14` tune [449]. The signal events for BP are generated using the `NMSSM` model file [137,450–452], with the masses, couplings, and branching ratios computed using `NMSSMTools`. Both signal and background events have been generated at the leading order, and higher-order effects are incorporated through K factors. Details of the generation-level cuts implemented in `MG5aMC@NLO v2.9.16` and cross-sections for the various processes have been included in Appendix A.2. Subsequently, showering and hadronization is performed using `Pythia-8` [373, 374], and fast detector response simuatation is performed with `Delphes-3.5.0` [259], uti-

lizing the default HL-LHC configuration card [375].

We select events containing exactly three isolated leptons l in the final state with transverse momentum $p_{T,\ell} \geq 15$ GeV and pseudorapidity $|\eta| < 4.0$. For electrons and muons, we impose the isolation criteria,

$$\frac{\sum p_T^{\Delta R < 0.2}}{p_{T,\ell'}} < 0.1 \quad \ell' = e, \mu, \tag{4.10}$$

where $\sum p_T^{\Delta R < 0.2}$ represents the sum of the transverse momentum of all other objects within a cone of radius $\Delta R \leq 0.2$ centred around the candidate lepton $\ell' = \{e, \mu\}$ carrying transverse momentum $p_{T,\ell'}$. Electrons and muons originating from the leptonically decaying τ's are also subject to the isolation criteria in Eq. (4.10). For hadronically decaying tau leptons, τ_h, we apply tau-jet tagging efficiencies derived from CMS using the DeepTau algorithm [453]. These efficiencies are valid for τ_h with $p_{T,\tau_h} > 20$ GeV and within $|\eta| < 2.3$. In other kinematic regions, we adopt the default tau-jet tagging efficiencies provided in the HL-LHC configuration card. We also impose $p_{T,\ell_1} > 32$ GeV and $p_{T,\ell_2} > 20$ GeV, where ℓ_1 and ℓ_2 are the isolated leptons with the highest and 2nd highest transverse momentum, respectively. Furthermore, two of the isolated leptons are required to form a same flavor opposite sign (SFOS) lepton pair with invariant mass close to the mass of the Z boson, $|m_Z - m_{\ell\ell}^{SFOS}| < 15$ GeV. The basic event selection cuts discussed until this point are summarized in Table 4.2.

Basic selection cuts
$n_{\ell'} = 3$
$p_{T\ell_1,\ell_2,\ell_3} > 32, 20, 15$ GeV
$|m_Z - m_{\ell\ell}| < 15$ GeV

Table 4.2: Summary of basic selection cuts.

As discussed previously, a characteristic feature of our signal process is the presence of the light CP-even Higgs boson H_1 in the final state, which predominantly decays into a $b\bar{b}$ pair. For our benchmark point BP, H_1 with mass $m_{H_1} = 14.2$ GeV originates from the decay mode $\widetilde{\chi}_2^0 \to H_1 \widetilde{\chi}_1^0$, where $\widetilde{\chi}_2^0$ and $\widetilde{\chi}_1^0$ have masses of 123.9 and 20.5 GeV, respectively. The relatively lower mass of H_1 coupled with the considerable mass difference between $\{\widetilde{\chi}_1^0 + H_1\}$ pair and the parent particle $\widetilde{\chi}_2^0$, results in boosted H_1, leading to collimated $b\bar{b}$ decay products which are typically challenging to resolve. The angular separation between the decay

product of the light Higgs, $\Delta R_{b\bar{b}}$, depends on the Higgs mass m_{H_1} and its transverse momentum $p_T^{H_1}$ as approximated by $\Delta R_{b\bar{b}} \simeq m_{H_1}/(p_T^{H_1}\sqrt{z(1-z)})$ [454], where z and $1-z$ denote the fractions of momentum carried by the two decay products. Parton-level analysis shows a peak at $\Delta R_{b\bar{b}} \sim 0.2$, which reflects $p_{T,H_1} >> m_{H_1}$. Given the relatively smaller $\Delta R_{b\bar{b}}$, we employ jet substructure techniques to identify the Higgs jet as a fatjet capable of capturing the inherent $b\bar{b}$ pair. We utilize the particle-flow (PF) algorithm [455,456] to reconstruct fat-jets using e-flow objects in `Delphes` [259]. These e-flow objects are comprised of PF tracks, including charged particle tracks, and PF towers, including neutral particles and charged particles without any associated tracks, with corrected calorimeter smearings. The electrons and muons are separately included in the PF objects. These objects are given as input to the Cambridge-Achen algorithm [457] with the jet radius parameter of $R = 0.7$ and the minimum p_T threshold of > 40 GeV, implemented in the `FastJet v3.2.1` [458] setup. The fatjets within $|\eta| < 4.0$ are further groomed using the SoftDrop technique [459] with free parameters $\beta = 0$ and $z_{cut} = 0.1$, following standard CMS strategies [263]. To identify the soft-dropped fatjets as the light Higgs jets, we employ the Mass-drop tagger [454,460] with parameters $\mu = 0.667$ and $y_{cut} > 0.01$, which identifies the two subjets j_a and j_b within the fatjets. j_a and j_b are then matched with the B-hadrons (the truth-level b-quarks just before hadronization) with $p_T > 10$ GeV and $|\eta| < 2.5$ at the generator-level, using a matching cone of radius $R < min(0.3, \Delta R_{j_a,j_b}/2)$, where $\Delta R_{j_a,j_b}$ represents the separation between j_a and j_b. This choice is motivated from Ref. [454]. If both subjets satisfy these criteria, the fatjet is identified as a tagged light Higgs jet H^j. In events with more than one H^j, the one with invariant mass closest to m_{H_1} is associated with the light singlet-dominated Higgs boson H_1. In this analysis, we impose the criteria, $n_{H^j} = 1$, where n_{H^j} is the number of tagged light Higgs fatjets. For our benchmark BP with $m_{H_1} = 14.2$ GeV, the tagging efficiency of this method is roughly 20%. In the remainder of this analysis, we will refer to the tagged H_1 jet as H_1^j, while the two b-quark matched subjets within the H_1 jet will be referred to as b_1 and b_2. In Fig. 4.8, we illustrate the mass distribution of the tagged Higgs jet, $m_{H_1^j}$, for the signal process $pp \to \widetilde{\chi}_1^\pm \widetilde{\chi}_3^0 \to ZW^\pm H_1 + \not{E}_T \to 3\ell + b\bar{b} + \not{E}_T$ (see Eq. (4.9)) and the dominant background processes. The $m_{H_1^j}$ distribution for the signal exhibits a sharp peak near m_{H_1}, owing to the comparatively smaller decay width of H_1 ($\Gamma_{H_1} = 9.47 \times 10^{-7}$ GeV), implying good mass resolution. On the other hand, the $m_{H_1^j}$ distributions for the background processes are flatter and do not exhibit any discernible sharp peaks. As such, the $m_{H_1^j}$ observable demonstrates an excellent potential for background reduction. We would like to
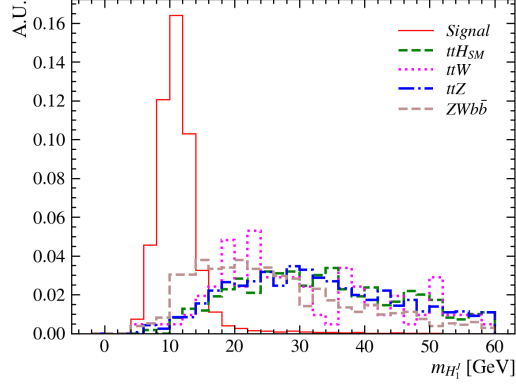
Figure 4.8: Distribution for the invariant mass of the tagged light Higgs jet H_1^j in the $pp \to \widetilde{\chi}_1^\pm \widetilde{\chi}_3^0 + \widetilde{\chi}_1^\pm \widetilde{\chi}_4^0 \to ZWH_1 + \cancel{E}_T \to 3\ell + b\overline{b} + \text{met}$ channel at the HL-LHC, corresponding to the benchmark point BP. Distributions for the dominant background processes are also illustrated.

note that a similar methodology can be extended to tau jets in scenarios where H_1 decays to $\tau_h\tau_h$ jets, offering further possibilities to improve the discovery potential of the signal at the LHC.

We perform a cut-based collider analysis by optimizing the selection cuts on

- $\Delta R(b_1, b_2)$: ΔR separation between the two b-like subjets associated with H_1^j,

- $\cancel{E}_T$: missing transverse energy,

- $\Delta R(\ell_W, H_{1_{b_1 b_2}})$: ΔR separation between the non-SFOS lepton l_W and $H_{1_{b_1 b_2}}$,

- $\Delta R(Z_{\ell\ell}^{SFOS}, H_{1_{b_1 b_2}})$: ΔR separation between the reconstructed Z boson and $H_{1_{b_1 b_2}}$,

- H_T: scalar sum of the transverse momentum of the three isolated leptons and the reconstructed H_I^j ,

- $m_{H_1^j}$: invariant mass of the reconstructed H_1 fatjet, and

- $M_T(H_1^j, \cancel{E}_T)$: transverse mass of the Higgs and missing energy system, defined as:

$$M_T(H_1^j, \cancel{E}_T) = \sqrt{m_{H_1^j}^2 + 2(E_T^{H_1^j}\cancel{E}_T - \overrightarrow{p}_T^{H_1^b}.\overrightarrow{\cancel{p}}_T)}. \tag{4.11}$$

155

We tailor a signal region SR to maximize the signal significance σ_S for the signal process in Eq. (4.9) for the benchmark point BP (see Table 4.1). The signal significance σ_S is defined as,

$$\sigma_S = \frac{S}{\sqrt{B + (B * \delta_S)^2}}, \tag{4.12}$$

where S and B are the signal and background yields, respectively, and δ_S represents the systematic uncertainty.
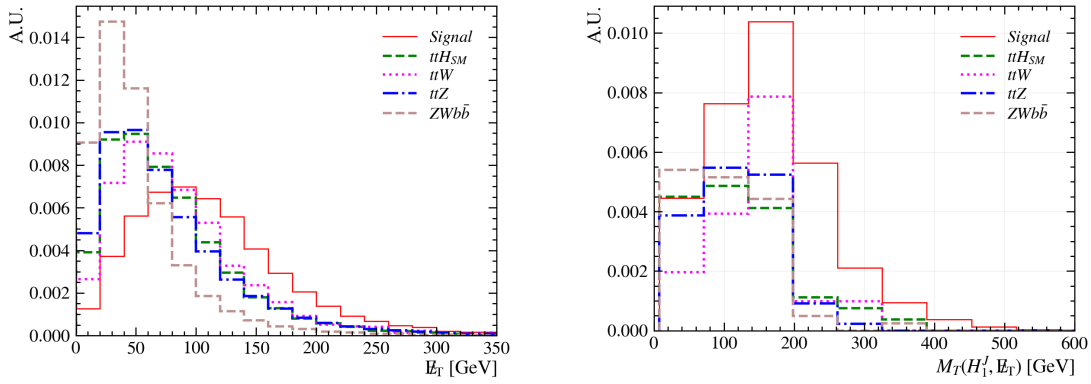

Figure 4.9: Distributions for the missing transverse energy $\not{E}_{\mathrm{T}}$ (*left*) and the transverse mass of the light Higgs fatjet and missing energy system $M_T(H_1^j, \not{E}_{\mathrm{T}})$ (*right*) in the $pp \to \widetilde{\chi}_1^{\pm} \widetilde{\chi}_3^0 + \widetilde{\chi}_1^{\pm} \widetilde{\chi}_4^0 \to ZW H_1 + \not{E}_{\mathrm{T}} \to 3\ell + \mathrm{b\overline{b}} + \mathrm{met}$ channel at the HL-LHC, for benchmark point BP. Distributions for the dominant backgrounds are also shown.

We consider various combinations of selection cuts on the kinematic observables, aiming to maximize σ_S for the signal process. It is observed that the subset of observables $\{\not{E}_{\mathrm{T}}, \mathrm{m}_{\mathrm{H}_1^j}, \mathrm{M}_{\mathrm{T}}(\mathrm{H}_1^j, \not{E}_{\mathrm{T}})\}$ leads to the most optimal σ_S. In Fig. 4.9, we illustrate the $\not{E}_{\mathrm{T}}$ and $M_T(H_1^j, \not{E}_{\mathrm{T}})$ distributions for the signal process and the dominant backgrounds: $t\bar{t}Z$, $t\bar{t}W$, $t\bar{t}H_{SM}$ and $ZWb\bar{b}$, after imposing the basic selection cuts in Table 4.2. The $\not{E}_{\mathrm{T}}$ distribution for the signal falls slowly compared to the backgrounds, with the tails extending to comparatively higher values. The $M_T(H_1^j, \not{E}_{\mathrm{T}})$ distribution for the signal displays a peak at $M_T(H_1^j, \not{E}_{\mathrm{T}}) \sim 150$ GeV, while the background processes peak at smaller values. The optimized selection cuts, applied sequentially, are listed in Table 4.3, along with the signal and background yields at the $\sqrt{s} = 14$ TeV LHC with $\mathcal{L} = 3000 \ fb^{-1}$. The event yields have been computed as $\sigma \times \mathrm{BR} \times \epsilon \times \mathcal{L}$, where $\sigma \times \mathrm{BR}$ are the production rates and ϵ is the efficiency

defined as the ratio of the events that pass the cuts to the total number of events. The signal significance values, computed using Eq. (4.12), are also presented for hypothetical scenarios with null and 5% systematic uncertainties. We obtain a signal significance of $\lesssim 1$ upon the imposition of the basic selection cuts. At this stage, the signal over background ratio stands at roughly 10^{-4}. Imposing $n_{Hj} \geq 1$ and requiring the invariant mass of the H_1 fatjet to be less than 18 GeV resulted in $\sigma_S = 7.1$ and 6.7 for $\delta_S = 0$ and 5%, respectively, with $S/B \sim 1$. We further impose a minimum threshold on $M_T(H_1^J, \not{E}_{\mathrm{T}}) > 150$ GeV, which improved σ_S to ~ 7.1 and 7.0, respectively. Our results indicate that the benchmark point BP can be probed at the HL-LHC through searches in the $pp \to ZW^{\pm}H_1 \to 3\ell + b\bar{b} + \not{E}_{\mathrm{T}}$ channel with discovery potential ($\sigma_S > 5\sigma$).

	SIG	ttW	ttZ	ttH_{SM}	$ZWb\bar{b}$	VVV	$VV+jets$	VH_{SM}	$ttVV$	tH_{SM}	σ_s	
											$\delta_S = 0$	$\delta_S = 5\%$
$\sigma \times \mathrm{BR} \times \ell$	2168	1207357	2009863	1173873	160243	903398	252096000	5368320	26438	169591	0.1	2×10^{-4}
Baseline Selection	402	2205	23181	5290	1136	5888	529371	14173	211	322	0.5	0.01
$\not{E}_{\mathrm{T}} \geq 60$ GeV	317	1372	12082	2904	332	2521	121223	3029	138	93	0.8	0.04
$n_{Hj} = 1$	53	37	285	147	38	14	135	18	4	< 1	2.0	1.2
$m_{H_1^j} \leq 18$ GeV	51	4	24	11	8	0	0	0	0	0	7.1	6.7
$M_T(H_1^j, \not{E}_{\mathrm{T}}) \geq 150$ GeV	26	2	7	3	1	0	0	0	0	0	7.1	7.0

Table 4.3: Signal and background yields in the $pp \to \widetilde{\chi}_1^{\pm}\widetilde{\chi}_3^0 + \widetilde{\chi}_1^{\pm}\widetilde{\chi}_4^0 \to ZWH_1 + \not{E}_{\mathrm{T}} \to 3\ell + \mathrm{b\bar{b}} + \mathrm{met}$ channel at the HL-LHC. The yields are presented at each step of the cut-based analysis for the benchmark point BP and the background processes including $ttW, ttZ, ttH_{SM}, ZWb\bar{b}, VVV, VV+jets, VH_{SM}, ttVV$ and tH_{SM}. Signal significance at the HL-LHC is also presented for two scenarios: null and 5% systematic uncertainties.

Through this benchmark analysis, our goal is to emphasize the importance of conducting targeted searches specifically designed for the allowed parameter points. It is also worth noting that the search strategy employed in this analysis could impact other regions of the currently allowed parameter space, especially in the low $m_{\widetilde{\chi}_1^0}$ regime where resonant s-channel annihilation plays a primary role in achieving the correct or underabundant DM relic density. Investigating the triple-boson final states involving H_1 or A_1 could be promising in these scenarios, and distinct signal regions could be designed for the parameter points featuring a light Higgs boson by adapting the cuts on the kinematic variables considered in these analyses. We intend to explore these aspects in future work.

4.6 Conclusion

In this work, we focused on exploring the parameter space within the NMSSM framework where a Singlino-dominated neutralino is a viable candidate for thermal dark matter. We concentrated on regions where the neutralino LSP's relic abundance is smaller than the observed cold dark matter relic density. The parameter space of our interest is constrained by various colliders and astrophysical probes, including LEP, rare B-meson decays, Higgs signal strengths, BSM Higgs searches, electroweakinos, sparticle searches at the LHC, and DM direct detection experiments. It is observed that a notable fraction of the currently allowed points are well within the reach of future spin-independent direct detection experiments. However, several currently allowed parameter points also lie below the neutrino scattering floor, rendering them inaccessible to future spin-independent direct detection probes.

In the low mass regime of the LSP neutralino, $m_{\widetilde{\chi}_1^0} < m_Z/2$, resonant annihilation via the s-channel exchange of a light A_1 or H_1 with mass $\sim 2m_{\widetilde{\chi}_1^0}$ is primarily responsible in achieving consistency with the upper limit on relic density. However, at higher LSP masses, $m_{\widetilde{\chi}_1^0} \gtrsim m_{H_{SM}}/2$, the absence of an additional BSM Higgs boson at twice the LSP mass, as prohibited by the Higgs mass rule, restricts efficient DM dilution in the early universe through resonant annihilation via Higgs exchange. In this mass regime, consistency with the relic density constraints is achieved through co-annihilation with the NLSPs such as $\widetilde{\chi}_2^0$ and $\widetilde{\chi}_1^\pm$. Assisted co-annihilation, where the $\widetilde{\chi}_1^0$ and the NLSP are in thermal equilibrium, also contributes significantly to DM annihilation before freeze-out.

Having identified the currently allowed parameter space, we then turned our attention to exploring non-conventional search channels to probe them at the HL-LHC. We particularly focus on identifying channels that would be rather challenging to access within the widely explored phenomenological-MSSM scenario. In this context, we explored the prospects of triple boson final states originating from direct electroweakino pair production in Sec. 4.4. We considered a benchmark point BP from the low LSP mass regime with $m_{\widetilde{\chi}_1^0} = 20.5$ GeV from our allowed parameter space, featuring a light singlet-dominated pseudoscalar Higgs boson with twice the LSP mass and scalar Higgs boson at $m_{H_1} = 14.2$ GeV. We analyzed the production rates for all potential electroweakino pair-produced final states involving triple bosons. Our investigation revealed that the $ZWH_1 + \slashed{E}_{\mathrm{T}}$ final state achieved the highest production rate for BP. This channel is particularly intriguing due to the presence of the light H_1, making it specific to the NMSSM framework. We performed

a detailed collider analysis in the $pp \to \widetilde{\chi}_1^\pm \widetilde{\chi}_3^0 + \widetilde{\chi}_1^\pm \widetilde{\chi}_4^0 \to ZW(H_1 \to b\bar{b}) + \not{E}_{\mathrm{T}} \to 3\ell + \mathrm{b\bar{b}} + \not{E}_{\mathrm{T}}$ channel for BP in Sec. 4.5. Considering the boosted nature of H_1, we perform a fatjet analysis and identify the two b-like subjets within the fatjets to effectively identify the Higgs jet. We have presented the details of the optimized selection cuts in Table 4.3 and obtained a signal significance of $\sim 7\sigma$, accounting for a systematic uncertainty of 5%. This illustrates the potential discovery capability of BP at the HL-LHC through searches in this channel.

Our results indicate the promising potential of performing benchmark-specific dedicated searches at the colliders to complement the conventional search strategies. It may be worth extending the search channel considered in this work to explore other allowed regions within our parameter space of interest. Furthermore, resonant heavy Higgs production decaying into the same electroweakino pairs could offer additional probes to further boost the sensitivity at the future colliders. We defer these explorations to a future work.

APPENDIX A

APPENDIX FOR CHAPTER 3

A.1 Indirect detection
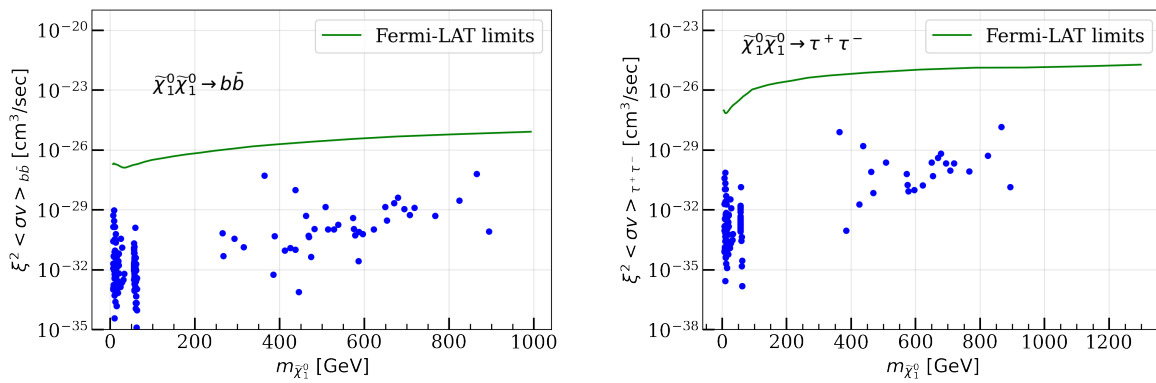
Figure A.1: Allowed parameter space points are shown in the plane of ξ^2 scaled thermally averaged LSP DM annihilation cross section times velocity in the $b\bar{b}$ (*left*) and $\tau\tau$ (*right*) channels versus the LSP neutralino mass $m_{\widetilde{\chi}_1^0}$.

A.2 Summarising the cross-sections and generator level cuts for the SM backgrounds

Backgrounds	Process	Generation-level cuts ($\ell = e^{\pm}, \mu^{\pm}, \tau^{\pm}$) (NA : Not Applied)	Cross section (fb)
ttZ	$pp \to t\bar{t}Z$	NA	1046.9
ttW	$pp \to t\bar{t}W^{\pm}$	NA	628.8
ttH_{SM}	$pp \to t\bar{t}H_{SM}$	NA	611.4
$ZWb\bar{b}$	$pp \to ZW^{\pm}b\bar{b}$	$p_{T,b} > 15$ GeV, $\|\eta_b\| < 4, \Delta R_{b,b} > 0.2$	83.46
VVV	$pp \to VVV, (V = W^{\pm}, Z)$	NA	470.5
VH_{SM}	$pp \to VH_{SM}$	NA	2796
$ttVV$	$pp \to t\bar{t}VV$	NA	13.77
tH_{SM}	model loop SM $pp > W^{\pm} \to H_{SM}\ t/\bar{t}\ b/\bar{b}$ [QCD]	$m_{\ell^+\ell^-} > 30$ GeV	3.18
	model loop SM no b mass $pp \to H_{SM}\ t/\bar{t}\ j\ \$\$\ W^{\pm}$ [QCD]		85.15
$VV + jets$	$pp \to VVj$ $pp \to VVjj$	$p_{t,j} > 20$ GeV, $\|\eta_j\| < 4, \Delta R_{j.j} > 0.2$	131300

Table A.1: Generation level cuts and cross-sections for the various Standard Model backgrounds used in the analyses. Cross-sections are obtained from `Madgraph` LO value multiplied by the K factors.

BIBLIOGRAPHY

[1] Georges Aad et al. Observation of a new particle in the search for the Standard Model Higgs boson with the ATLAS detector at the LHC. *Phys. Lett. B*, 716:1–29, 2012. arXiv:1207.7214, doi:10.1016/j.physletb.2012.08.020.

[2] Serguei Chatrchyan et al. Observation of a New Boson at a Mass of 125 GeV with the CMS Experiment at the LHC. *Phys. Lett. B*, 716:30–61, 2012. arXiv:1207.7235, doi:10.1016/j.physletb.2012.08.021.

[3] Abdus Salam. Weak and Electromagnetic Interactions. *Conf. Proc. C*, 680519:367–377, 1968. doi:10.1142/9789812795915_0034.

[4] Steven Weinberg. A Model of Leptons. *Phys. Rev. Lett.*, 19:1264–1266, 1967. doi:10.1103/PhysRevLett.19.1264.

[5] Sheldon L. Glashow. Partial-symmetries of weak interactions. *Nuclear Physics*, 22(4):579–588, 1961. URL: https://www.sciencedirect.com/science/article/pii/0029558261904692, doi:10.1016/0029-5582(61)90469-2.

[6] Murray Gell-Mann. A Schematic Model of Baryons and Mesons. *Phys. Lett.*, 8:214–215, 1964. doi:10.1016/S0031-9163(64)92001-3.

[7] Sudhir K. Vempati. Introduction to MSSM. 1 2012. arXiv:1201.0334.

[8] Peter W. Higgs. Broken symmetries and the masses of gauge bosons. *Phys. Rev. Lett.*, 13:508–509, Oct 1964. URL: https://link.aps.org/doi/10.1103/PhysRevLett.13.508, doi:10.1103/PhysRevLett.13.508.

[9] F. Englert and R. Brout. Broken symmetry and the mass of gauge vector mesons. *Phys. Rev. Lett.*, 13:321–323, Aug 1964. URL: https://link.aps.org/doi/10.1103/PhysRevLett.13.321, doi:10.1103/PhysRevLett.13.321.

[10] T. W. B. Kibble. Symmetry breaking in nonAbelian gauge theories. *Phys. Rev.*, 155:1554–1561, 1967. doi:10.1103/PhysRev.155.1554.

[11] G. S. Guralnik, C. R. Hagen, and T. W. B. Kibble. Global Conservation Laws and Massless Particles. *Phys. Rev. Lett.*, 13:585–587, 1964. doi:10.1103/PhysRevLett.13.585.

[12] P. A. Zyla et al. Review of Particle Physics. *PTEP*, 2020(8):083C01, 2020. doi:10.1093/ptep/ptaa104.

[13] Jens Erler and Matthias Schott. Electroweak Precision Tests of the Standard Model after the Discovery of the Higgs Boson. *Prog. Part. Nucl. Phys.*, 106:68–119, 2019. arXiv:1902.05142, doi:10.1016/j.ppnp.2019.02.007.

[14] K. A. Olive et al. Review of Particle Physics. *Chin. Phys. C*, 38:090001, 2014. doi:10.1088/1674-1137/38/9/090001.

[15] Roel Aaij et al. Test of lepton universality in beauty-quark decays. *Nature Phys.*, 18(3):277–282, 2022. [Addendum: Nature Phys. 19, (2023)]. arXiv:2103.11769, doi:10.1038/s41567-023-02095-3.

[16] Andreas Crivellin and Martin Hoferichter. Hints of lepton flavor universality violations. *Science*, 374(6571):1051, 2021. arXiv:2111.12739, doi:10.1126/science.abk2450.

[17] Li-Sheng Geng, Benjamín Grinstein, Sebastian Jäger, Shuang-Yi Li, Jorge Martin Camalich, and Rui-Xiang Shi. Implications of new evidence for lepton-universality violation in b→sℓ+ℓ- decays. *Phys. Rev. D*, 104(3):035029, 2021. arXiv:2103.12738, doi:10.1103/PhysRevD.104.035029.

[18] Nicola Cabibbo. Unitary symmetry and leptonic decays. *Phys. Rev. Lett.*, 10:531–533, Jun 1963. URL: https://link.aps.org/doi/10.1103/PhysRevLett.10.531, doi:10.1103/PhysRevLett.10.531.

[19] Makoto Kobayashi and Toshihide Maskawa. CP-Violation in the Renormalizable Theory of Weak Interaction. *Progress of Theoretical Physics*, 49(2):652–657, 02 1973. arXiv:https://academic.oup.com/ptp/article-pdf/49/2/652/5257692/49-2-652.pdf, doi:10.1143/PTP.49.652.

[20] Ling-Lie Chau and Wai-Yee Keung. Comments on the parametrization of the kobayashi-maskawa matrix. *Phys. Rev. Lett.*, 53:1802–1805, Nov 1984. URL: https://link.aps.org/doi/10.1103/PhysRevLett.53.1802, doi:10.1103/PhysRevLett.53.1802.

[21] Y. Fukuda et al. Evidence for oscillation of atmospheric neutrinos. *Phys. Rev. Lett.*, 81:1562–1567, 1998. arXiv:hep-ex/9807003, doi:10.1103/PhysRevLett.81.1562.

[22] Claudio Giganti, Stéphane Lavignac, and Marco Zito. Neutrino oscillations: The rise of the PMNS paradigm. *Prog. Part. Nucl. Phys.*, 98:1–54, 2018. arXiv:1710.00715, doi:10.1016/j.ppnp.2017.10.001.

[23] F. J. Hasert et al. Observation of Neutrino Like Interactions Without Muon Or Electron in the Gargamelle Neutrino Experiment. *Phys. Lett. B*, 46:138–140, 1973. doi:10.1016/0370-2693(73)90499-1.

[24] F.J. Hasert, H. Faissner, W. Krenz, J. Von Krogh, et al. Search for elastic muon-neutrino electron scattering. *Physics Letters B*, 46(1):121–124, 1973. URL: https://www.sciencedirect.com/science/article/pii/0370269373904942, doi:10.1016/0370-2693(73)90494-2.

[25] G. Arnison et al. Experimental Observation of Isolated Large Transverse Energy Electrons with Associated Missing Energy at $\sqrt{s} = 540$ GeV. *Phys. Lett. B*, 122:103–116, 1983. doi:10.1016/0370-2693(83)91177-2.

[26] M. Banner et al. Observation of Single Isolated Electrons of High Transverse Momentum in Events with Missing Transverse Energy at the CERN anti-p p Collider. *Phys. Lett. B*, 122:476–485, 1983. doi:10.1016/0370-2693(83)91605-2.

[27] G. Arnison et al. Experimental Observation of Lepton Pairs of Invariant Mass Around 95-GeV/c**2 at the CERN SPS Collider. *Phys. Lett. B*, 126:398–410, 1983. doi:10.1016/0370-2693(83)90188-0.

[28] P. Bagnaia et al. Evidence for $Z^0 \to e^+e^-$ at the CERN $\overline{p}p$ Collider. *Phys. Lett. B*, 129:130–140, 1983. `doi:10.1016/0370-2693(83)90744-X`.

[29] S. L. Glashow, J. Iliopoulos, and L. Maiani. Weak Interactions with Lepton-Hadron Symmetry. *Phys. Rev. D*, 2:1285–1292, 1970. `doi:10.1103/PhysRevD.2.1285`.

[30] S. Schael et al. Electroweak Measurements in Electron-Positron Collisions at W-Boson-Pair Energies at LEP. *Phys. Rept.*, 532:119–244, 2013. `arXiv:1302.3415`, `doi:10.1016/j.physrep.2013.07.004`.

[31] F. Abe et al. Observation of top quark production in $\overline{p}p$ collisions. *Phys. Rev. Lett.*, 74:2626–2631, 1995. `arXiv:hep-ex/9503002`, `doi:10.1103/PhysRevLett.74.2626`.

[32] S. Abachi et al. Observation of the top quark. *Phys. Rev. Lett.*, 74:2632–2637, 1995. `arXiv:hep-ex/9503003`, `doi:10.1103/PhysRevLett.74.2632`.

[33] G. W. Bennett et al. Final Report of the Muon E821 Anomalous Magnetic Moment Measurement at BNL. *Phys. Rev. D*, 73:072003, 2006. `arXiv:hep-ex/0602035`, `doi:10.1103/PhysRevD.73.072003`.

[34] D. M. Webber et al. Measurement of the Positive Muon Lifetime and Determination of the Fermi Constant to Part-per-Million Precision. *Phys. Rev. Lett.*, 106:041803, 2011. `arXiv:1010.0991`, `doi:10.1103/PhysRevLett.106.079901`.

[35] C.Y. Prescott et al. Parity non-conservation in inelastic electron scattering. *Physics Letters B*, 77(3):347–352, 1978. URL: `https://www.sciencedirect.com/science/article/pii/0370269378907220`, `doi:10.1016/0370-2693(78)90722-0`.

[36] C.Y. Prescott et al. Further measurements of parity non-conservation in inelastic electron scattering. *Physics Letters B*, 84(4):524–528, 1979. URL: `https://www.sciencedirect.com/science/article/pii/037026937991253X`, `doi:10.1016/0370-2693(79)91253-X`.

[37] S. C. Bennett and C. E. Wieman. Measurement of the $6S \to 7S$ transition polarizability in atomic cesium and an improved test of the standard model. *Phys. Rev. Lett.*, 82:2484–2487, Mar 1999. URL: `https://link.aps.org/doi/10.1103/PhysRevLett.82.2484`, `doi:10.1103/PhysRevLett.82.2484`.

[38] M. Baak, M. Goebel, J. Haller, A. Hoecker, D. Kennedy, R. Kogler, K. Moenig, M. Schott, and J. Stelzer. The Electroweak Fit of the Standard Model after the Discovery of a New Boson at the LHC. *Eur. Phys. J. C*, 72:2205, 2012. `arXiv:1209.2716`, `doi:10.1140/epjc/s10052-012-2205-9`.

[39] Johannes Haller, Andreas Hoecker, Roman Kogler, Klaus Mönig, and Jörg Stelzer. Status of the global electroweak fit with Gfitter in the light of new precision measurements. *PoS*, ICHEP2022:897, 11 2022. `arXiv:2211.07665`, `doi:10.22323/1.414.0897`.

[40] Shinya Kanemura, Takahiro Kubota, and Eiichi Takasugi. Lee-quigg-thacker bounds for higgs boson masses in a two-doublet model. *Physics Letters B*, 313(1):155–160, 1993. URL: `https://www.sciencedirect.com/science/article/pii/0370269393912052`, `doi:10.1016/0370-2693(93)91205-2`.

[41] N. Cabibbo, L. Maiani, G. Parisi, and R. Petronzio. Bounds on the Fermions and Higgs Boson Masses in Grand Unified Theories. *Nucl. Phys. B*, 158:295–305, 1979. `doi:10.1016/0550-3213(79)90167-6`.

[42] J. Ellis, J. R. Espinosa, G. F. Giudice, A. Hoecker, and A. Riotto. The Probable Fate of the Standard Model. *Phys. Lett. B*, 679:369–375, 2009. `arXiv:0906.0954`, `doi:10.1016/j.physletb.2009.07.054`.

[43] Giuseppe Degrassi, Stefano Di Vita, Joan Elias-Miro, Jose R. Espinosa, Gian F. Giudice, Gino Isidori, and Alessandro Strumia. Higgs mass and vacuum stability in the Standard Model at NNLO. *JHEP*, 08:098, 2012. arXiv:1205.6497, doi:10.1007/JHEP08(2012)098.

[44] G. Altarelli, T. Sjostrand, and F. Zwirner, editors. *Physics at LEP2: Vol. 1*, CERN Yellow Reports: Conference Proceedings, 2 1996. doi:10.5170/CERN-1996-001-V-1.

[45] Marumi M. Kado and Christopher G. Tully. The searches for higgs bosons at lep. *Annual Review of Nuclear and Particle Science*, 52(1):65–113, 2002. doi:10.1146/annurev.nucl.52.050102.090656.

[46] Updated Combination of CDF and D0 Searches for Standard Model Higgs Boson Production with up to 10.0 fb^{-1} of Data. 7 2012. arXiv:1207.0449.

[47] Georges Aad et al. A detailed map of Higgs boson interactions by the ATLAS experiment ten years after the discovery. *Nature*, 607(7917):52–59, 2022. [Erratum: Nature 612, E24 (2022)]. arXiv:2207.00092, doi:10.1038/s41586-022-04893-w.

[48] Marco Bonvini, Simone Marzani, Claudio Muselli, and Luca Rottoli. On the Higgs cross section at N^{3}LO+N^{3}LL and its uncertainty. *JHEP*, 08:105, 2016. arXiv:1603.08000, doi:10.1007/JHEP08(2016)105.

[49] D. de Florian et al. Handbook of LHC Higgs Cross Sections: 4. Deciphering the Nature of the Higgs Sector. 2/2017, 10 2016. arXiv:1610.07922, doi:10.23731/CYRM-2017-002.

[50] JulieMalcles. Sm higgs production cross sections at $\sqrt{s} = 13$ tev (update in cern report4 2016), 2023. https://twiki.cern.ch/twiki/bin/view/LHCPhysics/CERNYellowReportPageAt13TeV.

[51] Robert Harlander, Michael Kramer, and Markus Schumacher. Bottom-quark associated Higgs-boson production: reconciling the four- and five-flavour scheme approach. 12 2011. arXiv:1112.3478.

[52] Albert M Sirunyan et al. Observation of t$\bar{t}$H production. *Phys. Rev. Lett.*, 120(23):231801, 2018. arXiv:1804.02610, doi:10.1103/PhysRevLett.120.231801.

[53] M. Aaboud et al. Observation of Higgs boson production in association with a top quark pair at the LHC with the ATLAS detector. *Phys. Lett. B*, 784:173–191, 2018. arXiv:1806.00425, doi:10.1016/j.physletb.2018.07.035.

[54] Morad Aaboud et al. Observation of $H \to b\bar{b}$ decays and VH production with the ATLAS detector. *Phys. Lett. B*, 786:59–86, 2018. arXiv:1808.08238, doi:10.1016/j.physletb.2018.09.013.

[55] A. M. Sirunyan et al. Observation of Higgs boson decay to bottom quarks. *Phys. Rev. Lett.*, 121(12):121801, 2018. arXiv:1808.08242, doi:10.1103/PhysRevLett.121.121801.

[56] Albert M Sirunyan et al. Observation of the Higgs boson decay to a pair of τ leptons with the CMS detector. *Phys. Lett. B*, 779:283–316, 2018. arXiv:1708.00373, doi:10.1016/j.physletb.2018.02.004.

[57] Morad Aaboud et al. Cross-section measurements of the Higgs boson decaying into a pair of τ-leptons in proton-proton collisions at $\sqrt{s} = 13$ TeV with the ATLAS detector. *Phys. Rev. D*, 99:072001, 2019. arXiv:1811.08856, doi:10.1103/PhysRevD.99.072001.

[58] Georges Aad et al. Evidence for the Higgs Boson Decay to a Z Boson and a Photon at the LHC. *Phys. Rev. Lett.*, 132:021803, 2024. arXiv:2309.03501, doi:10.1103/PhysRevLett.132.021803.

[59] Georges Aad et al. Measurement of Top Quark Polarization in Top-Antitop Events from Proton-Proton Collisions at $\sqrt{s}$ = 7 TeV Using the ATLAS Detector. *Phys. Rev. Lett.*, 111(23):232002, 2013. arXiv:1307.6511, doi:10.1103/PhysRevLett.111.232002.

[60] Markus Cristinziani and Martijn Mulders. Top-quark physics at the Large Hadron Collider. *J. Phys. G*, 44(6):063001, 2017. arXiv:1606.00327, doi:10.1088/1361-6471/44/6/063001.

[61] Cen Zhang and Scott Willenbrock. Effective-Field-Theory Approach to Top-Quark Production and Decay. *Phys. Rev. D*, 83:034006, 2011. arXiv:1008.3869, doi:10.1103/PhysRevD.83.034006.

[62] M. Fischer, S. Groote, J. G. Korner, and M. C. Mauser. Complete angular analysis of polarized top decay at O(alpha(s)). *Phys. Rev. D*, 65:054036, 2002. arXiv:hep-ph/0101322, doi:10.1103/PhysRevD.65.054036.

[63] Andrzej Czarnecki. QCD corrections to the decay t —> W b in dimensional regularization. *Phys. Lett. B*, 252:467–470, 1990. doi:10.1016/0370-2693(90)90571-M.

[64] Chong Sheng Li, Robert J. Oakes, and Tzu Chiang Yuan. QCD corrections to $t \rightarrow W^+b$. *Phys. Rev. D*, 43:3759–3762, 1991. doi:10.1103/PhysRevD.43.3759.

[65] Werner Bernreuther and Zong-Guo Si. Top quark spin correlations and polarization at the LHC: standard model predictions and effects of anomalous top chromo moments. *Phys. Lett. B*, 725:115–122, 2013. [Erratum: Phys.Lett.B 744, 413–413 (2015)]. arXiv:1305.2066, doi:10.1016/j.physletb.2013.06.051.

[66] Werner Bernreuther, Michael Fuecker, and Zong-Guo Si. Weak interaction corrections to hadronic top quark pair production. *Phys. Rev. D*, 74:113005, 2006. arXiv:hep-ph/0610334, doi:10.1103/PhysRevD.74.113005.

[67] Werner Bernreuther, Michael Fucker, and Zong-Guo Si. Weak interaction corrections to hadronic top quark pair production: Contributions from quark-gluon and b anti-b induced reactions. *Phys. Rev. D*, 78:017503, 2008. arXiv:0804.1237, doi:10.1103/PhysRevD.78.017503.

[68] Johann H. Kuhn, A. Scharf, and P. Uwer. Electroweak effects in top-quark pair production at hadron colliders. *Eur. Phys. J. C*, 51:37–53, 2007. arXiv:hep-ph/0610335, doi:10.1140/epjc/s10052-007-0275-x.

[69] J. H. Kühn, A. Scharf, and P. Uwer. Weak Interactions in Top-Quark Pair Production at Hadron Colliders: An Update. *Phys. Rev. D*, 91(1):014020, 2015. arXiv:1305.5773, doi:10.1103/PhysRevD.91.014020.

[70] W. G. D. Dharmaratna and Gary R. Goldstein. Gluon fusion as a source for massive-quark polarization. *Phys. Rev. D*, 41:1731–1735, Mar 1990. URL: https://link.aps.org/doi/10.1103/PhysRevD.41.1731, doi:10.1103/PhysRevD.41.1731.

[71] Werner Bernreuther, Arnd Brandenburg, and Peter Uwer. Transverse polarization of top quark pairs at the Tevatron and the large hadron collider. *Phys. Lett. B*, 368:153–162, 1996. arXiv:hep-ph/9510300, doi:10.1016/0370-2693(95)01475-6.

[72] G. L. Kane, G. A. Ladinsky, and C. P. Yuan. Using the top quark for testing standard-model polarization and CP predictions. *Phys. Rev. D*, 45:124–141, Jan 1992. URL: https://link.aps.org/doi/10.1103/PhysRevD.45.124, doi:10.1103/PhysRevD.45.124.

[73] Gregory Mahlon and Stephen J. Parke. Single top quark production at the LHC: Understanding spin. *Phys. Lett. B*, 476:323–330, 2000. arXiv:hep-ph/9912458, doi:10.1016/S0370-2693(00)00149-0.

[74] Reinhard Schwienhorst, C. P. Yuan, Charles Mueller, and Qing-Hong Cao. Single top quark production and decay in the *t*-channel at next-to-leading order at the LHC. *Phys. Rev. D*, 83:034019, 2011. `arXiv:1012.5132`, `doi:10.1103/PhysRevD.83.034019`.

[75] Georges Aad et al. Measurement of Spin Correlation in Top-Antitop Quark Events and Search for Top Squark Pair Production in pp Collisions at $\sqrt{s} = 8$ TeV Using the ATLAS Detector. *Phys. Rev. Lett.*, 114(14):142001, 2015. `arXiv:1412.4742`, `doi:10.1103/PhysRevLett.114.142001`.

[76] Werner Bernreuther, Dennis Heisler, and Zong-Guo Si. A set of top quark spin correlation and polarization observables for the LHC: Standard Model predictions and new physics contributions. *JHEP*, 12:026, 2015. `arXiv:1508.05271`, `doi:10.1007/JHEP12(2015)026`.

[77] Vardan Khachatryan et al. Search for anomalous Wtb couplings and flavour-changing neutral currents in t-channel single top quark production in pp collisions at $\sqrt{s} = 7$ and 8 TeV. *JHEP*, 02:028, 2017. `arXiv:1610.03545`, `doi:10.1007/JHEP02(2017)028`.

[78] Brock Tweedie. Better Hadronic Top Quark Polarimetry. *Phys. Rev. D*, 90(9):094010, 2014. `arXiv:1401.3021`, `doi:10.1103/PhysRevD.90.094010`.

[79] Arnd Brandenburg, Z. G. Si, and P. Uwer. QCD corrected spin analyzing power of jets in decays of polarized top quarks. *Phys. Lett. B*, 539:235–241, 2002. `arXiv:hep-ph/0205023`, `doi:10.1016/S0370-2693(02)02098-1`.

[80] W. Bernreuther, P. González, and C. Mellein. Decays of polarized top quarks to lepton, neutrino and jets at NLO QCD. *Eur. Phys. J. C*, 74(3):2815, 2014. `arXiv:1401.5930`, `doi:10.1140/epjc/s10052-014-2815-5`.

[81] Rohini M. Godbole, Kumar Rao, Saurabh D. Rindani, and Ritesh K. Singh. On measurement of top polarization as a probe of $t\bar{t}$ production mechanisms at the LHC. *JHEP*, 11:144, 2010. `arXiv:1010.1458`, `doi:10.1007/JHEP11(2010)144`.

[82] Jessie Shelton. Polarized tops from new physics: signals and observables. *Phys. Rev. D*, 79:014032, 2009. `arXiv:0811.0569`, `doi:10.1103/PhysRevD.79.014032`.

[83] T. M. C. Abbott et al. Dark Energy Survey Year 3 results: Cosmological constraints from galaxy clustering and weak lensing. *Phys. Rev. D*, 105(2):023520, 2022. `arXiv:2105.13549`, `doi:10.1103/PhysRevD.105.023520`.

[84] Shadab Alam et al. Completed SDSS-IV extended Baryon Oscillation Spectroscopic Survey: Cosmological implications from two decades of spectroscopic surveys at the Apache Point Observatory. *Phys. Rev. D*, 103(8):083533, 2021. `arXiv:2007.08991`, `doi:10.1103/PhysRevD.103.083533`.

[85] M. Aker et al. Direct neutrino-mass measurement with sub-electronvolt sensitivity. *Nature Phys.*, 18(2):160–166, 2022. `arXiv:2105.08533`, `doi:10.1038/s41567-021-01463-1`.

[86] V. N. Aseev et al. An upper limit on electron antineutrino mass from Troitsk experiment. *Phys. Rev. D*, 84:112003, 2011. `arXiv:1108.5034`, `doi:10.1103/PhysRevD.84.112003`.

[87] K. Assamagan et al. Upper limit of the muon-neutrino mass and charged pion mass from momentum analysis of a surface muon beam. *Phys. Rev. D*, 53:6065–6077, 1996. `doi:10.1103/PhysRevD.53.6065`.

[88] R. Barate et al. An Upper limit on the tau-neutrino mass from three-prong and five-prong tau decays. *Eur. Phys. J. C*, 2:395–406, 1998. `doi:10.1007/s100520050149`.

[89] X. Qian and P. Vogel. Neutrino mass hierarchy. *Progress in Particle and Nuclear Physics*, 83:1–30, 2015. URL: https://www.sciencedirect.com/science/article/pii/S0146641015000307, doi:10.1016/j.ppnp.2015.05.002.

[90] Laurent Canetti, Marco Drewes, and Mikhail Shaposhnikov. Matter and Antimatter in the Universe. *New J. Phys.*, 14:095012, 2012. arXiv:1204.4186, doi:10.1088/1367-2630/14/9/095012.

[91] N. Aghanim et al. Planck 2018 results. VI. Cosmological parameters. *Astron. Astrophys.*, 641:A6, 2020. [Erratum: Astron.Astrophys. 652, C4 (2021)]. arXiv:1807.06209, doi:10.1051/0004-6361/201833910.

[92] Richard H. Cyburt. Primordial nucleosynthesis for the new cosmology: Determining uncertainties and examining concordance. *Phys. Rev. D*, 70:023505, 2004. arXiv:astro-ph/0401091, doi:10.1103/PhysRevD.70.023505.

[93] A. D. Sakharov. Violation of CP Invariance, C asymmetry, and baryon asymmetry of the universe. *Pisma Zh. Eksp. Teor. Fiz.*, 5:32–35, 1967. doi:10.1070/PU1991v034n05ABEH002497.

[94] Stephen L. Adler. Axial-vector vertex in spinor electrodynamics. *Phys. Rev.*, 177:2426–2438, Jan 1969. URL: https://link.aps.org/doi/10.1103/PhysRev.177.2426, doi:10.1103/PhysRev.177.2426.

[95] J. S. Bell and R. Jackiw. A PCAC puzzle: $\pi^0 \to \gamma\gamma$ in the σ model. *Nuovo Cim. A*, 60:47–61, 1969. doi:10.1007/BF02823296.

[96] K. Kajantie, M. Laine, K. Rummukainen, and Mikhail E. Shaposhnikov. Is there a hot electroweak phase transition at $m_H \gtrsim m_W$? *Phys. Rev. Lett.*, 77:2887–2890, 1996. arXiv:hep-ph/9605288, doi:10.1103/PhysRevLett.77.2887.

[97] C. Jarlskog. Commutator of the quark mass matrices in the standard electroweak model and a measure of maximal CP nonconservation. *Phys. Rev. Lett.*, 55:1039–1042, Sep 1985. URL: https://link.aps.org/doi/10.1103/PhysRevLett.55.1039, doi:10.1103/PhysRevLett.55.1039.

[98] Vera C. Rubin and Jr. Ford, W. Kent. Rotation of the Andromeda Nebula from a Spectroscopic Survey of Emission Regions. , 159:379, February 1970. doi:10.1086/150317.

[99] Alejandro Ibarra. Neutrinos and dark matter. *AIP Conference Proceedings*, 1666(1):140004, 07 2015. arXiv:https://pubs.aip.org/aip/acp/article-pdf/doi/10.1063/1.4915588/13133116/140004_1_online.pdf, doi:10.1063/1.4915588.

[100] Genevieve Belanger, Alexander Pukhov, and Geraldine Servant. Dirac Neutrino Dark Matter. *JCAP*, 01:009, 2008. arXiv:0706.0526, doi:10.1088/1475-7516/2008/01/009.

[101] Manoranjan Dutta, Subhaditya Bhattacharya, Purusottam Ghosh, and Narendra Sahu. Singlet-Doublet Majorana Dark Matter and Neutrino Mass in a minimal Type-I Seesaw Scenario. *JCAP*, 03:008, 2021. arXiv:2009.00885, doi:10.1088/1475-7516/2021/03/008.

[102] N. Jarosik, C. L. Bennett, J. Dunkley, B. Gold, M. R. Greason, M. Halpern, R. S. Hill, G. Hinshaw, A. Kogut, E. Komatsu, D. Larson, M. Limon, S. S. Meyer, M. R. Nolta, N. Odegard, L. Page, K. M. Smith, D. N. Spergel, G. S. Tucker, J. L. Weiland, E. Wollack, and E. L. Wright. Seven-year wilkinson microwave anisotropy probe (wmap*) observations: Sky maps, systematic errors, and basic results. *The Astrophysical Journal Supplement Series*, 192(2):14, jan 2011. URL: https://dx.doi.org/10.1088/0067-0049/192/2/14, doi:10.1088/0067-0049/192/2/14.

BIBLIOGRAPHY

[103] P. A. R. Ade et al. Planck 2015 results. XIII. Cosmological parameters. *Astron. Astrophys.*, 594:A13, 2016. `arXiv:1502.01589`, `doi:10.1051/0004-6361/201525830`.

[104] Giorgio Arcadi, Maíra Dutra, Pradipta Ghosh, Manfred Lindner, Yann Mambrini, Mathias Pierre, Stefano Profumo, and Farinaldo S. Queiroz. The waning of the WIMP? A review of models, searches, and constraints. *Eur. Phys. J. C*, 78(3):203, 2018. `arXiv:1703.07364`, `doi:10.1140/epjc/s10052-018-5662-y`.

[105] Maira Dutra. *Origins for dark matter particles : from the "WIMP miracle" to the "FIMP wonder"*. PhD thesis, Orsay, LPT, 2019.

[106] Manuel Drees, Hoernisa Iminniyaz, and Mitsuru Kakizaki. Constraints on the very early universe from thermal WIMP dark matter. *Phys. Rev. D*, 76:103524, 2007. `arXiv:0704.1590`, `doi:10.1103/PhysRevD.76.103524`.

[107] C. Abel et al. Measurement of the Permanent Electric Dipole Moment of the Neutron. *Phys. Rev. Lett.*, 124(8):081803, 2020. `arXiv:2001.11966`, `doi:10.1103/PhysRevLett.124.081803`.

[108] Michael Dine. TASI lectures on the strong CP problem. In *Theoretical Advanced Study Institute in Elementary Particle Physics (TASI 2000): Flavor Physics for the Millennium*, pages 349–369, 6 2000. `arXiv:hep-ph/0011376`.

[109] R. D. Peccei and Helen R. Quinn. CP conservation in the presence of pseudoparticles. *Phys. Rev. Lett.*, 38:1440–1443, Jun 1977. URL: `https://link.aps.org/doi/10.1103/PhysRevLett.38.1440`, `doi:10.1103/PhysRevLett.38.1440`.

[110] R. D. Peccei and Helen R. Quinn. Constraints imposed by CP conservation in the presence of pseudoparticles. *Phys. Rev. D*, 16:1791–1797, Sep 1977. URL: `https://link.aps.org/doi/10.1103/PhysRevD.16.1791`, `doi:10.1103/PhysRevD.16.1791`.

[111] Abdelhak Djouadi. The Anatomy of electro-weak symmetry breaking. I: The Higgs boson in the standard model. *Phys. Rept.*, 457:1–216, 2008. `arXiv:hep-ph/0503172`, `doi:10.1016/j.physrep.2007.10.004`.

[112] S. Hirose et al. Measurement of the τ lepton polarization and $R(D^*)$ in the decay $\overline{B} \to D^*\tau^-\overline{\nu}_\tau$ with one-prong hadronic τ decays at Belle. *Phys. Rev. D*, 97(1):012004, 2018. `arXiv:1709.00129`, `doi:10.1103/PhysRevD.97.012004`.

[113] J. P. Lees, V. Poireau, et al. Evidence for an excess of $\overline{B} \to D^{(*)}\tau^-\overline{\nu}_\tau$ decays. *Phys. Rev. Lett.*, 109:101802, Sep 2012. URL: `https://link.aps.org/doi/10.1103/PhysRevLett.109.101802`, `doi:10.1103/PhysRevLett.109.101802`.

[114] J. P. Lees et al. Measurement of an Excess of $\overline{B} \to D^{(*)}\tau^-\overline{\nu}_\tau$ Decays and Implications for Charged Higgs Bosons. *Phys. Rev. D*, 88(7):072012, 2013. `arXiv:1303.0571`, `doi:10.1103/PhysRevD.88.072012`.

[115] R. Aaij et al. Measurement of the ratio of the $B^0 \to D^{*-}\tau^+\nu_\tau$ and $B^0 \to D^{*-}\mu^+\nu_\mu$ branching fractions using three-prong τ-lepton decays. *Phys. Rev. Lett.*, 120(17):171802, 2018. `arXiv:1708.08856`, `doi:10.1103/PhysRevLett.120.171802`.

[116] R. Aaij et al. Test of Lepton Flavor Universality by the measurement of the $B^0 \to D^{*-}\tau^+\nu_\tau$ branching fraction using three-prong τ decays. *Phys. Rev. D*, 97(7):072013, 2018. `arXiv:1711.02505`, `doi:10.1103/PhysRevD.97.072013`.

[117] R. Aaij et al. Test of lepton universality in $b \to s\ell^+\ell^-$ decays. *Phys. Rev. Lett.*, 131(5):051803, 2023. `arXiv:2212.09152`, `doi:10.1103/PhysRevLett.131.051803`.

[118] Roel Aaij et al. Measurement of the ratios of branching fractions $\mathcal{R}(D^*)$ and $\mathcal{R}(D^0)$. *Phys. Rev. Lett.*, 131:111802, 2023. arXiv:2302.02886, doi:10.1103/PhysRevLett.131.111802.

[119] Sidney Coleman and Jeffrey Mandula. All possible symmetries of the s matrix. *Phys. Rev.*, 159:1251–1256, Jul 1967. URL: https://link.aps.org/doi/10.1103/PhysRev.159.1251, doi:10.1103/PhysRev.159.1251.

[120] J. Wess and B. Zumino. Supergauge transformations in four dimensions. *Nuclear Physics B*, 70(1):39–50, 1974. URL: https://www.sciencedirect.com/science/article/pii/0550321374903551, doi:10.1016/0550-3213(74)90355-1.

[121] Manuel Drees, Rohini Godbole, and Probir Roy. *Theory and Phenomenology of Sparticles*. WORLD SCIENTIFIC, 2005. URL: https://www.worldscientific.com/doi/abs/10.1142/4001, arXiv:https://www.worldscientific.com/doi/pdf/10.1142/4001, doi:10.1142/4001.

[122] Stephen P. Martin. A Supersymmetry primer. *Adv. Ser. Direct. High Energy Phys.*, 18:1–98, 1998. arXiv:hep-ph/9709356, doi:10.1142/9789812839657_0001.

[123] M. Drees, R. Godbole, and P. Roy. *Theory and phenomenology of sparticles: An account of four-dimensional N=1 supersymmetry in high energy physics*. 2004.

[124] Abdelhak Djouadi. The Anatomy of electro-weak symmetry breaking. II. The Higgs bosons in the minimal supersymmetric model. *Phys. Rept.*, 459:1–241, 2008. arXiv:hep-ph/0503173, doi:10.1016/j.physrep.2007.10.005.

[125] H. Baer and X. Tata. *Weak scale supersymmetry: From superfields to scattering events*. Cambridge University Press, 5 2006.

[126] Ian Aitchison. *Supersymmetry in Particle Physics: An Elementary Introduction*. Cambridge University Press, 2007.

[127] Howard Baer and Michal Brhlik. QCD improved b —> s gamma constraints on the minimal supergravity model. *Phys. Rev. D*, 55:3201–3208, 1997. arXiv:hep-ph/9610224, doi:10.1103/PhysRevD.55.3201.

[128] Gordon L. Kane, Christopher F. Kolda, Leszek Roszkowski, and James D. Wells. Study of constrained minimal supersymmetry. *Phys. Rev. D*, 49:6173–6210, 1994. arXiv:hep-ph/9312272, doi:10.1103/PhysRevD.49.6173.

[129] A. Djouadi et al. The Minimal supersymmetric standard model: Group summary report. In *GDR (Groupement De Recherche) - Supersymetrie*, 12 1998. arXiv:hep-ph/9901246.

[130] John Ellis, Giovanni Ridolfi, and Fabio Zwirner. Radiative corrections to the masses of supersymmetric higgs bosons. *Physics Letters B*, 257(1):83–91, 1991. URL: https://www.sciencedirect.com/science/article/pii/037026939190863L, doi:10.1016/0370-2693(91)90863-L.

[131] Marcela Carena, H. E. Haber, S. Heinemeyer, W. Hollik, C. E. M. Wagner, and G. Weiglein. Reconciling the two loop diagrammatic and effective field theory computations of the mass of the lightest CP - even Higgs boson in the MSSM. *Nucl. Phys. B*, 580:29–57, 2000. arXiv:hep-ph/0001002, doi:10.1016/S0550-3213(00)00212-1.

[132] Patrick Draper and Heidi Rzehak. A Review of Higgs Mass Calculations in Supersymmetric Models. *Phys. Rept.*, 619:1–24, 2016. arXiv:1601.01890, doi:10.1016/j.physrep.2016.01.001.

[133] Michael Dine, Ann E. Nelson, Yosef Nir, and Yuri Shirman. New tools for low energy dynamical supersymmetry breaking. *Phys. Rev. D*, 53:2658–2669, Mar 1996. URL: https://link.aps.org/doi/10.1103/PhysRevD.53.2658, doi:10.1103/PhysRevD.53.2658.

BIBLIOGRAPHY

[134] Gian F. Giudice, Markus A. Luty, Hitoshi Murayama, and Riccardo Rattazzi. Gaugino mass without singlets. *JHEP*, 12:027, 1998. arXiv:hep-ph/9810442, doi:10.1088/1126-6708/1998/12/027.

[135] Lisa Randall and Raman Sundrum. Out of this world supersymmetry breaking. *Nucl. Phys. B*, 557:79–118, 1999. arXiv:hep-th/9810155, doi:10.1016/S0550-3213(99)00359-4.

[136] Jihn E. Kim and H.P. Nilles. The -problem and the strong cp-problem. *Physics Letters B*, 138(1):150–154, 1984. URL: https://www.sciencedirect.com/science/article/pii/0370269384918902, doi:10.1016/0370-2693(84)91890-2.

[137] Ulrich Ellwanger, Cyril Hugonie, and Ana M. Teixeira. The Next-to-Minimal Supersymmetric Standard Model. *Phys. Rept.*, 496:1–77, 2010. arXiv:0910.1785, doi:10.1016/j.physrep.2010.07.001.

[138] Amit Adhikary, Rahool Kumar Barman, Biplob Bhattacherjee, Amandip De, and Rohini M. Godbole. Exploring the Singlino-dominated Thermal Neutralino Dark Matter in the Z_3 invariant NMSSM. 8 2024. arXiv:2408.03656.

[139] Marcin Badziak, Marek Olechowski, and Pawel Szczerbiak. Blind spots for neutralino dark matter in the NMSSM. *JHEP*, 03:179, 2016. arXiv:1512.02472, doi:10.1007/JHEP03(2016)179.

[140] D. J. Miller, R. Nevzorov, and P. M. Zerwas. The Higgs sector of the next-to-minimal supersymmetric standard model. *Nucl. Phys. B*, 681:3–30, 2004. arXiv:hep-ph/0304049, doi:10.1016/j.nuclphysb.2003.12.021.

[141] Ulrich Ellwanger. Higgs Bosons in the Next-to-Minimal Supersymmetric Standard Model at the LHC. *Eur. Phys. J. C*, 71:1782, 2011. arXiv:1108.0157, doi:10.1140/epjc/s10052-011-1782-3.

[142] Armen Tumasyan et al. Search for supersymmetry in final states with two or three soft leptons and missing transverse momentum in proton-proton collisions at $\sqrt{s}$ = 13 TeV. *JHEP*, 04:091, 2022. arXiv:2111.06296, doi:10.1007/JHEP04(2022)091.

[143] Georges Aad et al. Searches for electroweak production of supersymmetric particles with compressed mass spectra in $\sqrt{s}$ = 13 TeV pp collisions with the ATLAS detector. *Phys. Rev. D*, 101(5):052005, 2020. arXiv:1911.12606, doi:10.1103/PhysRevD.101.052005.

[144] Lawrence Lee, Christian Ohm, Abner Soffer, and Tien-Tien Yu. Collider Searches for Long-Lived Particles Beyond the Standard Model. *Prog. Part. Nucl. Phys.*, 106:210–255, 2019. [Erratum: Prog.Part.Nucl.Phys. 122, 103912 (2022)]. arXiv:1810.12602, doi:10.1016/j.ppnp.2019.02.006.

[145] Matthew J. Strassler and Kathryn M. Zurek. Echoes of a hidden valley at hadron colliders. *Phys. Lett. B*, 651:374–379, 2007. arXiv:hep-ph/0604261, doi:10.1016/j.physletb.2007.06.055.

[146] Juliette Alimena, James Beacham, et al. Searching for long-lived particles beyond the standard model at the large hadron collider. *Journal of Physics G: Nuclear and Particle Physics*, 47(9):090501, sep 2020. URL: https://dx.doi.org/10.1088/1361-6471/ab4574, doi:10.1088/1361-6471/ab4574.

[147] Paul Langacker. The physics of heavy Z' gauge bosons. *Rev. Mod. Phys.*, 81:1199–1228, Aug 2009. URL: https://link.aps.org/doi/10.1103/RevModPhys.81.1199, doi:10.1103/RevModPhys.81.1199.

[148] Asli M Abdullahi, Pablo Barham Alzás, et al. *Journal of Physics G: Nuclear and Particle Physics*, 50(2):020501, jan 2023. URL: https://dx.doi.org/10.1088/1361-6471/ac98f9, doi:10.1088/1361-6471/ac98f9.

[149] Yi Cai, Tao Han, Tong Li, and Richard Ruiz. Lepton Number Violation: Seesaw Models and Their Collider Tests. *Front. in Phys.*, 6:40, 2018. arXiv:1711.02180, doi:10.3389/fphy.2018.00040.

[150] Scott D. Thomas and James D. Wells. Phenomenology of Massive Vectorlike Doublet Leptons. *Phys. Rev. Lett.*, 81:34–37, 1998. arXiv:hep-ph/9804359, doi:10.1103/PhysRevLett.81.34.

[151] Marco Cirelli, Nicolao Fornengo, and Alessandro Strumia. Minimal dark matter. *Nucl. Phys. B*, 753:178–194, 2006. arXiv:hep-ph/0512090, doi:10.1016/j.nuclphysb.2006.07.012.

[152] Pavel Fileviez Perez, Hiren H. Patel, Michael. J. Ramsey-Musolf, and Kai Wang. Triplet Scalars and Dark Matter at the LHC. *Phys. Rev. D*, 79:055024, 2009. arXiv:0811.3957, doi:10.1103/PhysRevD.79.055024.

[153] David Tucker-Smith and Neal Weiner. Inelastic dark matter. *Phys. Rev. D*, 64:043502, 2001. arXiv:hep-ph/0101138, doi:10.1103/PhysRevD.64.043502.

[154] Yang Bai and Tim M. P. Tait. Inelastic Dark Matter at the LHC. *Phys. Lett. B*, 710:335–338, 2012. arXiv:1109.4144, doi:10.1016/j.physletb.2012.03.011.

[155] Neal Weiner and Itay Yavin. How Dark Are Majorana WIMPs? Signals from MiDM and Rayleigh Dark Matter. *Phys. Rev. D*, 86:075021, 2012. arXiv:1206.2910, doi:10.1103/PhysRevD.86.075021.

[156] Eder Izaguirre, Gordan Krnjaic, and Brian Shuve. Discovering Inelastic Thermal-Relic Dark Matter at Colliders. *Phys. Rev. D*, 93(6):063523, 2016. arXiv:1508.03050, doi:10.1103/PhysRevD.93.063523.

[157] Kim Griest and David Seckel. Three exceptions in the calculation of relic abundances. *Phys. Rev. D*, 43:3191–3203, May 1991. URL: https://link.aps.org/doi/10.1103/PhysRevD.43.3191, doi:10.1103/PhysRevD.43.3191.

[158] Michael J. Baker et al. The Coannihilation Codex. *JHEP*, 12:120, 2015. arXiv:1510.03434, doi:10.1007/JHEP12(2015)120.

[159] Valentin V. Khoze, Alexis D. Plascencia, and Kazuki Sakurai. Simplified models of dark matter with a long-lived co-annihilation partner. *JHEP*, 06:041, 2017. arXiv:1702.00750, doi:10.1007/JHEP06(2017)041.

[160] Mathias Garny, Jan Heisig, Benedikt Lülf, and Stefan Vogl. Coannihilation without chemical equilibrium. *Phys. Rev. D*, 96(10):103521, 2017. arXiv:1705.09292, doi:10.1103/PhysRevD.96.103521.

[161] Yonit Hochberg, Eric Kuflik, and Hitoshi Murayama. SIMP Spectroscopy. *JHEP*, 05:090, 2016. arXiv:1512.07917, doi:10.1007/JHEP05(2016)090.

[162] Lawrence J. Hall, Karsten Jedamzik, John March-Russell, and Stephen M. West. Freeze-In Production of FIMP Dark Matter. *JHEP*, 03:080, 2010. arXiv:0911.1120, doi:10.1007/JHEP03(2010)080.

[163] Raymond T. Co, Francesco D'Eramo, Lawrence J. Hall, and Duccio Pappadopulo. Freeze-In Dark Matter with Displaced Signatures at Colliders. *JCAP*, 12:024, 2015. arXiv:1506.07532, doi:10.1088/1475-7516/2015/12/024.

[164] Andre G. Hessler, Alejandro Ibarra, Emiliano Molinaro, and Stefan Vogl. Probing the scotogenic FIMP at the LHC. *JHEP*, 01:100, 2017. arXiv:1611.09540, doi:10.1007/JHEP01(2017)100.

[165] Avirup Ghosh, Tanmoy Mondal, and Biswarup Mukhopadhyaya. Heavy stable charged tracks as signatures of non-thermal dark matter at the LHC : a study in some non-supersymmetric scenarios. *JHEP*, 12:136, 2017. arXiv:1706.06815, doi:10.1007/JHEP12(2017)136.

[166] G. Bélanger et al. LHC-friendly minimal freeze-in models. *JHEP*, 02:186, 2019. arXiv:1811.05478, doi:10.1007/JHEP02(2019)186.

[167] Andreas Goudelis, Kirtimaan A. Mohan, and Dipan Sengupta. Clockworking FIMPs. *JHEP*, 10:014, 2018. arXiv:1807.06642, doi:10.1007/JHEP10(2018)014.

[168] Mathias Garny and Jan Heisig. Interplay of super-WIMP and freeze-in production of dark matter. *Phys. Rev. D*, 98(9):095031, 2018. arXiv:1809.10135, doi:10.1103/PhysRevD.98.095031.

[169] Jamei Antonelli. Searches for long-lived particles at CMS. https://indico.cern.ch/event/432527/contributions/1072042/. [38th International Conference of High Energy Physics (ICHEP), 3-10 August, 2016].

[170] A.M. Sirunyan, A. Tumasyan, W. Adam, et al. Search for disappearing tracks in proton-proton collisions at s=13tev. *Physics Letters B*, 806:135502, 2020. URL: https://www.sciencedirect.com/science/article/pii/S0370269320303063, doi:10.1016/j.physletb.2020.135502.

[171] Search for heavy stable charged particles with 12.9 fb^{-1} of 2016 data. Technical report, CERN, Geneva, 2016. URL: https://cds.cern.ch/record/2205281.

[172] Georges Aad et al. Search for heavy, long-lived, charged particles with large ionisation energy loss in *pp* collisions at $\sqrt{s} = 13$ TeV using the ATLAS experiment and the full Run 2 dataset. *JHEP*, 2306:158, 2023. arXiv:2205.06013, doi:10.1007/JHEP06(2023)158.

[173] Search for fractionally charged particles in pp collisions at $\sqrt{s} = 13$ TeV. Technical report, CERN, Geneva, 2022. URL: https://cds.cern.ch/record/2841994.

[174] Albert M Sirunyan et al. Search for long-lived particles using displaced jets in proton-proton collisions at $\sqrt{s} = 13$ TeV. *Phys. Rev. D*, 104(1):012015, 2021. arXiv:2012.01581, doi:10.1103/PhysRevD.104.012015.

[175] Armen Tumasyan et al. Search for long-lived heavy neutral leptons with displaced vertices in proton-proton collisions at $\sqrt{s}$ =13 TeV. *JHEP*, 07:081, 2022. arXiv:2201.05578, doi:10.1007/JHEP07(2022)081.

[176] Georges Aad et al. Search for Heavy Neutral Leptons in Decays of W Bosons Using a Dilepton Displaced Vertex in s=13 TeV pp Collisions with the ATLAS Detector. *Phys. Rev. Lett.*, 131(6):061803, 2023. arXiv:2204.11988, doi:10.1103/PhysRevLett.131.061803.

[177] Georges Aad et al. Search for long-lived, massive particles in events with displaced vertices and multiple jets in pp collisions at $\sqrt{s} = 13$ TeV with the ATLAS detector. *JHEP*, 2306:200, 2023. arXiv:2301.13866, doi:10.1007/JHEP06(2023)200.

[178] Wayne Hu, Rennan Barkana, and Andrei Gruzinov. Cold and fuzzy dark matter. *Phys. Rev. Lett.*, 85:1158–1161, 2000. arXiv:astro-ph/0003365, doi:10.1103/PhysRevLett.85.1158.

[179] Brian C. Lacki and John F. Beacom. Primordial Black Holes as Dark Matter: Almost All or Almost Nothing. *Astrophys. J. Lett.*, 720:L67–L71, 2010. arXiv:1003.3466, doi:10.1088/2041-8205/720/1/L67.

[180] Sebastien Clesse and Juan García-Bellido. Seven Hints for Primordial Black Hole Dark Matter. *Phys. Dark Univ.*, 22:137–146, 2018. arXiv:1711.10458, doi:10.1016/j.dark.2018.08.004.

[181] Steven Weinberg. Cosmological constraints on the scale of supersymmetry breaking. *Phys. Rev. Lett.*, 48:1303–1306, May 1982. URL: https://link.aps.org/doi/10.1103/PhysRevLett.48.1303, doi:10.1103/PhysRevLett.48.1303.

[182] John Ellis, D.V. Nanopoulos, and Subir Sarkar. The cosmology of decaying gravitinos. *Nuclear Physics B*, 259(1):175–188, 1985. URL: https://www.sciencedirect.com/science/article/pii/0550321385903062, doi:10.1016/0550-3213(85)90306-2.

[183] Mark W. Goodman and Edward Witten. Detectability of Certain Dark Matter Candidates. *Phys. Rev. D*, 31:3059, 1985. doi:10.1103/PhysRevD.31.3059.

[184] John Vergados. *On the Direct Detection of Dark Matter*, pages 69–100. Springer Berlin Heidelberg, Berlin, Heidelberg, 2007. doi:10.1007/978-3-540-71013-4_3.

[185] Laura Baudis. Direct dark matter detection: the next decade. *Phys. Dark Univ.*, 1:94–108, 2012. arXiv:1211.7222, doi:10.1016/j.dark.2012.10.006.

[186] Marc Schumann. Direct Detection of WIMP Dark Matter: Concepts and Status. *J. Phys. G*, 46(10):103003, 2019. arXiv:1903.03026, doi:10.1088/1361-6471/ab2ea5.

[187] Gintaras Duda, Ann Kemper, and Paolo Gondolo. Model Independent Form Factors for Spin Independent Neutralino-Nucleon Scattering from Elastic Electron Scattering Data. *JCAP*, 04:012, 2007. arXiv:hep-ph/0608035, doi:10.1088/1475-7516/2007/04/012.

[188] J. Aalbers et al. First dark matter search results from the lux-zeplin (lz) experiment. *Phys. Rev. Lett.*, 131:041002, Jul 2023. URL: https://link.aps.org/doi/10.1103/PhysRevLett.131.041002, doi:10.1103/PhysRevLett.131.041002.

[189] R. L. Workman et al. Review of Particle Physics. *PTEP*, 2022:083C01, 2022. doi:10.1093/ptep/ptac097.

[190] Julien Billard et al. Direct detection of dark matter—APPEC committee report*. *Rept. Prog. Phys.*, 85(5):056201, 2022. arXiv:2104.07634, doi:10.1088/1361-6633/ac5754.

[191] C. Amole et al. Dark matter search results from the complete exposure of the pico-60 c_3f_8 bubble chamber. *Phys. Rev. D*, 100:022001, Jul 2019. URL: https://link.aps.org/doi/10.1103/PhysRevD.100.022001, doi:10.1103/PhysRevD.100.022001.

[192] Georges Aad et al. Search for dark matter in association with an energetic photon in pp collisions at $\sqrt{s}$ = 13 TeV with the ATLAS detector. *JHEP*, 02:226, 2021. arXiv:2011.05259, doi:10.1007/JHEP02(2021)226.

[193] Albert M Sirunyan et al. Search for new physics in final states with a single photon and missing transverse momentum in proton-proton collisions at $\sqrt{s}$ = 13 TeV. *JHEP*, 02:074, 2019. arXiv:1810.00196, doi:10.1007/JHEP02(2019)074.

[194] M. Aaboud et al. Search for dark matter in events with a hadronically decaying vector boson and missing transverse momentum in pp collisions at $\sqrt{s}$ = 13 TeV with the ATLAS detector. *JHEP*, 10:180, 2018. arXiv:1807.11471, doi:10.1007/JHEP10(2018)180.

[195] A. Albert et al. Searching for Dark Matter Annihilation in Recently Discovered Milky Way Satellites with Fermi-LAT. *Astrophys. J.*, 834(2):110, 2017. arXiv:1611.03184, doi:10.3847/1538-4357/834/2/110.

[196] M. N. Mazziotta, A. Cuoco, P. De La Torre Luque, F. Loparco, and D. Serini. Search for dark matter signatures in the cosmic-ray electron and positron spectrum measured by the Fermi Large Area Telescope. *PoS*, ICRC2019:531, 2020. doi:10.22323/1.358.0531.

[197] Viviana Gammaldi, Judit Pérez-Romero, Javier Coronado-Blázquez, Mattia Di Mauro, Ekaterina Karukes, Miguel Angel Sánchez-Conde, and Paolo Salucci. Dark Matter search in dwarf irregular galaxies with the Fermi Large Area Telescope. *PoS*, ICRC2021:509, 2021. `arXiv:2109.11291`, `doi:10.22323/1.395.0509`.

[198] H. Abdalla et al. Search for Dark Matter Annihilation Signals in the H.E.S.S. Inner Galaxy Survey. *Phys. Rev. Lett.*, 129(11):111101, 2022. `arXiv:2207.10471`, `doi:10.1103/PhysRevLett.129.111101`.

[199] Hassan Abdalla et al. Combined dark matter searches towards dwarf spheroidal galaxies with Fermi-LAT, HAWC, H.E.S.S., MAGIC, and VERITAS. *PoS*, ICRC2021:528, 2021. `arXiv:2108.13646`, `doi:10.22323/1.395.0528`.

[200] V. A. Acciari et al. Combined searches for dark matter in dwarf spheroidal galaxies observed with the MAGIC telescopes, including new data from Coma Berenices and Draco. *Phys. Dark Univ.*, 35:100912, 2022. `arXiv:2111.15009`, `doi:10.1016/j.dark.2021.100912`.

[201] H. Abe et al. Search for Gamma-Ray Spectral Lines from Dark Matter Annihilation up to 100 TeV toward the Galactic Center with MAGIC. *Phys. Rev. Lett.*, 130(6):061002, 2023. `arXiv:2212.10527`, `doi:10.1103/PhysRevLett.130.061002`.

[202] M. G. Aartsen et al. Search for annihilating dark matter in the Sun with 3 years of IceCube data. *Eur. Phys. J. C*, 77(3):146, 2017. [Erratum: Eur.Phys.J.C 79, 214 (2019)]. `arXiv:1612.05949`, `doi:10.1140/epjc/s10052-017-4689-9`.

[203] M. G. Aartsen et al. Search for Neutrinos from Dark Matter Self-Annihilations in the center of the Milky Way with 3 years of IceCube/DeepCore. *Eur. Phys. J. C*, 77(9):627, 2017. `arXiv:1705.08103`, `doi:10.1140/epjc/s10052-017-5213-y`.

[204] M. Ageron et al. ANTARES: the first undersea neutrino telescope. *Nucl. Instrum. Meth. A*, 656:11–38, 2011. `arXiv:1104.1607`, `doi:10.1016/j.nima.2011.06.103`.

[205] S. Adrian-Martinez et al. Limits on Dark Matter Annihilation in the Sun using the ANTARES Neutrino Telescope. *Phys. Lett. B*, 759:69–74, 2016. `arXiv:1603.02228`, `doi:10.1016/j.physletb.2016.05.019`.

[206] M. Aguilar, Ali Cavasonza, et al. Antiproton flux, antiproton-to-proton flux ratio, and properties of elementary particle fluxes in primary cosmic rays measured with the alpha magnetic spectrometer on the international space station. *Phys. Rev. Lett.*, 117:091103, Aug 2016. URL: `https://link.aps.org/doi/10.1103/PhysRevLett.117.091103`, `doi:10.1103/PhysRevLett.117.091103`.

[207] M. Aguilar, Ali Cavasonza, et al. Towards understanding the origin of cosmic-ray positrons. *Phys. Rev. Lett.*, 122:041102, Jan 2019. URL: `https://link.aps.org/doi/10.1103/PhysRevLett.122.041102`, `doi:10.1103/PhysRevLett.122.041102`.

[208] Amit Chakraborty, Amandip De, Rohini M. Godbole, and Monoranjan Guchait. Tagging a boosted top quark with a τ final state. *Phys. Rev. D*, 108(3):035011, 2023. `arXiv:2304.12846`, `doi:10.1103/PhysRevD.108.035011`.

[209] R. Kehoe, M. Narain, and A. Kumar. Review of Top Quark Physics Results. *Int. J. Mod. Phys. A*, 23:353–470, 2008. `arXiv:0712.2733`, `doi:10.1142/S0217751X08039293`.

[210] P. S. Bhupal Dev, A. Djouadi, R. M. Godbole, M. M. Muhlleitner, and S. D. Rindani. Determining the CP properties of the Higgs boson. *Phys. Rev. Lett.*, 100:051801, 2008. `arXiv:0707.2878`, `doi:10.1103/PhysRevLett.100.051801`.

[211] Saurabh D. Rindani and Pankaj Sharma. Probing anomalous tbW couplings in single-top production using top polarization at the Large Hadron Collider. *JHEP*, 11:082, 2011. `arXiv:1107.2597`, `doi:10.1007/JHEP11(2011)082`.

[212] Saurabh D. Rindani, Rui Santos, and Pankaj Sharma. Measuring the charged Higgs mass and distinguishing between models with top-quark observables. *JHEP*, 11:188, 2013. `arXiv:1307.1158`, `doi:10.1007/JHEP11(2013)188`.

[213] Fawzi Boudjema, Rohini M. Godbole, Diego Guadagnoli, and Kirtimaan A. Mohan. Lab-frame observables for probing the top-Higgs interaction. *Phys. Rev. D*, 92(1):015019, 2015. `arXiv:1501.03157`, `doi:10.1103/PhysRevD.92.015019`.

[214] Hans Peter Nilles. Supersymmetry, Supergravity and Particle Physics. *Phys. Rept.*, 110:1–162, 1984. `doi:10.1016/0370-1573(84)90008-5`.

[215] J. Wess and J. Bagger. *Supersymmetry and supergravity*. Princeton University Press, Princeton, NJ, USA, 1992.

[216] Howard E. Haber and Gordon L. Kane. The Search for Supersymmetry: Probing Physics Beyond the Standard Model. *Phys. Rept.*, 117:75–263, 1985. `doi:10.1016/0370-1573(85)90051-1`.

[217] David B. Kaplan and Howard Georgi. SU(2) x U(1) Breaking by Vacuum Misalignment. *Phys. Lett. B*, 136:183–186, 1984. `doi:10.1016/0370-2693(84)91177-8`.

[218] Martin Schmaltz and David Tucker-Smith. Little Higgs review. *Ann. Rev. Nucl. Part. Sci.*, 55:229–270, 2005. `arXiv:hep-ph/0502182`, `doi:10.1146/annurev.nucl.55.090704.151502`.

[219] Lisa Randall and Raman Sundrum. Large mass hierarchy from a small extra dimension. *Phys. Rev. Lett.*, 83:3370–3373, Oct 1999. URL: `https://link.aps.org/doi/10.1103/PhysRevLett.83.3370`, `doi:10.1103/PhysRevLett.83.3370`.

[220] Ulrich Husemann. Top-quark physics: Status and prospects. *Progress in Particle and Nuclear Physics*, 95:48–97, Jul 2017. URL: `http://dx.doi.org/10.1016/j.ppnp.2017.03.002`, `doi:10.1016/j.ppnp.2017.03.002`.

[221] M. Beneke et al. Top quark physics. In *Workshop on Standard Model Physics (and more) at the LHC (First Plenary Meeting)*, pages 419–529, 3 2000. `arXiv:hep-ph/0003033`.

[222] M. Jezabek and Johann H. Kuhn. Lepton Spectra from Heavy Quark Decay. *Nucl. Phys. B*, 320:20–44, 1989. `doi:10.1016/0550-3213(89)90209-5`.

[223] M. Jezabek. Top quark physics. *Nucl. Phys. B Proc. Suppl.*, 37(2):197, 1994. `arXiv:hep-ph/9406411`, `doi:10.1016/0920-5632(94)90677-7`.

[224] Werner Bernreuther. Top quark physics at the LHC. *J. Phys. G*, 35:083001, 2008. `arXiv:0805.1333`, `doi:10.1088/0954-3899/35/8/083001`.

[225] Saurabh D. Rindani. Effect of anomalous t b W vertex on decay lepton distributions in e+ e- —> t anti-t and CP violating asymmetries. *Pramana*, 54:791–812, 2000. `arXiv:hep-ph/0002006`, `doi:10.1007/s12043-000-0176-0`.

[226] Bohdan Grzadkowski and Zenro Hioki. New hints for testing anomalous top quark interactions at future linear colliders. *Phys. Lett. B*, 476:87–94, 2000. `arXiv:hep-ph/9911505`, `doi:10.1016/S0370-2693(00)00101-5`.

[227] Zenro Hioki. Probing anomalous top couplings through the final lepton angular and energy distributions at polarized NLC. In *Theory Workshop on Physics at Linear Colliders*, pages 169–177, 4 2001. `arXiv:hep-ph/0104105`.

[228] Kazumasa Ohkuma. Effects of top quark anomalous decay couplings at gamma gamma colliders. *Nucl. Phys. B Proc. Suppl.*, 111:285–287, 2002. `arXiv:hep-ph/0202126`, `doi:10.1016/S0920-5632(02)01723-1`.

[229] Bohdan Grzadkowski and Zenro Hioki. Angular distribution of leptons in general $t\bar{t}$ production and decay. *Phys. Lett. B*, 529:82–86, 2002. arXiv:hep-ph/0112361, doi:10.1016/S0370-2693(02)01250-9.

[230] Bohdan Grzadkowski and Zenro Hioki. Decoupling of anomalous top decay vertices in angular distribution of secondary particles. *Phys. Lett. B*, 557:55–59, 2003. arXiv:hep-ph/0208079, doi:10.1016/S0370-2693(03)00187-4.

[231] Zenro Hioki. A New decoupling theorem in top quark physics. In *International Workshop on Linear Colliders (LCWS 2002)*, pages 333–338, 10 2002. arXiv:hep-ph/0210224.

[232] Rohini M. Godbole, Saurabh D. Rindani, and Ritesh K. Singh. Study of CP property of the Higgs at a photon collider using gamma gamma —> t anti-t —> lX. *Phys. Rev. D*, 67:095009, 2003. [Erratum: Phys.Rev.D 71, 039902 (2005)]. arXiv:hep-ph/0211136, doi:10.1103/PhysRevD.71.039902.

[233] Rohini M. Godbole, Saurabh D. Rindani, and Ritesh K. Singh. Lepton distribution as a probe of new physics in production and decay of the t quark and its polarization. *JHEP*, 12:021, 2006. arXiv:hep-ph/0605100, doi:10.1088/1126-6708/2006/12/021.

[234] Rohini M. Godbole, Michael E. Peskin, Saurabh D. Rindani, and Ritesh K. Singh. Why the angular distribution of the top decay lepton is unchanged by anomalous tbW couplings. *Phys. Lett. B*, 790:322–325, 2019. arXiv:1809.06285, doi:10.1016/j.physletb.2019.01.022.

[235] Gavin P. Salam. Towards Jetography. *Eur. Phys. J. C*, 67:637–686, 2010. arXiv:0906.1833, doi:10.1140/epjc/s10052-010-1314-6.

[236] Jesse Thaler and Lian-Tao Wang. Strategies to Identify Boosted Tops. *JHEP*, 07:092, 2008. arXiv:0806.0023, doi:10.1088/1126-6708/2008/07/092.

[237] David E. Kaplan, Keith Rehermann, Matthew D. Schwartz, and Brock Tweedie. Top Tagging: A Method for Identifying Boosted Hadronically Decaying Top Quarks. *Phys. Rev. Lett.*, 101:142001, 2008. arXiv:0806.0848, doi:10.1103/PhysRevLett.101.142001.

[238] Tilman Plehn and Michael Spannowsky. Top Tagging. *J. Phys. G*, 39:083001, 2012. arXiv:1112.4441, doi:10.1088/0954-3899/39/8/083001.

[239] Leandro G. Almeida, Mihailo Backović, Mathieu Cliche, Seung J. Lee, and Maxim Perelstein. Playing Tag with ANN: Boosted Top Identification with Pattern Recognition. *JHEP*, 07:086, 2015. arXiv:1501.05968, doi:10.1007/JHEP07(2015)086.

[240] Gregor Kasieczka, Tilman Plehn, Anja Butter, Kyle Cranmer, Dipsikha Debnath, Barry M. Dillon, Malcolm Fairbairn, Darius A. Faroughy, Wojtek Fedorko, Christophe Gay, and et al. The machine learning landscape of top taggers. *SciPost Physics*, 7(1), Jul 2019. URL: http://dx.doi.org/10.21468/SciPostPhys.7.1.014, doi:10.21468/scipostphys.7.1.014.

[241] Gregor Kasieczka, Tilman Plehn, Michael Russell, and Torben Schell. Deep-learning Top Taggers or The End of QCD? *JHEP*, 05:006, 2017. arXiv:1701.08784, doi:10.1007/JHEP05(2017)006.

[242] Soham Bhattacharya, Monoranjan Guchait, and Aravind H. Vijay. Boosted top quark tagging and polarization measurement using machine learning. *Phys. Rev. D*, 105(4):042005, 2022. arXiv:2010.11778, doi:10.1103/PhysRevD.105.042005.

[243] Biplob Bhattacherjee, Camellia Bose, Amit Chakraborty, and Rhitaja Sengupta. Boosted top tagging and its interpretation using Shapley values. 12 2022. `arXiv:2212.11606`.

[244] Andrew J. Larkoski, Ian Moult, and Benjamin Nachman. Jet Substructure at the Large Hadron Collider: A Review of Recent Advances in Theory and Machine Learning. *Phys. Rept.*, 841:1–63, 2020. `arXiv:1709.04464`, `doi:10.1016/j.physrep.2019.11.001`.

[245] Roman Kogler et al. Jet Substructure at the Large Hadron Collider: Experimental Review. *Rev. Mod. Phys.*, 91(4):045003, 2019. `arXiv:1803.06991`, `doi:10.1103/RevModPhys.91.045003`.

[246] Suman Chatterjee, Rohini Godbole, and Tuhin S. Roy. Jets with electrons from boosted top quarks. *Journal of High Energy Physics*, 2020(1), Jan 2020. URL: `http://dx.doi.org/10.1007/JHEP01(2020)170`, `doi:10.1007/jhep01(2020)170`.

[247] B. K. Bullock, Kaoru Hagiwara, and Alan D. Martin. Tau polarization and its correlations as a probe of new physics. *Nucl. Phys. B*, 395:499–533, 1993. `doi:10.1016/0550-3213(93)90045-Q`.

[248] R. M. Godbole, Monoranjan Guchait, and D. P. Roy. Using tau polarization to probe the stau co-annihilation region of the minimal supergravity model at the lhc. *Phys. Rev. D*, 79:095015, May 2009. URL: `https://link.aps.org/doi/10.1103/PhysRevD.79.095015`, `doi:10.1103/PhysRevD.79.095015`.

[249] Monoranjan Guchait and D. P. Roy. Using Tau Polarisation for Charged Higgs Boson and SUSY Searches at the LHC. pages 205–212, 8 2008. `arXiv:0808.0438`, `doi:10.1007/978-81-8489-295-6_13`.

[250] Thomas Gajdosik, Rohini M. Godbole, and Sabine Kraml. Fermion polarization in sfermion decays as a probe of CP phases in the MSSM. *JHEP*, 09:051, 2004. `arXiv:hep-ph/0405167`, `doi:10.1088/1126-6708/2004/09/051`.

[251] Lawrence J. Hall and Mahiko Suzuki. Explicit R-Parity Breaking in Supersymmetric Models. *Nucl. Phys. B*, 231:419–444, 1984. `doi:10.1016/0550-3213(84)90513-3`.

[252] J. C. Romao, M. A. Diaz, M. Hirsch, W. Porod, and J. W. F Valle. A Supersymmetric solution to the solar and atmospheric neutrino problems. *Phys. Rev. D*, 61:071703, 2000. `arXiv:hep-ph/9907499`, `doi:10.1103/PhysRevD.61.071703`.

[253] Eung Jin Chun, Sunghoon Jung, Hyun Min Lee, and Seong Chan Park. Stop and Sbottom LSP with R-parity Violation. *Phys. Rev. D*, 90:115023, 2014. `arXiv:1408.4508`, `doi:10.1103/PhysRevD.90.115023`.

[254] Zack Sullivan. Fully differential w' production and decay at next-to-leading order in qcd. *Physical Review D*, 66(7), Oct 2002. URL: `http://dx.doi.org/10.1103/PhysRevD.66.075011`, `doi:10.1103/physrevd.66.075011`.

[255] Fawzi Boudjema and Ritesh K. Singh. A Model independent spin analysis of fundamental particles using azimuthal asymmetries. *JHEP*, 07:028, 2009. `arXiv:0903.4705`, `doi:10.1088/1126-6708/2009/07/028`.

[256] J. Alwall, R. Frederix, S. Frixione, V. Hirschi, F. Maltoni, O. Mattelaer, H. S. Shao, T. Stelzer, P. Torrielli, and M. Zaro. The automated computation of tree-level and next-to-leading order differential cross sections, and their matching to parton shower simulations. *JHEP*, 07:079, 2014. `arXiv:1405.0301`, `doi:10.1007/JHEP07(2014)079`.

[257] Pierre Artoisenet, Rikkert Frederix, Olivier Mattelaer, and Robbert Rietkerk. Automatic spin-entangled decays of heavy resonances in Monte Carlo simulations. *JHEP*, 03:015, 2013. `arXiv:1212.3460`, `doi:10.1007/JHEP03(2013)015`.

[258] Torbjörn Sjöstrand, Stefan Ask, Jesper R. Christiansen, Richard Corke, Nishita Desai, Philip Ilten, Stephen Mrenna, Stefan Prestel, Christine O. Rasmussen, and Peter Z. Skands. An introduction to PYTHIA 8.2. *Comput. Phys. Commun.*, 191:159–177, 2015. arXiv:1410.3012, doi:10.1016/j.cpc.2015.01.024.

[259] J. de Favereau, C. Delaere, P. Demin, A. Giammanco, V. Lemaître, A. Mertens, and M. Selvaggi. DELPHES 3, A modular framework for fast simulation of a generic collider experiment. *JHEP*, 02:057, 2014. arXiv:1307.6346, doi:10.1007/JHEP02(2014)057.

[260] Matteo Cacciari, Gavin P Salam, and Gregory Soyez. The anti-ktjet clustering algorithm. *Journal of High Energy Physics*, 2008(04):063–063, Apr 2008. URL: http://dx.doi.org/10.1088/1126-6708/2008/04/063, doi:10.1088/1126-6708/2008/04/063.

[261] Matteo Cacciari, Gavin P. Salam, and Gregory Soyez. Fastjet user manual. *The European Physical Journal C*, 72(3), Mar 2012. URL: http://dx.doi.org/10.1140/epjc/s10052-012-1896-2, doi:10.1140/epjc/s10052-012-1896-2.

[262] Andrew J. Larkoski, Simone Marzani, Gregory Soyez, and Jesse Thaler. Soft drop. *Journal of High Energy Physics*, 2014(5), May 2014. URL: http://dx.doi.org/10.1007/JHEP05(2014)146, doi:10.1007/jhep05(2014)146.

[263] Albert M Sirunyan et al. Identification of heavy, energetic, hadronically decaying particles using machine-learning techniques. *JINST*, 15(06):P06005, 2020. arXiv:2004.08262, doi:10.1088/1748-0221/15/06/P06005.

[264] Giuseppe Bagliesi. Tau tagging at Atlas and CMS. In *17th Symposium on Hadron Collider Physics 2006 (HCP 2006)*, 7 2007. arXiv:0707.0928.

[265] Andrey Katz, Minho Son, and Brock Tweedie. Ditau-Jet Tagging and Boosted Higgses from a Multi-TeV Resonance. *Phys. Rev. D*, 83:114033, 2011. arXiv:1011.4523, doi:10.1103/PhysRevD.83.114033.

[266] S. Gennai, F. Moortgat, L. Wendland, A. Nikitenko, S. Wakefield, G. Bagliesi, S. Dutta, A. Kalinowski, M. Konecki, and D. Kotlinski. Tau jet reconstruction and tagging at high level trigger and off-line. *Eur. Phys. J. C*, 46S1:1–21, 2006. doi:10.1140/epjcd/s2006-02-001-y.

[267] The CMS Collaboration. Tau jet reconstruction and tagging with cms. *Eur. Phys. J. C*, 46:1–21, 2006. doi:10.1140/epjcd/s2006-02-001-y.

[268] Georges Aad et al. ATLAS b-jet identification performance and efficiency measurement with $t\bar{t}$ events in pp collisions at $\sqrt{s} = 13$ TeV. *Eur. Phys. J. C*, 79(11):970, 2019. arXiv:1907.05120, doi:10.1140/epjc/s10052-019-7450-8.

[269] Serguei Chatrchyan et al. Identification of b-Quark Jets with the CMS Experiment. *JINST*, 8:P04013, 2013. arXiv:1211.4462, doi:10.1088/1748-0221/8/04/P04013.

[270] Jesse Thaler and Ken Van Tilburg. Identifying boosted objects with n-subjettiness. *Journal of High Energy Physics*, 2011(3), Mar 2011. URL: http://dx.doi.org/10.1007/JHEP03(2011)015, doi:10.1007/jhep03(2011)015.

[271] Andreas Hocker et al. TMVA - Toolkit for Multivariate Data Analysis. 3 2007. arXiv:physics/0703039.

[272] Yoav Freund and Robert E Schapire. A decision-theoretic generalization of on-line learning and an application to boosting. *Journal of Computer and System Sciences*, 55(1):119–139, 1997. URL: https://www.sciencedirect.com/science/article/pii/S002200009791504X, doi:10.1006/jcss.1997.1504.

[273] G. Belanger, R. M. Godbole, L. Hartgring, and I. Niessen. Top Polarization in Stop Production at the LHC. *JHEP*, 05:167, 2013. `arXiv:1212.3526`, `doi:10.1007/JHEP05(2013)167`.

[274] Rohini M. Godbole, Lisa Hartgring, Irene Niessen, and Chris D. White. Top polarisation studies in $H^- t$ and Wt production. *JHEP*, 01:011, 2012. `arXiv:1111.0759`, `doi:10.1007/JHEP01(2012)011`.

[275] Rohini M. Godbole, Gaurav Mendiratta, and Saurabh Rindani. Looking for bSM physics using top-quark polarization and decay-lepton kinematic asymmetries. *Phys. Rev. D*, 92(9):094013, 2015. `arXiv:1506.07486`, `doi:10.1103/PhysRevD.92.094013`.

[276] V. Arunprasath, Rohini M. Godbole, and Ritesh K. Singh. Polarization of a top quark produced in the decay of a gluino or a stop in an arbitrary frame. *Phys. Rev. D*, 95(7):076012, 2017. `arXiv:1612.03803`, `doi:10.1103/PhysRevD.95.076012`.

[277] Rohini Godbole, Monoranjan Guchait, Charanjit K. Khosa, Jayita Lahiri, Seema Sharma, and Aravind H. Vijay. Boosted Top quark polarization. *Phys. Rev. D*, 100(5):056010, 2019. `arXiv:1902.08096`, `doi:10.1103/PhysRevD.100.056010`.

[278] Genevieve Belanger, Rohini M. Godbole, Charanjit K. Khosa, and Saurabh D. Rindani. Probing CP nature of a mediator in associated production of dark matter with single top quark. In *11th International Workshop on Top Quark Physics*, 11 2018. `arXiv:1811.11048`.

[279] David Krohn, Jessie Shelton, and Lian-Tao Wang. Measuring the Polarization of Boosted Hadronic Tops. *JHEP*, 07:041, 2010. `arXiv:0909.3855`, `doi:10.1007/JHEP07(2010)041`.

[280] Yoshio Kitadono and Hsiang-nan Li. Jet substructures of boosted polarized hadronic top quarks. *Phys. Rev. D*, 93(5):054043, 2016. `arXiv:1511.08675`, `doi:10.1103/PhysRevD.93.054043`.

[281] Amit Adhikary, Rahool Kumar Barman, Biplob Bhattacherjee, Amandip De, Rohini M. Godbole, and Suchita Kulkarni. Long-lived NLSP in the NMSSM. *Phys. Rev. D*, 108(3):035020, 2023. `arXiv:2207.00600`, `doi:10.1103/PhysRevD.108.035020`.

[282] M. Tanabashi et al. Review of Particle Physics. *Phys. Rev. D*, 98(3):030001, 2018. `doi:10.1103/PhysRevD.98.030001`.

[283] Eldad Gildener and Steven Weinberg. Symmetry breaking and scalar bosons. *Phys. Rev. D*, 13:3333–3341, Jun 1976. URL: `https://link.aps.org/doi/10.1103/PhysRevD.13.3333`, `doi:10.1103/PhysRevD.13.3333`.

[284] Leonard Susskind. Dynamics of spontaneous symmetry breaking in the weinberg-salam theory. *Phys. Rev. D*, 20:2619–2625, Nov 1979. URL: `https://link.aps.org/doi/10.1103/PhysRevD.20.2619`, `doi:10.1103/PhysRevD.20.2619`.

[285] Gerard 't Hooft. Naturalness, chiral symmetry, and spontaneous chiral symmetry breaking. *NATO Sci. Ser. B*, 59:135–157, 1980. `doi:10.1007/978-1-4684-7571-5_9`.

[286] H.P. Nilles. Supersymmetry, supergravity and particle physics. *Physics Reports*, 110(1):1–162, 1984. URL: `https://www.sciencedirect.com/science/article/pii/0370157384900085`, `doi:10.1016/0370-1573(84)90008-5`.

[287] H.E. Haber and G.L. Kane. The search for supersymmetry: Probing physics beyond the standard model. *Physics Reports*, 117(2):75–263, 1985. URL: https://www.sciencedirect.com/science/article/pii/0370157385900511, doi:10.1016/0370-1573(85)90051-1.

[288] Howard Baer and Xerxes Tata. *Weak Scale Supersymmetry: From Superfields to Scattering Events*. Cambridge University Press, 2006. doi:10.1017/CBO9780511617270.

[289] Gianfranco Bertone, Dan Hooper, and Joseph Silk. Particle dark matter: Evidence, candidates and constraints. *Phys. Rept.*, 405:279–390, 2005. arXiv:hep-ph/0404175, doi:10.1016/j.physrep.2004.08.031.

[290] G. Belanger. Dark matter and the LHC. *Nucl. Phys. B Proc. Suppl.*, 194:5–10, 2009. arXiv:0907.0770, doi:10.1016/j.nuclphysbps.2009.07.037.

[291] Rahool Kumar Barman, Genevieve Belanger, and Rohini M. Godbole. Status of low mass LSP in SUSY. *Eur. Phys. J. ST*, 229(21):3159–3185, 2020. arXiv:2010.11674, doi:10.1140/epjst/e2020-000198-1.

[292] Benjamin W. Lee and Steven Weinberg. Cosmological lower bound on heavy-neutrino masses. *Phys. Rev. Lett.*, 39:165–168, Jul 1977. URL: https://link.aps.org/doi/10.1103/PhysRevLett.39.165, doi:10.1103/PhysRevLett.39.165.

[293] Takeo Moroi and Lisa Randall. Wino cold dark matter from anomaly mediated SUSY breaking. *Nucl. Phys. B*, 570:455–472, 2000. arXiv:hep-ph/9906527, doi:10.1016/S0550-3213(99)00748-8.

[294] Katherine Garrett and Gintaras Duda. Dark Matter: A Primer. *Adv. Astron.*, 2011:968283, 2011. arXiv:1006.2483, doi:10.1155/2011/968283.

[295] Graciela B. Gelmini and Paolo Gondolo. Neutralino with the right cold dark matter abundance in (almost) any supersymmetric model. *Phys. Rev. D*, 74:023510, 2006. arXiv:hep-ph/0602230, doi:10.1103/PhysRevD.74.023510.

[296] Howard Baer, Ki-Young Choi, Jihn E. Kim, and Leszek Roszkowski. Dark matter production in the early Universe: beyond the thermal WIMP paradigm. *Phys. Rept.*, 555:1–60, 2015. arXiv:1407.0017, doi:10.1016/j.physrep.2014.10.002.

[297] Luis Aparicio, Michele Cicoli, Bhaskar Dutta, Sven Krippendorf, Anshuman Maharana, Francesco Muia, and Fernando Quevedo. Non-thermal CMSSM with a 125 GeV Higgs. *JHEP*, 05:098, 2015. arXiv:1502.05672, doi:10.1007/JHEP05(2015)098.

[298] Luis Aparicio, Michele Cicoli, Bhaskar Dutta, Francesco Muia, and Fernando Quevedo. Light Higgsino Dark Matter from Non-thermal Cosmology. *JHEP*, 11:038, 2016. arXiv:1607.00004, doi:10.1007/JHEP11(2016)038.

[299] Leszek Roszkowski, Sebastian Trojanowski, and Krzysztof Turzynski. Towards understanding thermal history of the Universe through direct and indirect detection of dark matter. *JCAP*, 10:005, 2017. arXiv:1703.00841, doi:10.1088/1475-7516/2017/10/005.

[300] Rahool Kumar Barman, Genevieve Belanger, Biplob Bhattacherjee, Rohini Godbole, Gaurav Mendiratta, and Dipan Sengupta. Invisible decay of the Higgs boson in the context of a thermal and nonthermal relic in MSSM. *Phys. Rev. D*, 95(9):095018, 2017. arXiv:1703.03838, doi:10.1103/PhysRevD.95.095018.

[301] Toby Falk, Keith A. Olive, and Mark Srednicki. Heavy sneutrinos as dark matter. *Phys. Lett. B*, 339:248–251, 1994. arXiv:hep-ph/9409270, doi:10.1016/0370-2693(94)90639-4.

[302] Armen Tumasyan et al. Search for chargino-neutralino production in events with Higgs and W bosons using 137 fb^{-1} of proton-proton collisions at $\sqrt{s} = 13$ TeV. *JHEP*, 10:045, 2021. arXiv:2107.12553, doi:10.1007/JHEP10(2021)045.

[303] Search for charginos and neutralinos in final states with two boosted hadronically decaying bosons and missing transverse momentum in pp collisions at $\sqrt{s} = 13$ TeV with the atlas detector. *Phys. Rev. D*, 104:112010, Dec 2021. URL: https://link.aps.org/doi/10.1103/PhysRevD.104.112010, doi:10.1103/PhysRevD.104.112010.

[304] Lorenzo Calibbi, Jonas M. Lindert, Toshihiko Ota, and Yasutaka Takanishi. Cornering light Neutralino Dark Matter at the LHC. *JHEP*, 10:132, 2013. arXiv:1307.4119, doi:10.1007/JHEP10(2013)132.

[305] Geneviève Bélanger, Guillaume Drieu La Rochelle, Béranger Dumont, Rohini M. Godbole, Sabine Kraml, and Suchita Kulkarni. LHC constraints on light neutralino dark matter in the MSSM. *Phys. Lett. B*, 726:773–780, 2013. arXiv:1308.3735, doi:10.1016/j.physletb.2013.09.059.

[306] M. Cahill-Rowley, J. L. Hewett, A. Ismail, and T. G. Rizzo. Lessons and prospects from the pMSSM after LHC Run I. *Phys. Rev. D*, 91(5):055002, 2015. arXiv:1407.4130, doi:10.1103/PhysRevD.91.055002.

[307] Junjie Cao, Yangle He, Liangliang Shang, Wei Su, and Yang Zhang. Testing the light dark matter scenario of the MSSM at the LHC. *JHEP*, 03:207, 2016. arXiv:1511.05386, doi:10.1007/JHEP03(2016)207.

[308] N. Arkani-Hamed, A. Delgado, and G. F. Giudice. The Well-tempered neutralino. *Nucl. Phys. B*, 741:108–130, 2006. arXiv:hep-ph/0601041, doi:10.1016/j.nuclphysb.2006.02.010.

[309] Howard Baer, Vernon Barger, and Hasan Serce. SUSY under siege from direct and indirect WIMP detection experiments. *Phys. Rev. D*, 94(11):115019, 2016. arXiv:1609.06735, doi:10.1103/PhysRevD.94.115019.

[310] Manimala Chakraborti, Utpal Chattopadhyay, and Sujoy Poddar. How light a higgsino or a wino dark matter can become in a compressed scenario of MSSM. *JHEP*, 09:064, 2017. arXiv:1702.03954, doi:10.1007/JHEP09(2017)064.

[311] Jihn E. Kim and Hans Peter Nilles. The mu Problem and the Strong CP Problem. *Phys. Lett. B*, 138:150–154, 1984. doi:10.1016/0370-2693(84)91890-2.

[312] H.P. Nilles, M. Srednicki, and D. Wyler. Weak interaction breakdown induced by supergravity. *Physics Letters B*, 120(4):346–348, 1983. URL: https://www.sciencedirect.com/science/article/pii/0370269383904604, doi:10.1016/0370-2693(83)90460-4.

[313] J. Ellis, J. F. Gunion, H. E. Haber, L. Roszkowski, and F. Zwirner. Higgs bosons in a nonminimal supersymmetric model. *Phys. Rev. D*, 39:844–869, Feb 1989. URL: https://link.aps.org/doi/10.1103/PhysRevD.39.844, doi:10.1103/PhysRevD.39.844.

[314] Ulrich Ellwanger, Michel Rausch de Traubenberg, and Carlos A. Savoy. Particle spectrum in supersymmetric models with a gauge singlet. *Phys. Lett. B*, 315:331–337, 1993. arXiv:hep-ph/9307322, doi:10.1016/0370-2693(93)91621-S.

[315] S. A. Abel, Subir Sarkar, and I. B. Whittingham. Neutralino dark matter in a class of unified theories. *Nucl. Phys. B*, 392:83–110, 1993. arXiv:hep-ph/9209292, doi:10.1016/0550-3213(93)90198-X.

[316] Jonathan Kozaczuk and Stefano Profumo. Light NMSSM neutralino dark matter in the wake of CDMS II and a 126 GeV Higgs boson. *Phys. Rev. D*, 89(9):095012, 2014. arXiv:1308.5705, doi:10.1103/PhysRevD.89.095012.

[317] Junjie Cao, Chengcheng Han, Lei Wu, Peiwen Wu, and Jin Min Yang. A light SUSY dark matter after CDMS-II, LUX and LHC Higgs data. *JHEP*, 05:056, 2014. `arXiv:1311.0678`, `doi:10.1007/JHEP05(2014)056`.

[318] Tao Han, Zhen Liu, and Shufang Su. Light Neutralino Dark Matter: Direct/Indirect Detection and Collider Searches. *JHEP*, 08:093, 2014. `arXiv:1406.1181`, `doi:10.1007/JHEP08(2014)093`.

[319] Ulrich Ellwanger and Cyril Hugonie. The semi-constrained NMSSM satisfying bounds from the LHC, LUX and Planck. *JHEP*, 08:046, 2014. `arXiv:1405.6647`, `doi:10.1007/JHEP08(2014)046`.

[320] Junjie Cao, Demin Li, Jingwei Lian, Yuanfang Yue, and Haijing Zhou. Singlino-dominated dark matter in general NMSSM. *JHEP*, 06:176, 2021. `arXiv:2102.05317`, `doi:10.1007/JHEP06(2021)176`.

[321] Haijing Zhou, Junjie Cao, Jingwei Lian, and Di Zhang. Singlino-dominated dark matter in Z3-symmetric NMSSM. *Phys. Rev. D*, 104(1):015017, 2021. `arXiv:2102.05309`, `doi:10.1103/PhysRevD.104.015017`.

[322] Rahool Kumar Barman, Genevieve Bélanger, Biplob Bhattacherjee, Rohini Godbole, Dipan Sengupta, and Xerxes Tata. Current bounds and future prospects of light neutralino dark matter in NMSSM. *Phys. Rev. D*, 103(1):015029, 2021. `arXiv:2006.07854`, `doi:10.1103/PhysRevD.103.015029`.

[323] Monoranjan Guchait and Arnab Roy. Light Singlino Dark Matter at the LHC. *Phys. Rev. D*, 102(7):075023, 2020. `arXiv:2005.05190`, `doi:10.1103/PhysRevD.102.075023`.

[324] Haiying Cai, Hsin-Chia Cheng, and John Terning. A Quirky Little Higgs Model. *JHEP*, 05:045, 2009. `arXiv:0812.0843`, `doi:10.1088/1126-6708/2009/05/045`.

[325] Z. Chacko, Hock-Seng Goh, and Roni Harnik. The Twin Higgs: Natural electroweak breaking from mirror symmetry. *Phys. Rev. Lett.*, 96:231802, 2006. `arXiv:hep-ph/0506256`, `doi:10.1103/PhysRevLett.96.231802`.

[326] Matthew Baumgart, Clifford Cheung, Joshua T. Ruderman, Lian-Tao Wang, and Itay Yavin. Non-Abelian Dark Sectors and Their Collider Signatures. *JHEP*, 04:014, 2009. `arXiv:0901.0283`, `doi:10.1088/1126-6708/2009/04/014`.

[327] David E. Kaplan, Markus A. Luty, and Kathryn M. Zurek. Asymmetric Dark Matter. *Phys. Rev. D*, 79:115016, 2009. `arXiv:0901.4117`, `doi:10.1103/PhysRevD.79.115016`.

[328] Keith R. Dienes and Brooks Thomas. Dynamical Dark Matter: I. Theoretical Overview. *Phys. Rev. D*, 85:083523, 2012. `arXiv:1106.4546`, `doi:10.1103/PhysRevD.85.083523`.

[329] Keith R. Dienes, Shufang Su, and Brooks Thomas. Distinguishing Dynamical Dark Matter at the LHC. *Phys. Rev. D*, 86:054008, 2012. `arXiv:1204.4183`, `doi:10.1103/PhysRevD.86.054008`.

[330] Juliette Alimena et al. Searching for long-lived particles beyond the Standard Model at the Large Hadron Collider. *J. Phys. G*, 47(9):090501, 2020. `arXiv:1903.04497`, `doi:10.1088/1361-6471/ab4574`.

[331] R. Barbier et al. R-parity violating supersymmetry. *Phys. Rept.*, 420:1–202, 2005. `arXiv:hep-ph/0406039`, `doi:10.1016/j.physrep.2005.08.006`.

[332] Savas Dimopoulos, Michael Dine, Stuart Raby, and Scott D. Thomas. Experimental signatures of low-energy gauge mediated supersymmetry breaking. *Phys. Rev. Lett.*, 76:3494–3497, 1996. `arXiv:hep-ph/9601367`, `doi:10.1103/PhysRevLett.76.3494`.

[333] G. F. Giudice and R. Rattazzi. Theories with gauge mediated supersymmetry breaking. *Phys. Rept.*, 322:419–499, 1999. arXiv:hep-ph/9801271, doi:10.1016/S0370-1573(99)00042-3.

[334] Jonathan L. Feng, Takeo Moroi, Lisa Randall, Matthew Strassler, and Shu-fang Su. Discovering supersymmetry at the Tevatron in wino LSP scenarios. *Phys. Rev. Lett.*, 83:1731–1734, 1999. arXiv:hep-ph/9904250, doi:10.1103/PhysRevLett.83.1731.

[335] JiJi Fan and Matthew Reece. In Wino Veritas? Indirect Searches Shed Light on Neutralino Dark Matter. *JHEP*, 10:124, 2013. arXiv:1307.4400, doi:10.1007/JHEP10(2013)124.

[336] Joseph Bramante, Nishita Desai, Patrick Fox, Adam Martin, Bryan Ostdiek, and Tilman Plehn. Towards the Final Word on Neutralino Dark Matter. *Phys. Rev. D*, 93(6):063525, 2016. arXiv:1510.03460, doi:10.1103/PhysRevD.93.063525.

[337] Alexander Kusenko, Paul Langacker, and Gino Segre. Phase transitions and vacuum tunneling into charge and color breaking minima in the MSSM. *Phys. Rev. D*, 54:5824–5834, 1996. arXiv:hep-ph/9602414, doi:10.1103/PhysRevD.54.5824.

[338] Debtosh Chowdhury, Rohini M. Godbole, Kirtimaan A. Mohan, and Sudhir K. Vempati. Charge and Color Breaking Constraints in MSSM after the Higgs Discovery at LHC. *JHEP*, 02:110, 2014. [Erratum: JHEP 03, 149 (2018)]. arXiv:1310.1932, doi:10.1007/JHEP02(2014)110.

[339] Felix Brummer, Sabine Kraml, and Suchita Kulkarni. Anatomy of maximal stop mixing in the MSSM. *JHEP*, 08:089, 2012. arXiv:1204.5977, doi:10.1007/JHEP08(2012)089.

[340] Ulrich Ellwanger, John F Gunion, and Cyril Hugonie. Nmhdecay: A fortran code for the higgs masses, couplings and decay widths in the nmssm. *Journal of High Energy Physics*, 2005(02):066–066, Mar 2005. URL: http://dx.doi.org/10.1088/1126-6708/2005/02/066, doi:10.1088/1126-6708/2005/02/066.

[341] Ulrich Ellwanger and Cyril Hugonie. Nmhdecay 2.1: An updated program for sparticle masses, higgs masses, couplings and decay widths in the nmssm. *Computer Physics Communications*, 175(4):290–303, Aug 2006. URL: http://dx.doi.org/10.1016/j.cpc.2006.04.004, doi:10.1016/j.cpc.2006.04.004.

[342] Georges Aad et al. Combined Measurement of the Higgs Boson Mass in pp Collisions at $\sqrt{s} = 7$ and 8 TeV with the ATLAS and CMS Experiments. *Phys. Rev. Lett.*, 114:191803, 2015. arXiv:1503.07589, doi:10.1103/PhysRevLett.114.191803.

[343] B. C. Allanach, A. Djouadi, J. L. Kneur, W. Porod, and P. Slavich. Precise determination of the neutral Higgs boson masses in the MSSM. *JHEP*, 09:044, 2004. arXiv:hep-ph/0406166, doi:10.1088/1126-6708/2004/09/044.

[344] S. Heinemeyer, W. Hollik, H. Rzehak, and G. Weiglein. The Higgs sector of the complex MSSM at two-loop order: QCD contributions. *Phys. Lett. B*, 652:300–309, 2007. arXiv:0705.0746, doi:10.1016/j.physletb.2007.07.030.

[345] S. Borowka, T. Hahn, S. Heinemeyer, G. Heinrich, and W. Hollik. Renormalization scheme dependence of the two-loop QCD corrections to the neutral Higgs-boson masses in the MSSM. *Eur. Phys. J. C*, 75(9):424, 2015. arXiv:1505.03133, doi:10.1140/epjc/s10052-015-3648-6.

[346] LEPSUSYWG Aleph Delphi L3 and OPAL experiment note LEPSUSYWG/01-03.1. Combined lep chargino mass limts. http://lepsusy.web.cern.ch/lepsusy.

[347] G. Abbiendi et al. Search for chargino and neutralino production at s**(1/2) = 192-GeV to 209 GeV at LEP. *Eur. Phys. J. C*, 35:1–20, 2004. arXiv:hep-ex/0401026, doi:10.1140/epjc/s2004-01758-8.

[348] S. Schael et al. Precision electroweak measurements on the *Z* resonance. *Phys. Rept.*, 427:257–454, 2006. arXiv:hep-ex/0509008, doi:10.1016/j.physrep.2005.12.006.

[349] Albert M Sirunyan et al. Measurements of Higgs boson production cross sections and couplings in the diphoton decay channel at $\sqrt{s}$ = 13 TeV. *JHEP*, 07:027, 2021. arXiv:2103.06956, doi:10.1007/JHEP07(2021)027.

[350] Measurement of Higgs boson production in association with a W or Z boson in the H $\rightarrow$ WW decay channel. Technical report, CERN, Geneva, 2021. URL: https://cds.cern.ch/record/2758367.

[351] Albert M Sirunyan et al. Measurement of the inclusive and differential Higgs boson production cross sections in the leptonic WW decay mode at $\sqrt{s} = 13$ TeV. *JHEP*, 03:003, 2021. arXiv:2007.01984, doi:10.1007/JHEP03(2021)003.

[352] Measurement of Higgs boson production in the decay channel with a pair of τ leptons. Technical report, CERN, Geneva, 2020. URL: https://cds.cern.ch/record/2725590.

[353] Albert M Sirunyan et al. Measurements of properties of the Higgs boson decaying into the four-lepton final state in pp collisions at $\sqrt{s} = 13$ TeV. *JHEP*, 11:047, 2017. arXiv:1706.09936, doi:10.1007/JHEP11(2017)047.

[354] Rahool Kumar Barman, Biplob Bhattacherjee, Arghya Choudhury, Debtosh Chowdhury, Jayita Lahiri, and Shamayita Ray. Current status of MSSM Higgs sector with LHC 13 TeV data. *Eur. Phys. J. Plus*, 134(4):150, 2019. arXiv:1608.02573, doi:10.1140/epjp/i2019-12566-5.

[355] Yasmine Sara Amhis et al. Averages of *b*-hadron, *c*-hadron, and τ-lepton properties as of 2018. 9 2019. arXiv:1909.12524.

[356] The LHCb Collaboration. Combination of the ATLAS, CMS and LHCb results on the $B^0_{(s)} \rightarrow \mu^+\mu^-$ decays. 2020.

[357] Roel Aaij et al. Precise measurement of the f_s/f_d ratio of fragmentation fractions and of B^0_s decay branching fractions. 3 2021. arXiv:2103.06810.

[358] G. Bélanger, F. Boudjema, A. Pukhov, and A. Semenov. micromegas: A program for calculating the relic density in the mssm. *Computer Physics Communications*, 149(2):103–120, Dec 2002. URL: http://dx.doi.org/10.1016/S0010-4655(02)00596-9, doi:10.1016/s0010-4655(02)00596-9.

[359] G. Belanger, F. Boudjema, C. Hugonie, A. Pukhov, and A. Semenov. Relic density of dark matter in the NMSSM. *JCAP*, 09:001, 2005. arXiv:hep-ph/0505142, doi:10.1088/1475-7516/2005/09/001.

[360] Geneviève Bélanger, Fawzi Boudjema, Andreas Goudelis, Alexander Pukhov, and Bryan Zaldivar. micrOMEGAs5.0 : Freeze-in. *Comput. Phys. Commun.*, 231:173–186, 2018. arXiv:1801.03509, doi:10.1016/j.cpc.2018.04.027.

[361] Ulrich Ellwanger and Cyril Hugonie. The higgsino–singlino sector of the NMSSM: combined constraints from dark matter and the LHC. *Eur. Phys. J. C*, 78(9):735, 2018. arXiv:1806.09478, doi:10.1140/epjc/s10052-018-6204-3.

[362] E. Aprile and OTHERS. Dark matter search results from a one ton-year exposure of xenon1t. *Phys. Rev. Lett.*, 121:111302, Sep 2018. URL: https://link.aps.org/doi/10.1103/PhysRevLett.121.111302, doi:10.1103/PhysRevLett.121.111302.

[363] Yue Meng et al. Dark Matter Search Results from the PandaX-4T Commissioning Run. *Phys. Rev. Lett.*, 127(26):261802, 2021. arXiv:2107.13438, doi:10.1103/PhysRevLett.127.261802.

[364] E. Aprile et al. Constraining the spin-dependent WIMP-nucleon cross sections with XENON1T. *Phys. Rev. Lett.*, 122(14):141301, 2019. arXiv:1902.03234, doi:10.1103/PhysRevLett.122.141301.

[365] P. Cushman et al. Working Group Report: WIMP Dark Matter Direct Detection. In *Community Summer Study 2013: Snowmass on the Mississippi*, 10 2013. arXiv:1310.8327.

[366] D. S. Akerib et al. Results on the Spin-Dependent Scattering of Weakly Interacting Massive Particles on Nucleons from the Run 3 Data of the LUX Experiment. *Phys. Rev. Lett.*, 116(16):161302, 2016. arXiv:1602.03489, doi:10.1103/PhysRevLett.116.161302.

[367] Debottam Das, Ulrich Ellwanger, and Ana M. Teixeira. NMSDECAY: A Fortran Code for Supersymmetric Particle Decays in the Next-to-Minimal Supersymmetric Standard Model. *Comput. Phys. Commun.*, 183:774–779, 2012. arXiv:1106.5633, doi:10.1016/j.cpc.2011.11.021.

[368] W. Beenakker, R. Hopker, and M. Spira. PROSPINO: A Program for the production of supersymmetric particles in next-to-leading order QCD. 11 1996. arXiv:hep-ph/9611232.

[369] Rojalin Padhan, Manimala Mitra, Suchita Kulkarni, and Frank F. Deppisch. Displaced fat-jets and tracks to probe boosted right-handed neutrinos in the $U(1)_{B-L}$ model. *Eur. Phys. J. C*, 82(10):858, 2022. arXiv:2203.06114, doi:10.1140/epjc/s10052-022-10819-7.

[370] Shankha Banerjee, Biplob Bhattacherjee, Andreas Goudelis, Björn Herrmann, Dipan Sengupta, and Rhitaja Sengupta. Determining the lifetime of long-lived particles at the HL-LHC. *Eur. Phys. J. C*, 81(2):172, 2021. arXiv:1912.06669, doi:10.1140/epjc/s10052-021-08945-9.

[371] Serguei Chatrchyan et al. Search in Leptonic Channels for Heavy Resonances Decaying to Long-Lived Neutral Particles. *JHEP*, 02:085, 2013. arXiv:1211.2472, doi:10.1007/JHEP02(2013)085.

[372] Georges Aad et al. Search for displaced muonic lepton jets from light Higgs boson decay in proton-proton collisions at $\sqrt{s}$ = 7 TeV with the ATLAS detector. *Phys. Lett. B*, 721:32–50, 2013. arXiv:1210.0435, doi:10.1016/j.physletb.2013.02.058.

[373] Torbjorn Sjostrand, Stephen Mrenna, and Peter Z. Skands. PYTHIA 6.4 Physics and Manual. *JHEP*, 05:026, 2006. arXiv:hep-ph/0603175, doi:10.1088/1126-6708/2006/05/026.

[374] Torbjorn Sjostrand, Stephen Mrenna, and Peter Z. Skands. A Brief Introduction to PYTHIA 8.1. *Comput. Phys. Commun.*, 178:852–867, 2008. arXiv:0710.3820, doi:10.1016/j.cpc.2008.01.036.

[375] Michele Selvaggi et al. Beta card for HL-LHC and HE-LHC studies, December 2017. https://github.com/delphes/delphes/blob/master/cards/delphes_card_HLLHC.tcl.

[376] Michele Selvaggi, Pavel Demin, Christophe Delaere, Kevin Pedro, Joschka Lingemann, simonspa, Philip Harris, Sho Iwamoto, Geonmo Ryu, Joshua Ellis, Chase, and Adarsh Pyarelal. delphes/delphes: Delphes-3.4.2pre11. 2017.

[377] Morad Aaboud et al. Search for long-lived, massive particles in events with displaced vertices and missing transverse momentum in $\sqrt{s}$ = 13 TeV pp collisions with the ATLAS detector. *Phys. Rev. D*, 97(5):052012, 2018. arXiv:1710.04901, doi:10.1103/PhysRevD.97.052012.

[378] Albert M Sirunyan et al. Search for long-lived particles using nonprompt jets and missing transverse momentum with proton-proton collisions at $\sqrt{s}$ = 13 TeV. *Phys. Lett. B*, 797:134876, 2019. `arXiv:1906.06441`, `doi:10.1016/j.physletb.2019.134876`.

[379] Biplob Bhattacherjee, Swagata Mukherjee, Rhitaja Sengupta, and Prabhat Solanki. Triggering long-lived particles in HL-LHC and the challenges in the rst stage of the trigger system. *JHEP*, 08:141, 2020. `arXiv:2003.03943`, `doi:10.1007/JHEP08(2020)141`.

[380] Alexandre Zabi, Jeffrey Wayne Berryhill, Emmanuelle Perez, and Alexander D. Tapper. The Phase-2 Upgrade of the CMS Level-1 Trigger. 2020.

[381] Biplob Bhattacherjee, Tapasi Ghosh, Rhitaja Sengupta, and Prabhat Solanki. Dedicated Triggers for Displaced Jets using Timing Information from Electromagnetic Calorimeter at HL-LHC. 12 2021. `arXiv:2112.04518`.

[382] Georges Aad et al. Search for exotic decays of the Higgs boson into long-lived particles in pp collisions at $\sqrt{s}$ = 13 TeV using displaced vertices in the ATLAS inner detector. *JHEP*, 11:229, 2021. `arXiv:2107.06092`, `doi:10.1007/JHEP11(2021)229`.

[383] Armen Tumasyan et al. Search for long-lived particles produced in association with a Z boson in proton-proton collisions at $\sqrt{s}$ = 13 TeV. *JHEP*, 03:160, 2022. `arXiv:2110.13218`, `doi:10.1007/JHEP03(2022)160`.

[384] A. M. Sirunyan et al. Search for long-lived particles decaying to jets with displaced vertices in proton-proton collisions at $\sqrt{s}$ = 13 TeV. *Phys. Rev. D*, 104(5):052011, 2021. `arXiv:2104.13474`, `doi:10.1103/PhysRevD.104.052011`.

[385] The Phase-2 Upgrade of the CMS Level-1 Trigger. Technical report, CERN, Geneva, Apr 2020. Final version. URL: `https://cds.cern.ch/record/2714892`.

[386] CMS Collaboration. The Phase-2 Upgrade of the CMS Data Acquisition and High Level Trigger. Technical report, CERN, Geneva, Mar 2021. This is the final version of the document, approved by the LHCC. URL: `https://cds.cern.ch/record/2759072`.

[387] M. Aaboud et al. Performance of the ATLAS Track Reconstruction Algorithms in Dense Environments in LHC Run 2. *Eur. Phys. J. C*, 77(10):673, 2017. `arXiv:1704.07983`, `doi:10.1140/epjc/s10052-017-5225-7`.

[388] Dan Hooper and Edward A. Baltz. Strategies for Determining the Nature of Dark Matter. *Ann. Rev. Nucl. Part. Sci.*, 58:293–314, 2008. `arXiv:0802.0702`, `doi:10.1146/annurev.nucl.58.110707.171217`.

[389] Jonathan L. Feng. Dark Matter Candidates from Particle Physics and Methods of Detection. *Ann. Rev. Astron. Astrophys.*, 48:495–545, 2010. `arXiv:1003.0904`, `doi:10.1146/annurev-astro-082708-101659`.

[390] Jessica Goodman, Masahiro Ibe, Arvind Rajaraman, William Shepherd, Tim M. P. Tait, and Hai-Bo Yu. Constraints on Light Majorana dark Matter from Colliders. *Phys. Lett. B*, 695:185–188, 2011. `arXiv:1005.1286`, `doi:10.1016/j.physletb.2010.11.009`.

[391] Patrick J. Fox, Roni Harnik, Joachim Kopp, and Yuhsin Tsai. Missing Energy Signatures of Dark Matter at the LHC. *Phys. Rev. D*, 85:056011, 2012. `arXiv:1109.4398`, `doi:10.1103/PhysRevD.85.056011`.

[392] D. S. Akerib et al. Projected WIMP sensitivity of the LUX-ZEPLIN dark matter experiment. *Phys. Rev. D*, 101(5):052002, 2020. `arXiv:1802.06039`, `doi:10.1103/PhysRevD.101.052002`.

[393] Junjie Cao, Lei Meng, Yuanfang Yue, Haijing Zhou, and Pengxuan Zhu. Suppressing the scattering of WIMP dark matter and nucleons in supersymmetric theories. *Phys. Rev. D*, 101(7):075003, 2020. `arXiv:1910.14317`, `doi:10.1103/PhysRevD.101.075003`.

[394] Peisi Huang, Roger A. Roglans, Daniel D. Spiegel, Yitian Sun, and Carlos E. M. Wagner. Constraints on Supersymmetric Dark Matter for Heavy Scalar Superpartners. *Phys. Rev. D*, 95(9):095021, 2017. `arXiv:1701.02737`, `doi:10.1103/PhysRevD.95.095021`.

[395] Marcin Badziak, Marek Olechowski, and Pawel Szczerbiak. Is well-tempered neutralino in MSSM still alive after 2016 LUX results? *Phys. Lett. B*, 770:226–235, 2017. `arXiv:1701.05869`, `doi:10.1016/j.physletb.2017.04.059`.

[396] Murat Abdughani, Lei Wu, and Jin Min Yang. Status and prospects of light bino–higgsino dark matter in natural SUSY. *Eur. Phys. J. C*, 78(1):4, 2018. `arXiv:1705.09164`, `doi:10.1140/epjc/s10052-017-5485-2`.

[397] J. A. Casas, J. R. Espinosa, and I. Hidalgo. The MSSM fine tuning problem: A Way out. *JHEP*, 01:008, 2004. `arXiv:hep-ph/0310137`, `doi:10.1088/1126-6708/2004/01/008`.

[398] Melissa van Beekveld, Sascha Caron, and Roberto Ruiz de Austri. The current status of fine-tuning in supersymmetry. *JHEP*, 01:147, 2020. `arXiv:1906.10706`, `doi:10.1007/JHEP01(2020)147`.

[399] Ulrich Ellwanger, Gregory Espitalier-Noel, and Cyril Hugonie. Naturalness and Fine Tuning in the NMSSM: Implications of Early LHC Results. *JHEP*, 09:105, 2011. `arXiv:1107.2472`, `doi:10.1007/JHEP09(2011)105`.

[400] M. Maniatis. The Next-to-Minimal Supersymmetric extension of the Standard Model reviewed. *Int. J. Mod. Phys. A*, 25:3505–3602, 2010. `arXiv:0906.0777`, `doi:10.1142/S0217751X10049827`.

[401] Jinrui Huang, Tao Liu, Lian-Tao Wang, and Felix Yu. Supersymmetric Exotic Decays of the 125 GeV Higgs Boson. *Phys. Rev. Lett.*, 112(22):221803, 2014. `arXiv:1309.6633`, `doi:10.1103/PhysRevLett.112.221803`.

[402] Ulrich Ellwanger and Ana M. Teixeira. NMSSM with a singlino LSP: possible challenges for searches for supersymmetry at the LHC. *JHEP*, 10:113, 2014. `arXiv:1406.7221`, `doi:10.1007/JHEP10(2014)113`.

[403] Sebastian Baum, Marcela Carena, Nausheen R. Shah, and Carlos E. M. Wagner. Higgs portals for thermal Dark Matter. EFT perspectives and the NMSSM. *JHEP*, 04:069, 2018. `arXiv:1712.09873`, `doi:10.1007/JHEP04(2018)069`.

[404] Waleed Abdallah, Arindam Chatterjee, and AseshKrishna Datta. Revisiting singlino dark matter of the natural Z_3-symmetric NMSSM in the light of LHC. *JHEP*, 09:095, 2019. `arXiv:1907.06270`, `doi:10.1007/JHEP09(2019)095`.

[405] Ulrich Ellwanger, Cyril Hugonie, Stephen F. King, and Stefano Moretti. NMSSM Explanation for Excesses in the Search for Neutralinos and Charginos and a 95 GeV Higgs Boson. 4 2024. `arXiv:2404.19338`.

[406] Sebastian Baum, Nausheen R. Shah, and Katherine Freese. The NMSSM is within Reach of the LHC: Mass Correlations \& Decay Signatures. *JHEP*, 04:011, 2019. `arXiv:1901.02332`, `doi:10.1007/JHEP04(2019)011`.

[407] Florian Domingo, Jong Soo Kim, Víctor Martín Lozano, Pablo Martin-Ramiro, and Roberto Ruiz de Austri. Confronting the neutralino and chargino sector of the NMSSM with the multilepton searches at the LHC. *Phys. Rev. D*, 101(7):075010, 2020. `arXiv:1812.05186`, `doi:10.1103/PhysRevD.101.075010`.

[408] Junjie Cao, Yangle He, Liangliang Shang, Yang Zhang, and Pengxuan Zhu. Current status of a natural NMSSM in light of LHC 13 TeV data and XENON-1T results. *Phys. Rev. D*, 99(7):075020, 2019. `arXiv:1810.09143`, `doi:10.1103/PhysRevD.99.075020`.

BIBLIOGRAPHY

[409] Junjie Cao, Xinglong Jia, Lei Meng, Yuanfang Yue, and Di Zhang. Status of the singlino-dominated dark matter in general Next-to-Minimal Supersymmetric Standard Model. *JHEP*, 03:198, 2023. arXiv:2210.08769, doi:10.1007/JHEP03(2023)198.

[410] Junjie Cao, Fei Li, Jingwei Lian, Yusi Pan, and Di Zhang. Impact of LHC probes of SUSY and recent measurement of $(g-2)$ on $\mathbb{Z}_3$-NMSSM. *Sci. China Phys. Mech. Astron.*, 65(9):291012, 2022. arXiv:2204.04710, doi:10.1007/s11433-022-1927-9.

[411] Lei Meng, Junjie Cao, and Shenshen Yang. Dark Matter Physics in General NMSSM. 5 2024. arXiv:2405.07036.

[412] Qian-Fei Xiang, Xiao-Jun Bi, Peng-Fei Yin, and Zhao-Huan Yu. Searching for Singlino-Higgsino Dark Matter in the NMSSM. *Phys. Rev. D*, 94(5):055031, 2016. arXiv:1606.02149, doi:10.1103/PhysRevD.94.055031.

[413] Ulrich Ellwanger. Present Status and Future Tests of the Higgsino-Singlino Sector in the NMSSM. *JHEP*, 02:051, 2017. arXiv:1612.06574, doi:10.1007/JHEP02(2017)051.

[414] Jong Soo Kim and Tirtha Sankar Ray. The higgsino-singlino world at the large hadron collider. *Eur. Phys. J. C*, 75:40, 2015. arXiv:1405.3700, doi:10.1140/epjc/s10052-015-3281-4.

[415] Debottam Das, Ulrich Ellwanger, and Ana M. Teixeira. Modified Signals for Supersymmetry in the NMSSM with a Singlino-like LSP. *JHEP*, 04:067, 2012. arXiv:1202.5244, doi:10.1007/JHEP04(2012)067.

[416] Georges Aad et al. Evidence for the production of three massive vector bosons with the ATLAS detector. *Phys. Lett. B*, 798:134913, 2019. arXiv:1903.10415, doi:10.1016/j.physletb.2019.134913.

[417] G. Aad et al. Observation of WWW Production in pp Collisions at $\sqrt{s}$ =13 TeV with the ATLAS Detector. *Phys. Rev. Lett.*, 129(6):061803, 2022. arXiv:2201.13045, doi:10.1103/PhysRevLett.129.061803.

[418] Albert M Sirunyan et al. Observation of the Production of Three Massive Gauge Bosons at $\sqrt{s}$ =13 TeV. *Phys. Rev. Lett.*, 125(15):151802, 2020. arXiv:2006.11191, doi:10.1103/PhysRevLett.125.151802.

[419] Observation of heavy triboson production in leptonic final states in proton-proton collisions at $\sqrt{s} = 13$ TeV. Technical report, CERN, Geneva, 2020. URL: https://cds.cern.ch/record/2714899.

[420] David G. Cerdeño, Pradipta Ghosh, Chan Beom Park, and Miguel Peiró. Collider signatures of a light NMSSM pseudoscalar in neutralino decays in the light of LHC results. *JHEP*, 02:048, 2014. arXiv:1307.7601, doi:10.1007/JHEP02(2014)048.

[421] Bhaskar Dutta, Yu Gao, and Bibhushan Shakya. Light Higgsino Decays as a Probe of the NMSSM. *Phys. Rev. D*, 91(3):035016, 2015. arXiv:1412.2774, doi:10.1103/PhysRevD.91.035016.

[422] Florian Domingo. Decays of a NMSSM CP-odd Higgs in the low-mass region. *JHEP*, 03:052, 2017. arXiv:1612.06538, doi:10.1007/JHEP03(2017)052.

[423] Ulrich Ellwanger and Stefano Moretti. Possible Explanation of the Electron Positron Anomaly at 17 MeV in ^8Be Transitions Through a Light Pseudoscalar. *JHEP*, 11:039, 2016. arXiv:1609.01669, doi:10.1007/JHEP11(2016)039.

[424] Ulrich Ellwanger, John F. Gunion, and Cyril Hugonie. NMHDECAY: A Fortran code for the Higgs masses, couplings and decay widths in the NMSSM. *JHEP*, 02:066, 2005. arXiv:hep-ph/0406215, doi:10.1088/1126-6708/2005/02/066.

[425] Ulrich Ellwanger and Cyril Hugonie. Nmhdecay 2.1: An updated program for sparticle masses, higgs masses, couplings and decay widths in the nmssm. *Computer Physics Communications*, 175(4):290–303, 2006. URL: https://www.sciencedirect.com/science/article/pii/S0010465506001883, doi:10.1016/j.cpc.2006.04.004.

[426] G. Belanger, F. Boudjema, A. Pukhov, and A. Semenov. MicrOMEGAs 2.0: A Program to calculate the relic density of dark matter in a generic model. *Comput. Phys. Commun.*, 176:367–382, 2007. arXiv:hep-ph/0607059, doi:10.1016/j.cpc.2006.11.008.

[427] G. Belanger, F. Boudjema, A. Pukhov, and A. Semenov. Dark matter direct detection rate in a generic model with micrOMEGAs 2.2. *Comput. Phys. Commun.*, 180:747–767, 2009. arXiv:0803.2360, doi:10.1016/j.cpc.2008.11.019.

[428] D. Barducci, G. Belanger, J. Bernon, F. Boudjema, J. Da Silva, S. Kraml, U. Laa, and A. Pukhov. Collider limits on new physics within micrOMEGAs_4.3. *Comput. Phys. Commun.*, 222:327–338, 2018. arXiv:1606.03834, doi:10.1016/j.cpc.2017.08.028.

[429] Philip Bechtle, Sven Heinemeyer, Oscar Stål, Tim Stefaniak, and Georg Weiglein. $HiggsSignals$: Confronting arbitrary Higgs sectors with measurements at the Tevatron and the LHC. *Eur. Phys. J. C*, 74(2):2711, 2014. arXiv:1305.1933, doi:10.1140/epjc/s10052-013-2711-4.

[430] Philip Bechtle, Sven Heinemeyer, Oscar Stål, Tim Stefaniak, and Georg Weiglein. Probing the Standard Model with Higgs signal rates from the Tevatron, the LHC and a future ILC. *JHEP*, 11:039, 2014. arXiv:1403.1582, doi:10.1007/JHEP11(2014)039.

[431] Gaël Alguero, Jan Heisig, Charanjit K. Khosa, Sabine Kraml, Suchita Kulkarni, Andre Lessa, Humberto Reyes-González, Wolfgang Waltenberger, and Alicia Wongel. Constraining new physics with SModelS version 2. *JHEP*, 08:068, 2022. arXiv:2112.00769, doi:10.1007/JHEP08(2022)068.

[432] Mohammad Mahdi Altakach, Sabine Kraml, Andre Lessa, Sahana Narasimha, Timothée Pascal, and Wolfgang Waltenberger. SModelS v2.3: enabling global likelihood analyses. *SciPost Phys.*, 15:185, 2023. arXiv:2306.17676, doi:10.21468/SciPostPhys.15.5.185.

[433] Philip Bechtle, Oliver Brein, Sven Heinemeyer, Georg Weiglein, and Karina E. Williams. HiggsBounds: Confronting Arbitrary Higgs Sectors with Exclusion Bounds from LEP and the Tevatron. *Comput. Phys. Commun.*, 181:138–167, 2010. arXiv:0811.4169, doi:10.1016/j.cpc.2009.09.003.

[434] Philip Bechtle, Oliver Brein, Sven Heinemeyer, Georg Weiglein, and Karina E. Williams. HiggsBounds 2.0.0: Confronting Neutral and Charged Higgs Sector Predictions with Exclusion Bounds from LEP and the Tevatron. *Comput. Phys. Commun.*, 182:2605–2631, 2011. arXiv:1102.1898, doi:10.1016/j.cpc.2011.07.015.

[435] Philip Bechtle, Oliver Brein, Sven Heinemeyer, Oscar Stål, Tim Stefaniak, Georg Weiglein, and Karina E. Williams. HiggsBounds − 4: Improved Tests of Extended Higgs Sectors against Exclusion Bounds from LEP, the Tevatron and the LHC. *Eur. Phys. J. C*, 74(3):2693, 2014. arXiv:1311.0055, doi:10.1140/epjc/s10052-013-2693-2.

[436] R. Agnese et al. Projected Sensitivity of the SuperCDMS SNOLAB experiment. *Phys. Rev. D*, 95(8):082002, 2017. arXiv:1610.00006, doi:10.1103/PhysRevD.95.082002.

[437] Future dark matter searches with low-radioactivity argon. Input to the European Particle Physics Strategy Update 2018-2020 (2018). URL: https://indico.cern.ch/event/765096/contributions/3295671/attachments/1785196/2906164/DarkSide-Argo_ESPP_Dec_17_2017.pdf.

[438] Marc Schumann, Laura Baudis, Lukas Bütikofer, Alexander Kish, and Marco Selvi. Dark matter sensitivity of multi-ton liquid xenon detectors. *JCAP*, 10:016, 2015. arXiv:1506.08309, doi:10.1088/1475-7516/2015/10/016.

[439] J. Aalbers et al. DARWIN: towards the ultimate dark matter detector. *JCAP*, 11:017, 2016. arXiv:1606.07001, doi:10.1088/1475-7516/2016/11/017.

[440] M. Badziak, M. Olechowski, and P. Szczerbiak. Blind spots for neutralinos in NMSSM with light singlet scalar. *PoS*, PLANCK2015:130, 2015. arXiv:1601.00768.

[441] Subhojit Roy and Carlos E. M. Wagner. Dark Matter searches with photons at the LHC. *JHEP*, 04:106, 2024. arXiv:2401.08917, doi:10.1007/JHEP04(2024)106.

[442] A. Djouadi, U. Ellwanger, and A. M. Teixeira. Phenomenology of the constrained NMSSM. *JHEP*, 04:031, 2009. arXiv:0811.2699, doi:10.1088/1126-6708/2009/04/031.

[443] Georges Aad et al. Search for direct production of charginos and neutralinos in events with three leptons and missing transverse momentum in $\sqrt{s} = 8$TeV pp collisions with the ATLAS detector. *JHEP*, 04:169, 2014. arXiv:1402.7029, doi:10.1007/JHEP04(2014)169.

[444] Morad Aaboud et al. Search for the direct production of charginos and neutralinos in final states with tau leptons in $\sqrt{s} = 13$ TeV pp collisions with the ATLAS detector. *Eur. Phys. J. C*, 78(2):154, 2018. arXiv:1708.07875, doi:10.1140/epjc/s10052-018-5583-9.

[445] Georges Aad et al. Search for chargino-neutralino production with mass splittings near the electroweak scale in three-lepton final states in $\sqrt{s}$=13 TeV pp collisions with the ATLAS detector. *Phys. Rev. D*, 101(7):072001, 2020. arXiv:1912.08479, doi:10.1103/PhysRevD.101.072001.

[446] Armen Tumasyan et al. Search for electroweak production of charginos and neutralinos at s=13TeV in final states containing hadronic decays of WW, WZ, or WH and missing transverse momentum. *Phys. Lett. B*, 842:137460, 2023. arXiv:2205.09597, doi:10.1016/j.physletb.2022.137460.

[447] Georges Aad et al. Search for direct production of electroweakinos in final states with one lepton, jets and missing transverse momentum in pp collisions at $\sqrt{s} = 13$ TeV with the ATLAS detector. *JHEP*, 12:167, 2023. arXiv:2310.08171, doi:10.1007/JHEP12(2023)167.

[448] Richard D. Ball et al. Parton distributions for the LHC Run II. *JHEP*, 04:040, 2015. arXiv:1410.8849, doi:10.1007/JHEP04(2015)040.

[449] ATLAS Run 1 Pythia8 tunes. Technical Report ATL-PHYS-PUB-2014-021, CERN, Geneva, Nov 2014. URL: http://cds.cern.ch/record/1966419.

[450] A. Djouadi et al. Benchmark scenarios for the NMSSM. *JHEP*, 07:002, 2008. arXiv:0801.4321, doi:10.1088/1126-6708/2008/07/002.

[451] Peter Z. Skands et al. SUSY Les Houches accord: Interfacing SUSY spectrum calculators, decay packages, and event generators. *JHEP*, 07:036, 2004. arXiv:hep-ph/0311123, doi:10.1088/1126-6708/2004/07/036.

[452] B. C. Allanach et al. SUSY Les Houches Accord 2. *Comput. Phys. Commun.*, 180:8–25, 2009. arXiv:0801.0045, doi:10.1016/j.cpc.2008.08.004.

[453] Armen Tumasyan et al. Identification of hadronic tau lepton decays using a deep neural network. *JINST*, 17:P07023, 2022. `arXiv:2201.08458`, `doi:10.1088/1748-0221/17/07/P07023`.

[454] Jonathan M. Butterworth, Adam R. Davison, Mathieu Rubin, and Gavin P. Salam. Jet substructure as a new Higgs search channel at the LHC. *Phys. Rev. Lett.*, 100:242001, 2008. `arXiv:0802.2470`, `doi:10.1103/PhysRevLett.100.242001`.

[455] Morad Aaboud et al. Jet reconstruction and performance using particle flow with the ATLAS Detector. *Eur. Phys. J. C*, 77(7):466, 2017. `arXiv:1703.10485`, `doi:10.1140/epjc/s10052-017-5031-2`.

[456] Particle-Flow Event Reconstruction in CMS and Performance for Jets, Taus, and MET. 4 2009.

[457] Yuri L. Dokshitzer, G. D. Leder, S. Moretti, and B. R. Webber. Better jet clustering algorithms. *JHEP*, 08:001, 1997. `arXiv:hep-ph/9707323`, `doi:10.1088/1126-6708/1997/08/001`.

[458] Matteo Cacciari, Gavin P. Salam, and Gregory Soyez. FastJet User Manual. *Eur. Phys. J. C*, 72:1896, 2012. `arXiv:1111.6097`, `doi:10.1140/epjc/s10052-012-1896-2`.

[459] Andrew J. Larkoski, Simone Marzani, Gregory Soyez, and Jesse Thaler. Soft Drop. *JHEP*, 05:146, 2014. `arXiv:1402.2657`, `doi:10.1007/JHEP05(2014)146`.

[460] Mrinal Dasgupta, Alessandro Fregoso, Simone Marzani, and Gavin P. Salam. Towards an understanding of jet substructure. *JHEP*, 09:029, 2013. `arXiv:1307.0007`, `doi:10.1007/JHEP09(2013)029`.